SANDIA REPORT

SAND2007-4088
Unlimited Release
Printed July 2007

Development and Validation of Bonded Composite Doubler Repairs for Commercial Aircraft

Dennis Roach and Kirk Rackow

Work sponsored by:
FAA William J. Hughes Technical Center

Prepared by
Sandia National Laboratories
Albuquerque, New Mexico 87185 and Livermore, California 94550

Sandia is a multiprogram laboratory operated by Sandia Corporation, a Lockheed Martin Company, for the United States Department of Energy's National Nuclear Security Administration under Contract DE-AC04-94AL85000.

Issued by Sandia National Laboratories, operated for the United States Department of Energy by Sandia Corporation.

Available to DOE and DOE contractors from
U.S. Department of Energy
Office of Scientific and Technical Information
P.O. Box 62
Oak Ridge, TN 37831

Telephone: (865)576-8401
Facsimile: (865)576-5728
E-Mail: reports@adonis.osti.gov
Online ordering: http://www.osti.gov/bridge

Available to the public from
U.S. Department of Commerce
National Technical Information Service
5285 Port Royal Rd
Springfield, VA 22161

Telephone: (800)553-6847
Facsimile: (703)605-6900
E-Mail: orders@ntis.fedworld.gov
Online order: http://www.ntis.gov/help/ordermethods.asp?loc=7-4-0#online

SAND2007-4088
Unlimited Release
Printed July 2007

Development and Validation of Bonded Composite Doubler Repairs for Commercial Aircraft

Dennis Roach
Kirk Rackow
Infrastructure Assurance and Nondestructive Inspection Department, 6416

Sandia National Laboratories
P. O. Box 5800
Albuquerque, NM 87185-0615

ABSTRACT

A typical aircraft can experience over 2,000 fatigue cycles (cabin pressurizations) and even greater flight hours in a single year. An unavoidable by-product of aircraft use is that crack, impact, and corrosion flaws develop throughout the aircraft's skin and substructure elements. Economic barriers to the purchase of new aircraft have placed even greater demands on efficient and safe repair methods. The use of bonded composite doublers offers the airframe manufacturers and aircraft maintenance facilities a cost effective method to safely extend the lives of their aircraft. Instead of riveting multiple steel or aluminum plates to facilitate an aircraft repair, it is now possible to bond a single Boron-Epoxy composite doubler to the damaged structure. The FAA's Airworthiness Assurance Center at Sandia National Labs (AANC), Boeing, and Federal Express completed a pilot program to validate and introduce composite doubler repair technology to the U.S. commercial aircraft industry. This project focused on repair of DC-10 fuselage structure and its primary goal was to demonstrate routine use of this repair technology using niche applications that streamline the design-to-installation process. As composite doubler repairs gradually appear in the commercial aircraft arena, successful flight operation data is being accumulated. These commercial aircraft repairs are not only demonstrating the engineering and economic advantages of composite doubler technology but they are also establishing the ability of commercial maintenance depots to safely adopt this repair technique.

This report presents the array of engineering activities that were completed in order to make this technology available for widespread commercial aircraft use. Focused laboratory testing was conducted to compliment the field data and to address specific issues regarding damage tolerance and flaw growth in composite doubler repairs. Fatigue and strength tests were performed on a

simulated wing repair using a substandard design and a flawed installation. In addition, the new Sol-Gel surface preparation technique was evaluated. Fatigue coupon tests produced Sol-Gel results that could be compared with a large performance database from conventional, riveted repairs. It was demonstrated that not only can composite doublers perform well in severe off-design conditions (low doubler stiffness and presence of defects in doubler installation) but that the Sol-Gel surface preparation technique is easier and quicker to carry out while still producing optimum bonding properties. Nondestructive inspection (NDI) methods were developed so that the potential for disbond and delamination growth could be monitored and crack growth mitigation could be quantified. The NDI methods were validated using full-scale test articles and the FedEx aircraft installations. It was demonstrated that specialized NDI techniques can detect flaws in composite doubler installations before they reach critical size. Probability of Detection studies were integrated into the FedEx training in order to quantify the ability of aircraft maintenance depots to properly monitor these repairs. In addition, Boeing Structural Repair and Nondestructive Testing Manuals were modified to include composite doubler repair and inspection procedures. This report presents the results from the FedEx Pilot Program that involved installation and surveillance of numerous repairs on operating aircraft. Results from critical NDI evaluations are reported in light of damage tolerance assessments for bonded composite doublers. This work has produced significant interest from airlines and aircraft manufacturers. The successful Pilot Program produced flight performance history to establish the durability of bonded composite patches as a permanent repair on commercial aircraft structures. This report discusses both the laboratory data and Pilot Program results from repair installations on operating aircraft to introduce composite doubler repairs into mainstream commercial aircraft use.

This work was performed for the Federal Aviation Administration under Work-for-Others agreement 027941007. Sandia National Laboratories is a multiprogram laboratory operated by Sandia Corporation, a Lockheed Martin Company, for the United States Department of Energy's National Nuclear Security Administration under contract DE-AC04-94AL85000. This document is currently under review by the FAA for parallel publication by the Department of Transportation.

Acknowledgements

The operation and maintenance of commercial aircraft requires the frequent interaction of multiple agencies. The unique nature of this program accentuated the need for these close ties and the program's success hinged on close cooperation among all participants. Federal Express engineering and shop personnel worked with the Sandia Labs AANC to set up the infrastructure for the repairs and assist in the composite doubler installations. The authors would like to acknowledge the following FedEx participants: Mark Collins, Dave Cervantes, Ed Sawyer, Glen Maiden, Bill Cusato, Mike Guitterez, Chris Roselli, Dave Halloway, and Armen Tashdjian. Team members at Boeing included: Nik Sheth, Cong Duong, Jeff Tom, Jun Hu, Steve Feldman, Gerry Bonnar, Miles Nomura, Bill Jappe and Dwight Wilson. Special thanks go to the FAA participants who provided guidance and direction on all aspects of this program. Ron Atmur and Bob Easton provided oversight and review from the FAA Aircraft Certification Office in Long Beach. Additional guidance was contributed by Al Broz (FAA Chief Scientist NDI), Larry Ilcewicz (FAA National Resource Specialist Composites), and Rusty Jones (FAA National Resource Specialist NDI). Project management duties were carried out by Dave Galella, Rob Pappas, and Paul Swindell at the FAA's William J. Hughes Technical Center. Support for the structural health monitoring work was provided by Rob Hannum at Acellent Technologies (piezoelectric sensors) and Steven Kreger at Blue Road Research (fiber optics). Specific contributions to the NDI information presented here came from Waylon DeLong at Sandia Labs. This work was funded by the FAA William J. Hughes Technical Center under a U.S. Department of Transportation contract.

Development and Validation of Bonded Composite Doubler Repairs for Commercial Aircraft

TABLE OF CONTENTS

Development and Validation of Bonded Composite Doubler Repairs for Commercial Aircraft

1.0 INTRODUCTION

The number of commercial airframes exceeding twenty years of service continues to grow. In addition, Service Life Extension Programs are becoming more prevalent and test and evaluation programs are presently being conducted to extend the "economic" service life of commercial airframes to thirty years. A typical aircraft can experience over 2,000 fatigue cycles (cabin pressurizations) and even greater flight hours in a single year. An unavoidable by-product of aircraft use is that crack and corrosion flaws develop throughout the aircraft's skin and substructure elements. Economic barriers to the purchase of new aircraft have created an aging aircraft fleet and placed even greater demands on efficient and safe repair methods. The use of bonded composite doublers offers the airframe manufacturers and aircraft maintenance facilities a cost effective method to safely extend the lives of their aircraft.

1.1 Project Overview

The FAA's Airworthiness Assurance Center at Sandia National Labs (AANC) completed a program with Boeing and Federal Express to validate and introduce composite doubler repair technology to the U.S. commercial aircraft industry. The team also included participants from the FAA Long Beach Aircraft Certification Office (ACO), and the FAA's William J. Hughes Technical Center so that FAA oversight remained constant throughout the project. This project focuses on repair of DC-10 structure and builds on the foundation of the successful L-1011 door corner repair that was completed by the AANC, Lockheed-Martin, and Delta Air Lines [1]. The L-1011 composite doubler repair was installed in 1997 and did not develop any flaws in over three years of service. As a follow-on effort, this DC-10 repair program investigated design, analysis, performance (durability, flaw containment, reliability), installation, and nondestructive inspection issues. The multi-year Pilot Program, involving repair of DC-10 aircraft in the FedEx fleet, demonstrated the successful, routine use of composite doubler repairs on commercial aircraft.

The primary goal of this program was to move the technology into niche applications and to streamline the design-to-installation process. Using the data accumulated to date, the team has designed and analyzed repairs and developed inspection techniques for an array of composite doubler repairs with high-use fuselage skin applications. The general DC-10 repair areas which provide a high payoff to FedEx and which minimize design and installation complexities were identified as follows: 1) gouges, dents, lightning strike, and impact skin damage, and 2) corrosion grind outs in surface skin. This report presents the engineering activities used to evaluate the technology, as well as the steps that have been taken by industry to make this technology available for widespread commercial aircraft use.

As part of the successful pilot program, an infrastructure was put in place to accommodate the routine use of composite doublers. This was done by adding their designs alongside the riveted metallic repair tables commonly found in OEM Structural Repair Manuals (SRM). Using these look-up tables, maintenance facilities can have the option of choosing the traditional metallic repair or the "equivalent" composite doubler repair. In addition, Boeing prepared Material Specifications to allow for the use of Boron-Epoxy composite material on their aircraft. The summary of the aircraft repair activity with Boeing and FedEx follows.

Goal: Produce array of composite doubler repairs for commercial aircraft that provide engineering and economic benefits to operators; demonstrate streamlined design-to-installation process that eliminates the need to precede each repair with a lengthy research and development study; modify Structural Repair and NDT Manuals to include the composite doubler repair process and allow for widespread use of technology.

Approach: Utilize experience base of team members to produce an applicable and beneficial repair project; minimize disruption of normal maintenance activities; construct pre-fabricated array of repairs to allow for quick repair turnaround of damaged aircraft.

Target Aircraft: DC-10/MD-11

Applications Chosen: Damage to fuselage skin; these applications provide high use locations and ease of installation.

1.2 Background

Repairs and reinforcing doublers using bonded composites have numerous advantages over mechanically fastened repairs. Adhesive bonding eliminates stress concentrations, and new potential crack initiation sites caused by additional fastener holes. Composites are readily formed into complex shapes permitting the repair of irregular components. Also, composite doublers can be tailored to meet specific anisotropy needs thus eliminating the undesirable stiffening of a structure in directions other than those required. Other advantages include corrosion resistance, a high strength-to-weight ratio, and potential time savings in installation. The economic advantages stem primarily from time savings in installation and the secondary effect of reduced aircraft downtime. Exact dollar values depend on the complexity of the repair installation and the number of repairs installed.

DC-10 Aircraft Application Background - The use of bonded composite doublers offers the airframe manufacturers and airline maintenance facilities a cost effective technique to safely extend the lives of their aircraft. Instead of riveting multiple metallic plates to facilitate an aircraft repair, it is now possible to bond a single Boron-Epoxy composite doubler to the damaged structure. The tasks completed in the DC-10 effort addressed feasibility, technology limitations, design, analysis, structural integrity, inspection, and FAA oversight issues. This installation program represents a major step towards widespread use of composite doublers. This

effort concentrated on common, high use aircraft skin repairs to quickly accumulate both installation and flight performance history. This allowed a track record to be created within the FAA community that demonstrated the proper use of composite doublers.

A design and analysis process was conducted to produce a repair set with as wide an application regime as possible. Fuselage skins up to 0.080" thick could be repaired with the composite doublers. The doubler footprint could include frames and longerons but not production joints or finger doubler joints. Repairs for 1", 3", and 5" diameter damage were designed and analyzed. All of the repairs were 13 ply, quasi-isotropic doublers with symmetrical lay-ups.

Installation in Typical Aircraft Maintenance Depots - An infrastructure for supporting routine use of composite doublers was demonstrated at the Federal Express LAX maintenance facility. The family of composite doubler repairs were laid up in advance in order to be quickly available for repairs. Composite doubler installation job cards were prepared from Engineering Authorization (EA) documents produced by FedEx engineers. Specialized training for composite shop and NDI shop personnel was completed to allow workers to properly carry out each job card. All composite doublers installed during the Pilot Program were closely monitored by frequent inspections to accumulate flight performance history and to validate the entire repair process as implemented by a commercial carrier. This approach demonstrated to the FAA that composite doubler repair technology can be safely transferred to industry.

Typical Composite Doubler Installation - Figure 1 shows a typical bonded composite doubler repair over a cracked parent aluminum structure. Sample composite doubler installations, showing two families of potential aircraft repair applications, are shown in Figure 2. The number of plies and fiber orientation are determined by the nature of the reinforcement required (i.e. stress field and configuration of original structure). Surface preparation is the most critical aspect of the doubler installation. This consists of paint removal, solvent clean, scotch-brite abrasion and chemical treatment to assure proper adhesion. Since the doubler must be installed in the field, vacuum bag pressure and thermal heat blankets, commonly used on in-situ honeycomb repairs, are used to cure the composite laminate and adhesive layer.

The taper at the edge of the doubler is used to produce a gradually increasing stress gradient in the area of primary load transfer. In some applications, such as the L-1011 door corner doubler design, lightning protection is provided by a copper wire mesh which is imbedded in an adhesive film and applied as a top ply over the doubler. The lightning protection ply has a larger footprint than the composite laminate in order to provide a conductive link between the copper mesh and the surrounding aluminum skin. Finally, a top ply of fiberglass is installed to supply mechanical and environmental protection for the installation. Figure 3 shows a riveted, metal repair for the door corner application shown in Fig. 2. The fastened repair consists of two layers of aluminum skin and two layers of titanium skin. In addition, each plate has a unique and complex shape and must be formed to match the fuselage contour. Finally, the plates are mounted to the aircraft using an intricate rivet pattern. The composite doubler repair on the Delta Airlines door corner produced a 50% reduction in installation man-hours versus the riveted repair shown in Fig. 3

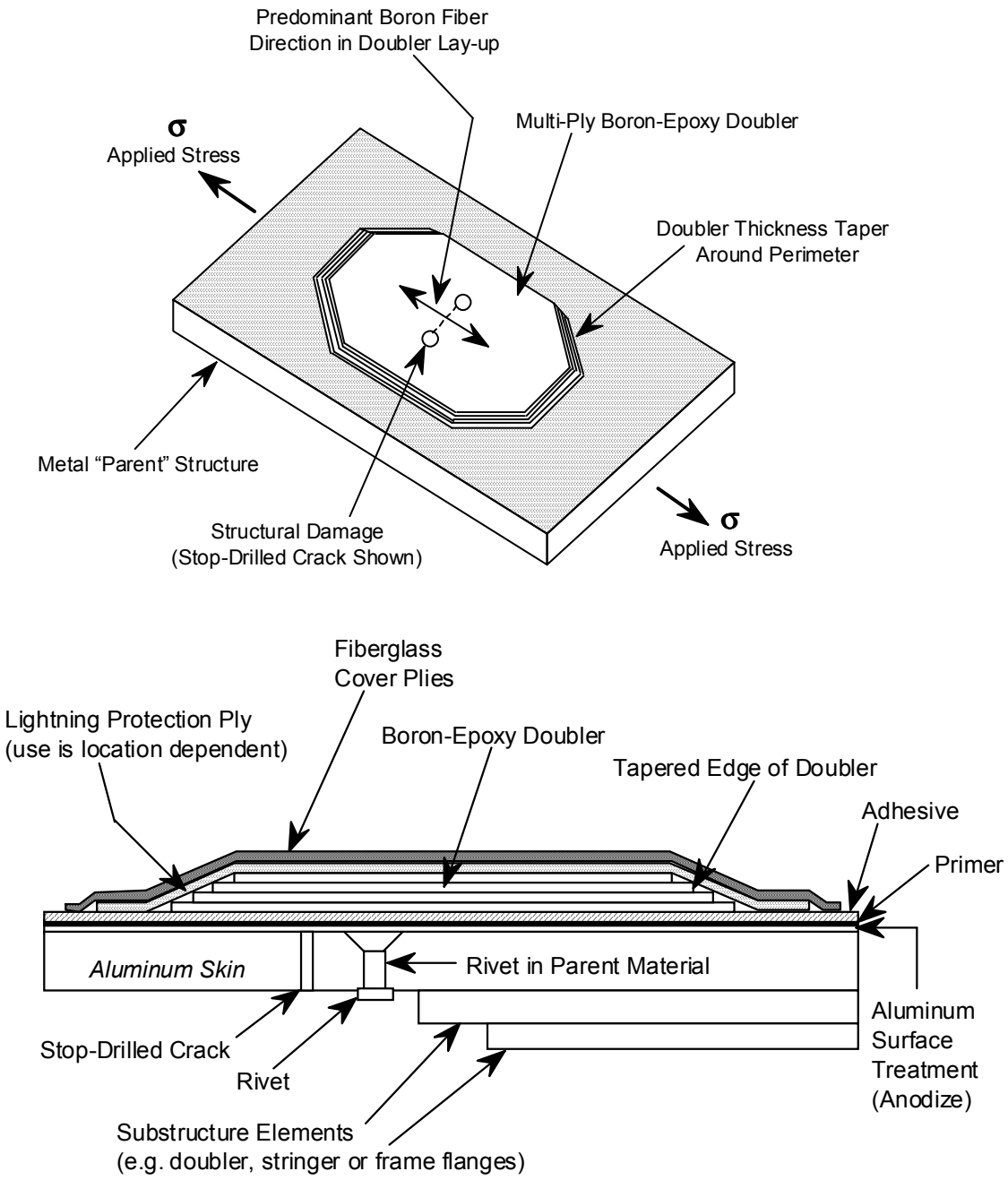

Figure 1: Schematic and Isometric Views of a Bonded Composite Doubler Installation on an Aluminum Skin

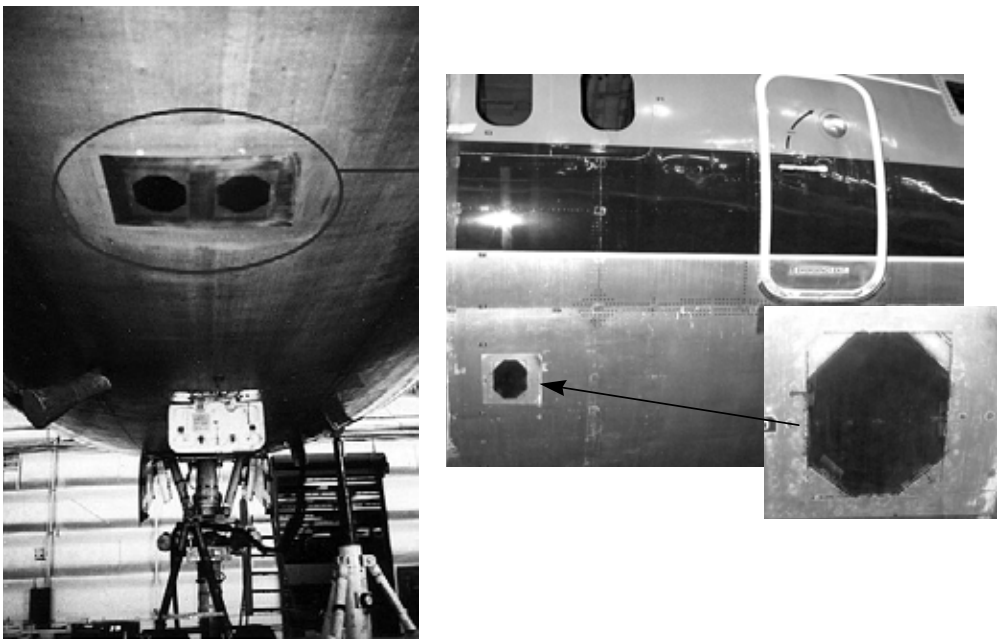

(a) Sample Fuselage Skin Repair
(composite doubler approx. 12" X 10")

(b) Sample Door Corner Repair – First Composite Doubler Repair (L-1011 Aircraft)
(composite doubler approx. 5 ft.^{2} footprint)

Figure 2: Sample Bonded Composite Doubler Installations Showing Two Families of Potential Repair Applications

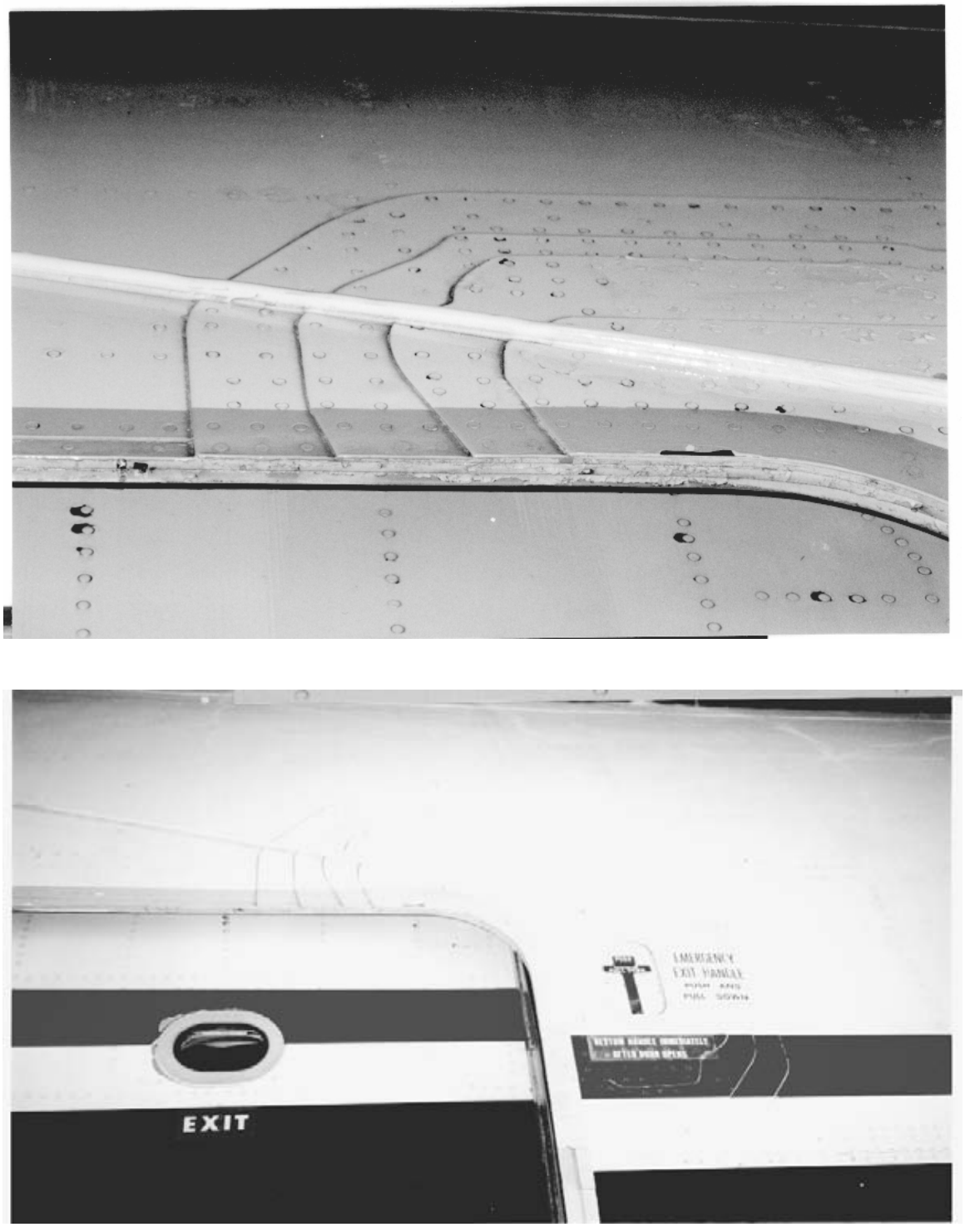

Figure 3: Conventional Door Corner Repair with Four Riveted Metal Plates; Close-Up View Shows Intricate Rivet Pattern and Complex Shape of Quadrupler Plates

1.3 Doubler Design Guidelines

Moving Technology into Routine Maintenance Programs - Reference [2] describes airframe maintenance programs from an airlines' perspective. It describes sources of aircraft damage and how the damage is addressed through inspection and repair tasks. A detailed maintenance program is required to ensure that an aircraft can be operated safely for an extended period of time. The emphasis of the maintenance program must be constantly adjusted to cater to the age of the fleet [2]. These revisions require the co-operation of the aircraft manufacturers, the airlines, and the airworthiness authority to ensure that changes made are technically correct, stringent enough to assure the aircraft's continued safety, with due consideration to the cost to the airline. Aircraft structures suffer continuous degradation throughout their service lives. Corrosion, fatigue, impact and accidental damage from assorted ground activities all contribute to this structural degradation. The airlines and aircraft maintenance depots accomplish permanent and interim repairs suited to the situation and in line with current industry practices. These acceptable repair practices must be continuously revisited and expanded to take advantage of new materials, new processes, and new techniques that offer both engineering and economic advantages. Through the steady and comprehensive introduction of test data, analyses, and in-service composite doubler installations on commercial aircraft a critical database has been assembled to accurately guide enhancements to formal maintenance programs. This is an important step in the evolution of composite doubler applications since it will eliminate the need for each bonded composite repair to be preceded by a lengthy research and testing program.

Doubler Design Guidelines – References [3-6] provide an excellent set of guidelines for designing composite doubler repairs. The primary issues to be addressed include the optimum location, size, shape, and laminate taper for the patches. The major factors that determine the patch design parameters are the stress levels at the repaired flaw, the stress levels in the composite doubler (maximum allowable fiber stresses), and the stress levels in the adhesive layer between the doubler and the aluminum skin. The important, fundamental results produced by Jones and Callinan in ref. [3] are worth reviewing in some detail in order to prepare for the damage tolerance discussions later in this report.

The ref. [3] crack repair study used a unidirectional Boron-Epoxy laminate (fiber perpendicular to crack) as a baseline design. The study found that for patches that cover the entire length of the crack, a one ply (0.0058" thick) patch reduces the stress intensity factor to 33.5% of its value for the unpatched crack. Furthermore, the rate of decrease in the stress intensity factor, K_{1P}, as the patch thickness increases was found to be quite low. A six layer patch, for example, produced a K_{1P} value of 19.5% of the unpatched value. Thus, an increase in patch thickness by a factor of 6 only produces an additional 14% reduction in the stress intensity factor. Another important finding of the ref. [8] study was that in thin patches, the stresses over the flaw (in both the patch and the adhesive) are critical. However, as the patch thickness is increased, the shear stresses in the adhesive at the edges of the patch footprint become critical and may exceed allowable limits. The findings summarized above produced a series of design requirements that are necessary to maintaining the structural integrity of a composite doubler repair [3].

1) Fiber Strain – For a maximum Boron fiber strain of 5,000 με, the stress in the fibers must satisfy

$$\sigma_f \leq 0.005\ E_{11} \qquad (1)$$

where E_{11} is Young's modulus in the direction of the fibers (28.0 X 10^6 psi). When the fiber stress concentration, K_f, is considered the governing equation for fiber strain becomes

$$\sigma_f = K_f \sigma \leq .14\ \text{lb/in}^2 \qquad (2)$$

Thus, if the applied stress, σ, is known the maximum permissible value of K_f and the minimum permissible patch thickness can be determined.

2) Shear Stress in Adhesive – For a maximum allowable adhesive shear stress of 7 KSI and considering the stress concentrations at the crack and at the edge of the patch, the following design equations must be satisfied

$$\tau_{a(c)} = K_{a(c)} \sigma \leq 7{,}000\ \text{lb/in}^2 \qquad (3)$$

$$\tau_{a(e)} = K_{a(e)} \sigma \leq 7{,}000\ \text{lb/in}^2 \qquad (4)$$

Equations (2) and (3) can be solved to produce a doubler thickness to satisfy the stress requirements at the crack (for both laminate and adhesive). However, this often produces adhesive stresses at the edge of the doubler that exceed those allowed by eq. (4). The adhesive stresses at the edge of the doubler can be reduced to admissible levels by stepping the thickness of the doubler from one or two plies at the outer perimeter to full thickness over a taper region. The length of the taper region is normally chosen to produce an edge taper ratio (taper depth-to-thickness increase ratio) of 10 to 30. Figure 1 shows a typical doubler edge taper used to gradually transfer load from the aluminum skin and reduce the shear stress in the adhesive. The design of the composite doublers for DC-10 skin damage encountered this need to balance doubler thickness with an appropriate edge taper [7]. Ref. [3] provides quantitative stress reductions corresponding to the use of stepped doublers. It also lists the effects of varying adhesive thickness and the difference between single- and double-sided repairs.

1.4 Damage Tolerance and Fracture Control Plan

1.4.1 Damage Tolerance and Analysis Methodologies

Inspection requirements (sensitivity and inspection intervals) are driven by Damage Tolerance Analyses (DTA). However, the stack of metal parent material (isotropic), composite lamina (anisotropic), and adhesive layers makes the analysis quite complex and hinders the calculation of an exact DTA. It is difficult to determine the effects of flaw size and the point at which a flaw size/location becomes critical. This is especially true of disbond, delamination, and porosity

flaws. Thus, an increased emphasis is placed on quantifying the probability that a flaw of a particular size and location will be detected by a piece of NDT equipment. *In any surveillance of aircraft structure there are three main aspects to the inspection requirements: 1) the damage tolerance analysis (DTA) which determines the flaw onset and growth data (especially critical flaw size information), 2) the sensitivity, accuracy, and repeatability of NDI techniques which, in concert with the DTA, establishes the minimum inspection intervals, and 3) the impediments that the NDI techniques must contend with while achieving the required level of sensitivity.* In addition to this report, detailed discussions on damage tolerance assessments for composite materials are presented in references [8-12].

The reference [11] observations mirror one of the primary results obtained in the damage tolerance assessment presented in this report: adhesively bonded doublers are extremely damage tolerant to large disbonds and other detrimental conditions such as impact and hot-wet conditioning. These results are quantified in Chapter 5 of this report. If, in fact, disbond and delamination flaws do not grow even under extreme environmental conditions, then an acceptable design should be predicated on the fact that the stresses in the adhesive are kept below a limiting or threshold value. As a result, reference [11] introduces an essential design methodology that considers damage tolerance. It uses a fatigue threshold load, P_f, and a fatigue threshold strain, ε_f, below which irreversible damage in the adhesive will not occur. For thin skin repairs, the equations used to determine the threshold load and strain values are as follows:

$$P_f = 2\,(t\,W_f\,ET)^{1/2} \tag{5}$$

$$\varepsilon_f = 2\,(t\,W_f\,E/T)^{1/2} \tag{6}$$

where,

t = thickness of the adhesive
T = thickness of the adherend (skin)
E = Young's modulus of the skin
W_f = threshold value of the strain energy density of the adhesive

W_f can be determined experimentally [12]. Ref. [11] also describes the maximum load, P_{max}, that can be carried by a bond in a symmetrical bonded joint as,

$$P_{max} = 2\,(t\,W_c\,ET)^{1/2} \tag{7}$$

where W_c is the maximum strain energy density of the adhesive. Thus, composite doubler repair design guidelines are that P_{max} is greater than the ultimate load for the repaired structure and that P_f is greater than the limit load. Ref. [11] also points out that these critical design variables are affected by the loading rate. A conservative estimate for P_{max} can be obtained by using the value of the maximum von Mises equivalent stress in the adhesive, σ_e, as measured in high strain rate tests. For FM73, the adhesive used in this study, $\sigma_e = P_{max}$ = 5,800 psi and the threshold stress σ_{th} = 3,600 psi. This analysis approach clearly shows the importance of the adhesive in determining the overall performance of the bonded repair. The effects of the inelastic strain build-up in the adhesive layer can accumulate with each load cycle. This hysteresis must be

considered when determining the loads and fatigue cycles necessary to reach the maximum strain. The approach outlined above has been in composite doubler design to address damage tolerance provisions of the U.S. Federal Aviation Regulations (FAR) Part 25.

The abilities of nondestructive inspection techniques to meet the DTA flaw detection requirements are presented in references [13-17]. The fundamental result from the ref. [14] NDI study and Section 5 of this report is that a team of NDI techniques can identify flaws well before they reach critical size. Crack detection in the parent aluminum material can be accomplished using conventional eddy current and X-ray techniques. Also, ultrasonic and thermography methods have been successfully applied to the problem of disbond and delamination detection.

1.4.2 Analysis of Composite Repairs

Numerous efforts have developed, refined, and advanced the use of methodologies needed to analyze composite doubler installations. Obviously, this is a critical element in the repair process since a badly implemented repair is detrimental to fatigue life and may lead to the near-term loss of structural integrity. The difficulties associated with analyzing the stress fields and flaw tolerance of various composite doubler designs and installations are highlighted in references [8-10]. Doubler design and analysis studies [11, 18-25] have led to computer codes and turn-key software [26-27] for streamlining the analyses. These developments have taken great strides to eliminate the approximations and limitations in composite doubler DTA. In references [8] and [20], Baker presents an extensive study of crack growth in repaired panels under constant amplitude and spectrum loading. The installation variables evaluated were: 1) doubler disbond size, 2) applied stress, 3) doubler thickness, 4) min-to-max stress ratios (R ratio), and 5) temperature.

In refs. [8] and [20], a predictive capability for the growth of cracks repaired with composite doublers was developed using Rose's analytical model [21] and experimental fatigue studies. The important stress variables include the stress range, $\Delta\sigma_\infty$, and stress ratio, R, where,

$$\Delta\sigma_\infty = \sigma_{max} - \sigma_{min} \tag{8}$$

$$R = \sigma_{min/}\, \sigma_{max} \tag{9}$$

A Paris-type crack growth relationship is assumed between da/dN and ΔK for the repaired crack such that,

$$da/dN = f(\Delta K,R) = A_R \Delta K^{n(R)} \tag{10}$$

where a is the crack length, N is the number of fatigue cycles, and A_R and $n(R)$ are constants for a given R value. Tests results in [8] and [20] produced crack growth constants and were used to validate the model for crack mitigation effects of composite doublers. It was determined that Rose's model for predicting the stress-intensity range, ΔK, provides a good correlation with measured crack growth data (da/dN), however, anomalies were observed in the cases of

temperature and R-ratio effects. Estimates of crack growth in composite doublers containing various disbond sizes were also determined.

In lieu of using computationally expensive, three-dimensional finite element analyses, reference [22] presents the use of a simple analysis using Mindlin plate theory. The aluminum parent plate and composite doubler are modeled separately by the Mindlin plate finite element (using ANSYS) and the adhesive layer is modeled with effective springs connecting the doubler to the aluminum plate. The model showed excellent agreement with existing boundary element solutions and three-dimensional finite element solutions when calculating the stress intensity factors for double-sided patches. However, the Mindlin plate theory produced appreciably different K values than a three-dimensional FEM for single-sided doubler repairs. These results highlight some of the difficulties in modeling composite doubler repairs and the need for innovative schemes to address single-sided repairs.

Complete three dimensional FEM analyses of composite doubler repairs are provided in reference [23]. Ref. [23] addressed one-sided repairs and showed that the stress intensity factor reaches an asymptotic value, rather than increasing indefinitely as would be the case for an unrepaired crack. Furthermore, the stress intensity factor can be approximated by an analytical expression that provides a close, yet conservative, estimate for repairs over all crack lengths. While the stress intensity factor for a one-sided repair is much less than the unrepaired configuration, it exceeds the value for the corresponding two-sided repair. This analytical finding supports test results that show the secondary bending induced by the shift in neutral axis in a one-sided patch has a detrimental effect on the efficiency of bonded composite repairs.

No discussion of design and analysis methodologies is complete without a mention of a closely-coupled validation program. Reference [24] presents a detailed design and analysis validation effort to substantiate a safety-critical repair to an F-111 lower wing skin. The repair substantiation involved both detailed FEM stress analysis and structural testing ranging from coupons to quasi full-scale specimens representing a spar-stiffened wing box structure. The intercomparison of results provides a high level of confidence that the static residual strength has been restored to the original ultimate strength levels. It also provides a good foundation for the subsequent management of the repaired structure by establishing inspection intervals with sufficient safety factors.

The test results presented in this document and in reference [13] supplement the composite doubler analyses efforts described above and provide a basis of comparison with computational models. Analysis improvements, however, must be validated by successful flight performance of operational doublers. This can only be accumulated over a long period of time. Continued surveillance of installed doublers will provide quantitative flight performance history and produce a conservative safety factor. Thus, regardless of the excellent damage tolerance results accumulated to date, NDI will continue to play a critical role in the use of composite doublers.

The development and evaluation activities discussed in this report, along with references [13-16], were conducted in a fashion that allowed the results to be applied to aircraft repairs in general. The overall goal in this approach is to minimize and optimize the testing that must compliment

each new composite doubler installation. In order for composite doubler technology to be useful to the commercial aircraft industry, the design-to-installation cycle must be streamlined.

Need for Damage Tolerance Assessments - One of the primary concerns surrounding composite doubler technology pertains to long-term survivability, especially in the presence of non-optimum installations. This test program demonstrated the damage tolerance capabilities of bonded composite doublers. The fatigue and strength tests quantified the structural response and crack abatement capabilities of Boron-Epoxy doublers in the presence of worst case flaw scenarios. The engineered flaws included cracks in the parent material, disbonds in the adhesive layer, and impact damage to the composite laminate. Environmental conditions representing temperature and humidity exposure were also included in the coupon tests.

1.4.3 Damage Tolerance Assessment to Establish Inspection Intervals

Damage tolerance is the ability of an aircraft structure to sustain damage, without catastrophic failure, until such time that the component can be repaired or replaced. The U.S. Federal Aviation Requirements (FAR 25) specify that the residual strength shall not fall below limit load, P_L, which is the load anticipated to occur once in the life of an aircraft. This establishes the minimum permissible residual strength $\sigma_P = \sigma_L$. To varying degrees, the strength of composite doubler repairs are affected by crack, disbond, and delamination flaws. The residual strength as a function of flaw size can be calculated using fracture mechanics concepts. Figure 4 shows a sample residual strength diagram. The residual strength curve is used to relate this minimum permissible residual strength, σ_P, to a maximum permissible flaw size a_P.

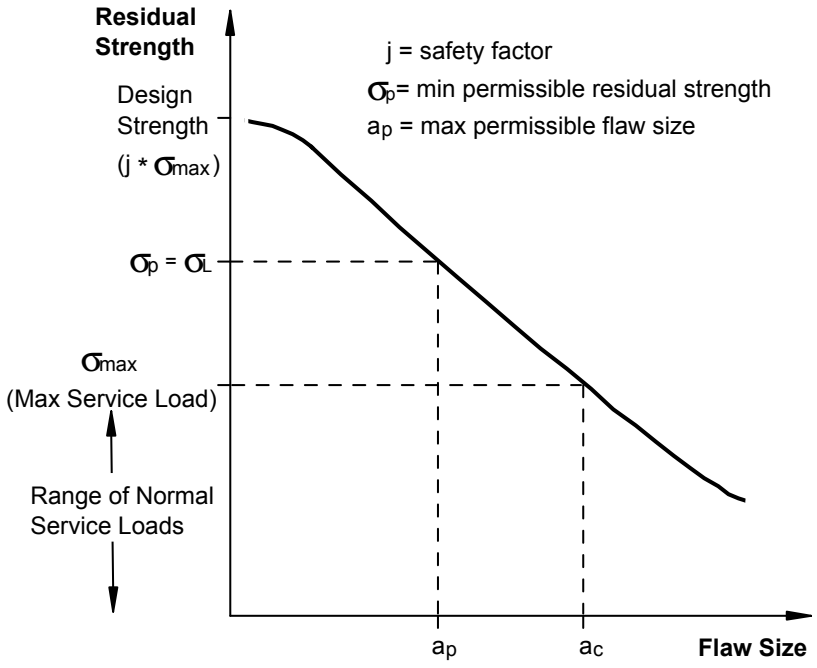

Figure 4: Residual Strength Curve

A fracture control plan is needed to safely address any possible flaws which may develop in a structure. Nondestructive inspection is the tool used to implement the fracture control plan. Once the maximum permissible flaw size is determined, the additional information needed to properly apply NDI is the flaw growth versus time or number of cycles. Figure 5 contains a flaw growth curve. The first item of note is the total time, or cycles, required to reach a_P. A second parameter of note is a_d which is the minimum detectable flaw size. A flaw smaller than a_d would likely be undetected and thus, inspections performed in the time frame prior to n_d would be of little value. The time, or number of cycles, associated with the bounding parameters a_d and a_P is set forth by the flaw growth curve and establishes *H(inspection)*. Safety is maintained by providing at least two inspections during *H(inspection)* to ensure flaw detection between a_d and a_P .

Inspection Intervals - An important NDI feature highlighted by Fig. 5 is the large effect that NDI sensitivity has on the required inspection interval. Two sample flaw detection levels a_d (1) and a_d (2) are shown along with their corresponding intervals n_d (1) and n_d (2) . Because of the gradual slope of the flaw growth curve in this region, it can be seen that the inspection interval H_1*(inspection)* can be much larger than H_2*(inspection)* if NDI can produce just a slightly better flaw detection capability. Since the detectable flaw size provides the basis for the inspection interval, it is essential that quantitative measures of flaw detection are performed for each NDI technique applied to the structure of interest. This quantitative measure is represented by a Probability of Detection (PoD) curve such as the one shown in Figure 6. Regardless of the flaw size, the PoD never quite reaches 1 (100% possibility of detection). Inspection sensitivity requirements normally ask for a 90-95% PoD at a_P. For any given inspection task, the PoD is affected by many factors such as: 1) the skill and experience of the inspector, 2) accessibility to the structure, 3) exposure of the inspection surface, and 4) confounding attributes such as underlying structure or the presence of rivets. Thus, the effects of circumstances on PoD must be accounted for in any NDI application and associated fracture control plan.

As an example of the DTA discussed above, reference [28] describes the design and analysis process used in the L-1011 program. It presents the typical data - stress, strength, safety factors, and damage tolerance - needed to validate a composite doubler design. The design was analyzed using a finite element model of the fuselage structure in the door region along with a series of other composite laminate and fatigue/fracture computer codes. Model results predicted the doubler stresses and the reduction in stress in the aluminum skin at the door corner. Peak stresses in the door corner region were reduced by approximately 30% and out-of-plane bending moments were reduced by a factor of 6. The analysis showed that the doubler provided the proper fatigue enhancement over the entire range of environmental conditions. The damage tolerance analysis indicated that the safety-limit of the structure is increased from 8,400 flights to 23,280 flights after the doubler installation (280% increase in safety-limit). It established an inspection interval for the aluminum and composite doubler of 4,500 flights.

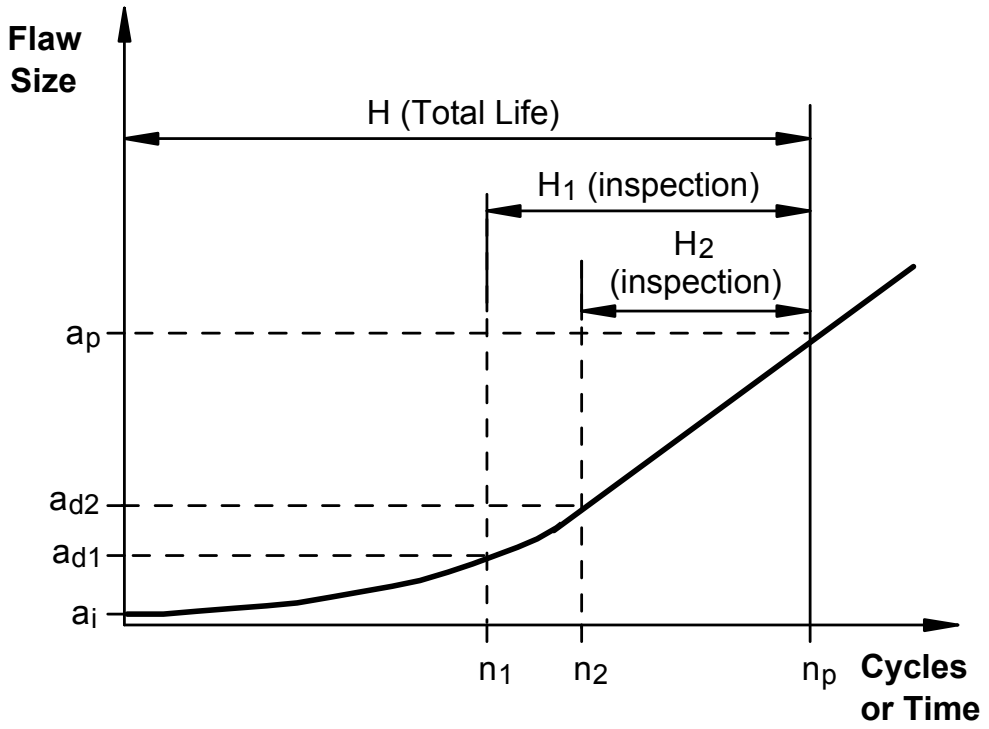

Figure 5: Crack Growth Curve Showing Time Available for Fracture Control

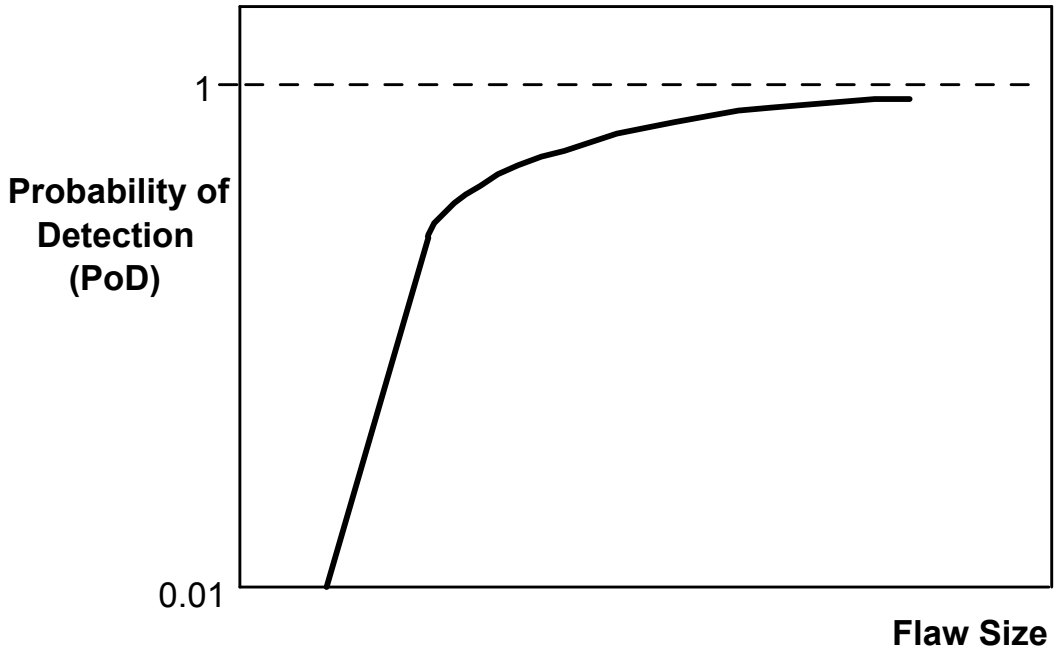

Figure 6: Probability of Flaw Detection vs. Flaw Size

1.5 Summary of Installation Process

All composite doublers were installed using either the Phosphoric Acid Non Tank Anodize (PANTA) surface preparation procedure and the Phosphoric Acid Containment System (PACS) equipment or the Sol-Gel surface preparation procedure. The Sol-Gel surface preparation procedure is discussed in Section 5.0. The PANTA installation procedure is provided in Boeing Specification D658-10183-1 (also listed as Textron specification 200008-001). This installation specification was used for the installation of over 150 Boron-Epoxy doublers on fatigue test specimens and for the installation of most Boron-Epoxy doublers on civil aircraft to date. Boeing Specification D658-10183-1 references a series of FAA-approved Boeing Aircraft Corporation (BAC) processes and Boeing Material Specifications (BMS) that are widely used by Boeing on commercial aircraft. The key installation steps – stemming from the general repair flowchart shown in Figure 7 - are summarized below.

Summary of Composite Doubler Installation Procedure

1. Aluminum Surface Preparation - Solvent clean per BAC 5750. Remove the oxide on the aluminum prior to Phosphoric Acid Anodize using Scotch Brite pads to achieve a 30 second water-break free condition per paragraph 6.6.9.2.2 of specification 200008-001. Phosphoric Acid Anodize (PAA) the aluminum surface using Phosphoric Acid Containment System (PACS) equipment as described in paragraph 6.6.9.2.2 of Boeing Specification D658-10183-1. Alternately, apply Sol-Gel chemical as per Boeing Structural Repair Manual.

2. Primer and Adhesive Process - Prime the PAA aluminum surface using Cytec BR-127 primer (or equivalent: EC3960), type 1, grade A per BMS 5-89 if used in conjunction with the PANTA process. Apply BR-6747 primer if used in conjunction with the Sol-Gel process. Co-cure the Cytec FM-73 (or equivalent: AF163) structural film adhesive per BMS 5-101 simultaneously with the Boron-Epoxy doubler.

3. Boron-Epoxy Doubler Installation and Cure - Lay up the 5521/4 Boron-Epoxy doubler in accordance with the application design drawing. Cure for 90 minutes at 250^{o}F or 180 minutes at 225^{o}F at 0.54 ATM vacuum bag pressure (equivalent atmospheric pressure is 7.35 psia) using standard "hot bonder." Use computer-controlled heat blankets to provide the proper temperature cure profile in the field. Use a series of thermocouples in an active feedback loop to maintain the proper temperature profile. Bag the doubler laminate in accordance with Figure 8. Note that one ply of bleeder cloth should be used for each 3-4 plies of boron/epoxy material in the doubler. Alternate temperature profiles can be used where lower cure temperatures are accompanied by longer cure times. The alternate temperature cures are:
    - 225^{o}F to 250^{o}F for 90 to 120 minutes
    - 210^{o}F to 225^{o}F for 180 to 210 minutes
    - 190^{o}F to 210^{o}F for 360 to 390 minutes

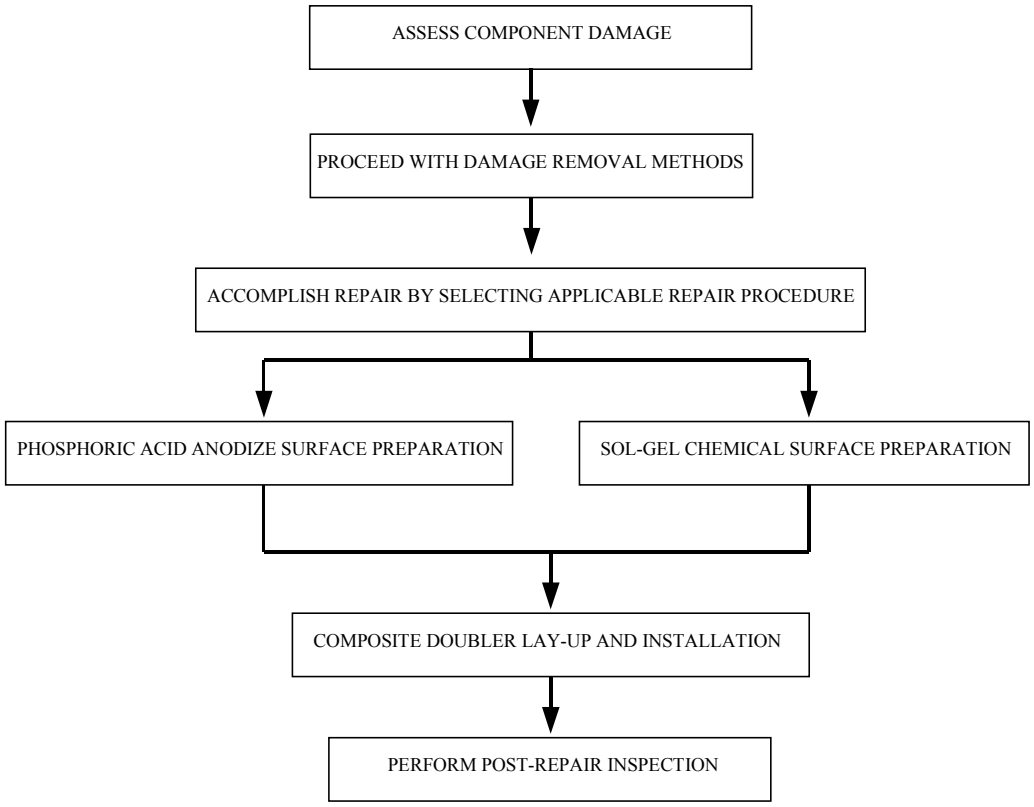

Figure 7: General Flowchart for Repair of Metallic Aircraft Structure Using Bonded Composite Repairs

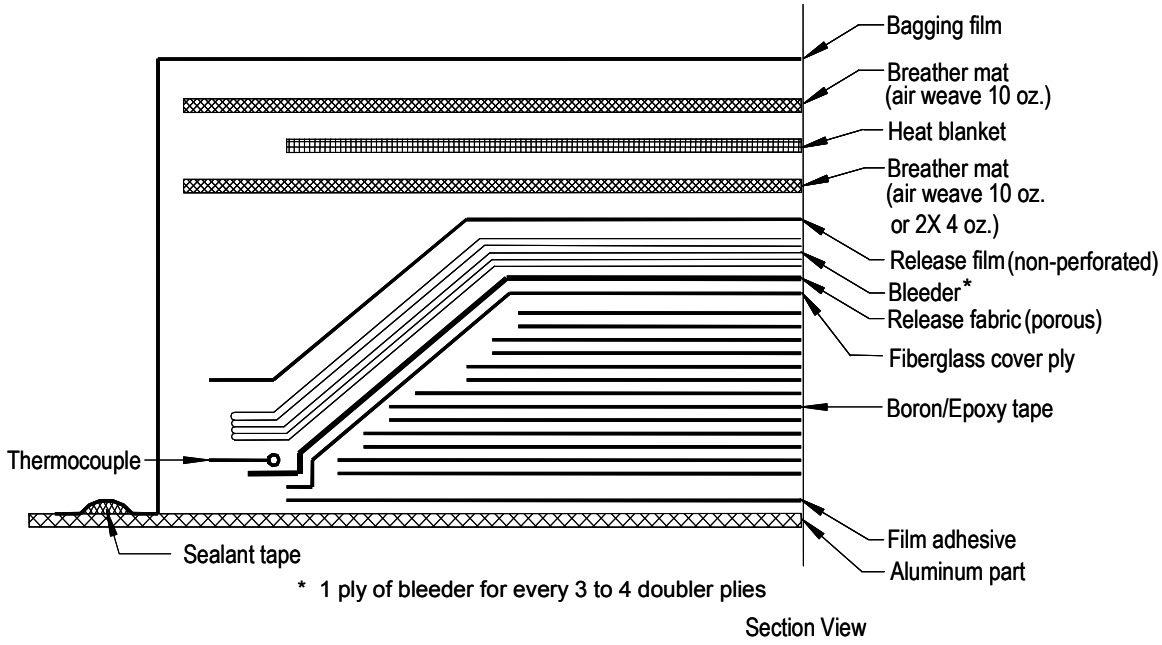

Figure 8: Vacuum Bagging for Cure of Doubler on Aluminum Skin

1.6 Technical and Economic Considerations

Cost-Benefit Assessment - A complete validation process must also include an assessment of the cost effectiveness of the new maintenance technique in light of the engineering advantages. This includes an analysis of the implementation costs represented by dollars, time, and resources that are used to carry out the maintenance practice (in this case aircraft repair and subsequent inspection). The aircraft repair process using bonded composite doublers has numerous advantages over conventional, mechanically fastened repairs. Following is a summary of the engineering and economic advantages. Table 1 compares the key features of composite doubler repairs with existing metallic doubler repair technology.

1.6.1 Engineering Advantages

The process of repairing airplane structures is time consuming and must be carefully engineered. A repair that is too stiff may result in a loss of fatigue life, continued growth of the crack being repaired, and the initiation of a new flaw in the undesirable high stress field around the patch. The use of rivets to apply conventional doublers exacerbates these problems. At present, there is a concern that when repairing multi-site or wide-spread fatigue damage using conventional methods, the close proximity of a large number of mechanically fastened repairs may lead to a compromise in the global damage tolerance of the structure. Numerous articles have addressed the myriad of concerns associated with repairing aircraft structures. Many of these repair difficulties can be addressed through the use of composite doublers. The aircraft repair process using bonded composite doublers has numerous advantages over conventional, mechanically fastened repairs.

1. **Adhesive bonding eliminates stress concentrations caused by additional fastener holes** - rivet holes create stress intensity factors (magnification) of 3 times the uniform stress field away from the metal doubler; the adhesive layer produces a gradual load transfer into the doubler and eliminates all stress risers. Adhesive bonding also makes repairs possible on structures that cannot tolerate additional fastener holes.

2. **Crack Mitigation Performance** - comprehensive fatigue testing has determined that the structure's fatigue life (resistance to crack growth) is improved 2.5 times greater than with metal doublers.

3. **Strength-to-Weight Ratio** - Composite laminates are over three times stronger than comparable metal repairs yet they are 50% lighter. Equivalent composite doublers can be up to 50% thinner than metal repairs. This reduces aircraft drag.

4. **Flexibility in Design** - The unidirectional strength of individual composite plies allows doublers to be tailored to meet specific anisotropy needs. This eliminates undesirable stiffening of a structure in directions other than those required. This feature works with item (1) to improve the fatigue life of the structure being repaired.

5. **Corrosion Resistance** - Boron-Epoxy material does not corrode and will not induce corrosion in the parent material. Metal doublers corrode over time. Corrosion beneath doublers, accelerated by water entrapment, is a common problem. Corrosion inspection, removal, and repair activities induce tremendous costs in the multi-billion dollar commercial aircraft maintenance industry.

6. **Formability** - Composite laminates are easily formed to fit the contour of fuselage sections and tight radius areas such as engine cowlings and leading edges of wings. Metal doublers can be formed to fit curved surfaces but this requires an additional machining process and incurs additional costs.

1.6.2 Economic Advantages

The economic advantages stem primarily from time savings in installation and the secondary effect of reduced aircraft downtime. Exact dollar values depend on the complexity of the repair installation and the number of repairs installed. In general, data accumulated to date using demonstration installations have indicated that it may be possible to realize a 50% - 60% savings in labor when applying composite doublers.

One of the most common aircraft repairs is the application of a doubler to a cracked, corroded, or dented surface skin (scab repairs). Composite doublers are particularly well suited to these type of repairs. Many of these repairs can be completed without accessing the inside of the aircraft structure. This can produce a large time savings if the comparable metallic doubler requires inside access to install the fasteners. These type of surface skin scab repairs can be found many times on a single aircraft. Thus, economies of scale come into play and the cost savings can be substantial when applied over a carrier's entire fleet.

An important by-product of the reduced man-hours needed to install a composite doubler repair is that it may be possible to return an aircraft to service earlier. In some cases, a composite doubler may allow for an overnight repair and eliminate any loss of service for an aircraft. Revenue loss for aircraft down time can be upwards of $100,000 per day. With approximately 10,000 aircraft flying in the U.S. commercial fleet, reduced aircraft downtime may represent the greatest potential for cost savings.

Aircraft Repair Feature	Bonded Composite Doublers	Riveted Metal Doublers	Advantage of Composites & Notes
Stress Field	• No need for additional fastener holes in structure • Bond provides a uniform stress filed	• New holes produce stress risers and fatigue crack initiation sites • Load transfer occurs exclusively at edge of doubler	• Produces gradual load transfer and more uniform stress field • Eliminates stress risers (stress magnification of 3 found in riveted doublers)
Fatigue Life	• Composite doubler can be tailored to provide stiffness only in the required directions • Bonded doubler provides uniform stress reduction in immediate vicinity of flaw	• Isotropic material produces uniform & sometimes undesirable stiffening in all directions	• Longer Fatigue Life: crack mitigation tests show less than half the crack growth over the same number of fatigue cycles (fatigue life improved by factor of 2.5) • Improved damage tolerance
Corrosion Resistance	• Boron-Epoxy material does not corrode or induce galvanic reaction in the parent aluminum material • Adhesive bonding process seals off material beneath it from all moisture	• Metal doublers will corrode over time • Installation provides location for water entrapment between doubler and parent aluminum structure; this accelerates corrosion process	• May eliminate follow-up maintenance costs (inspection, corrosion removal, replacement of metal doubler) • Avoids aggravation of initial flawed area
Aerodynamics	• Higher strength at reduced ply thickness allows for thinner doublers	• Typical repairs are two to four plates thick (0.125" to 0.375")	• Up to 50% decrease in thickness improves aerodynamics

Table 1: Comparison Between Bonded Composite Doubler Repair Technique and Riveted Metallic Doubler Aircraft Repairs

Aircraft Repair Feature	Bonded Composite Doublers	Riveted Metal Doublers	Advantage of Composites & Notes
Strength-to Weight	• Modulus = 28 msi • Tensile Strength = 225 ksi • Density = .066 lbs/in^3	• Modulus (alum/steel) = 10 / 30 msi • Tensile Strength (alum/steel) = 64 / 80 ksi • Density (alum/steel) = 0.100 / 0.283 lbs/in^3	• Strength properties exceed aluminum and steel • Improved fuel efficiency through reduction in aircraft weight (50% - 70% reduction in weight per doubler)
Method of Attachment to Aircraft	• Adhesive bonding	• Mechanical fasteners, rivets	• Certain structures, such as wing spars, cannot tolerate the addition of new holes (must be replaced rather than repaired) • Proper surface preparation and adhesive bonding processes are crucial to composite doublers
Formability	• Hand pressure can readily shape doubler to contoured surfaces (e.g. engine cowlings, wing leading edges)	• Machining process must be employed to provide proper contour on metal doublers in tight radii areas	• Eliminates additional step and associated costs

Table 1: Comparison Between Bonded Composite Doubler Repair Technique and Riveted Metallic Doubler Aircraft Repairs (continued)

Aircraft Repair Feature	Bonded Composite Doublers	Riveted Metal Doublers	Advantage of Composites & Notes
Installation Time	• Typical 1 ft.^{2} fuselage skin repair (12 man-hours)	• Typical 1 ft.^{2} fuselage skin repair (40 man-hours)	• Decreased aircraft down time • Maintenance cost savings due to reduced man-hours required
Material Cost	• Cost depends on size of doubler and number of plies • Typical 1 ft.^{2} skin repair doubler: $800 (20 plies)	• Depends on number of plates & rivets, metal type, and forming required • Typical 1 ft.^{2} skin repair doubler: $300 (including machining)	• Costs approximately 2.5 times comparable metal doublers • Greater material costs can be offset by savings in man-hours & decreased aircraft downtime

Table 1: Comparison Between Bonded Composite Doubler Repair Technique and Riveted Metallic Doubler Aircraft Repairs (continued)

2.0 DESIGN AND ANALYSIS OF FUSELAGE REPAIRS FOR WIDEBODY AIRCRAFT

2.1 Fuselage Repair Designs

Repair Category for Designs - gouges, dents, and corrosion grind-outs in fuselage skin (strive for high use locations and ease of installation). The fuselage designs accommodated repairs that encompass substructure elements.

Figure 9 shows a representative skin repair from the DC-10 Structural Repair Manual that can be replaced by the family of composite doublers developed in this DC-10 program. This repair schematic shows the conventional riveted, metallic doubler.

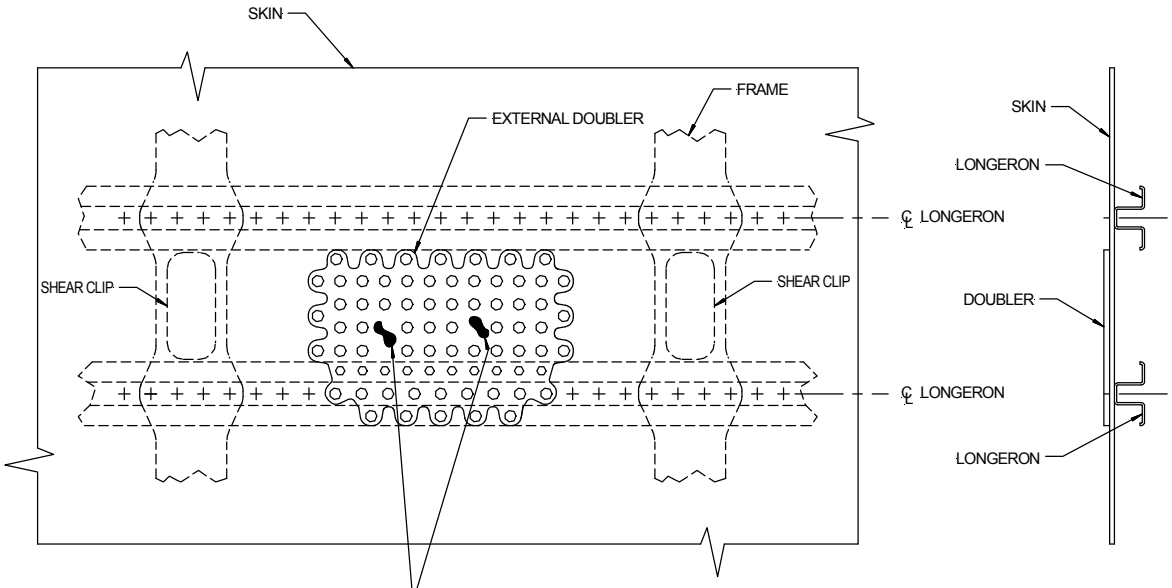

DAMAGE TOLERANCE INSPECTION REQUIREMENT		
INITIAL	REPETITIVE	REPLACEMENT
8,000	4,000	NA

Figure 9: Typical Fuselage Skin Damage To Be Repaired By Composite Doublers

Repair Designs - The family of composite doublers allowed for the repair of corrosion (internal and external), impact damage, and lightning strike damage to the DC-10 and MD-11 fuselage skins. The doublers were designed to restore the original static, fatigue, and durability capability of the structure. The design and analysis process was conducted to produce a repair set with as wide an application regime as possible. Fuselage skins up to 0.080" thick can be repaired with the family of composite doublers designed in this program. The doubler footprint may cover frames and longerons but not production joints or finger doubler joints. Repairs for 1", 3", and 5" diameter damage were designed and analyzed. All of the repairs are 13 ply, quasi-isotropic

doublers with symmetrical lay-ups. Figures 10 and 11 provide the details of the composite doubler designs for 1" and 3" diameter flaws, respectively.

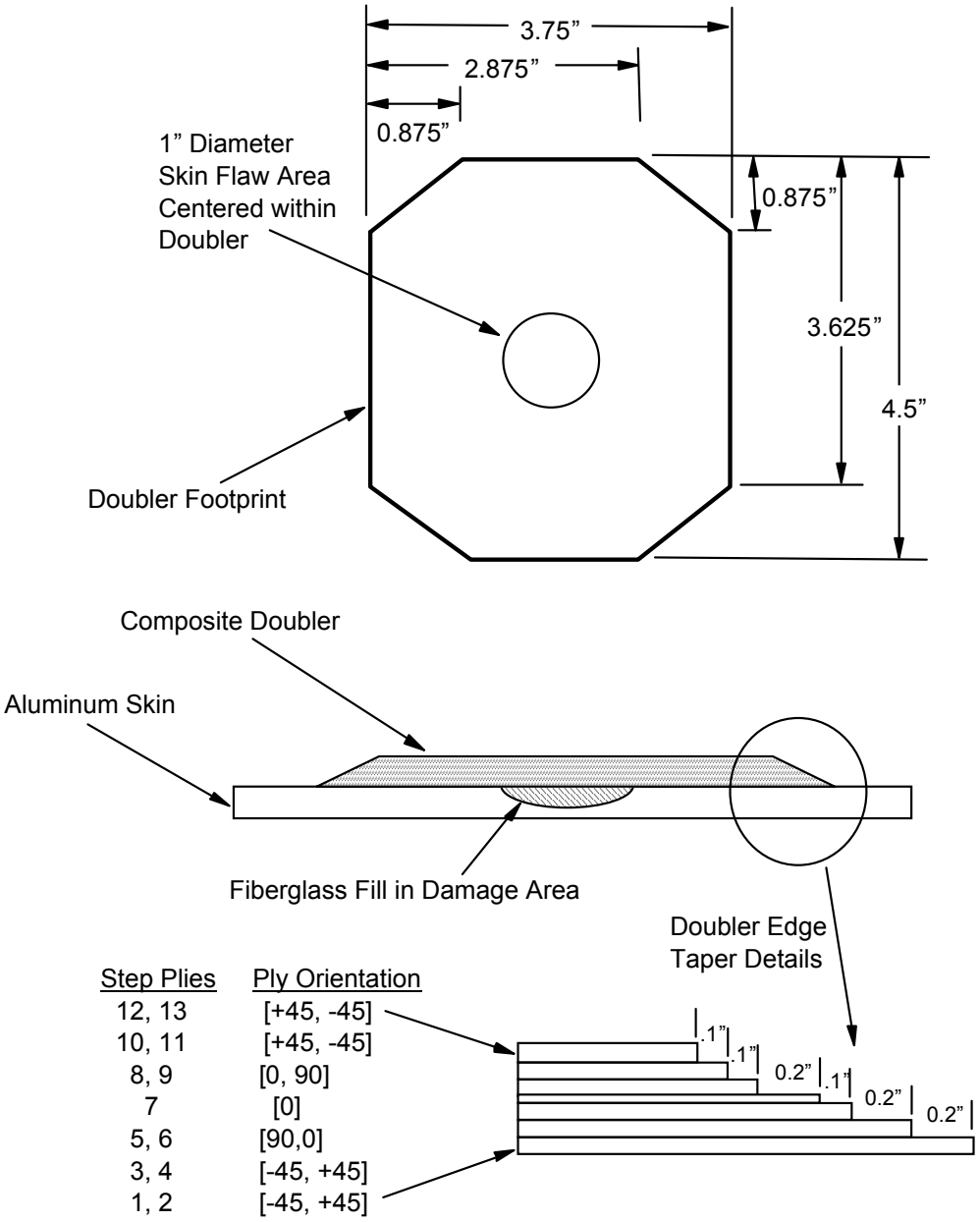

Skin: Aluminum 2024-T3

Patch: Boron/Epoxy, nominal lamina thickness = 0.0057

Install Per: Boeing Specification No. D658-10183-1
(also listed as Textron Specialty Materials
Specification No. 200008-001)

Figure 10: Composite Doubler Design for 1" Diameter Skin Flaws on DC-10 Aircraft

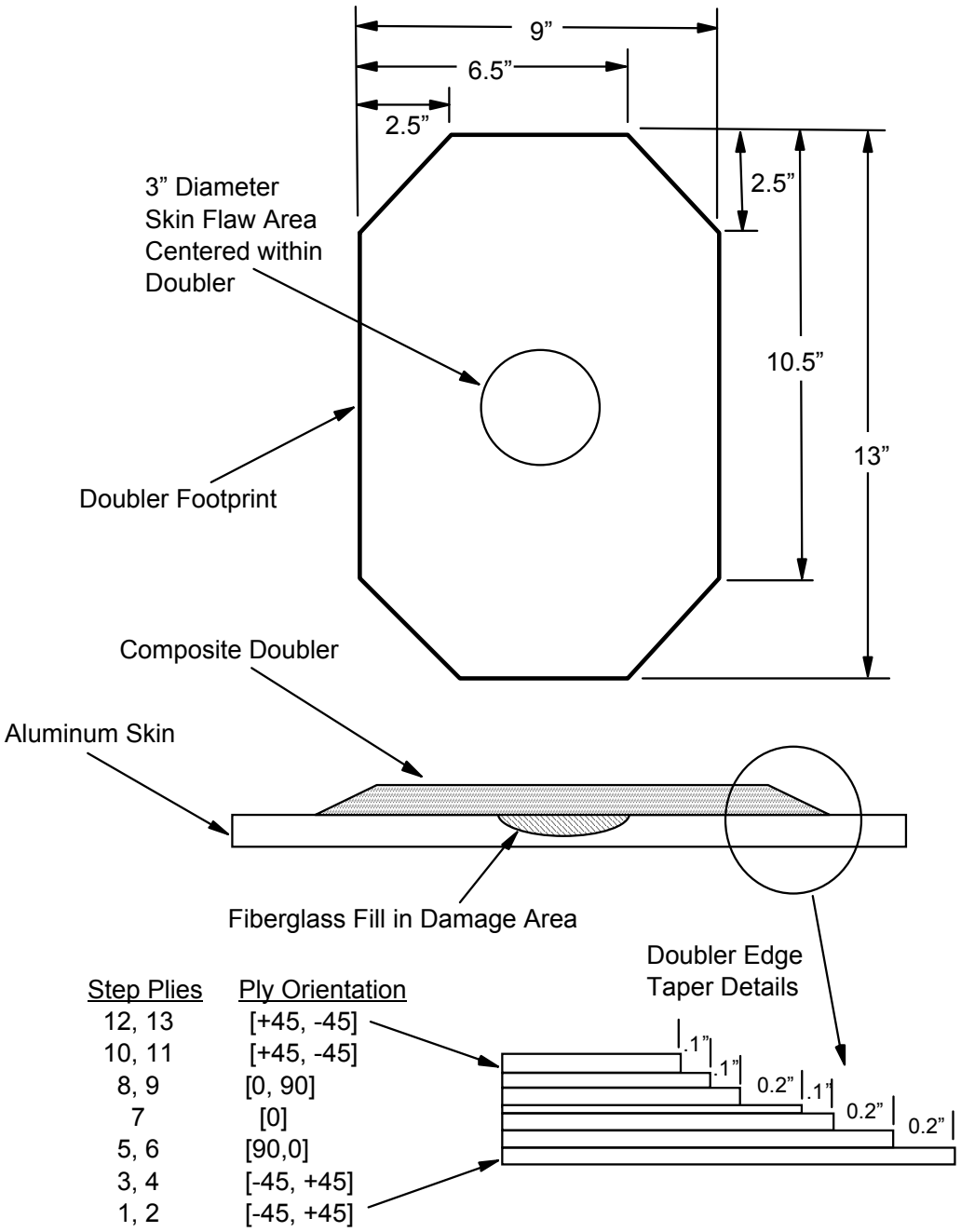

Skin: Aluminum 2024-T3

Patch: Boron/Epoxy, nominal lamina thickness = 0.0057

Install Per: Boeing Specification No. D658-10183-1
(also listed as Textron Specialty Materials
Specification No. 200008-001)

Figure 11: Composite Doubler Design for 3” Diameter Skin Flaws on DC-10 Aircraft

Engineering Drawings - An engineering drawing was prepared to guide the fabrication and installation of all composite doublers [1]. It includes the footprints for all three repair designs, as well as, a comprehensive set of notes to guide all fabrication, installation, QA, and inspection activities for the DC-10/MD-11 repairs. These drawings were added to the Structural Repair Manual (SRM) to allow for routine use of the composite doubler fuselage skin repairs. The SRM revision followed a successful composite repair pilot program with Federal Express (see Chapter 6.0).

2.2 Stress Analysis of Composite Doubler and Surrounding Aluminum Structure

2.2.1 Analysis Approach

The finite element model (FEM) was developed to assess the stress levels in each of the critical regions: 1) composite laminate, 2) adhesive layer, and 3) aluminum skin adjacent to the repair. A repair patch that is too thick could raise the stress levels in the surrounding aluminum above allowable levels. A repair patch that is too thin could result in excessive stress levels in the doubler. Finally, a repair with inadequate edge taper could produce high shear stresses in the adhesive layer at the edge of the doubler. The stress analysis was performed using NASTRAN and NASA FRANC2D/L FEM codes. A worst-case load scenario, including extreme shear loads, was applied to the design. In addition, the analysis conservatively assumed zero load transfer in the damaged area. The applied loading was a worst case DC-10/MD-11 stress spectrum of: $\sigma_{x(axial)}$ = 10.4 KSI, $\sigma_{y(hoop)}$ = 20.7 KSI, and $\tau_{xy(shear)}$ = 20 KSI.

2.2.2 Material Allowables

In order to proceed with the application of Boron-Epoxy (B-E) pre-preg, fiber-reinforced, composite material on an aircraft, it was necessary to complete a certification activity to ensure acceptable material properties. A Boeing Designated Engineering Representative (DER) for materials worked with Sandia Labs and Specialty Materials Inc. (SMI), producers of the B-E material to complete the certification of 5521 B-E for aviation use. The Douglas Material Specification (DMS) 2474 was issued by Boeing and submitted to the FAA Los Angeles Aircraft Certification Office (ACO) using a DER-approved 8110-3 form.

The new DMS 2474 "Boron Reinforced Epoxy Prepreg, 250^{o}F Cure" specification was issued to control the production of B-E 5521 used for fabrication or repair of aircraft assemblies. DMS 2474 was qualified to both an autoclave pressure cure process (to represent depot level repairs) and a vacuum bag oven cure process (to represent field level repairs). There were 11 tests conducted to produce the 12 material properties summarized in Table 2. The DMS also covers proper shipping, handling, and storage of B-E 5521 material.

In addition to the mechanical property values, the material allowables evaluation effort included items such as: Boron filament density measurements, quality assurance on fiber count, high pressure liquid chromatography (HPLC) analysis of the resin performed in accordance with the general approach given in ASTM E 682, infrared spectrum tests on the epoxy resin performed

per ASTM E 168, wet resin content measurements on the pre-preg material as per ASTM D 3529 and generation of Production Control Documents at SMI. Ultimate tensile strength and modulus were determined in accordance with ASTM D 3039. Ultimate compressive strength at failure was determined in accordance with ASTM D 695. The interlaminar short beam shear strength was determined in accordance with ASTM D 2344

Test*	Ply Orientation	**Test Temperature, ^{o}F**	**Specimen Precondition**	**Requirement**
Autoclave Cured Laminates				
Tensile Ultimate	0^{o} (6 ply)	RT	Dry	215,000
		180		210,000
Tensile Modulus	0^{o} (6 ply)	RT	Dry	24.9 – 31.7
Compression Ult.	0^{o} (8 ply)	-65	Dry	420,000
		RT		415,000
Short Beam Shear	0^{o} (6 ply)	RT	Dry	13,800
		180		10,600
Vacuum Bag Cured Laminates				
Tensile Ultimate	0^{o} (6 ply)	-75	Dry	190,000
		RT		188,000
	(0^{o}, +45^{o}, 0^{o}, -45^{o}, 0^{o})s (10 ply)	-75		115,000
		RT		110,000
Compression Ult.	0^{o} (6 ply)	RT	Dry	325,000

* 6 specimens of each; plus Infrared and High Pressure Liquid Chromatography Spectrum tests on epoxy resin.

Table 2: Production Certification Tests for 5521 Boron-Epoxy Uniaxial Tape

TEST	TEMP °F/COND	PLY ORIENT.	BATCH 1		BATCH B195		DMS 2474 REQ'T	
			AVG	MIN.	AVG.	MIN.	AVG.	MIN.
TENSILE ULTIMATE (KSI)	-75/ DRY	0^0	204.9	196.0	214.0	179.7	190	171
	RT/ DRY	0^0	190.0	188.7	199.9	191.9	188	169
	180/ WET	0^0	174.7	167.0	-	-	165	149
	RT/ SKY.	0^0	190.0	179.2	-	-	180	162
	-75/ DRY	$(0^0,+45^0, 0^0,-45^0,0^0)_s$	129.7	115.4	139.6	135.8	115	104
	RT/ DRY	$(0^0,+45^0, 0^0,-45^0,0^0)_s$	123.7	112.7	131.9	121.2	110	99
	180/ WET	$(0^0,+45^0, 0^0,-45^0,0^0)_s$	114.4	102.0	-	-	100	90
	RT/ SKY.	$(0^0,+45^0, 0^0,-45^0,0^0)_s$	116.3	105.4	-	-	105	95
TENSILE MODULUS (MSI)	-75/ DRY	0^0	25.1	24.4	29.1	27.3	22.1 – 30.0	
	RT/ DRY	0^0	26.3	25.5	28.4	27.6	23.2 – 30.0	
	180/ WET	0^0	24.2	23.1	-	-	21.4 – 27.0	
	RT/ SKY.	0^0	24.8	24.2	-	-	21.8 – 27.8	
	-75/ DRY	$(0^0,+45^0, 0^0,-45^0,0^0)_s$	17.6	16.2	18.6	18.3	14.9 – 20.3	
	RT/ DRY	$(0^0,+45^0, 0^0,-45^0,0^0)_s$	17.4	15.8	17.9	17.5	14.2 – 20.6	
	180/ WET	$(0^0,+45^0, 0^0,-45^0,0^0)_s$	16.0	14.2	-	-	12.4 – 19.6	
	RT/ SKY.	$(0^0,+45^0, 0^0,-45^0,0^0)_s$	16.6	15.9	-	-	14.6 – 18.6	
COMPRESSION ULTIMATE (KSI)	RT/ DRY	0^0	344	-	278.0	235.3	27	248
	RT / DE-ICE/	0^0	324	285	-	-	27	248
	RT/ MEK	0^0	332	272	-	-	27	248
	RT/ JP-4	0^0	326	272	-	-	27	248
	RT/ HYD OIL	0^0	323	284	-	-	27	248
	RT SKY.	0^0	342	326	-	-	27	248

Wet = 14 days exposure to 160°F/95% RH; RT = room temperature
All data, except interlaminar shear, normalized to 0.052" th./ply

Table 3: Laminate Mechanical Property Results for Oven-Cured Vacuum-Bagged Boron-Epoxy 5521 Pre-Preg Material

The resulting set of material properties used in the design analysis is summarized in Table 4. The adhesive properties match the existing Boeing composites manual design standard MDC9/B0330.

Material	F_{tu}	F_{ty}	F_{su}	Strain Allowable
Boron Lamina	185 KSI	185 KSI	14.7 KSI	4340x10-6 in/in
Adhesive	N/A	N/A	5.6 KSI	1750x10-6 in/in

The aluminum skin is 2024-T3 clad sheet and material properties are from Mil-handbook 5G section 3.2.3.

Material	F_{tu} (LT)	F_{ty} (LT)	F_{su}
2024-T3 Bare Sheet	63 KSI	42 KSI	39 KSI
2024-T3 Clad Sheet	61 KSI	40 KSI	38 KSI

Where F_{tu} = tension ultimate stress, F_{ty} = tension yield stress, and F_{su} = shear ultimate stress

Table 4: Boron-Epoxy and Aluminum Material Properties Used in the Composite Doubler Design Analysis

2.2.3 Stress Analysis Results

The maximum stresses produced in the composite doubler, adhesive layer, and surrounding skin during the worst case DC-10/MD-11 stress spectrum was as follows:

Design for 1" Diameter Repair

- Maximum Stress in Aluminum Skin

  σ_1 = 41.9 KSI (σ_{yield} = 47-50 KSI)

  σ_2 = -8 KSI

  τ_{max} = 22 KSI ($\tau_{allowable}$ = 39 KSI)

- Margin of Safety in Aluminum Skin

  Tension:

$$M.S. = \frac{F_{tu}}{\sigma_1} - 1 = \frac{61000}{41900} - 1 = +0.46$$

  Shear:

$$M.S. = \frac{F_{su}}{\tau_{max}} - 1 = \frac{38000}{22000} - 1 = +0.73$$

- Maximum Stress in Adhesive

  τ_{ZX} = 4.8 KSI ($\tau_{allowable}$ = 5.6 KSI)

  τ_{ZY} = 5 KSI ($\tau_{allowable}$ = 5.6 KSI)

- Margin of Safety in Adhesive

$$M.S. = \frac{F_{su}}{\tau_{max}} - 1 = \frac{5600}{5000} - 1 = +0.12$$

- Maximum Stress in Composite Doubler – Based on maximum strain failure criteria, the laminate critical load is determined from the transverse ply strain (ε_z) in the – 45° ply at the second tapered step up from the patch edge (base). The Margin of Safety is calculated based on the largest strain value found in the FEM.

$$M.S. = \frac{\varepsilon_2(\text{Allowable})}{\varepsilon_2(\text{Critical location in} - 45^\circ \text{ply})} - 1 = \frac{4340}{3735} - 1 = +0.16$$

- Contour Plots for the Limiting Transverse Strain – The stress magnitudes summarized above are shown in Figures 12 and 13.

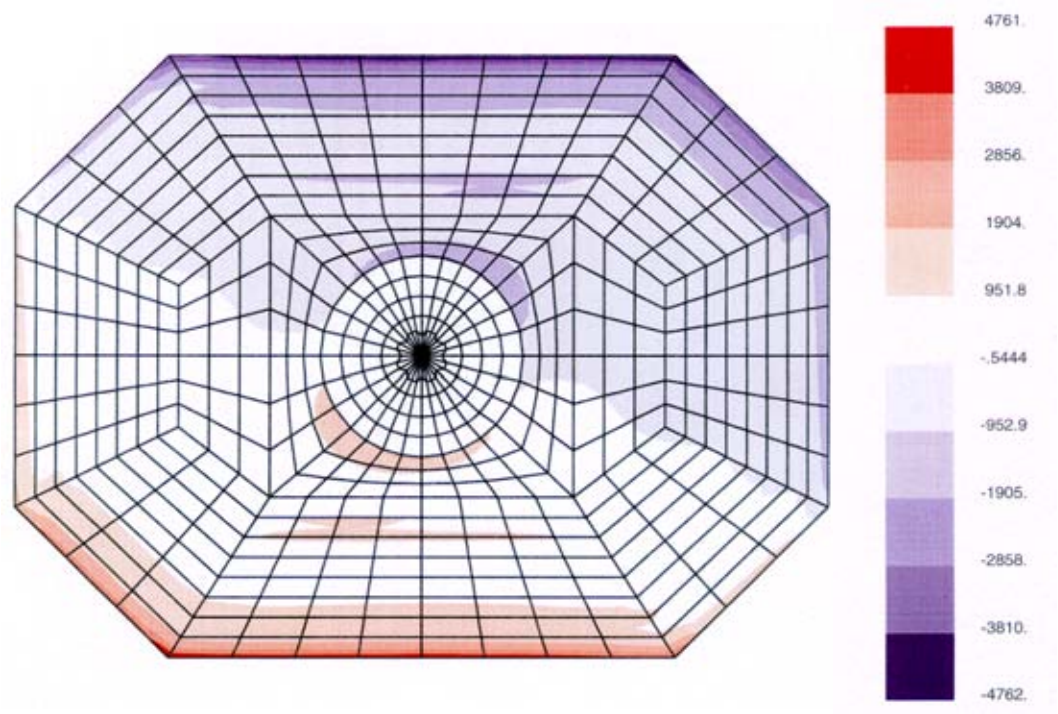

Figure 12: Shear Stress τ_{ZX} in Composite Doubler for 1" Diameter Repair Design and Worst Case Load Spectrum

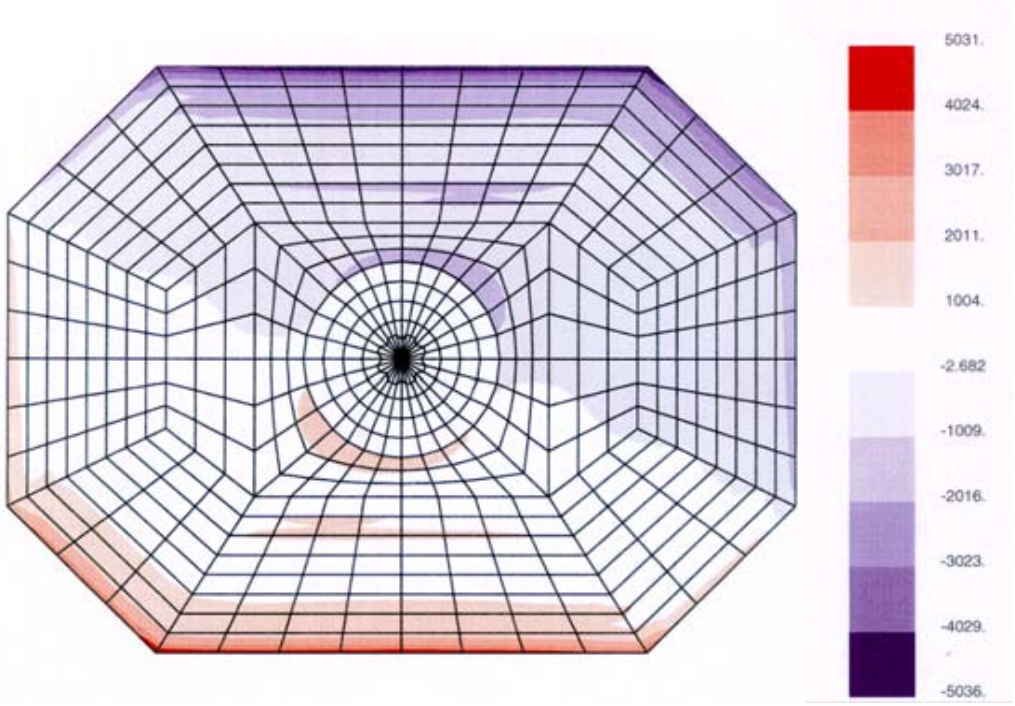

Figure 13: Shear Stress τ_{ZY} in Composite Doubler for 1" Diameter Repair Design and Worst Case Load Spectrum

Design for 3" Diameter Repair

- Maximum Stress in Aluminum Skin

  σ_1 = 44.2 KSI (σ_{yield} = 47-50 KSI)

  σ_2 = -1.6 KSI

  τ_{max} = 22.4 KSI ($\tau_{allowable}$ = 39 KSI)

- Margin of Safety in Aluminum Skin

  Tension:

$$M.S. = \frac{F_{tu}}{\sigma_1} - 1 = \frac{61000}{44200} - 1 = +0.38$$

  Shear:

$$M.S. = \frac{F_{su}}{\tau_{max}} - 1 = \frac{38000}{22400} - 1 = +0.70$$

- Maximum Stress in Adhesive

  τ_{ZX} = component has lower magnitude and is less critical than τ_{ZY}

  τ_{ZY} = 4.1 KSI ($\tau_{allowable}$ = 5.6 KSI)

- Margin of Safety in Adhesive

$$M.S. = \frac{F_{su}}{\tau_{max}} - 1 = \frac{5600}{4100} - 1 = +0.37$$

- Maximum Stress in Composite Doubler – Based on maximum strain failure criteria, the laminate critical load is determined from the transverse ply strain (ε_z) in the – 45° ply at the second tapered step up from the patch edge (base). The Margin of Safety is calculated based on the largest strain value found in the FEM.

$$M.S. = \frac{\varepsilon_2(\text{Allowable})}{\varepsilon_2(\text{Critical location in} - 45^\circ \text{ply})} - 1 = \frac{4340}{3340} - 1 = +0.30$$

- Contour plots for the Maximum Principal Stress tensors are shown in Figures 14, 15 and 16. The significant effects of the shear loading are evident. Note that the peak doubler stresses are confined to a small region where the doubler has its full thickness. Furthermore, the stresses in the critical tapered region of the doubler (primary load transfer zone) are 30% to 50% of those found in the surrounding skin. This type of load transfer matches general design goals for stress distribution around aircraft skin repairs (see also load transfer data in section 3.2).

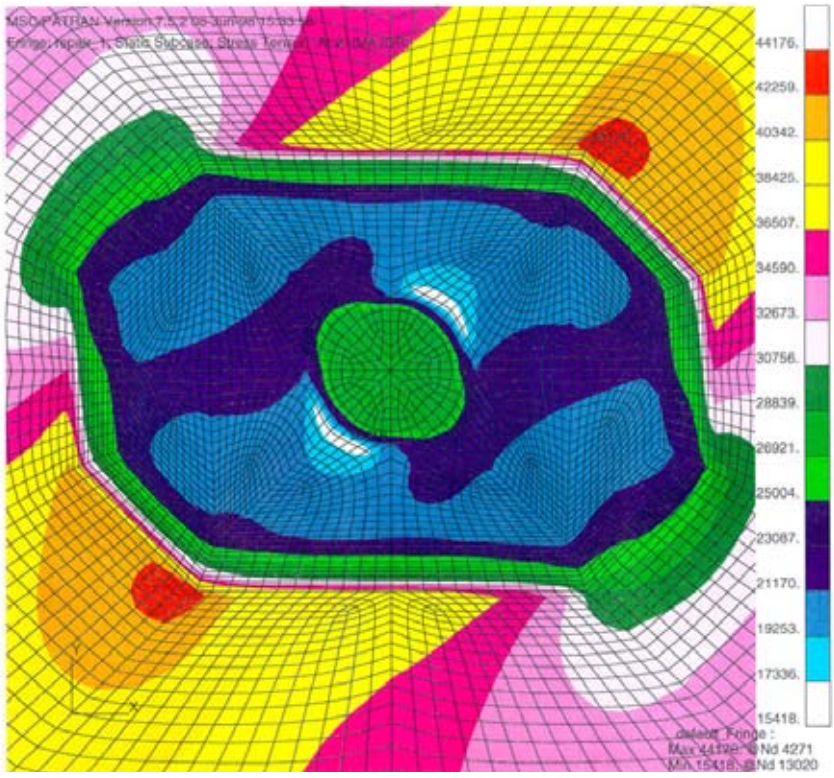

Figure 14: Maximum Principal Stress Tensor σ_1 in Composite Doubler and Aluminum Skin for 3" Diameter Repair Design and Worst Case Load Spectrum

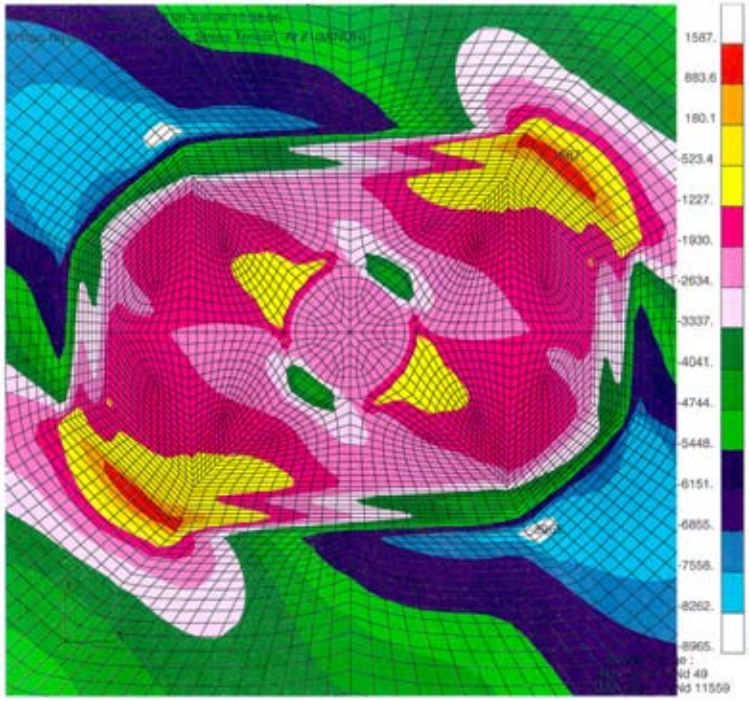

Figure 15: Maximum Principal Stress Tensor σ_2 in Composite Doubler and Aluminum Skin for 3" Diameter Repair Design and Worst Case Load Spectrum

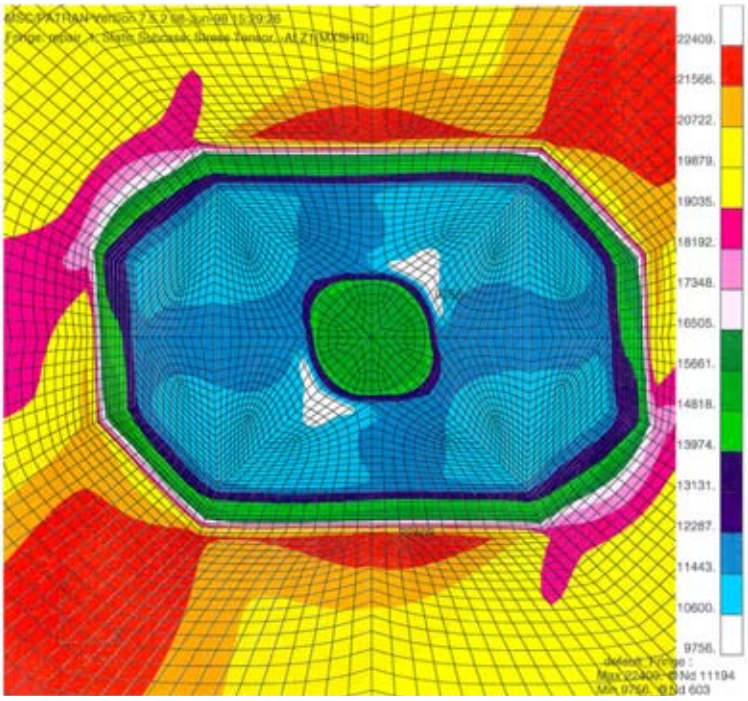

Figure 16: Maximum Principal Shear Stress Tensor γ_{12} in Composite Doubler and Aluminum Skin for 3" Diameter Repair Design and Worst Case Load Spectrum

Design for 5" Diameter Repair

- Maximum Stress in Aluminum Skin

  σ_1 = 44.9 KSI (σ_{yield} = 47-50 KSI)

  τ_{max} = 22.7 KSI ($\tau_{allowable}$ = 39 KSI)

- Margin of Safety in Aluminum Skin

  Tension:

$$M.S. = \frac{F_{tu}}{\sigma_1} - 1 = \frac{61000}{44900} - 1 = +0.36$$

  Shear:

$$M.S. = \frac{F_{su}}{\tau_{max}} - 1 = \frac{38000}{22700} - 1 = +0.67$$

- Maximum Stress in Adhesive

  τ_{ZX} = component has lower magnitude and is less critical than τ_{ZY}

  τ_{ZY} = 4.1 KSI ($\tau_{allowable}$ = 5.6 KSI)

- Margin of Safety in Adhesive

$$M.S. = \frac{F_{su}}{\tau_{max}} - 1 = \frac{5600}{4100} - 1 = +0.37$$

- Maximum Stress in Composite Doubler – Based on maximum strain failure criteria, the laminate critical load is determined from the transverse ply strain (ε_z) in the -45^o ply at the second tapered step up from the patch edge (base). The Margin of Safety is calculated based on the largest strain value found in the FEM.

$$M.S. = \frac{\varepsilon_2(\text{Allowable})}{\varepsilon_2(\text{Critical location in} - 45^o \text{ply})} - 1 = \frac{4340}{3735} - 1 = +0.16$$

- Contour plots for the Maximum Principal Stress tensors are shown in Figures 17 and 18. The significant effects of the shear loading are evident. Note that the peak doubler stresses are confined to a small region where the doubler has its full thickness. Furthermore, the stresses in the critical tapered region of the doubler (primary load transfer zone) are 30% to 50% of those found in the surrounding skin. This type of load transfer matches general design goals for stress distribution around aircraft skin repairs (see also load transfer data in sections 3.2).

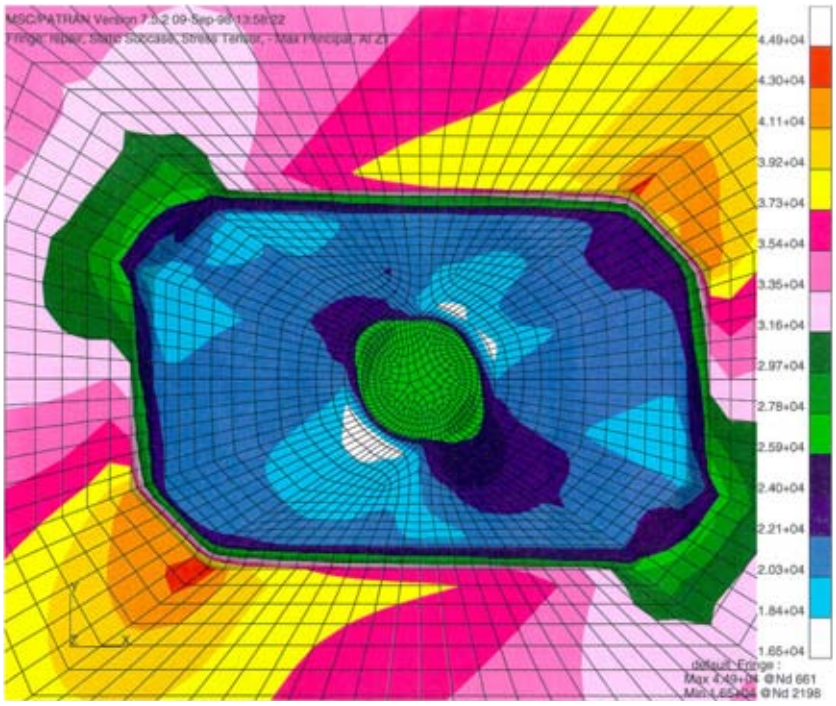

Figure 17: Maximum Principal Stress in Composite Doubler and Aluminum Skin for 5" Diameter Repair Design and Worst Case Load Spectrum

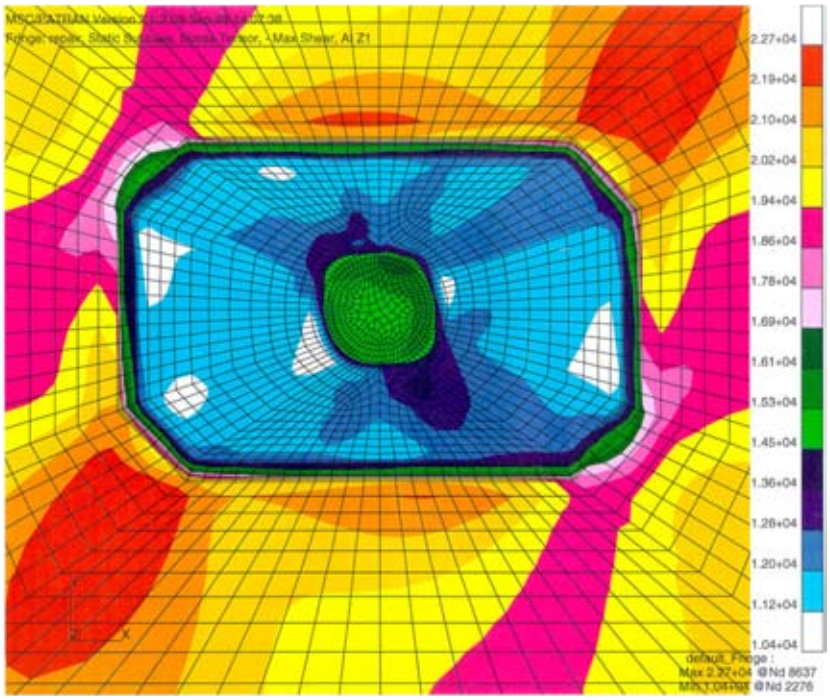

Figure 18: Maximum Principal Shear Stress in Composite Doubler and Aluminum Skin for 5" Diameter Repair Design and Worst Case Load Spectrum

2.3 Damage Tolerance Analysis – Stress Intensity Levels and Crack Growth Mitigation

The damage tolerance analysis studied skin, patch, and adhesive stresses in conjunction with potential failure modes. All of the designs produced acceptable margins of safety when subjected to the worst case flight load spectrum. The stress intensity (K_I) for the repaired and unrepaired configurations was determined using the CalcuRep program for aircraft repair analysis [9, 29]. Table 5 provides a comparison for the three composite patch sizes. The crack is assumed to be initially the same size as the damaged area. The stress level is 20.68 ksi.

Patch Size 4.5" x 3.75"		
Crack Length	K_I Repaired	K_I Unrepaired
1.0"	9.32	25.94
1.5"	9.32	31.77
2.0"	9.32	36.69
2.5"	9.32	41.02
3.0"	9.32	44.94

Patch Size 13" x 9"		
Crack Length	K_I Repaired	K_I Unrepaired
3.0"	9.06	44.94
3.5"	9.06	48.54
4.0"	9.06	51.89
4.5"	9.06	55.03
5.0"	9.06	58.01
6.0"	9.06	63.55
7.0"	9.06	68.64

Patch Size 21" x 13"		
Crack Length	K_I Repaired	K_I Unrepaired
5.0"	8.85	58.01
5.5"	8.85	60.84
6.0"	8.85	63.55
6.5"	8.85	66.14
7.0"	8.85	68.64
8.0"	8.85	73.38
9.0"	8.85	77.83
10.0"	8.85	82.04

Skin: AL 2024-T3 (t=0.080 inches)
Thermal Coefficient: 0.0

Table 5: Stress Intensity Factors for Unrepaired Skin and Skin Repaired with Composite Doubler

Using Walker's equation, below, with C = 6.76125E-10, p = 3.71980, q = 0.64647 and R = 0.0, *da* are determined for the K_I values listed in Table 5. The da/dN crack growth calculations are summarized in Table 6.

$$\frac{da}{dn} = C \times \left[(1-R)^q \times K_I \right]^p \qquad (11)$$

The crack growth analysis with and without the doubler present makes it possible to conservatively bound the inspection requirements. The rate of growth for the repaired configuration is significantly smaller than the unrepaired configuration. The rate of crack growth is 45 to 3900 times less. Crack mitigation is at least equal to the performance of the existing metal doubler repairs for these types of damage. Note that the crack growth mitigation remains the same with the doubler in place regardless of the length of the crack beneath the doubler. The design approach uses a typical maintenance rule that since the doubler is less than 2 bays in size,

normal maintenance activities are already in place to find any cracks that may originate in this area. The crack growth mitigation listed in Table 6 is shown graphically in Figure 19. Figure 19 shows the crack growth curves for the fuselage skin with and without a composite doubler repair (initial crack length = 1.0"). The repaired skin exhibits essentially no crack growth in over 8,000 cycles.

Patch Size 4.5" x 3.75"		
Crack Length	da for n=1 Repaired	da for n=1 Unrepaired
1.0"	2.729e-6	123.122e-6
1.5"	2.729e-6	261.355e-6
2.0"	2.729e-6	446.510e-6
2.5"	2.729e-6	676.158e-6
3.0"	2.729e-6	949.492e-6

Patch Size 13" x 9"		
Crack Length	da for n=1 Repaired	da for n=1 Unrepaired
3.0"	2.457e-6	949.492e-6
3.5"	2.457e-6	1265.00e-6
4.0"	2.457e-6	1621.00e-6
4.5"	2.457e-6	2017.00e-6
5.0"	2.457e-6	2454.00e-6
6.0"	2.457e-6	3446.00e-6
7.0"	2.457e-6	4589.00e-6

Patch Size 21" x 13"		
Crack Length	da for n=1 Repaired	da for n=1 Unrepaired
5.0"	2.251e-6	2454.00e-6
5.5"	2.251e-6	2930.00e-6
6.0"	2.251e-6	3446.00e-6
6.5"	2.251e-6	3998.00e-6
7.0"	2.251e-6	4589.00e-6
8.0"	2.251e-6	5883.00e-6
9.0"	2.251e-6	7323.00e-6
10.0"	2.251e-6	8909.00e-6

a = crack length
n = number of fatigue cycles
Skin: AL 2024-T3 (t=0.080 inches)

Table 6: Crack Growth Parameters for Unrepaired Skin and Skin Repaired with Composite Doubler

The concern is not whether the crack will grow but whether the adhesive bond stays intact. The inspection interval of every "C-check" is adequate to monitor the condition of the adhesive bond. Damage tolerance analyses and comprehensive testing has shown that disbond and delamination flaws experience almost zero growth under normal operating environments [1, 13]. Thus, the inspection requirements set forth in this program are conservative .

Overall Results for DC-10/MD11 Doubler Analysis – Results from analyses and tests validated the three DC-10/MD-11 skin repair designs. The results show that the doubler and adhesive exhibit sufficient strength to provide adequate fatigue enhancement through a wide range of environmental conditions. A crack growth analysis shows that the doubler increases the safety limit of the structure by a factor of 45. The doublers provide acceptable safety factors and the strain levels throughout the doublers and in the surrounding skin area are below the allowable levels. Finally, the analyses and test results indicate that an inspection interval of 4,500 flights (every “C”, “D”, or heavy maintenance check) is sufficient to provide more than one opportunity to find the necessary doubler installation flaws.

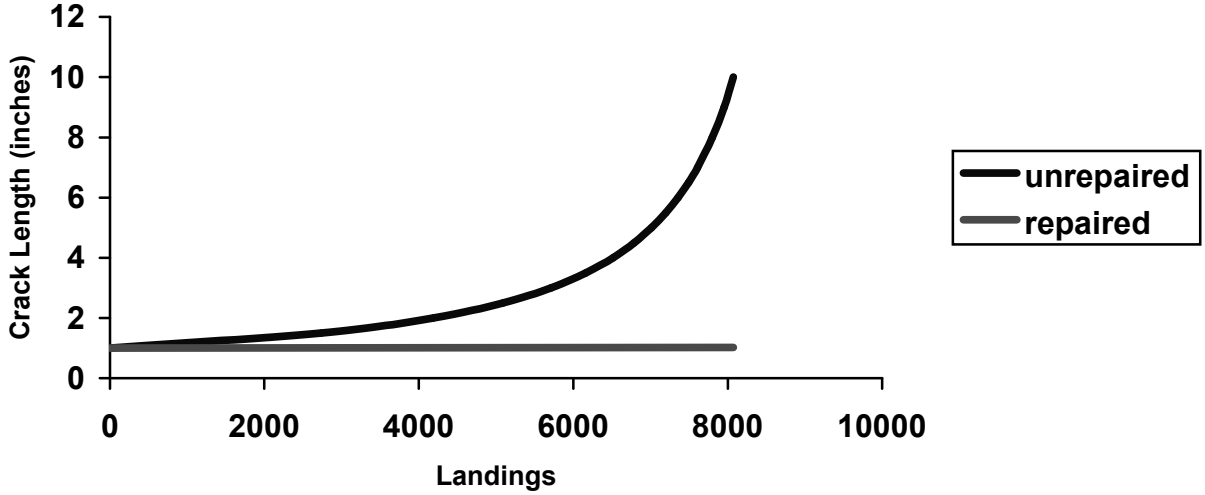

Figure 19: DC-10 Fuselage Crack Growth With and Without a Composite Doubler Repair

2.4 Structural Mechanics Tests to Assess Damage Tolerance and Crack Mitigation

2.4.1 Fatigue and Ultimate Strength

A series of fatigue and strength tests were conducted to study the damage tolerance of Boron-Epoxy composite doublers. Tension-tension fatigue and ultimate strength tests attempted to grow engineered flaws in coupons with composite doublers bonded to aluminum skin. An array of design parameters, including various flaw scenarios, the effects of surface impact, and other "off-design" conditions, were studied. A typical coupon configuration with large, engineered flaws is shown in Figure 20. Figure 21 shows the fatigue specimen mounted in the mechanical test machine. The structural tests were used to: 1) assess the potential for interply delaminations and disbonds between the aluminum and the laminate, and 2) determine the load transfer and crack mitigation capabilities of composite doublers in the presence of severe defects. A series of specimens were subjected to ultimate tension tests in order to determine strength values and failure modes. This test program demonstrated the damage tolerance capabilities of bonded composite doublers. The fatigue and strength tests quantified the structural response and crack abatement capabilities of Boron-Epoxy doublers in the presence of worst case flaw scenarios. The engineered flaws included cracks in the parent material, disbonds in the adhesive layer, and impact damage to the composite laminate. Environmental conditions representing temperature and humidity exposure were also included in the coupon tests.

It was demonstrated that even in the presence of extensive damage in the original structure (cracks, material loss) and in spite of non-optimum installations (adhesive disbonds), the composite doubler allowed the structure to survive more than 144,000 cycles of fatigue loading. Installation flaws in the composite laminate did not propagate over 216,000 fatigue cycles.

Furthermore, the added impediments of impact - severe enough to deform the parent aluminum skin - and hot-wet exposure did not affect the doubler's performance. Since the tests were conducting using extreme combinations of flaw scenarios (sizes and collocation) and excessive fatigue load spectrums, the performance parameters were arrived at in a conservative manner.

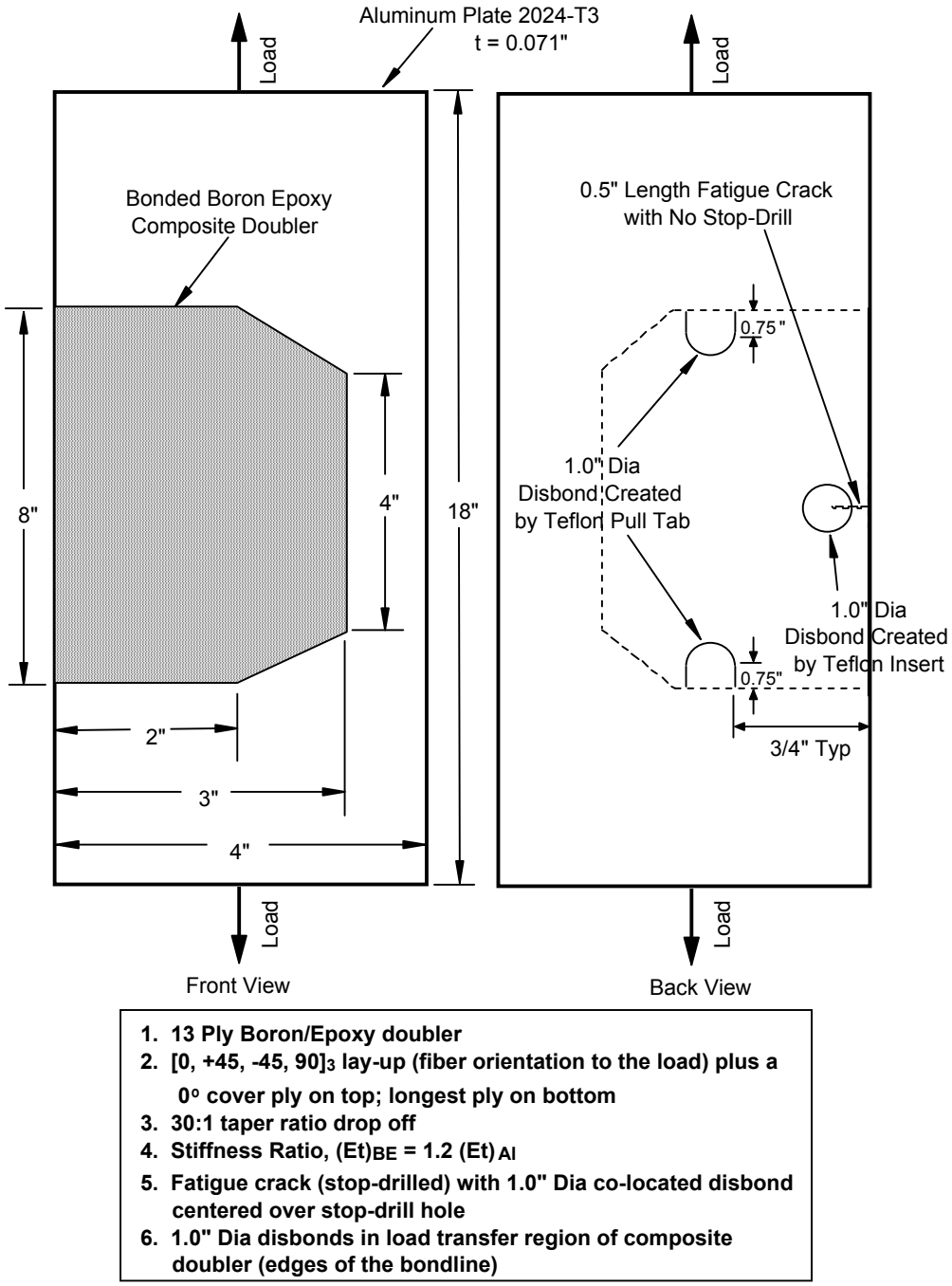

Figure 20: Composite Doubler Coupon for Damage Tolerance Fatigue Testing

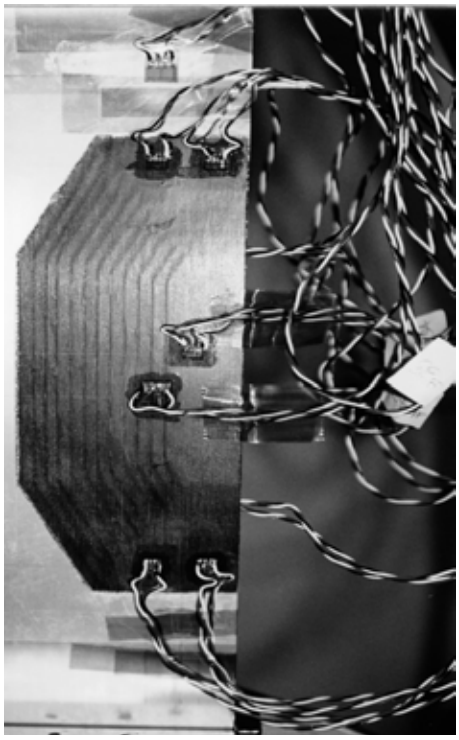

Figure 21: View of Composite Doubler Specimen Mounted in Machine for Damage Tolerance Tests

2.4.2 General Applicability of Results

The objective of this damage tolerance testing was to obtain a generic assessment of the ability of Boron-Epoxy doublers to reinforce and repair cracked aluminum structure [1]. By designing the specimens using the nondimensional stiffness ratio, it is possible to apply these results to various parent structure and composite laminate combinations. The nondimensional stiffness ratio parameter is used as the basis for applying the damage tolerance performance of composite doublers to the full spectrum of skin repair applications. This ratio compares the stiffness parameters, $E_x t$, of the composite laminate and the parent aluminum plate and is written as:

$$R = (E_x\, t_{laminate})_{BE} / (E_x\, t)_{Al} \qquad (12)$$

The number of plies and fiber orientations determine the extensional stiffness value for the Boron-Epoxy laminate. This test series utilized specimens with stiffness ratios of 1.2 and 1.3. The DC-10/MD-11 doubler designs have a stiffness ratio of 1.2. Independent studies by Lockheed, Boeing, and the military have all concluded that optimum doubler performance can be achieved with stiffness ratios of 1.1 to 1.4. Finally, it should be noted that all test specimens utilized a symmetrical 13 ply doubler similar to the family of DC-10/MD-11 designs. Thus, these performance results are directly applicable to the DC-10/MD-11 repairs.

2.4.3 Damage Tolerance Assessment in Light of Inspection Sensitivity

Figure 22 plots strain values at various locations around the composite doubler installation. Large strains found immediately adjacent to the doubler flaws emphasize the fact that relatively large disbond or delamination flaws (up to 1" diameter) in the composite doubler have only localized effects on strain and minimal effect on the overall doubler performance (i.e. undesirable strain relief over disbond but favorable load transfer immediately next to disbond). This statement is made relative to the inspection requirement which will result in the detection of disbonds/delaminations of 0.5" diameter or greater. Obviously, disbonds will affect the capabilities of composite doublers once they exceed some percentage of the doubler's total footprint area. The point at which disbonds become detrimental depends upon the size and location of the disbond and the strain field around the doubler. This study used flaws that were twice as large as the detectable limit to demonstrate the ability of composite doublers to tolerate extreme damage.

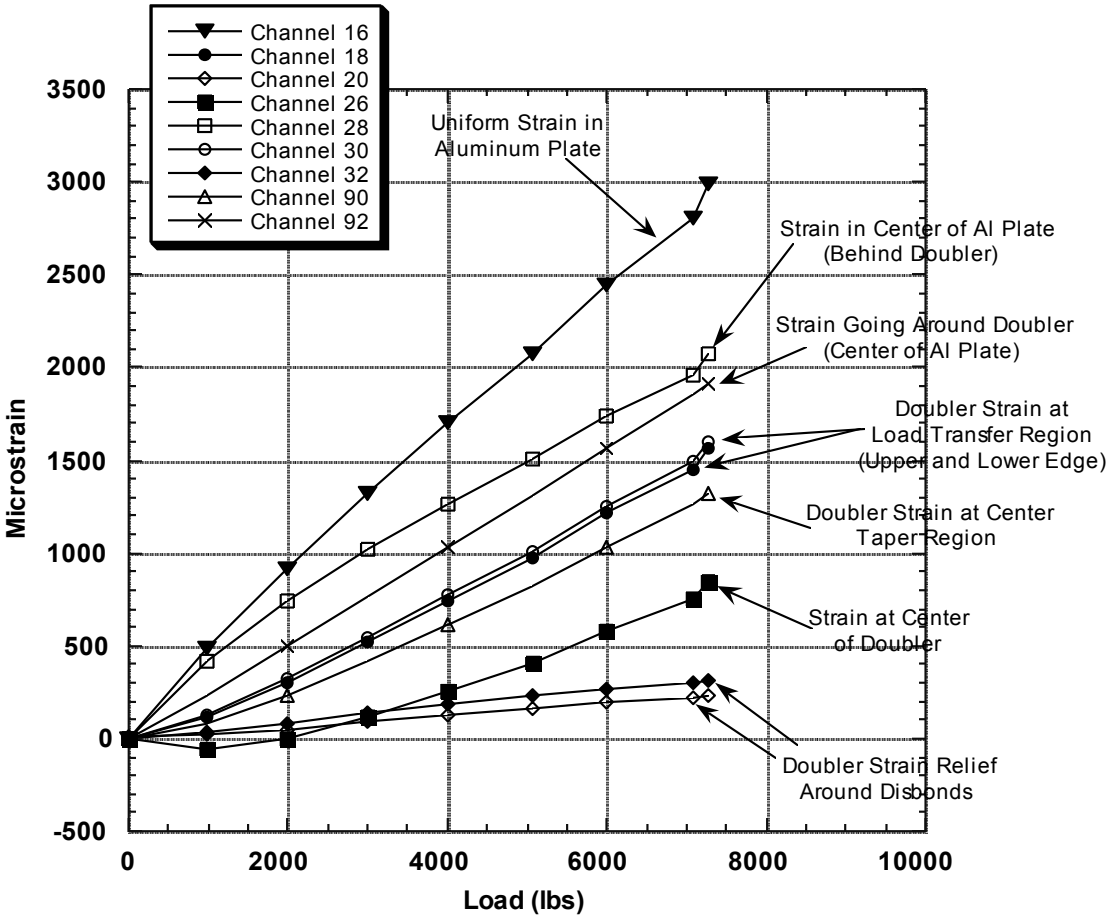

Figure 22: **Typical Axial Strain Field in Aluminum and Composite Doubler**

Similarly, the crack mitigation capabilities of Boron-Epoxy doublers were evaluated using large cracks which exceeded the inspection threshold. The damage tolerance tests presented in this document looked at crack growth beneath doublers of up to 3". The doublers were able to mitigate the crack growth by a factor of 20 versus the unrepaired aluminum. Test results showed that it would take two to three aircraft fatigue lifetimes (72,000 - 108,000 cycles) for a crack to propagate 1" beneath a reinforcing composite doubler. Finally, these tests showed that Boron-Epoxy composite doublers are able to achieve this performance level (i.e. reinforce and mitigate crack growth) even in the presence of extreme worst-case flaw scenarios. This demonstrates the exceptional damage tolerance of properly bonded Boron-Epoxy doublers.

2.4.4 Fatigue Tests: Flawed Specimens

The composite doublers produced significant crack growth mitigation when subjected to simulated pressure tension stress cycles. Even specimens with unabated fatigue cracks and co-located disbonds and impact damage were able to survive 144,000 fatigue cycles without specimen failure (less than 2" crack growth). During the course of fatigue cycling, all crack growth occurred in the aluminum plates. No fractures were found in any of the composite laminates. Comparisons with control specimens which did not have composite doubler reinforcement showed that the fatigue lifetime was extended by a factor of 20. Compare this number with the damage tolerance analysis results (Section 2.3) which determined fatigue life extension factors of 45 and greater. Both analysis and testing reveal that the application of NDI every 4,000 – 5,000 cycles is quite conservative. Crack growth (mitigation) data from the damage tolerance fatigue tests are shown graphically in Figure 23 and 24.

2.4.5 Fatigue Tests: Baseline (Unflawed) Specimens

The best basis of comparison for the performance characteristics discussed above was provided by specimens with normal installation and no flaws. These unflawed specimens showed that crack growth and disbonds/delaminations could be eliminated for at least 216,000 fatigue cycles *(6 design lifetimes with zero flaw growth).* Results from these specimens (0 crack growth) are shown in Figures 23 and 24. Configurations BE-5 and BER-7 are unflawed specimens.

2.4.6 Effects of Impact on Composite Doubler Performance

Following the composite doubler installation and prior to environmental conditioning, impact damage was imparted to many of the damage tolerance test specimens. The locations for impact damage were selected to induce the most adverse effect on crack growth mitigation and/or the ability of the doubler to transfer load. Impact sites were directly over the aluminum crack and along the edge of the doubler. The impact was performed with a 1 inch diameter steel hemisphere tip. A guide tube, lined with Teflon film, was used to direct the path of the impact mass. The specimens were fully supported by plates on the front and back side. The plates had appropriate window cut-outs to apply the impact damage. The magnitude of the impact was 25 $\pm$ 0.5 ft-lb (300 $\pm$ 5 in-lb). The impact damage was applied as per NASA specifications. This impact level was sufficient to produce 5/8" depth dents in the parent aluminum skin.

Following impact, the specimens were inspected ultrasonically to determine the extent of the resulting damage. The resulting flaw map (location, geometry, and depth) was recorded and the damage locations were marked directly on the specimens. In spite of the large skin deformations associated with the impact, most of the impact sites showed no sign of interply delamination or laminate-to-skin disbonds. Slight effects from the impact were observed in areas where the impact was applied directly over an engineered disbond. In these cases, the impact produced a small growth in the flaw. Some of the one inch diameter implanted disbonds, for example, became 1.25" in diameter. However, the key result from the impact tests was that there was no propagation of flaws from the impact areas. Before and after NDI tests revealed that the specimen profile was exactly the same before and after 144,000 to 180,000 cycles. Furthermore, separate NDI testing validated the ability of ultrasonics to detect and track damage stemming from impact.

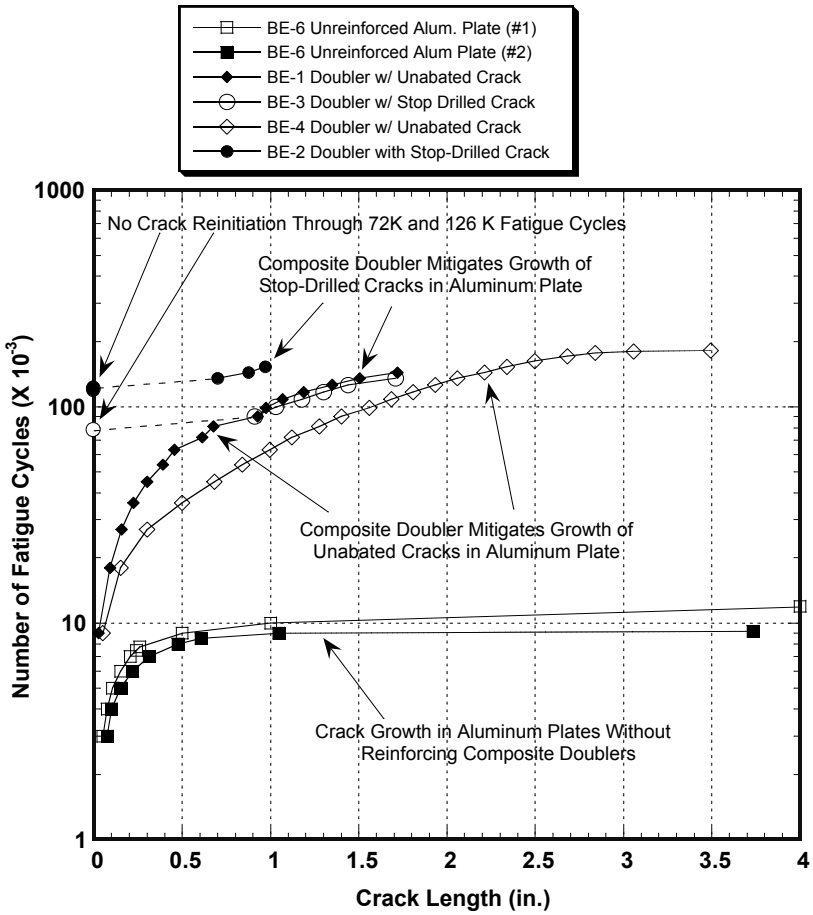

Figure 23: Fatigue Crack Growth in 2024-T3 Plates With and Without Reinforcing Composite Doublers (Configurations BE-1 to BE-6 Represent Variations on Flaw Scenarios)

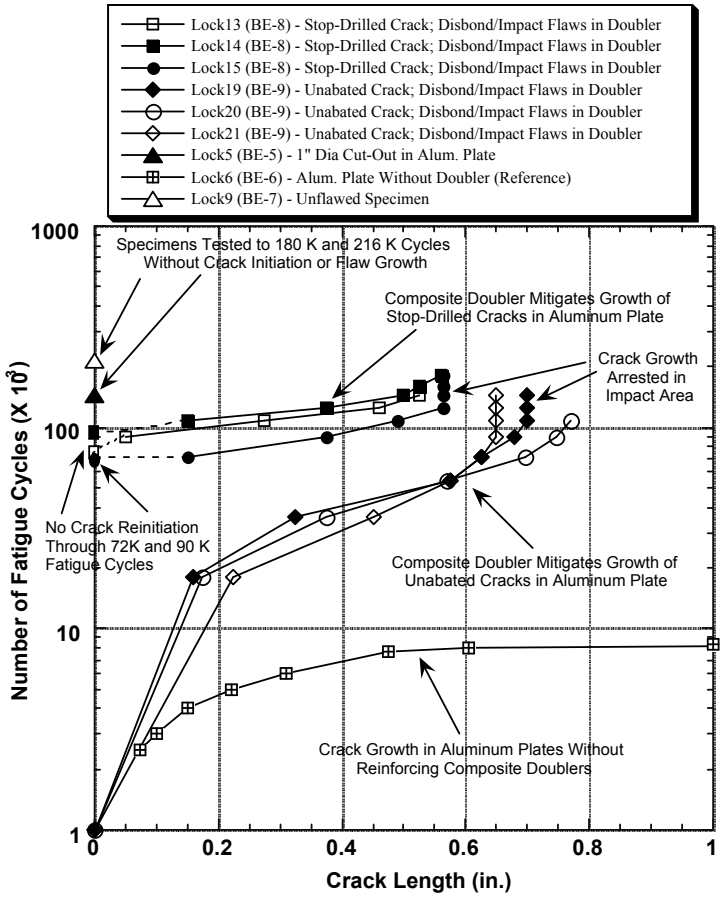

Figure 24: Fatigue Crack Growth in 2024-T3 Plates With and Without Reinforcing Composite Doublers (Configurations BE-5 to BE-9 Represent Variations on Severe Flaw Scenarios)

2.4.7 Adhesive Disbonds

The fatigue specimens contained engineered disbonds of 3 to 4 times the size detectable by the doubler inspection technique [14, 16-17]. Despite the fact that the disbonds were placed above fatigue cracks and in critical load transfer areas, it was observed that there was no growth in the disbonds over 144,000 to 216,000 fatigue cycles (four to six aircraft lifetimes). In addition, it was demonstrated that the large disbonds, representing almost 30% of the axial load transfer perimeter, did not decrease the overall composite doubler performance.

2.4.8 Stress/Strain Fields

The maximum doubler strains are found in the load transfer region around the perimeter (taper region) of the doubler. In all nine doubler flaw configurations, the strains monitored in this area were 45% - 55% of the total strain in the aluminum plate. This value remained constant over four fatigue lifetimes indicating that there was no deterioration in the bond strength. In each of

the fatigue specimens, the vast majority of the strain field remained unchanged over the course of the fatigue tests. For example, Figure 25 shows that the strains in the BE-7 configuration were undisturbed by 144,000 fatigue cycles.

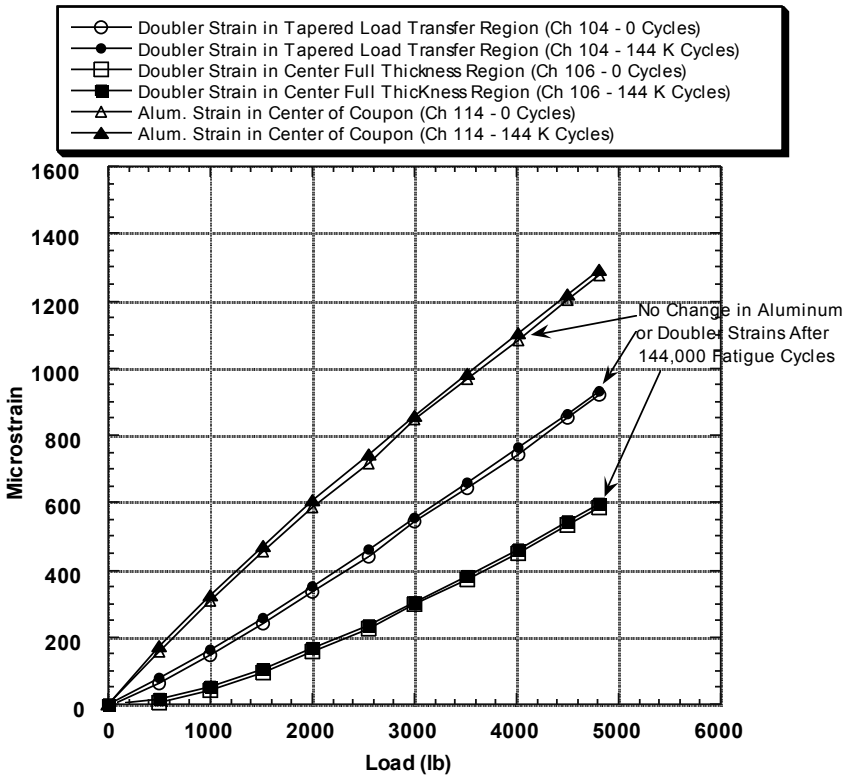

Figure 25: **Strain Field in Configuration BE-7 Remains Unchanged Over 144,000 Fatigue Cycles - No Flaw Growth in Doubler Installation**

During crack propagation, the stresses in the doubler increased to pick up the loads released by the plate. Data acquired during failure tests showed that the composite doubler was able to transmit stresses in the plastic regime and that extensive yielding of the aluminum was required to fail the installation. Also, stress risers, normally observed around flaws, were eliminated by the doubler (see Section 3.0).

2.4.9 Ultimate/Residual Strength

Post-fatigue load-to-failure tests produced residual strength values for the composite-aluminum specimens. Table 7 lists the ultimate tensile strength values obtained in this test series and the average values are summarized below. Duplicate tests on similar specimens showed that the results were repeatable. The maximum scatter within a single specimen configuration was 1.9%. The maximum scatter across all of the ultimate strength results was 7.0%. Even the existence of disbonds and fatigue cracks did not prevent the doubler-reinforced-plates from achieving static ultimate tensile strengths in excess of the 70 ksi Mil handbook listing for 2024-T3 material. This

demonstrated the ability of a Boron-Epoxy composite doubler to return a damaged aluminum structure to its original load carrying capacity.

Test Specimen	Avg. Ult. Strength
1. Plain 2024-T3 (unreinforced)	72.3 ksi
2. Unflawed composite doubler installation	70.5 ksi
3. Impact/disbond doublers over a stop-drilled crack	75.4 ksi
4. Multiple impact/disbond flaws over an unabated crack`	72.4 ksi

[Mil handbook ultimate strength value for 2024-T3 material = 70 ksi]

Specimen Configuration	Specimen Number	Flaw Summary	Ultimate Tensile Strength (psi) ⊕
BE-6	6A *	No composite doubler	72,570
BE-6	7A *	No composite doubler	72,060
BE-7	9 Δ	Unflawed doubler installation	70,530
BE-8	10	Impact/disbond doubler over a stop-drilled crack	75,490
BE-8	11	Impact/disbond doubler over a stop-drilled crack	75,480
BE-8	12	Impact/disbond doubler over a stop-drilled crack	75,310
BE-9	16	Multiple impact/disbond flaws over an unabated crack	72,450
BE-9	17	Multiple impact/disbond flaws over an unabated crack	73,010
BE-9	18	Multiple impact/disbond flaws over an unabated crack	71,680

⊕ Mil-Hndbk-5 Value for 2024-T3 Aluminum = 70,000 psi

* Non-fatigued aluminum coupons without composite doubler

Δ Post-fatigue test but specimen was still unflawed

Table 7: Results from Ultimate Tensile Strength Failure Tests

2.4.10 Overall Evaluation of Bonded Boron-Epoxy Composite Doublers: Crack Mitigation and Damage Tolerance

By combining the ultimate strength results with the crack mitigation results, it is possible to truly assess the capabilities and damage tolerance of bonded Boron-Epoxy composite doublers. In this test series, relatively severe installation flaws were engineered into the test specimens in order to

evaluate Boron-Epoxy doubler performance under worst case, off-design conditions. The engineered flaws were at least two times larger than those that can be detected by NDI. It was demonstrated that even in the presence of extensive damage in the original structure (cracks, material loss) and in spite of non-optimum installations (adhesive disbonds), the composite doubler allowed the structure to survive more than four design lifetimes of fatigue loading. Installation flaws in the composite laminate did not propagate over 216,000 fatigue cycles. Furthermore, the added impediments of impact (severe enough to deform the parent aluminum skin) and hot-wet exposure did not affect the doubler's performance [1]. Since the tests were conducting using extreme combinations of flaw scenarios (sizes and collocation) and excessive fatigue load spectrums, the performance parameters presented here were arrived at in a conservative manner.

3.0 VALIDATION OF COMPOSITE DOUBLER REPAIR DESIGN

3.1 Design of Experiment

Goal - to validate the following aspects of the DC-10/MD-11 composite doubler repair initiative: 1) repair design, 2) repair analysis approach – stress analysis and damage tolerance, 3) finite element analysis models, and 4) nondestructive inspection procedures.

Specimens – 1) one *corrosion* flaw with the maximum allowable material removal (50% thinning), and 2) one *impact damage* flaw with the extreme out-of-plane deformation of 3/8".

Test Approach – 1) start with the DC-10/MD-11 fuselage pressurization stress spectrum in tension-tension testing (0-10 KSI) and magnify to a 70% overtest by applying a 0-17 KSI tension load spectrum, 2) conservatively test each specimen for up to 4 lifetimes of DC-10 aircraft (160,000 cycles), 3) measure static strain fields at different stages of fatigue testing – assess changes in stress field and associated performance of composite doubler, 4) apply ultrasonic resonance (Bondmaster) NDI to each test specimen after 40,000, 80,000, 120,000, and 160,000 cycles, and 5) follow fatigue tests with a static ultimate test (residual strength) to determine design margins and performance of composite doubler when the parent material yields (plastic strain regime).

Test Description – Figures 26 and 27 show the two design validation test articles for the extreme skin corrosion and impact damage conditions that were used to assess the doubler design and analysis methodology. Figures 28 and 29 show the associated strain gage layouts. The specimens contain representative, yet upper extreme flaws and the composite doubler designed for the DC-10 aircraft repairs. The test approach utilized a magnified load spectrum and fatigue cycles equal to four design lifetimes of the DC-10 for validation (DC-10 design lifetime = 40,000 cycles; MD-11 design lifetime = 36,000 cycles). The test-certified model was then able to assess the doubler using more complex stress fields and boundary conditions (See Section 2.0). The tests included static, fatigue, and ultimate/residual strength tests. The ultrasonic inspection technique was interjected throughout the fatigue tests to continue sensitivity assessments (see item Section 5.0 for additional NDI discussions). Figures 30 and 31 show the DC-10-F1 (corrosion flaw) and DC-10-F2 (impact flaw) design validation test articles undergoing fatigue and strength testing.

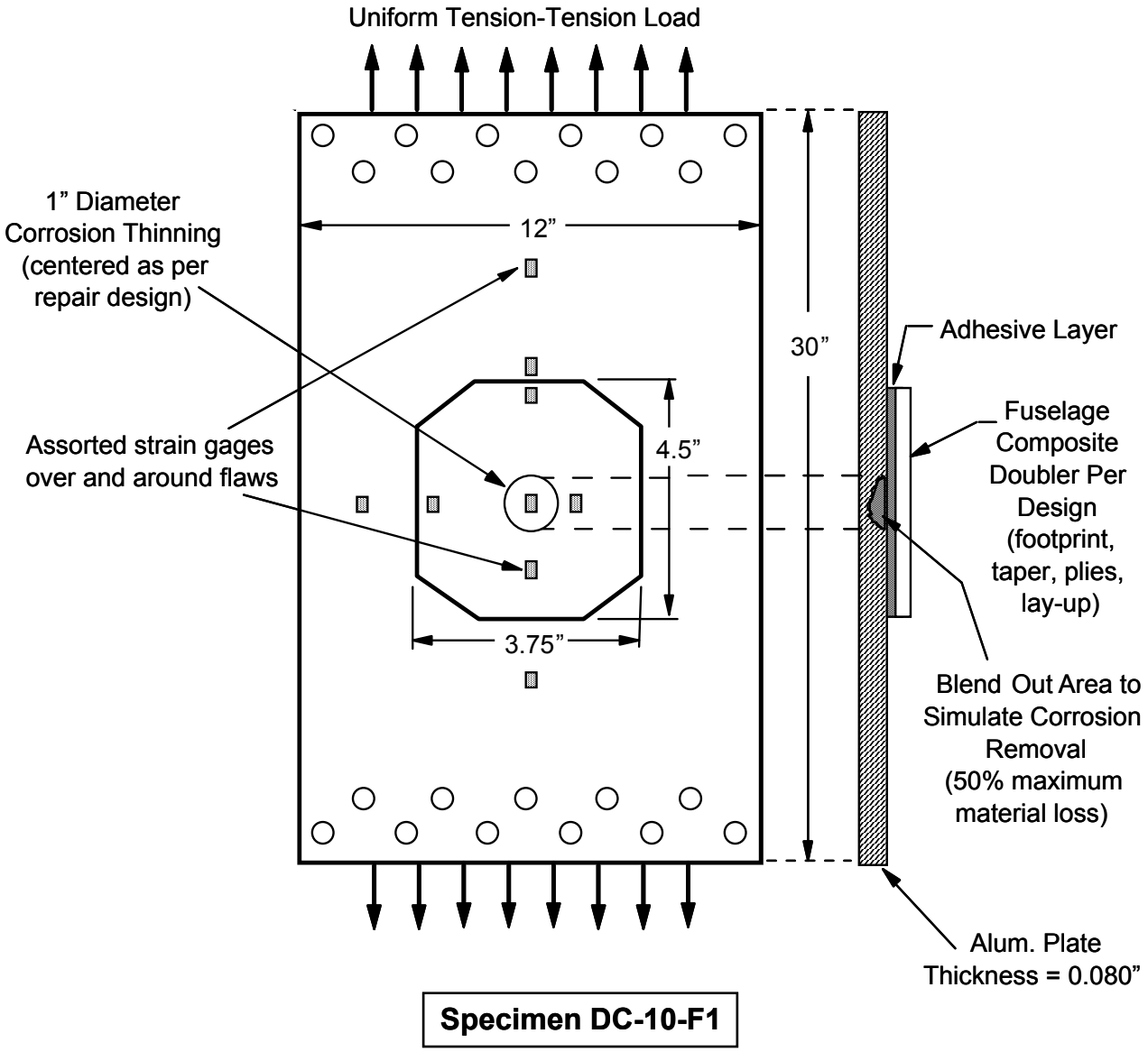

Figure 26: Design and NDI Validation Test Specimen for Family of DC-10 Composite Doubler Skin Repairs (Corrosion Skin Flaw)

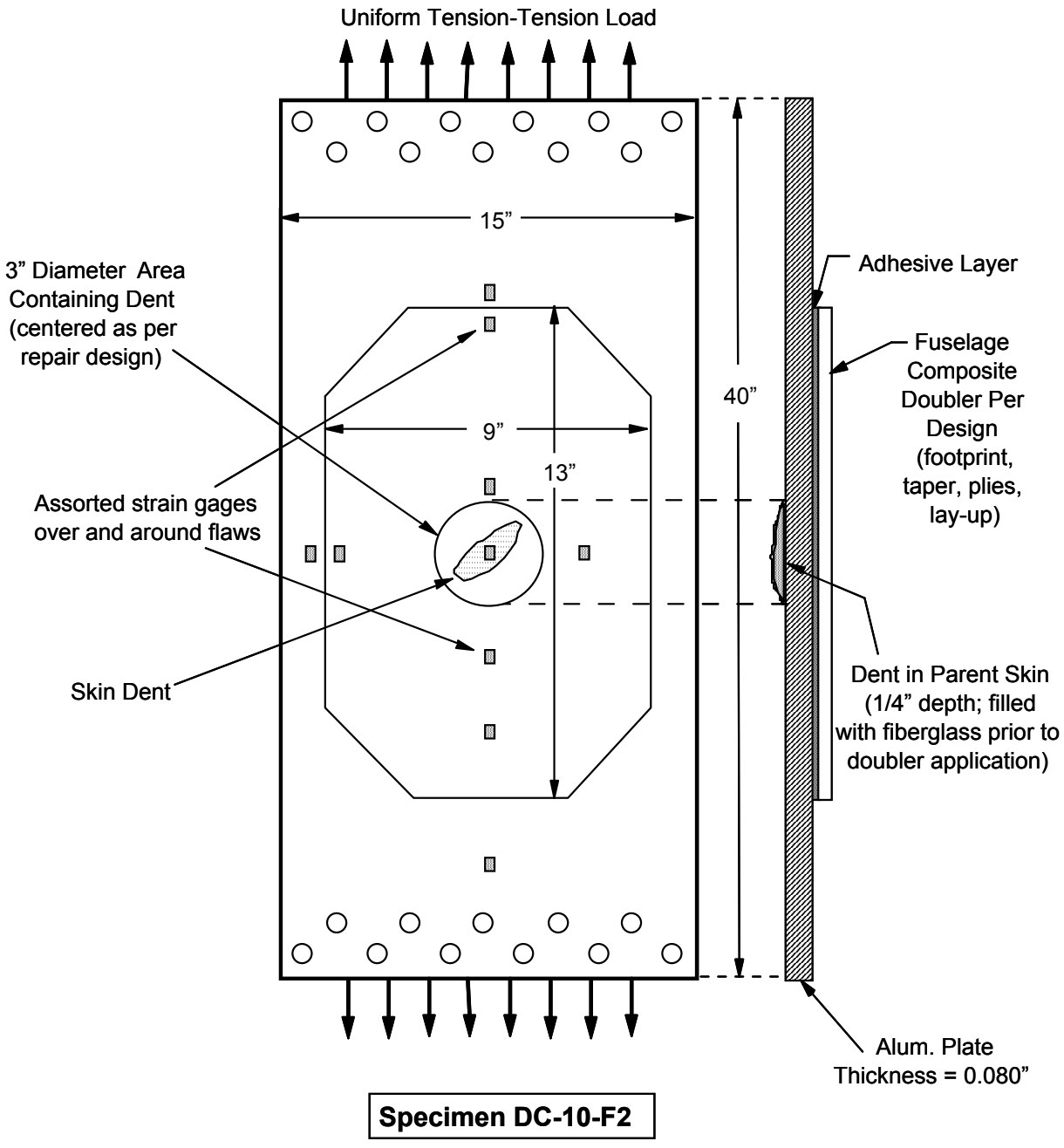

Figure 27: Design and NDI Validation Test Specimen for Family of DC-10 Composite Doubler Skin Repairs (Impact Damage Skin Flaw)

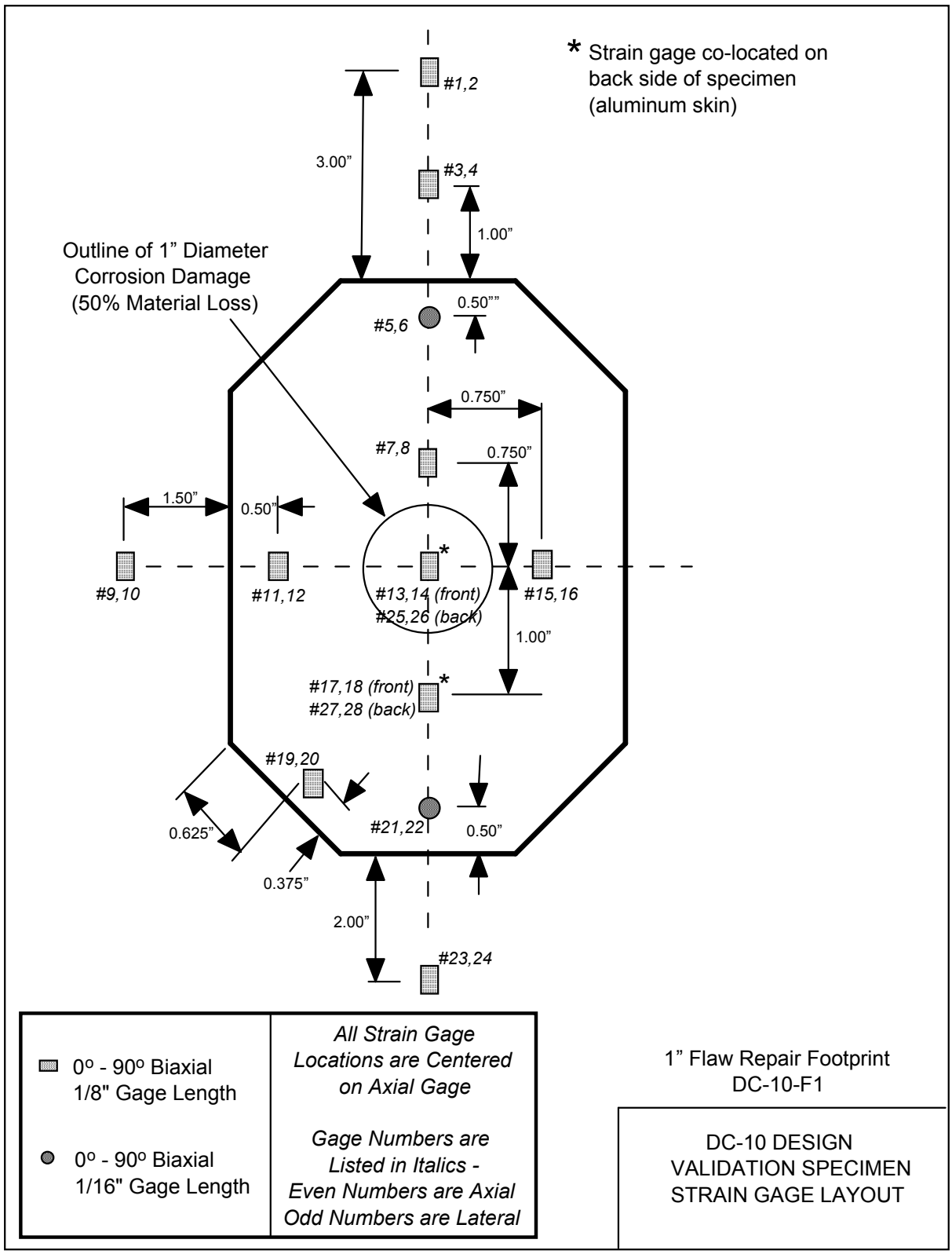

Figure 28: Strain Gage Layout for One Inch Flaw Repair Design Validation Test

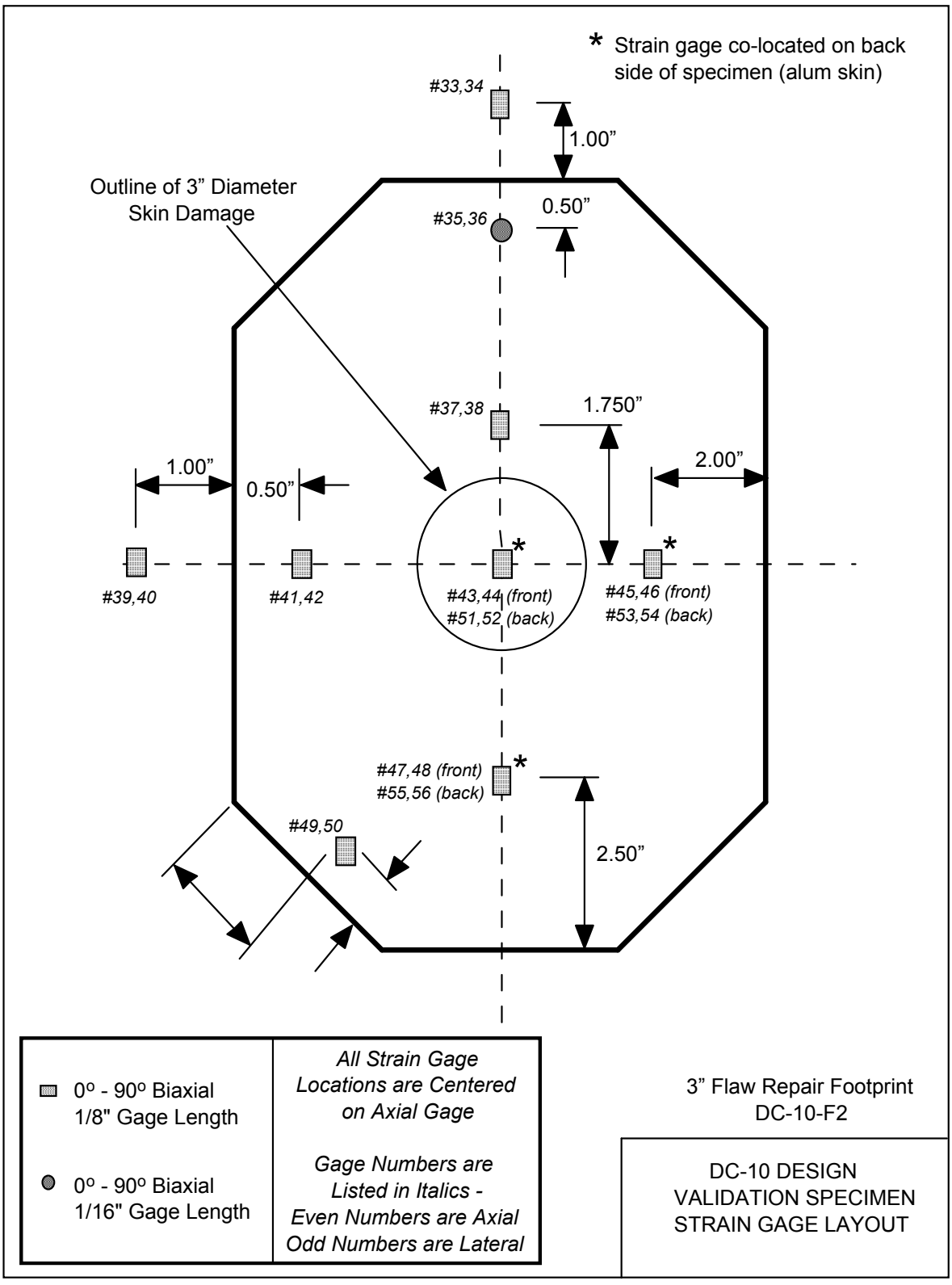

Figure 29: Strain Gage Layout for Three Inch Flaw Repair Design Validation Test

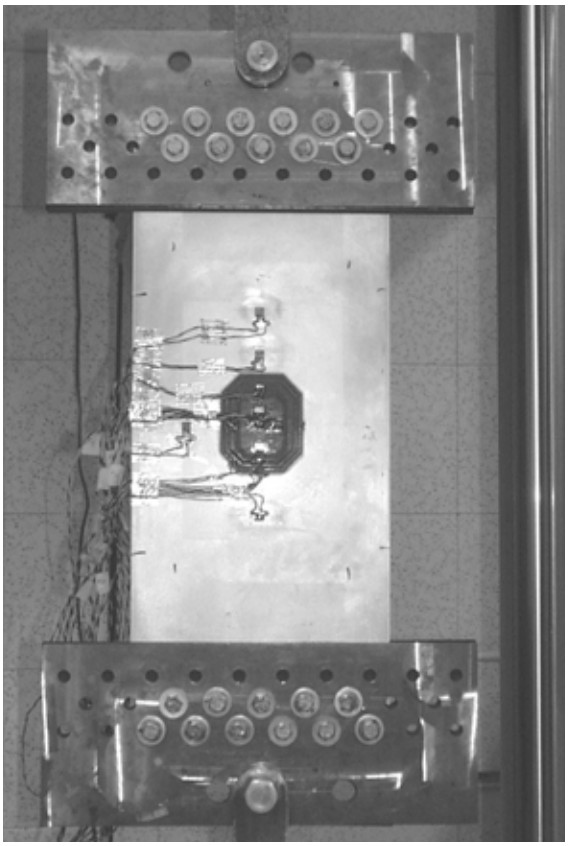

(a) Test Panel Mounted in Machine Grips

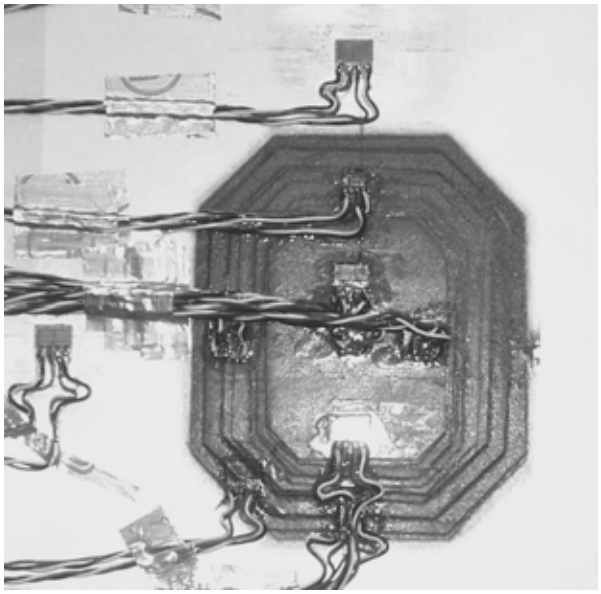

(b) Close-Up View of Doubler and Strain Gages

Figure 30: Set-Up for DC-10-F1 Composite Doubler Validation Test (Repair of 1" diameter flaws – 50% material thinning flaw)

(a) Test Panel Mounted in Machine Grips

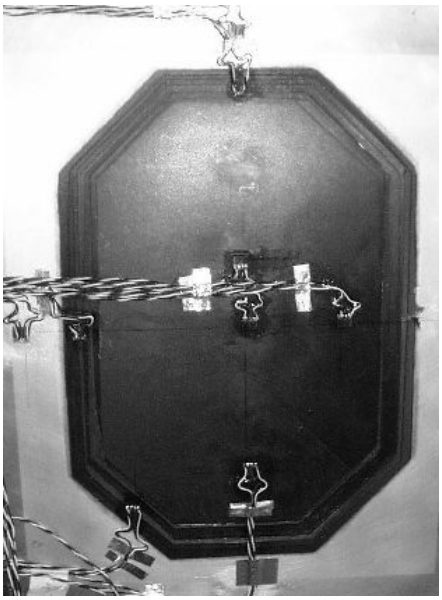

(b) Close-Up View of Doubler and Strain Gages

Figure 31: Set-Up for DC-10-F2 Composite Doubler Validation Test (Repair of 3" diameter flaws – 3/8" depth impact damage)

Output from Design Validation Tests - 1) demonstration of gouge/dent/corrosion repair installation, 2) comparison of stresses and strains with model, 3) assessment of post-repair fatigue life, 4) determination of ultimate strength of repair, and 5) validation of inspection

techniques under in-service conditions. Figures 28 and 29 show the strain gage layouts that were used to monitor: 1) the load transfer into the composite doublers and, 2) the strain field throughout the composite laminate and aluminum plate. The stress, strain, and load transfer values presented in this section quantify the doubler performance characteristics. They provide additional insights into the doubler's ability to resist crack initiation and mitigate crack growth.

3.2 Results from Specimen DC-10-F1 Design Validation Tests

3.2.1 Strain Field Assessment

In general, it was observed that all strain responses from the simulated fuselage pressurization loads were linear (see Figures 32-35). No residual strains were noted when the specimens were unloaded. Subsequent failure tests (see Section 3.2.4 below) showed that the strains induced by the fatigue load spectrum were well inside the linear elastic regime for the 2024-T3 aluminum and Boron-Epoxy composite materials. The strains monitored in the load transfer (tapered) region around the perimeter of the doubler were approximately 40%-50% of the total strain in the aluminum plate. This value remained constant over four fatigue lifetimes indicating that there was no deterioration in the bond strength. The strain in the aluminum plate beneath the doubler was reduced in accordance with the strain picked up by the composite doubler.

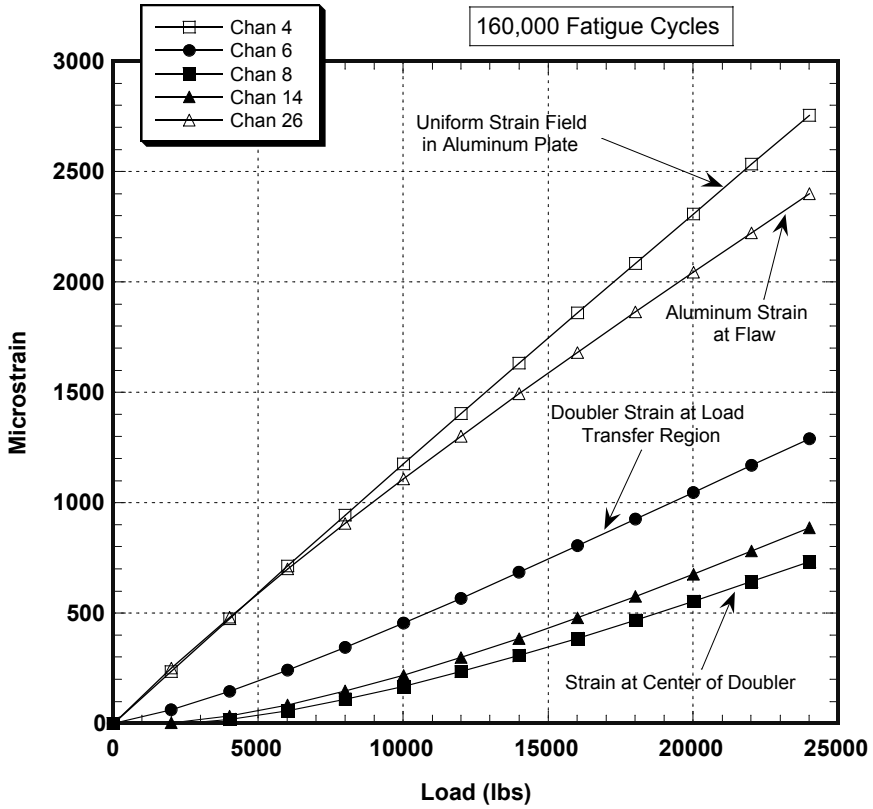

Figure 32: Axial Strain Field in Aluminum and Composite for DC-10-F1 Design (Repair of 1" diameter flaws – 50% material thinning flaw)

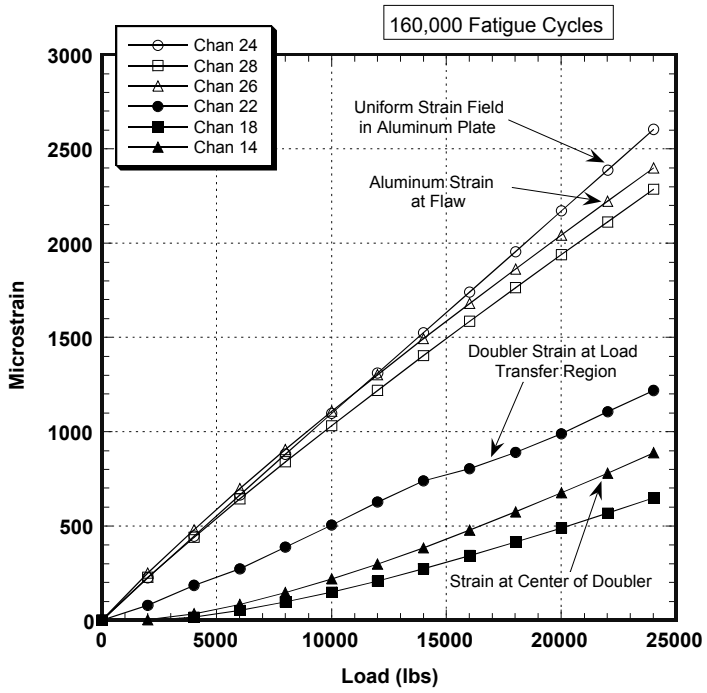

Figure 33: Axial Strain Field in Aluminum and Composite for DC-10-F1 Design (Repair of 1" diameter flaws – 50% material thinning flaw)

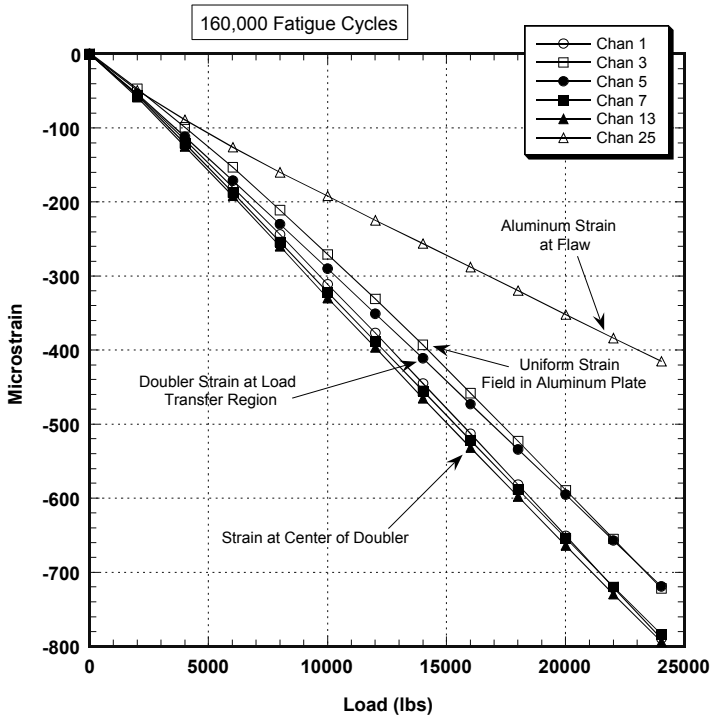

Figure 34: Lateral Strain Field in Aluminum and Composite for DC-10-F1 Design (Repair of 1" diameter flaws – 50% material thinning flaw)

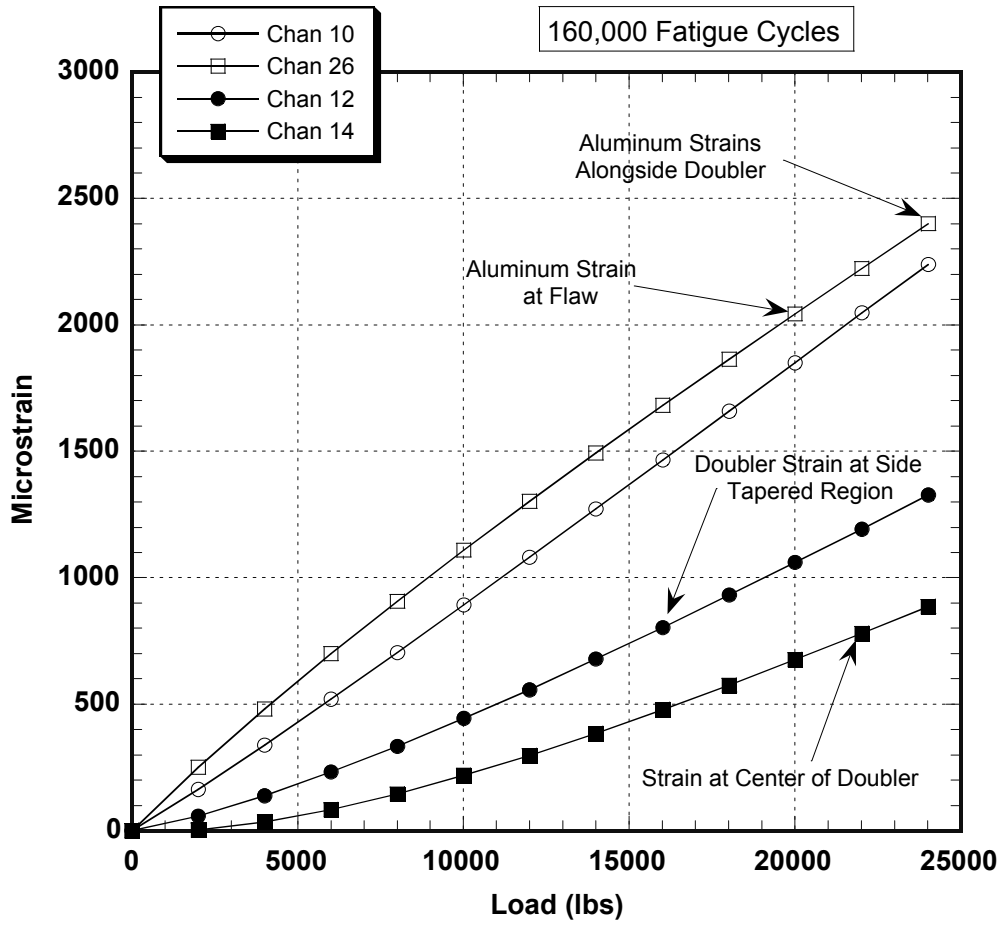

Figure 35: Axial Strain Field Along Midline of Doubler Installation for DC-10-F1 Design (Repair of 1" diameter flaws – 50% material thinning flaw)

3.2.2 Load Transfer (Doubler Efficiency)

Plots of percent load transfer were obtained by calculating the ratio between doubler strains and strains in corresponding portions of the aluminum parent skin. Figures 36 and 37 show the resulting load transfer plots for various doubler and aluminum reference channels $\{\varepsilon_{doubler} / \varepsilon_{alum(ref)}\}$. In the tapered portion of the doubler, the load transfer was consistently in the 40 - 60 % range. In the center, where the doubler reaches its maximum thickness of 13 plies, the load transfer was in the 30 - 50% range. Furthermore, these load transfer values remained constant over four fatigue lifetimes. This indicates that there was no deterioration in the bond strength.

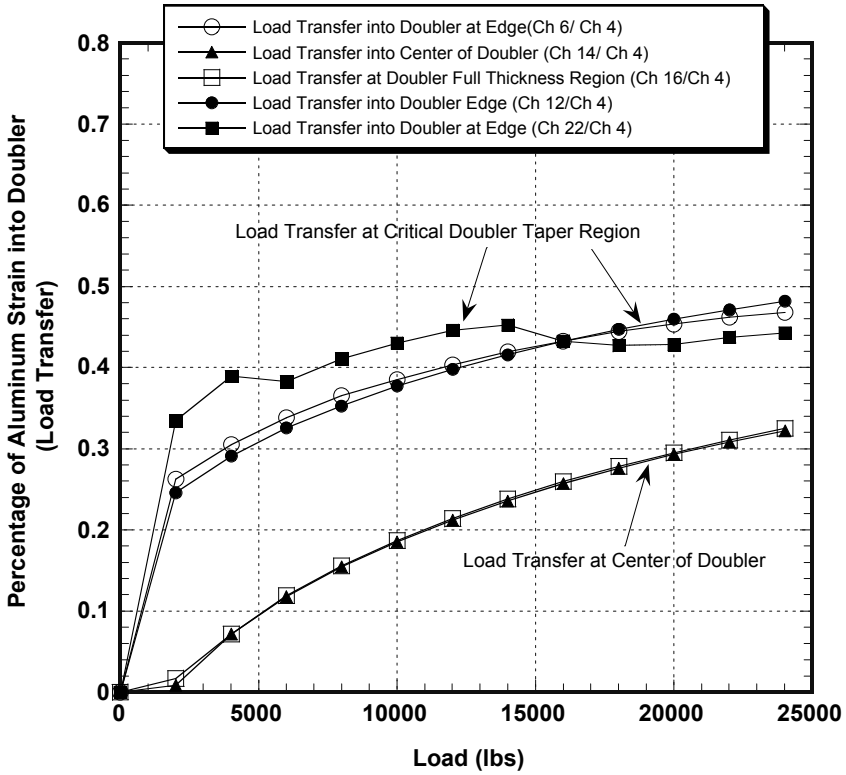

Figure 36: Load Transfer into Doubler for DC-10-F1 Validation Specimen

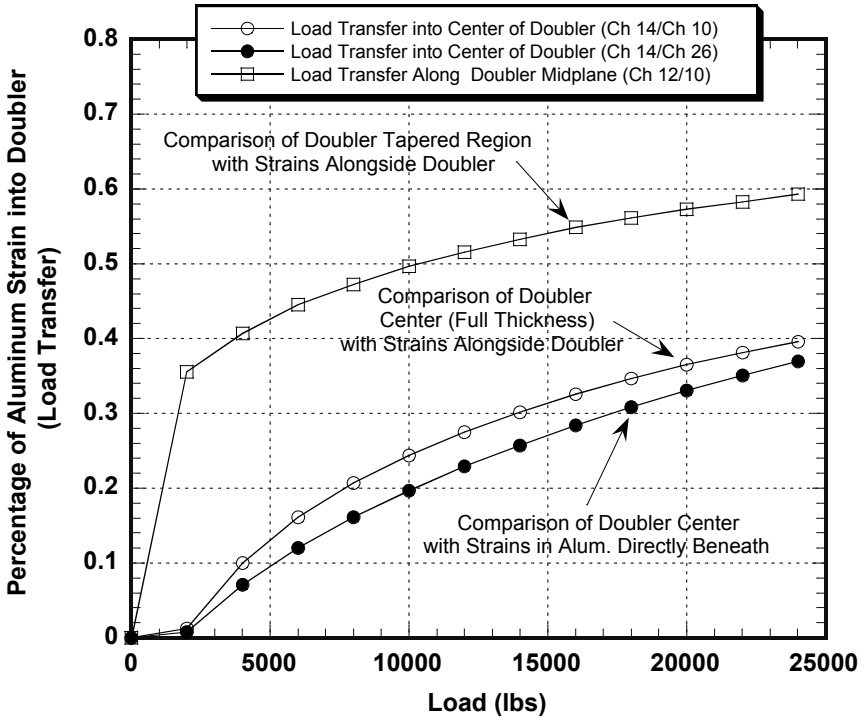

Figure 37: Aluminum-to-Composite Strain Ratios at Midplane of DC-10-F1 Doubler

3.2.3 Effect of Multiple Fatigue Lifetimes on Strain Fields (Patch Performance)

The strain fields remained unchanged over the course of the fatigue tests. Note how the 0 fatigue cycles and 160,000 fatigue cycle plots lie on top of each other in Figures 38-41. The exact match in strain levels before and after 160,000 fatigue cycles indicates that there was no deterioration in the bond strength. Nondestructive inspections of the test article (see Section 3.4) further quantified these results.

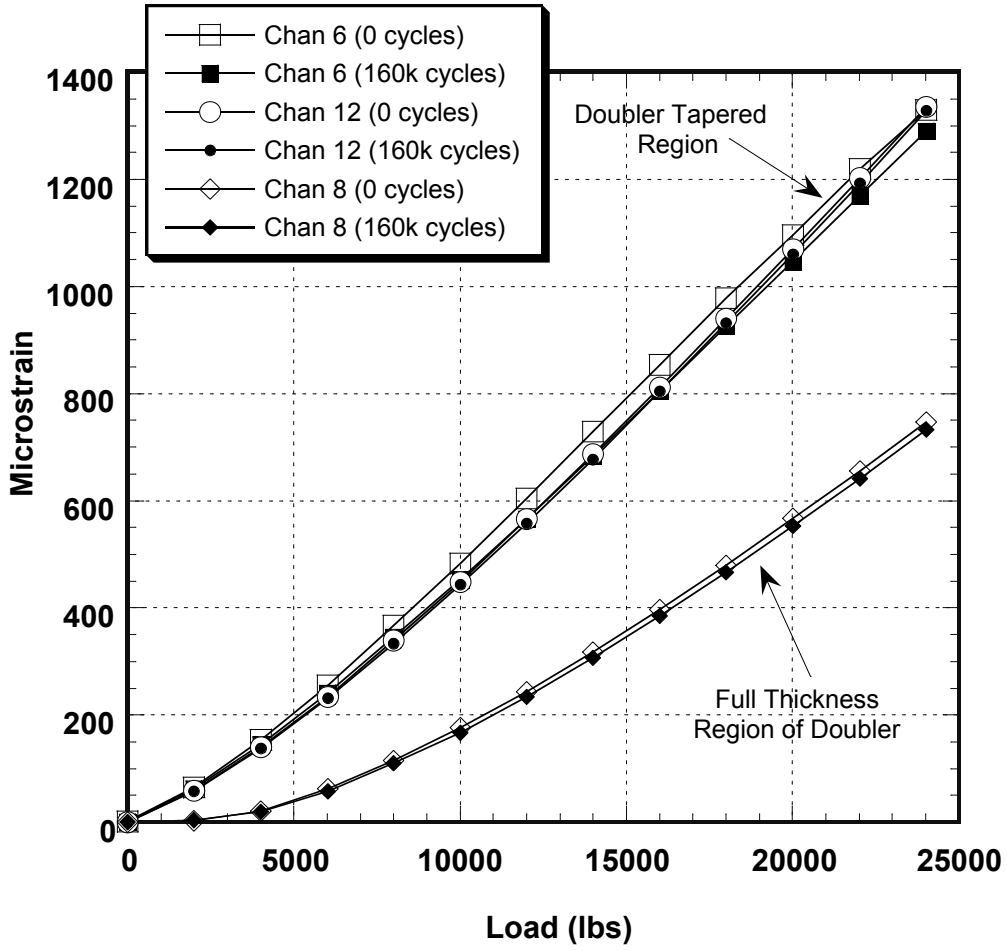

Figure 38: Strain Comparisons in DC-10-F1 Doubler - Before and After Fatigue Testing

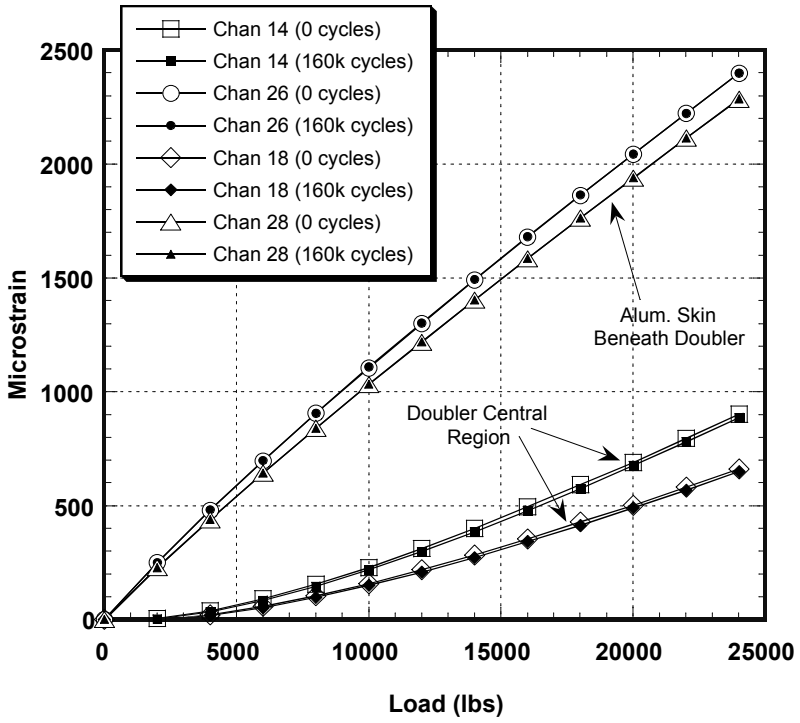

Figure 39: Strain Comparisons in DC-10-F1 Doubler - Before and After Fatigue Testing

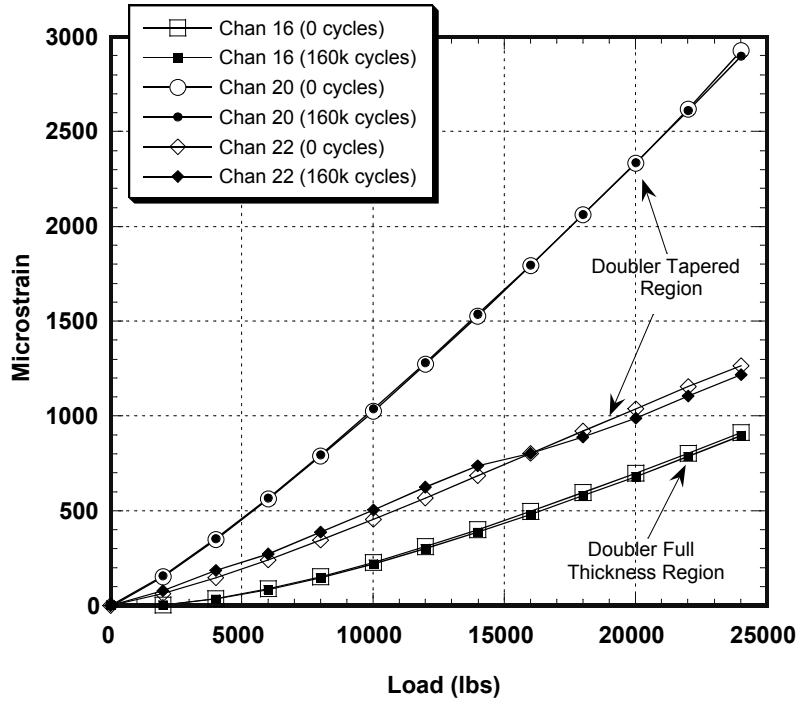

Figure 40: Strain Comparisons in DC-10-F1 Doubler - Before and After Fatigue Testing

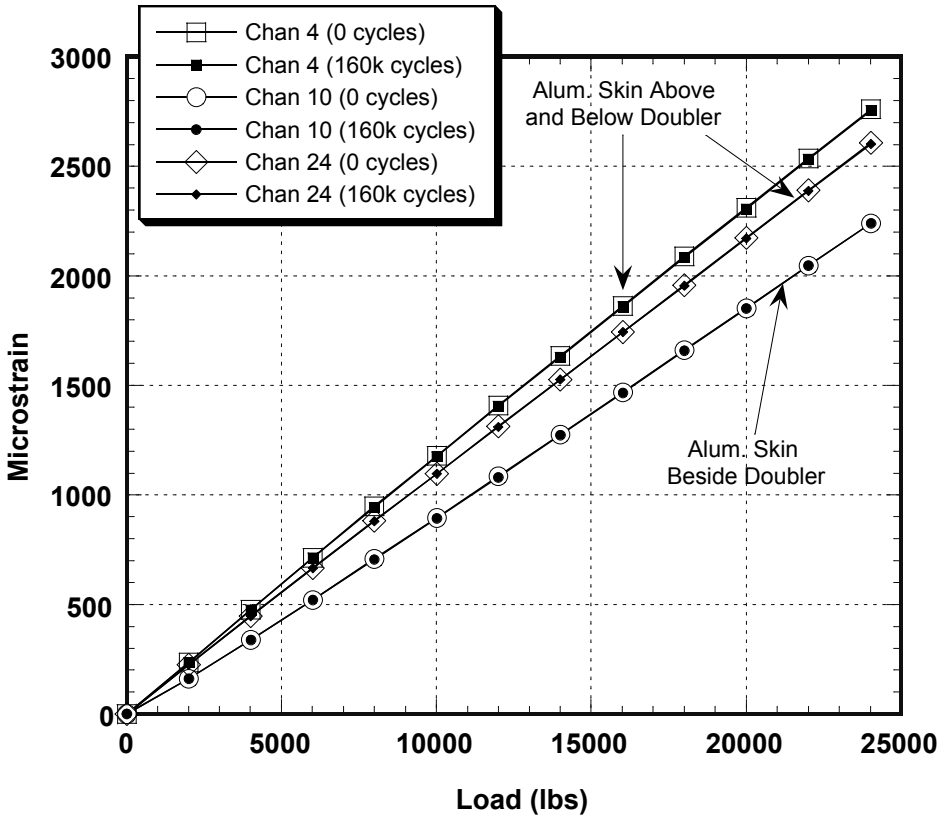

Figure 41: Strain Comparisons in Aluminum Skin Around DC-10-F1 Doubler - Before and After Fatigue Testing

3.2.4 Ultimate Strength Results

The DC-10-F1 design validation test specimen was subjected to ultimate tensile strength tests following the 160,000 cycles of fatigue loading. The uniaxial load was uniformly increased until the specimen failed. Failure was defined as the point at which the structure could no longer sustain an increasing load.

Figures 42-45 shows the strain field in specimen DC-10-F1 up through failure. The open shapes represent strains in the aluminum plate and the solid shapes plot the strains measured in the composite doubler. The aluminum plate away from the doubler (channels 4, 24, 25) began to yield at approximately 44,000 lbs. (45.8 ksi) while the doubler continued to increase its load in a linear fashion. The load was linearly increased until failure of the aluminum plate occurred at 53,500 lbs (55.7 ksi) and the specimen could no longer sustain an increasing load. This failure load does not represent the ultimate strength value for the specimen because the failure originated at the holes used to grip the specimen (see hole pattern in Fig. 26). It is often difficult to reach full ultimate failure load levels in specimens of this size because of the inherent weakness of the structure at the load application point. However, the ultimate strength tests were successful in loading the DC-10-F1 specimen into the plastic regime (past yielding).

The aluminum began its nonlinear response at the yield point indicated in Figs. 42-45. Similarly, the composite doubler showed a slightly nonlinear behavior at this same load level. But the Boron-Epoxy laminate did not yield. The material properties for Boron-Epoxy indicate a yield stress of 185 ksi. Further, after specimen failure, the strain gages on the doubler returned to zero indicating that the doubler did not undergo any permanent deformation. Thus, the nonlinear response in the doubler strain gages shows that the doubler is absorbing more strain and mirroring the response of the parent aluminum skin. *Figures 42-45 illustrate that the adhesive is able to transmit stresses in the plastic regime and that loading beyond the initial yield level is required to fail the repair installation.*

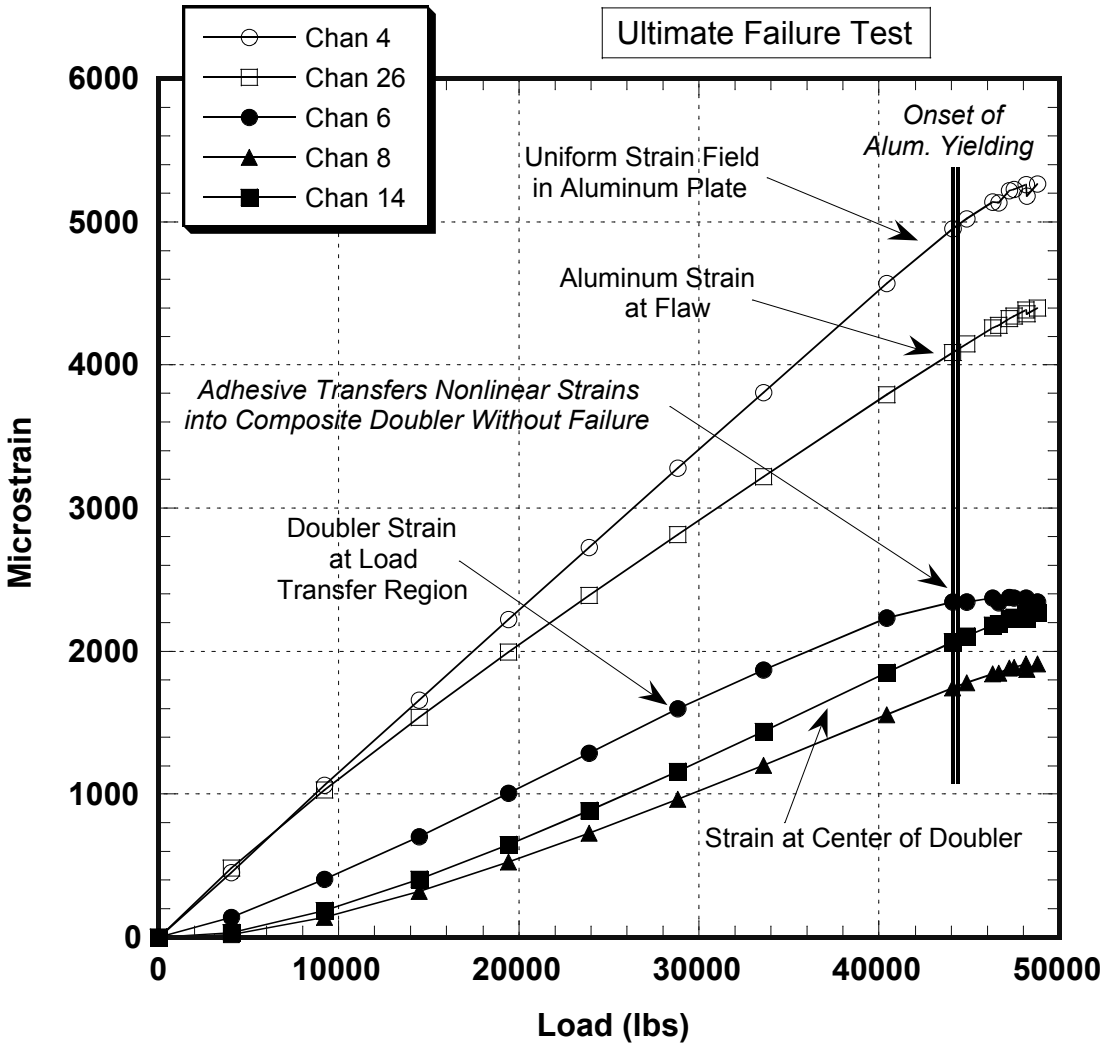

Figure 42: Axial Strain Field During Ultimate Failure Test of DC-10-F1 Design (Repair of 1" diameter flaws – 50% material thinning flaw)

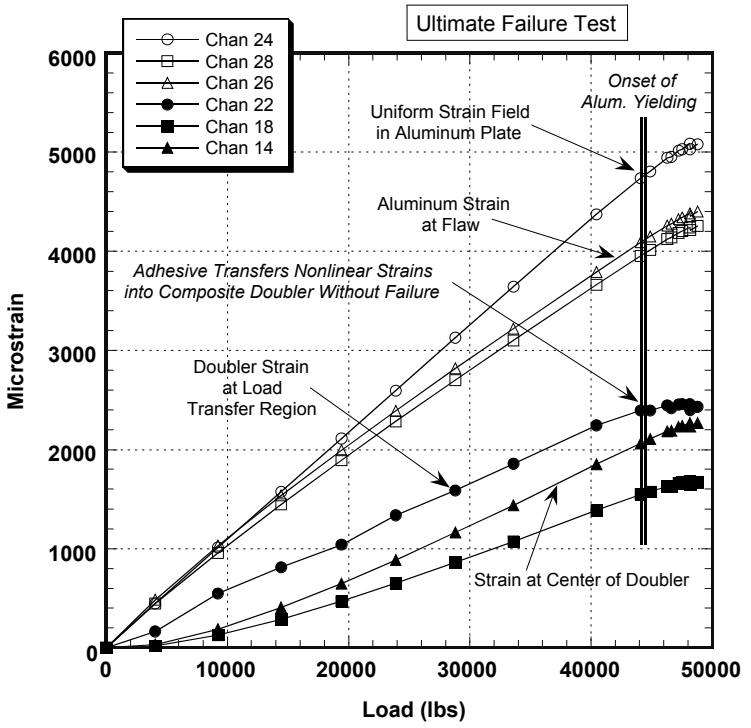

Figure 43: Axial Strain Field During Ultimate Failure Test of DC-10-F1 Design (Repair of 1" diameter flaws – 50% material thinning flaw)

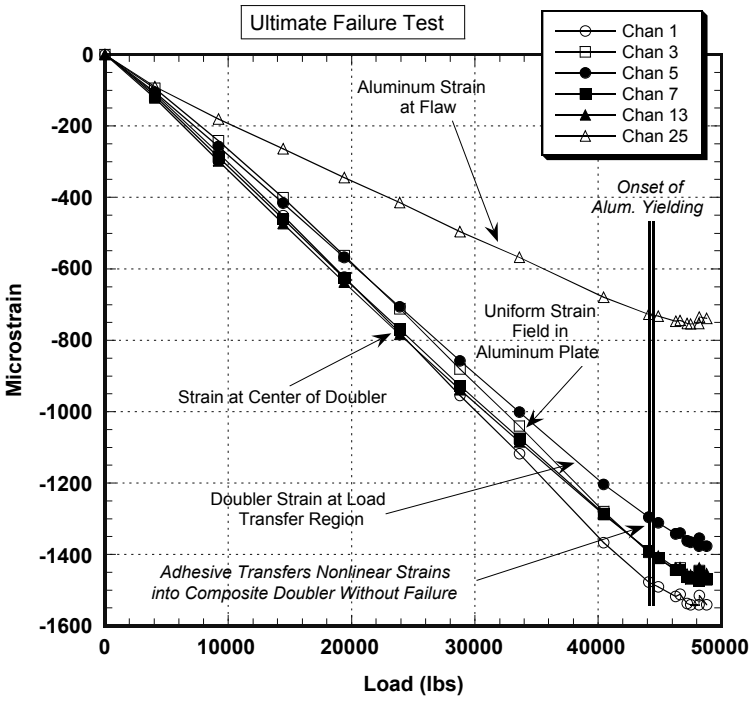

Figure 44: Lateral Strain Field During Ultimate Failure Test of DC-10-F1 Design (Repair of 1" diameter flaws – 50% material thinning flaw)

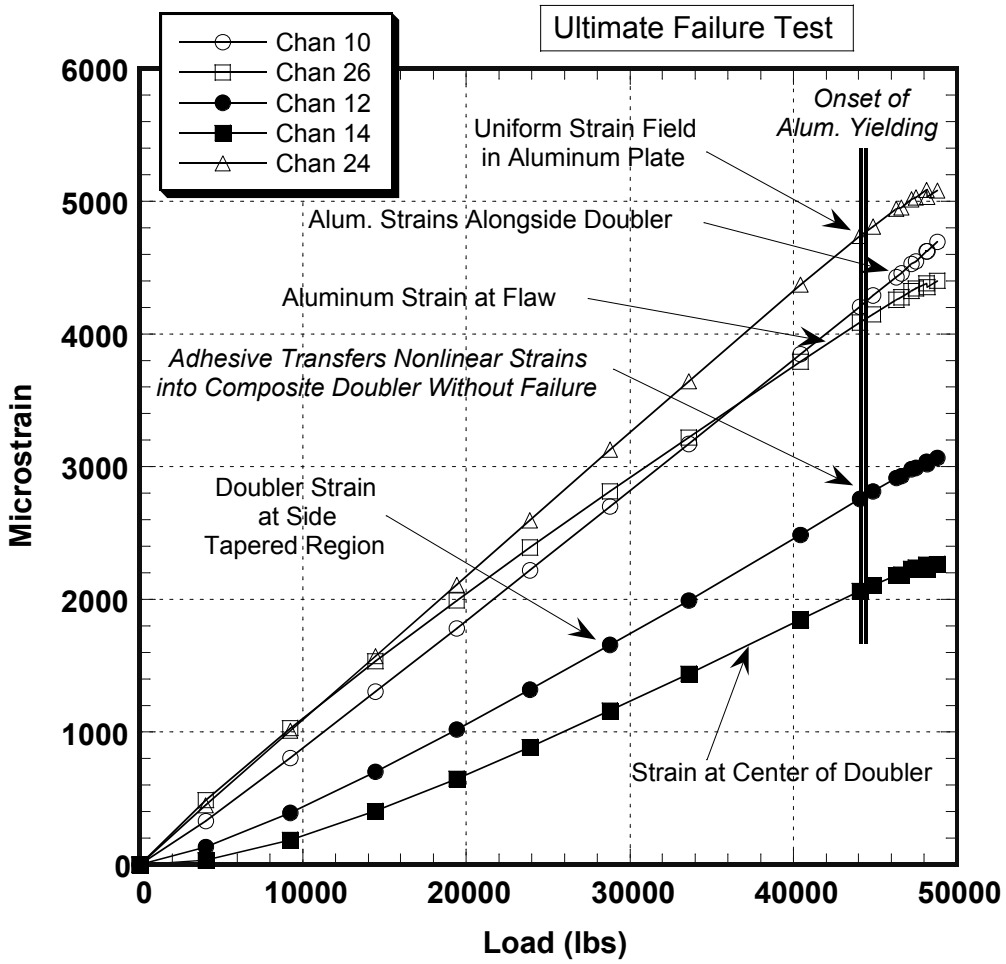

Figure 45: Axial Strain Field Along Midline of Doubler Installation During Ultimate Failure Test of DC-10-F1 Design
(Repair of 1" diameter flaws – 50% material thinning flaw)

3.3 Results from Specimen DC-10-F2 Design Validation Tests

3.3.1 Strain Field Assessment

In general, it was observed that all strain responses from the simulated fuselage pressurization loads were linear (see Figures 46-49). No residual strains were noted when the specimens were unloaded. Subsequent failure tests (see Section 3.3.4 below) showed that the strains induced by the fatigue load spectrum were well inside the linear elastic regime for the 2024-T3 aluminum and Boron-Epoxy composite materials. The strains monitored in the load transfer (tapered) region around the perimeter of the doubler were approximately 40%-50% of the total strain in the aluminum plate. This value remained constant over four fatigue lifetimes indicating that there was no deterioration in the bond strength. The strain in the aluminum plate beneath the doubler is reduced in accordance with the strain picked up by the composite doubler.

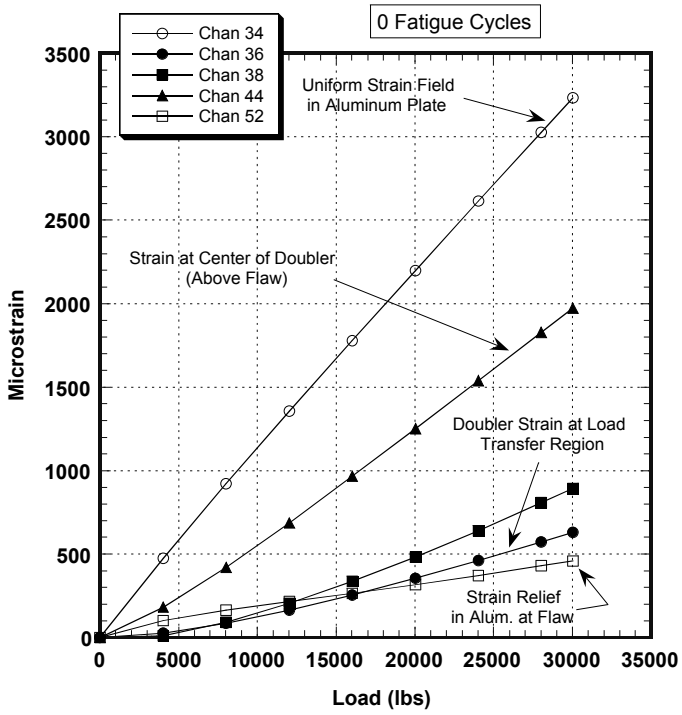

Figure 46: Axial Strain Field in Aluminum and Composite for DC-10-F2 Design (Repair of 3" diameter flaws – 3/8" depth impact damage)

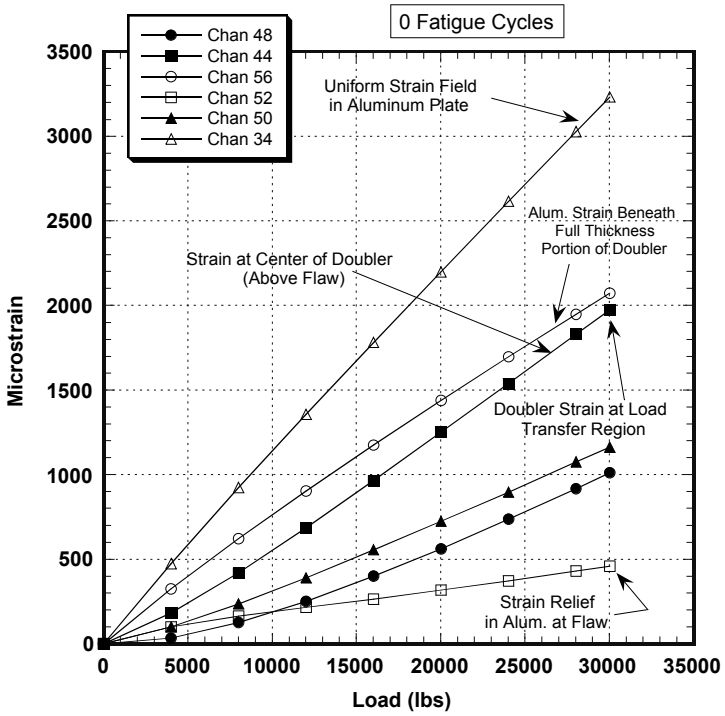

Figure 47: Axial Strain Field in Aluminum and Composite for DC-10-F2 Design (Repair of 3" diameter flaws – 3/8" depth impact damage)

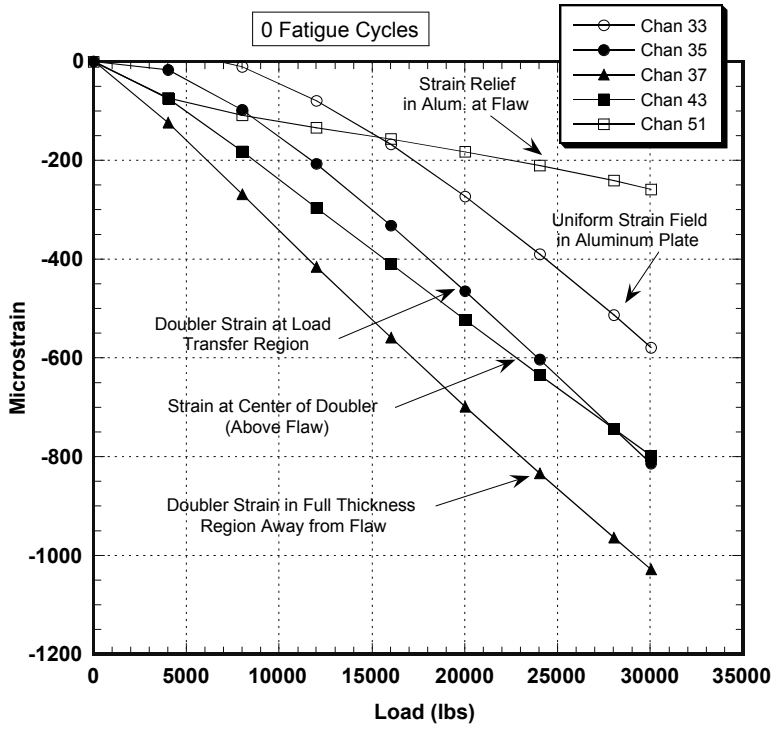

Figure 48: Lateral Strain Field in Aluminum and Composite for DC-10-F2 Design (Repair of 3" diameter flaws – 3/8" depth impact damage)

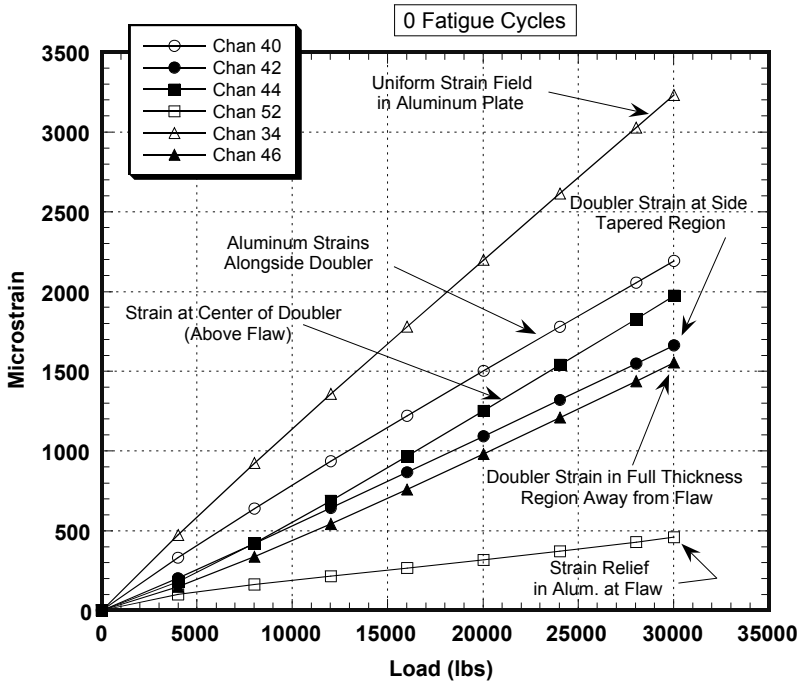

Figure 49: Axial Strain Field Along Midline of Doubler Installation for DC-10-F2 Design (Repair of 3" diameter flaws – 3/8" depth impact damage)

3.3.2 Load Transfer (Doubler Efficiency)

Plots of percent load transfer were obtained by calculating the ratio between doubler strains and strains in corresponding portions of the aluminum parent skin. Figures 50 -51 show the resulting load transfer plots for various doubler and aluminum reference channels $\{\varepsilon_{doubler} / \varepsilon_{alum(ref)}\}$. In the tapered portion of the doubler, the load transfer was consistently in the 30 - 50% range. In the center, where the doubler reaches its maximum thickness of 13 plies, the load transfer was in the 40 - 60% range. Furthermore, these load transfer values remained constant over four fatigue lifetimes. This indicates that there was no deterioration in the bond strength. Figure 52 shows a comparison of strains in the doubler to strains in the aluminum plate at a common location (stains in aluminum are beneath doubler). The lower curve, showing a 1:1 strain ratio, shows that the aluminum and doubler share the load equally in the full thickness region adjacent to the corrosion flaw. In the full thickness region directly over the flaw, the doubler absorbs much more of the load (doubler strains are 4.5 times the aluminum strain beneath). This is important since the goal is to relieve the plate strains in the vicinity of the flaw.

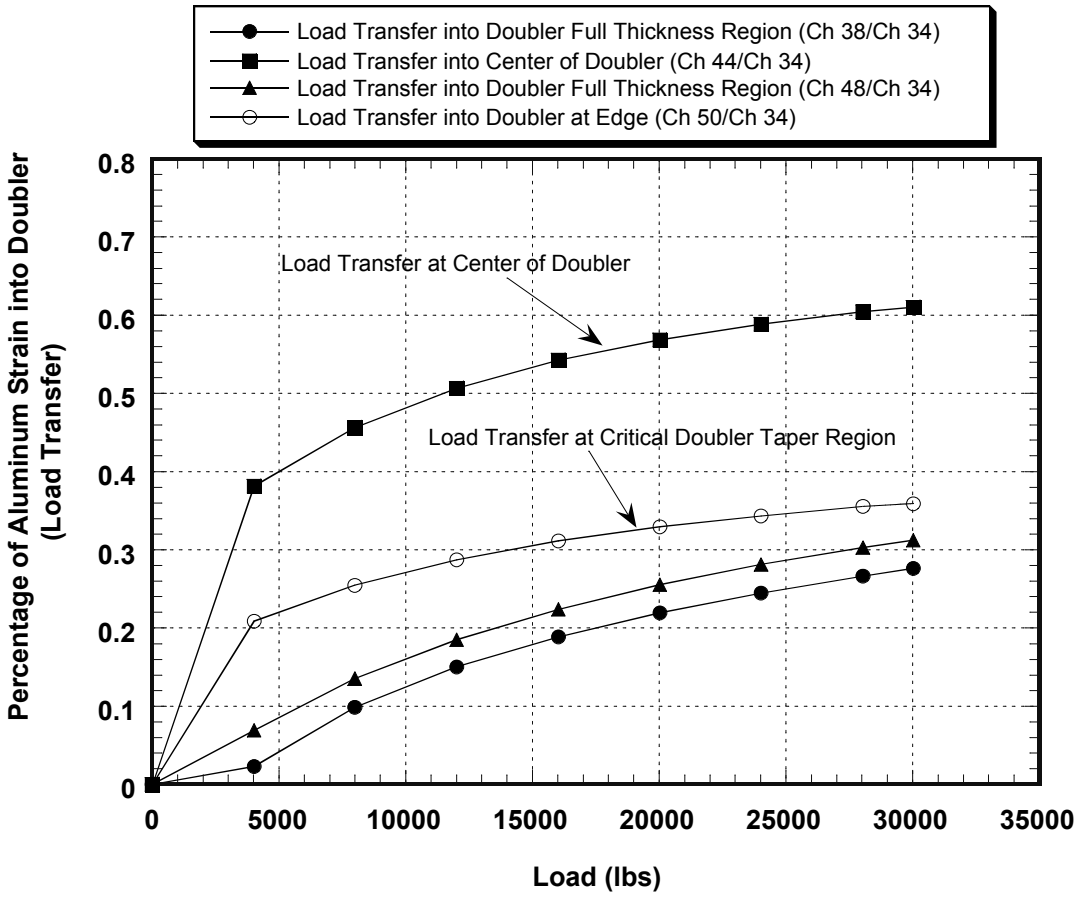

Figure 50: Load Transfer into Doubler for DC-10-F2 Validation Specimen

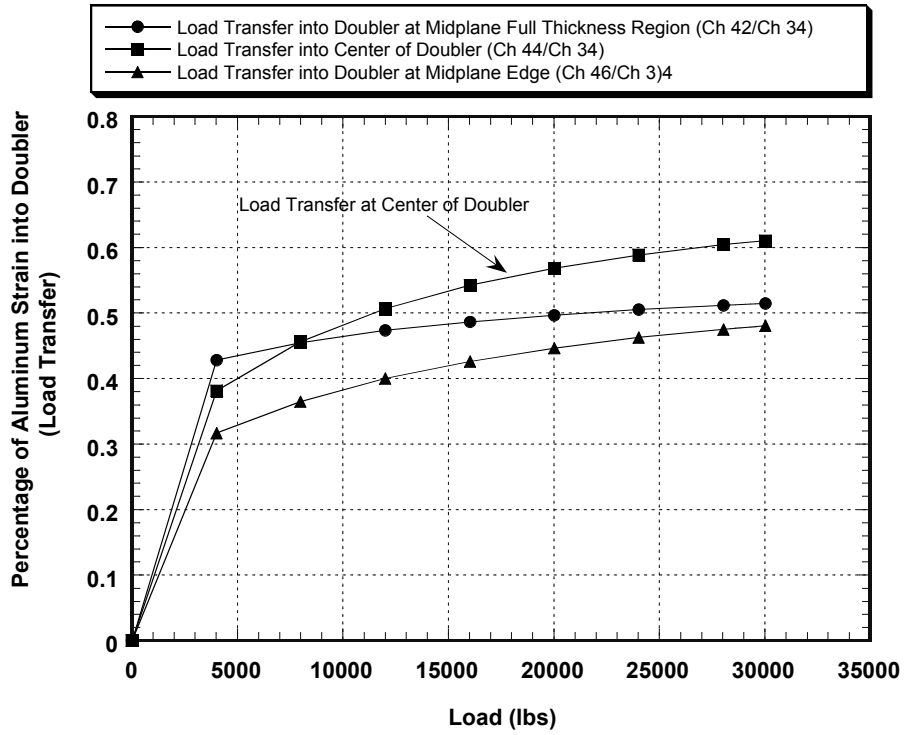

Figure 51: Load Transfer into Doubler at Midplane of DC-10-F2 Doubler

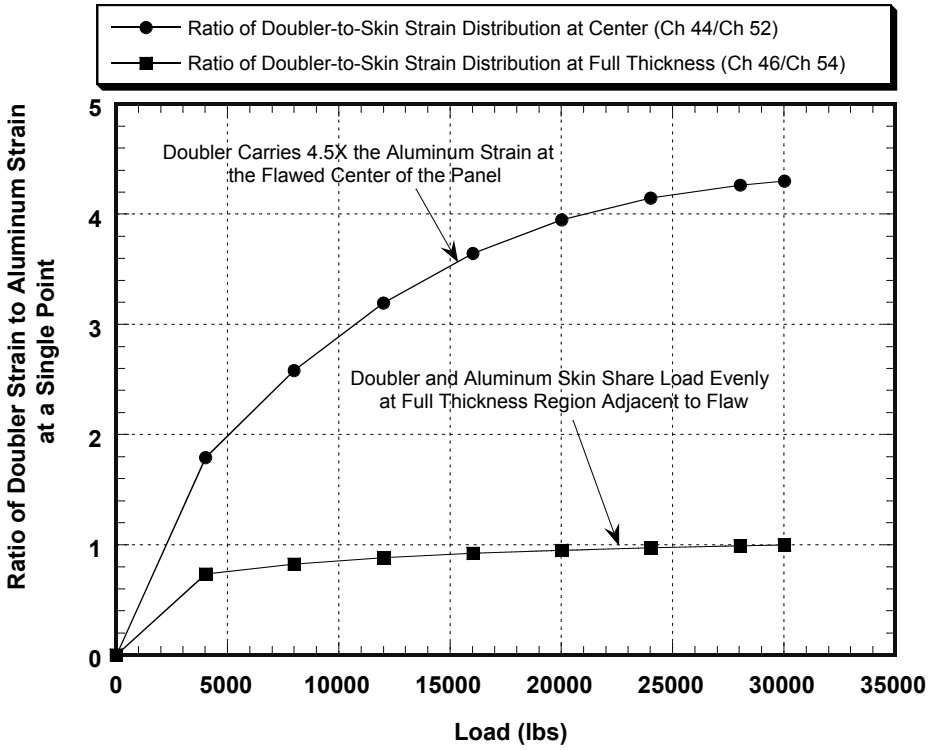

Figure 52: Composite-to-Aluminum Strain Ratios on DC-10-F2 Doubler

3.3.3 Effect of Multiple Fatigue Lifetimes on Strain Fields (Patch Performance)

The strain fields remained unchanged over the course of the fatigue tests. Note how the 0 fatigue cycles and 160,000 fatigue cycle plots lie on top of each other in Figures 53-55. The exact match in strain levels before and after 160,000 fatigue cycles indicates that there was no deterioration in the bond strength. Nondestructive inspections of the test article (see Section 3.4) further quantify these results.

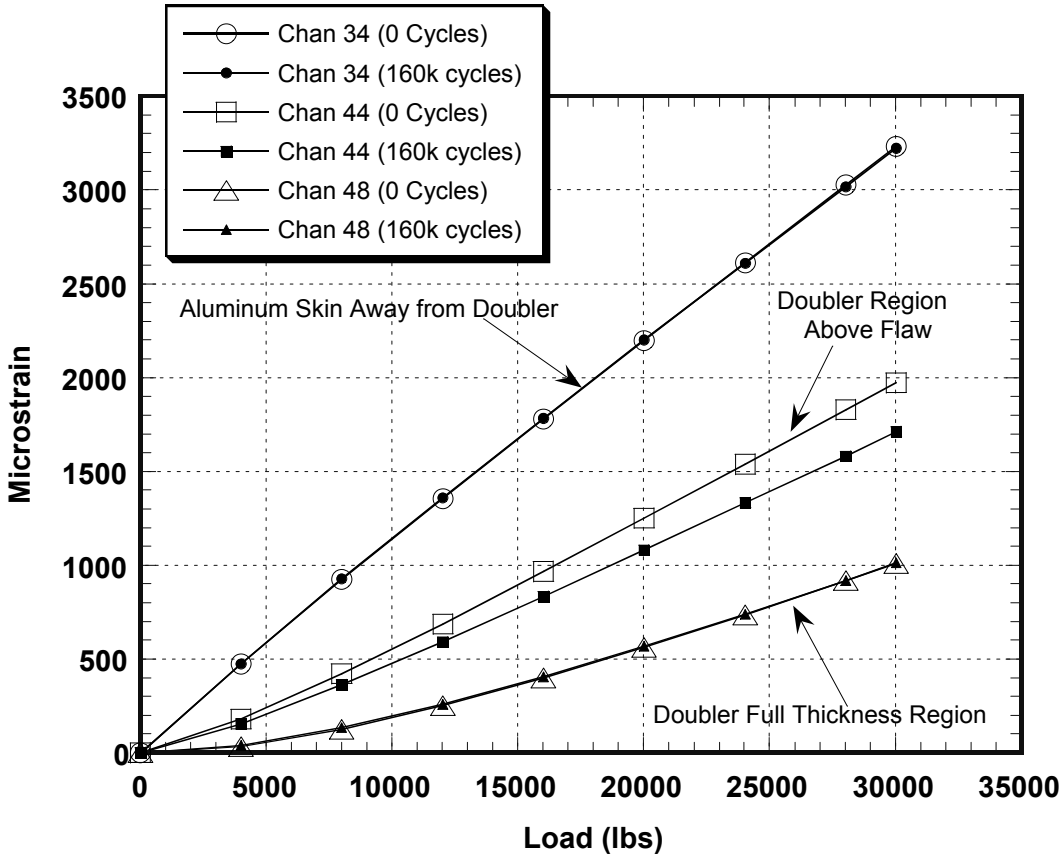

Figure 53: Strain Comparisons in DC-10-F2 Doubler - Before and After Fatigue Testing

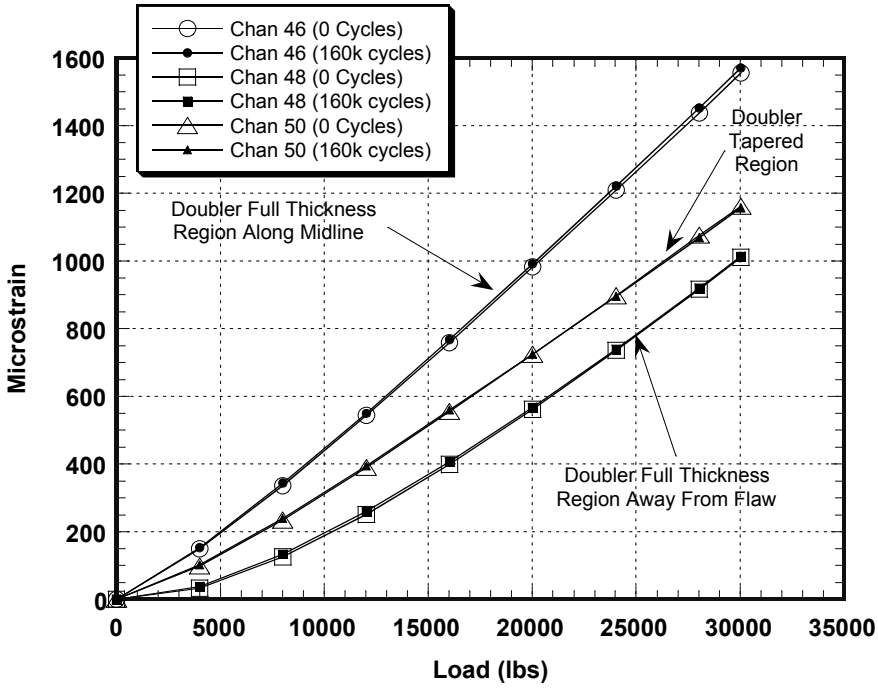

Figure 54: Strain Comparisons in DC-10-F2 Doubler - Before and After Fatigue Testing

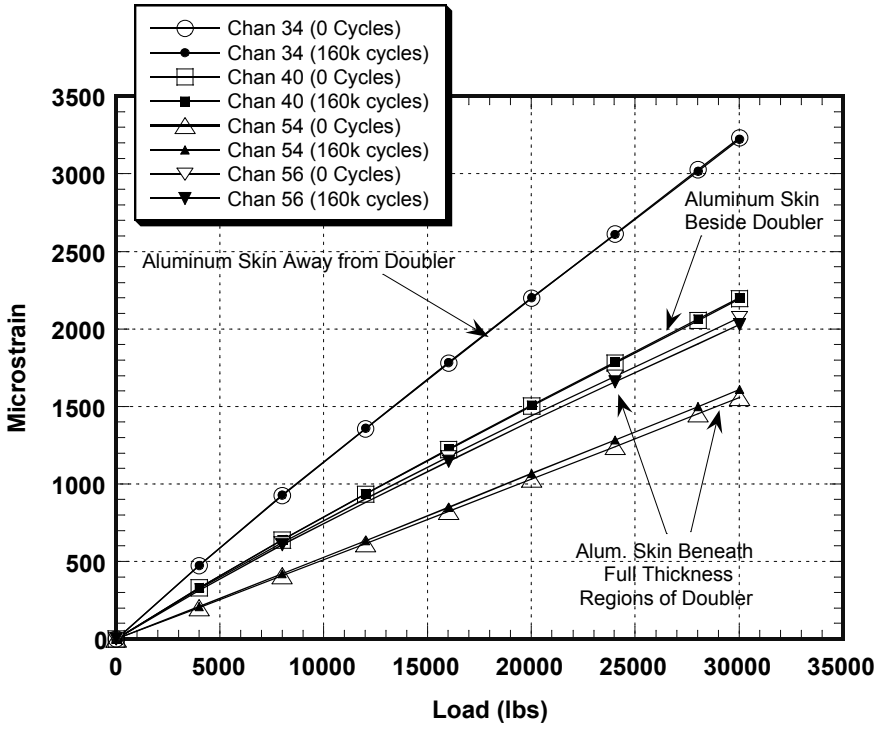

Figure 55: Strain Comparisons in Aluminum Skin Around DC-10-F2 Doubler - Before and After Fatigue Testing

3.3.4 Ultimate Strength Results

The DC-10-F2 design validation test specimen was subjected to ultimate tensile strength tests following the 160,000 cycles of fatigue loading. The uniaxial load was uniformly increased until the specimen failed. Failure was defined as the point at which the structure could no longer sustain an increasing load.

Figures 56-59 shows the strain field in specimen DC-10-F2 up through failure. The aluminum plate away from the doubler (channels 33, 34) began to yield at approximately 54,500 lbs. (45.4 ksi) while the doubler continued to increase its load in a linear fashion. The load was linearly increased until failure of the aluminum plate occurred at 64,220 lbs (53.5 ksi) and the specimen could no longer sustain an increasing load. This failure load does not represent the ultimate strength value for the specimen because the failure originated at the holes used to grip the specimen (see hole pattern in Fig. 27). It is often difficult to reach full ultimate failure load levels in specimens of this size because of the inherent weakness of the structure at the load application point. However, the ultimate strength tests were successful in loading the DC-10-F2 specimen into the plastic regime (past yielding).

The aluminum began its nonlinear response at the yield point indicated in Figs. 56-59. Similarly, the composite doubler showed a slightly nonlinear behavior at this same load level. But the Boron-Epoxy laminate did not yield. The material properties for Boron-Epoxy indicate a yield stress of 185 ksi. Further, after specimen failure, the strain gages on the doubler returned to zero indicating that the doubler did not undergo any permanent deformation. Thus, the nonlinear response in the doubler strain gages shows that the doubler is absorbing more strain and mirroring the response of the parent aluminum skin. Figures 56-59 illustrate that the adhesive is able to transmit stresses in the plastic regime and that loading beyond the initial yield level is required to fail the repair installation.

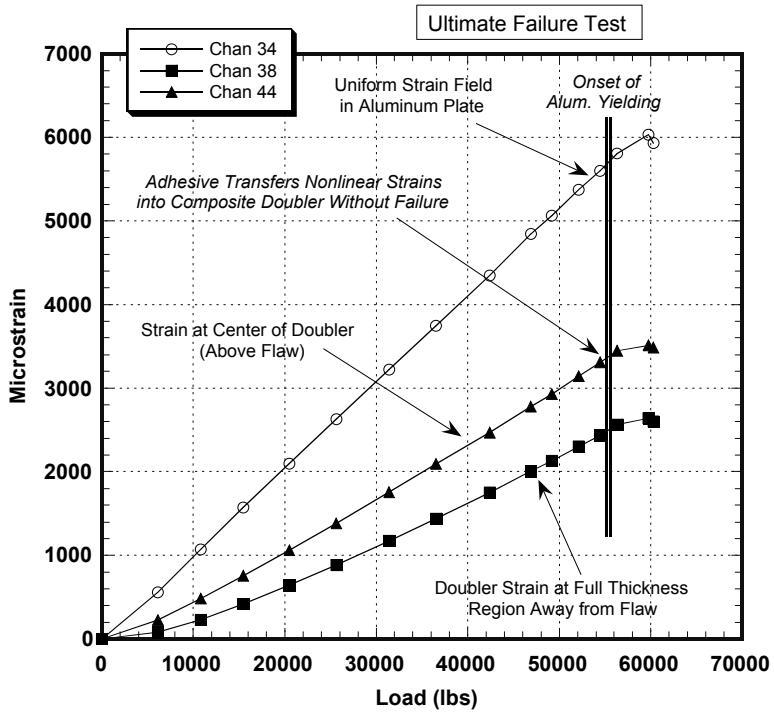

Figure 56: Axial Strain Field During Ultimate Failure Test of DC-10-F2 Design (Repair of 3" diameter flaws – 3/8" depth impact damage)

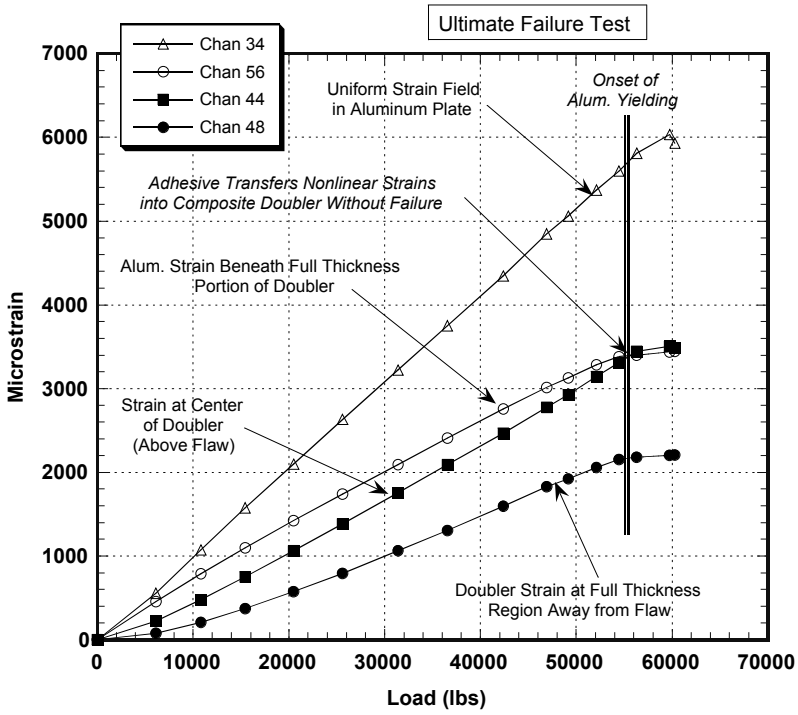

Figure 57: Axial Strain Field During Ultimate Failure Test of DC-10-F2 Design (Repair of 3" diameter flaws – 3/8" depth impact damage)

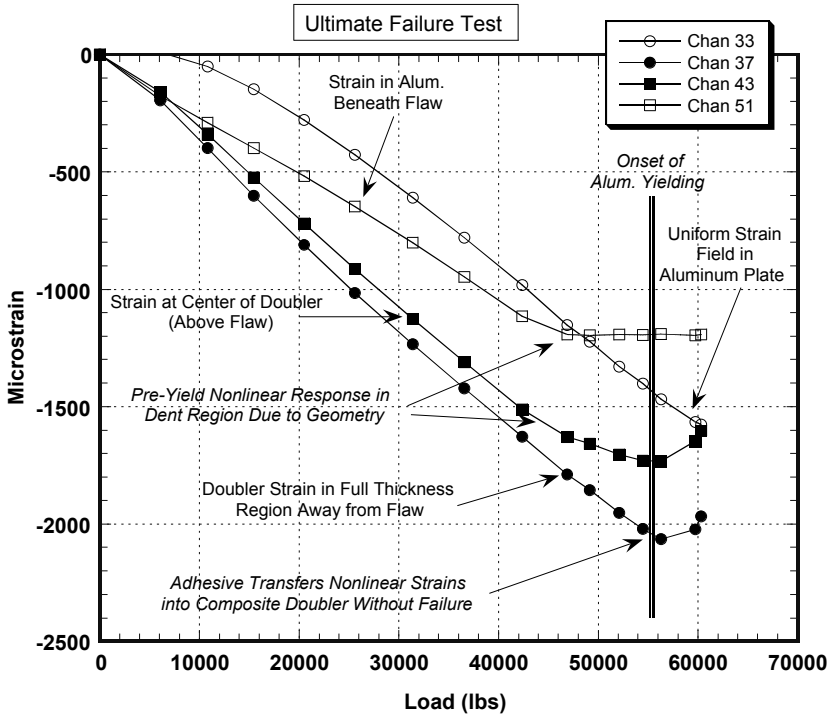

Figure 58: Lateral Strain Field During Ultimate Failure Test of DC-10-F2 Design (Repair of 3" diameter flaws – 3/8" depth impact damage)

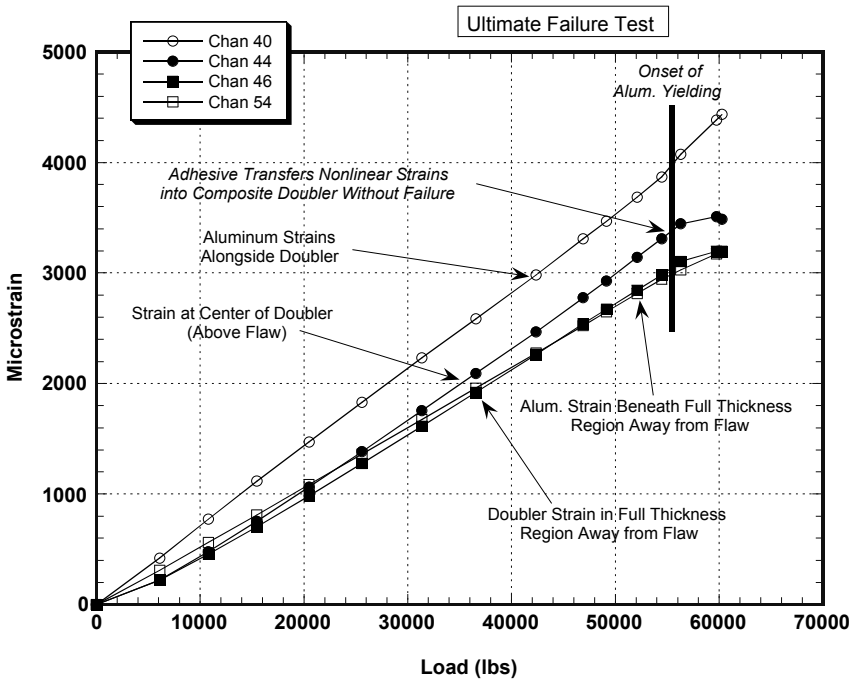

Figure 59: Axial Strain Field Along Midline of Doubler Panel During Ultimate Failure Test of DC-10-F2 Design (Repair of 3" diameter flaws – 3/8" depth impact damage)

3.4 Inspection of Specimens Before and After Fatigue Tests

These repair design validation tests assessed the potential for loss-of-adhesion flaws (disbonds and delaminations) to initiate and grow in the composite doubler installation. Disbonds can occur between the composite doubler and the aluminum skin while delaminations can develop between adjacent plies of Boron-Epoxy material.

Each of the design validation test specimens was inspected using a C-scan, through-transmission ultrasonic (TTU) inspections. C-scan technology uses information from single point A-scan waveforms to produce an area mapping of the inspection surface. The two-dimensional images are produced by digitizing point-by-point signal variations of an interrogating sensor while it is scanned over a surface [14, 17]. The TTU inspections were conducted in an immersion tank and represent the most accurate and sensitive form of nondestructive inspection for this type of structure. It is not fieldable for most aircraft applications but it served as the optimum reference for the hand-held ultrasonic pulse-echo technique. The pulse-echo ultrasonic (P-E UT) technique was applied to the test specimens while in the fatigue test machine and is the technique that was used in the field to monitor the aircraft installations. Comparisons between the TTU and P-E UT inspections showed excellent agreement and further validated the use of P-E ultrasonics for inspecting composite doublers in the field (see Section 6.0).

Figures 60 and 61 show C-scan images generated by the TTU inspection of specimens DC-10-F1 and DC-10-F2. Signal variations corresponding to disbonds and delaminations, as well as other anomalies in the parent material, are represented by dark black areas on the images. The four C-scan images in Figs. 60 and 61 compare the specimen flaw profiles before and after the fatigue and ultimate strength testing. *Side-by-side comparisons of the specimens show that the original engineered flaws, which were detected prior to testing, remained unchanged even after multiple fatigue lifetimes and loads that exceeded the yield strength of the aluminum skin. More importantly, the scans show that no new disbond or delamination flaws were produced by the fatigue overtest of four aircraft lifetimes.*

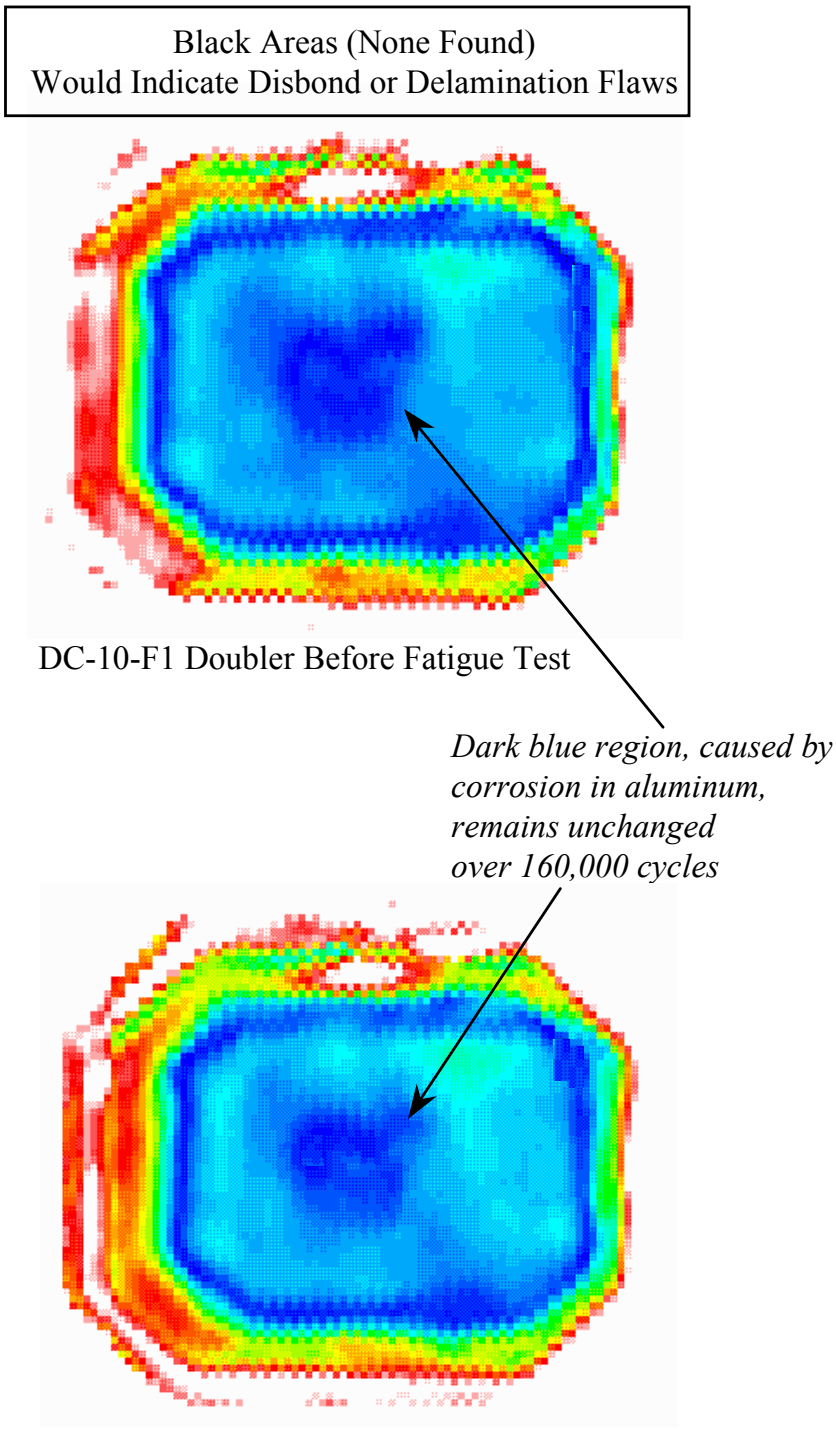

Figure 60: Ultrasonic C-Scan of DC-10-F1 Composite Doubler Before and After 160,000 Fatigue Cycles (Four Lifetimes of DC-10 Aircraft)

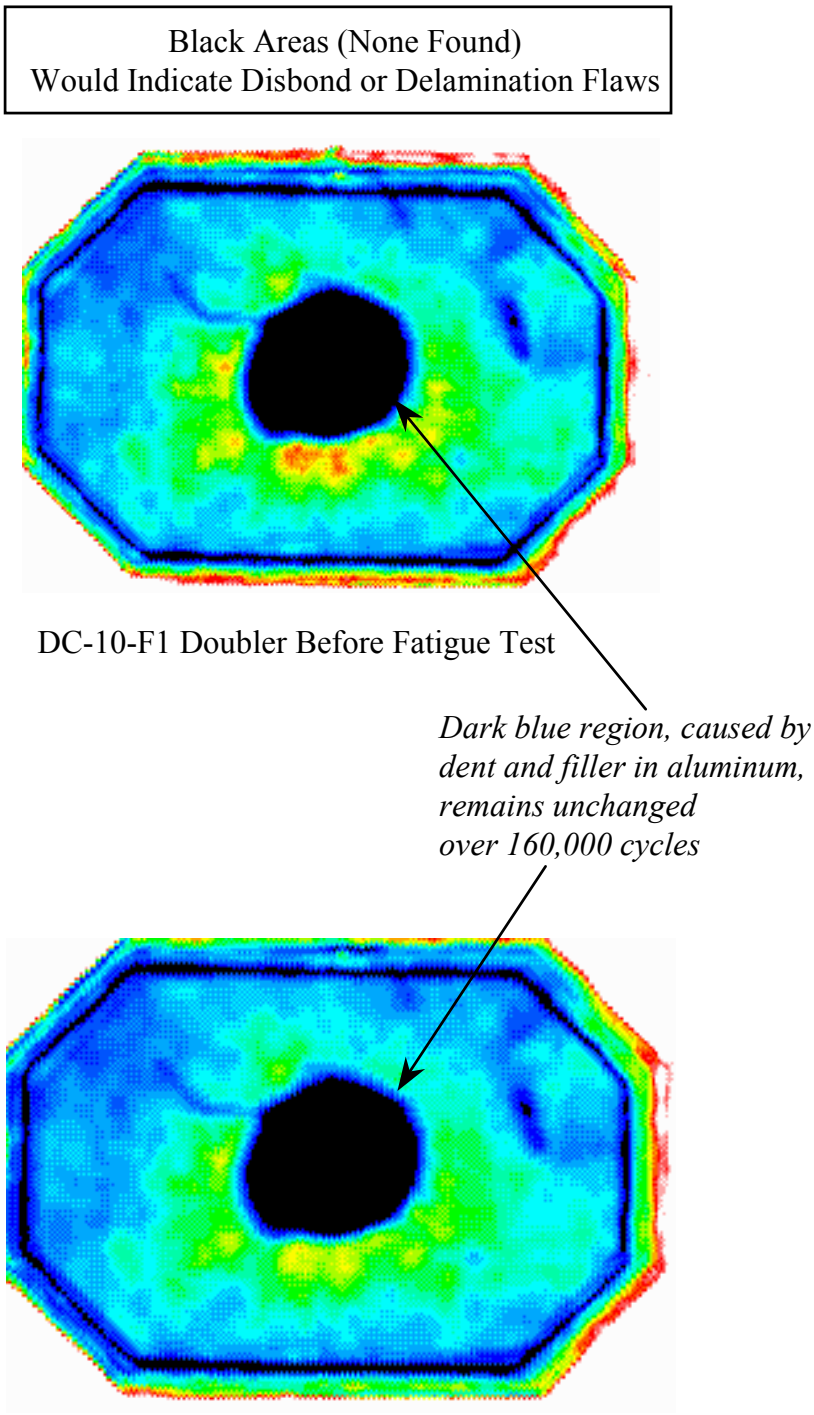

Figure 61: Ultrasonic C-Scan of DC-10-F2 Composite Doubler Before and After 160,000 Fatigue Cycles (Four Lifetimes of DC-10 Aircraft)

3.5 Validation of Analysis Code

The performance of the composite doubler repairs was analyzed using a finite element model (FEM) of the fuselage structure and Boron-Epoxy laminate. The design validation fatigue tests were limited in that they only simulated cabin pressure and did not account for all flight loads. The FEM analysis, however, included the complete spectrum of flight and pressurization loads. The tests described in this document were used to assess the general performance of composite doublers and to validate the analytical model. Results from the validated FEM were then used to predict the doubler stresses and the reduction in stress in the aluminum skin during extreme flight load scenarios (see Section 2.0).

Validation of the FEM consisted of comparisons between the analytical results, obtained under similar load conditions, and strain gage measurements obtained during the simulated pressure-fatigue tests. In general, comparisons with experimental data indicated that the FEM had sufficient accuracy (and conservatism) to support the Boron-Epoxy doubler design and analysis. Figures 62 and 63 compare experimental and analytical strain levels in the composite doubler and aluminum skin. In both cases the FEM is able to accurately predict the stress/strain field. The FEM predictions were particularly good in the area of greatest concern around the flawed region of the skin.

Due to differences in coefficients of thermal expansion between aluminum and Boron-Epoxy, all aluminum plate specimens with composite doublers possess some degree of residual curvature. As a result, an element of bending strain is also included in uniaxial tests such as this. The bending strains are close to zero at the midplane of the specimens (see excellent comparisons in Channels 42, 44, 46 in Fig. 51) and become more pronounced with distance from the midplane. The FEM did not attempt to model this bending phenomena. If the bending strains, obtained using strain readings from the front and back of the test specimen, are removed from the experimental data, the comparisons are improved further to the 10% range. Also, the FEM was an infinitely long plate with no boundary condition effects. The test articles had artificially high strains alongside the doublers since all load not absorbed by the doubler was required to travel through the narrow strips of aluminum on each side of the material. In spite of the differences in boundary conditions, the analytical results still compared favorably with the experimental measurements.

In the areas of greatest concern around the flaw and in the tapered region, the FEM analysis overestimated the strains in the doubler. This indicates that the FEM approach was conservative. The computer analysis and test data both verified the primary goal of the reinforcing doubler to reduce stress risers. Furthermore, the FEM was able to assess the damage tolerance and crack mitigation capabilities of the doubler using the full flight load spectrum. The associated damage tolerance analysis showed that the doubler exhibits sufficient strength to provide adequate fatigue enhancement over the full spectrum of environmental conditions (see Section 2.0).

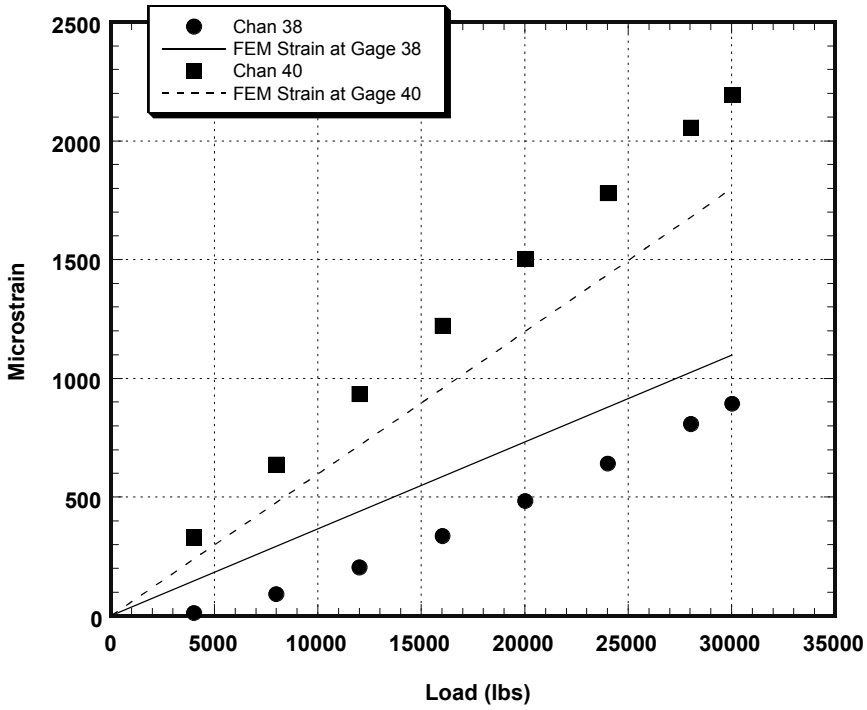

Figure 62: Comparison of Experimental and Analytical (FEM) Strains in the Composite Doubler and Parent Aluminum Skin

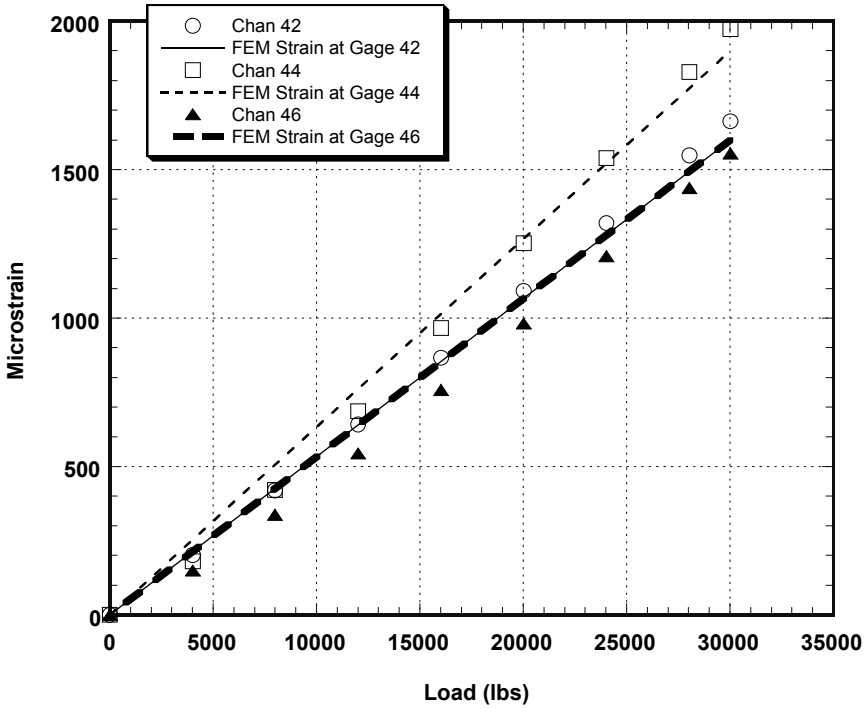

Figure 63: Comparison of Experimental and Analytical (FEM) Strains in the Composite Doubler

4.0 GENERAL VALIDATION OF COMPOSITE DOUBLER TECHNOLOGY USING FULL SCALE FATIGUE AND NDI TEST ARTICLE

4.1 Doubler and Test Article Design

The fatigue test article, representing a wing structure with a composite repair, was used to assess the general performance of the composite doubler and the MAUS inspection system. Overall, the objectives of this activity were: 1) provide structural response data (strain, load transfer, bending, residual strength) and *da/dN* (flaw growth) data in order to assess composite repair technology and analysis methods, 2) produce a changing flaw profile and assess ability of MAUS to track authentic changes in real, fatigue-induced flaws; perform investigation using a representative built-up airplane structure, and 3) provide initial flaw profile and subsequent flaw growth data along with residual strength failure information in order to relate them to proper maintenance dispositions (flaw size vs. recommended actions and predicted flaw growth/failure of structure).

Test Article and Fatigue Test Features - Figure 64 shows the fatigue test panel that mimics a wing configuration. It includes stiffeners and is sized to eliminate boundary condition effects on the doubler's performance. A summary of the key design features of the fatigue test article and related structural testing follows:

- Structural configuration simulates an actual aircraft structure - simplistic design provides realistic but straightforward article for assessing structural disposition tools (e.g. analysis methods, NDI tools)
- Skin: 0.125" th.; 2024-T3 aluminum..
- Stringers: 0.100" th.; 2024-T3 aluminum
- Stringers mounted using 3/16" dia. countersunk rivets with 1.25" rivet spacing; bay width = 5"
- Panel grip area and load train designed to produce ultimate stress levels in test article
- Panel reinforced at load application points so that axial load was applied along the neutral axis and secondary bending was eliminated
- Constant amplitude tension-tension fatigue loads produced 16 KSI stress across panel.

Composite Doubler Repair Features - The test article possessed a less-than-desirable stiffness ratio between the doubler and the parent structure in order to improve the chances of producing disbond, delamination, and crack flaw growth. In addition, different flaw engineering methods and off-design conditions (e.g. poor surface preparation) were employed to further optimize flaw growth opportunities. A mold release agent was applied to portions of the prepared bonding surface in an attempt to form weak bonds that would fail.

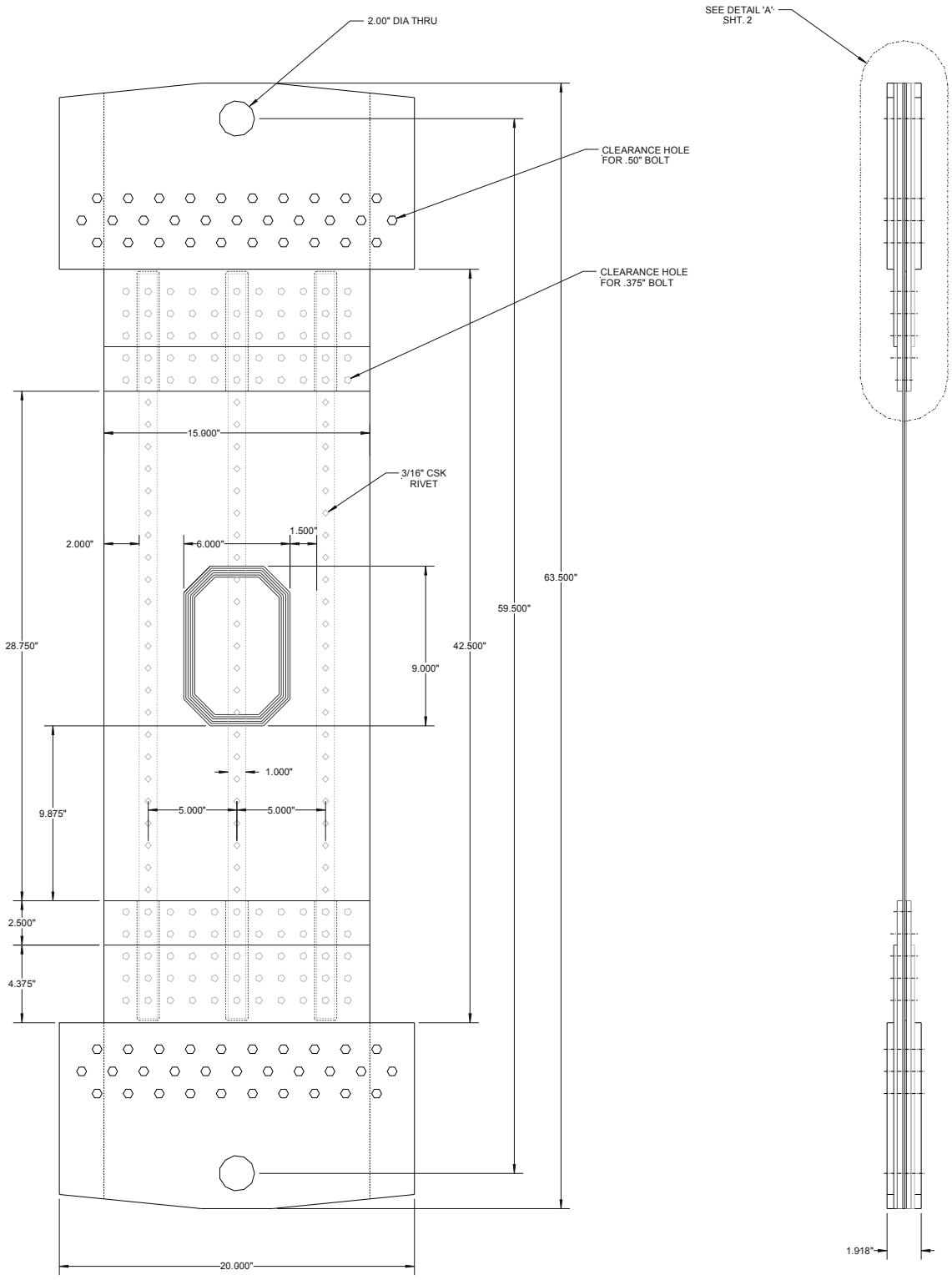

Figure 64: Full Scale Composite Doubler Design and Inspection Validation Fatigue Test Article

The composite doubler repair designed for this test article is shown in Figure 65. In addition to the flaw types shown (pillow inserts for delamination and disbond flaws, pre-cured adhesive disks for kissing disbonds, and pull tabs for doubler-to-skin disbonds), the dotted lines and cross-hatched areas around some of the flaws indicate the areas that were coated with the mold release agent.

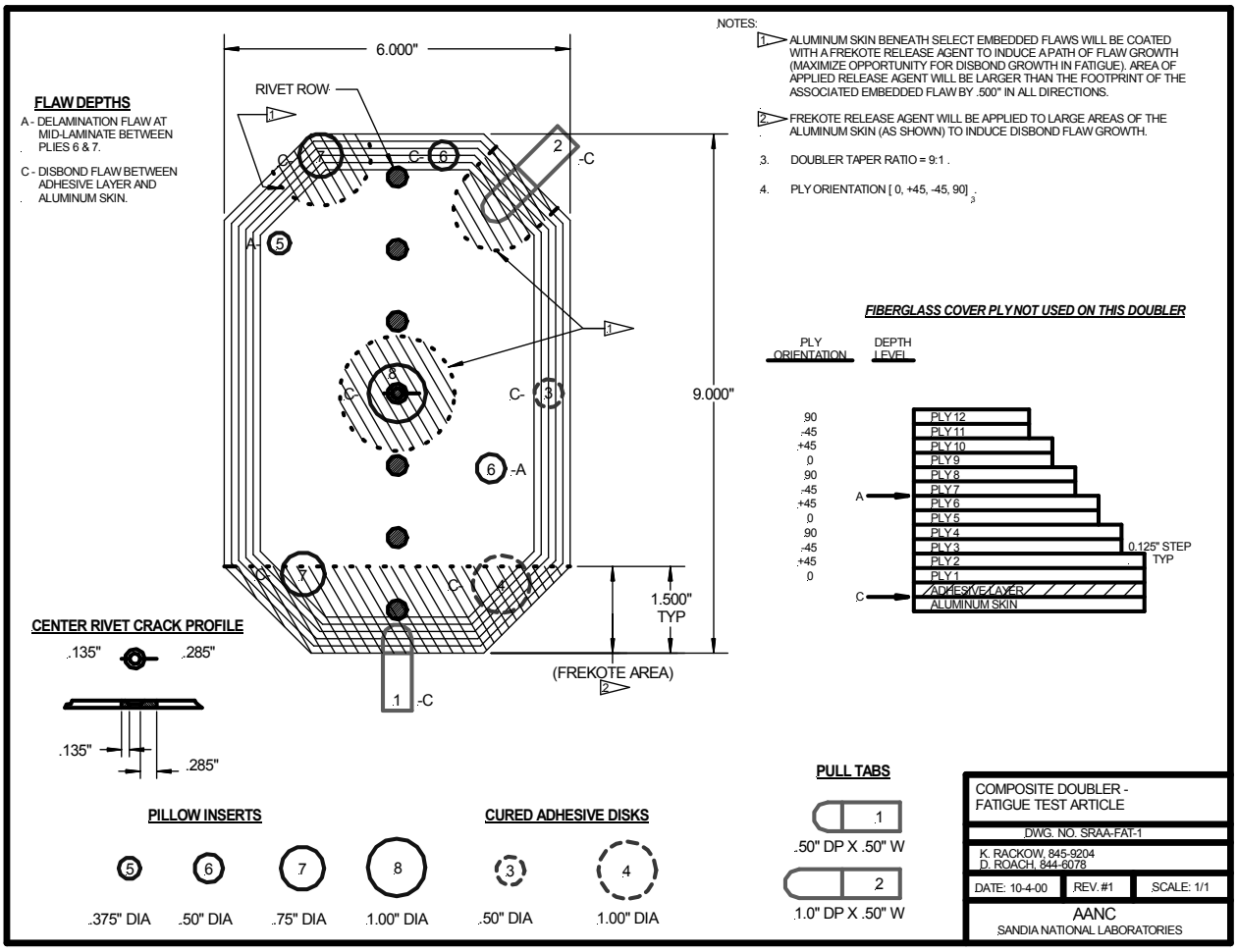

Figure 65: Composite Doubler Repair Design and Flaw Layout for Fatigue Test Article

Other pertinent features of the repair doubler design are:

- Overall doubler dimensions: 6" W X 9" H
- Doubler layout - 12 plies thick; ply orientation of $[0,+45,-45,90]_3$ to produce a quasi-isotropic doubler. Composite doubler designs for a wing structure would normally be primarily made of 0^o plies but this was a non-optimum design to improve the chances for flaw growth.

- Doubler stiffness ratio, R = 0.62; below recommended value of 1.0 - 1.2 in order to increase the likelihood of rapid crack growth and propagation of disbond/delamination flaws.

$$R = (E_x t_{laminate})_{BE} / (E_x t)_{Al}$$

$$= \frac{(11.873 \times 10^6 \text{ psi})(0.0684")}{(10.5 \times 10^6 \text{ psi})(0.100")}$$

$$R = 0.62 \quad \text{(for 12 plies on 0.100" th. skin)}$$

- Doubler taper ratio = 9:1 (five 0.125" steps over 12 plies) was used instead of the recommended value of 20:1 or greater. This was used to produce more extreme load transfer (smaller taper and higher shear stresses) and increase the likelihood of disbond initiation or growth at the edge of the patch.
- Composite doubler was installed to repair the two fatigue cracks shown at the center rivet site in Figure 64. Initial fatigue cracks were generated at the rivet site prior to stringer assembly and doubler installation.
- Composite doubler was installed using the surface sand and Silane chemical surface preparation process (See Section 5.0).

4.2 Eddy Current and Resonance Inspections Using MAUS Equipment

Since the late 1980's, Boeing has been evolving the Mobile Automated Scanner (MAUS) for inspecting a myriad of aircraft materials and structural configurations [30-31]. It is now used widely to inspect composite and metallic structures in production and field environments. An array of ultrasonic and eddy current inspection methods have been incorporated into the MAUS platform. These inspection techniques are integrated into an automated data acquisition approach to combine fast inspection capability with C-scan data presentation. Repeatable deployment of NDI probes along with sophisticated real time analysis of analog data produces greater flaw detection sensitivity. The two-dimensional, color-coded maps (C-scans) produced by the MAUS highlight flaws or other anomalies within the structure. User-specified settings determine how the system deals with the set of waveforms acquired by the interrogating transducer as it moves over the surface.

Figure 66 shows the fatigue test article during fatigue testing and the MAUS scanning the doubler. The test article was inspected with the MAUS device (eddy current and resonance mode) before any testing was performed in order to establish a baseline flaw profile. MAUS inspections were interjected periodically during fatigue testing to track any flaw growth. Two highly sensitive NDI techniques were used to provide the basis of comparison for the MAUS results. For crack detection, very precise crack growth data was obtained from EC pencil probe inspections applied directly to the cracked surface (back side of specimen). These results were compared to the MAUS inspections conducted via eddy current C-scans through the doubler. Through-transmission ultrasonics (TTU) provided the referee data regarding disbond and delamination onset and growth. The TTU inspections were conducted before and after the fatigue tests. Additional feedback on the MAUS performance was also provided by pulse-echo

ultrasonic inspections that were performed in-situ using hand held probes and a Quantum inspection device.

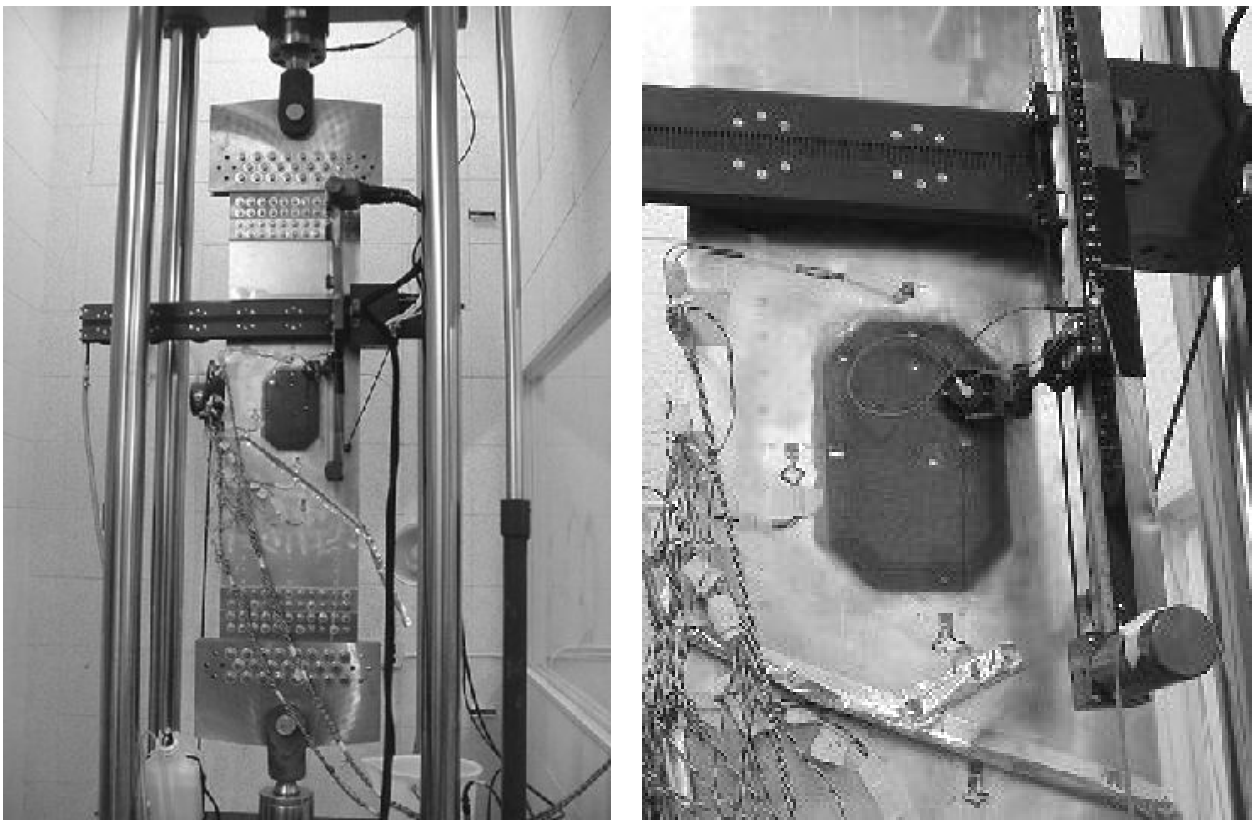

Figure 66: Fatigue Test of Simulated Wing Structure and MAUS Inspection

The MAUS eddy current inspections for crack detection were performed with a 5 KHz probe. A sample MAUS eddy current image of the two cracks emanating from the center rivet site is given in Figure 67. Figure 68 compares crack lengths measured using an eddy current pencil probe (100 KHz and 500 KHz in direct contact with cracked surface) with the crack lengths determined from MAUS images such as the one shown in Figure 67 (MAUS inspections through the doubler). Although no specific feedback training was provided for inspectors to use the crack image as a means for ascertaining crack length, Figure 68 shows that the MAUS was able to accurately track the growth of both cracks emanating from the center of the rivet. In most measurements there was less than a 5% difference between the MAUS crack length predictions and those determined by the referee EC pencil probe technique.

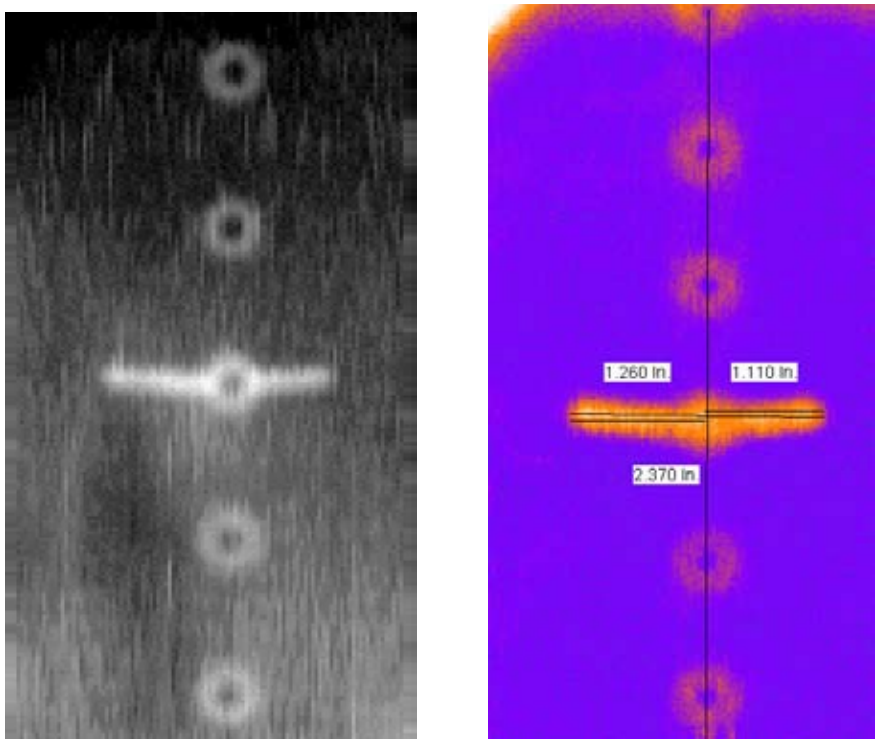

Figure 67: MAUS Eddy Current X and Y (annotated) Crack Images After 80,000 Fatigue Cycles

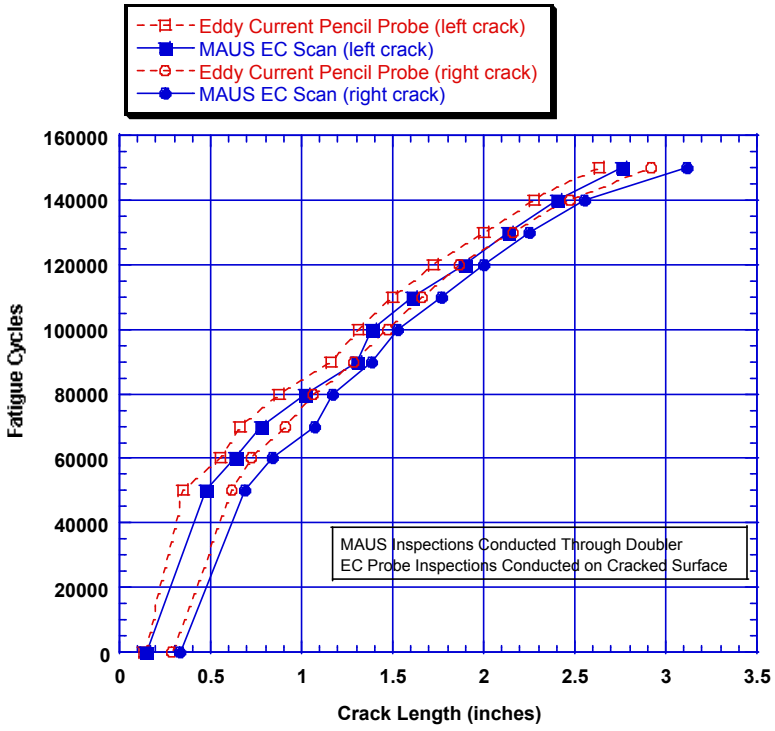

Figure 68: Comparison of Pencil Probe Surface Crack Inspections with MAUS Eddy Current Scans Through the Composite Doubler

Disbond and delamination growth was also monitored during the fatigue tests. Figure 69 shows the MAUS resonance scan image of the test article prior to fatigue testing. Also shown for reference is a schematic indicating the size and location of the doubler flaws. The solid lines in the schematic represent the flaw inserts or pull tabs while the dotted lines indicate the regions where the mold release was applied around select flaws. There is complete correlation between the engineered flaw drawing and the flaw map provided by the MAUS scan. Note also that the MAUS was able to detect the presence of the mold release regions even though these areas were not disbonded. Rather, these were weak bond regions as evidenced by the fact that feeler gages could not be inserted into the edges of the mold release regions. The MAUS resonance mode inspection was able to differentiate the relatively weak bonds in the mold release regions from the stronger "full strength" bonds in the remainder of the doubler.

Figure 70 contains the MAUS resonance scan after the completion of 150,000 fatigue cycles. It can be seen that there was essentially no change in the flaw profile with the exception of the region around the crack growth. Crack propagation in the specimens, and the accompanying displacements as the crack opened each cycle, produced cohesive failure (cracking) in the adhesive. However, this failure was localized about the length of the crack and did not result in any disbonds (adhesive failure). This result was ascertained by visually noting the presence of adhesive on both the aluminum and composite laminate (i.e. adhesive fractured at high strains but it did not disbond). Thus, the full strength of the adhesive was achieved. Post-test inspections via through-transmission ultrasonic inspection showed that the flaw profile remained unchanged over 150,000 cycles.

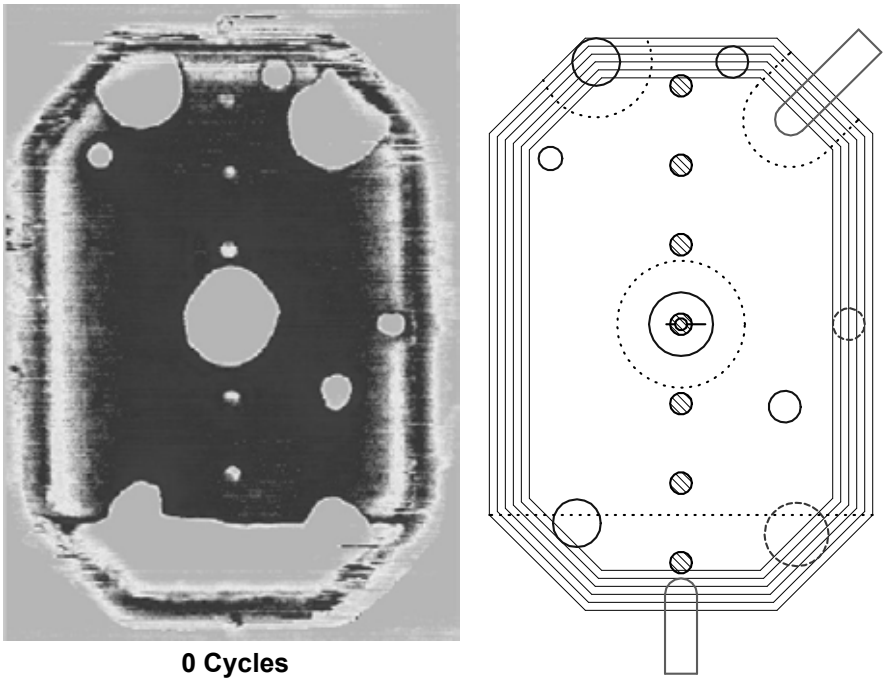

Figure 69: MAUS Resonance Scan of Fatigue Test Article Doubler Before Fatigue Loading

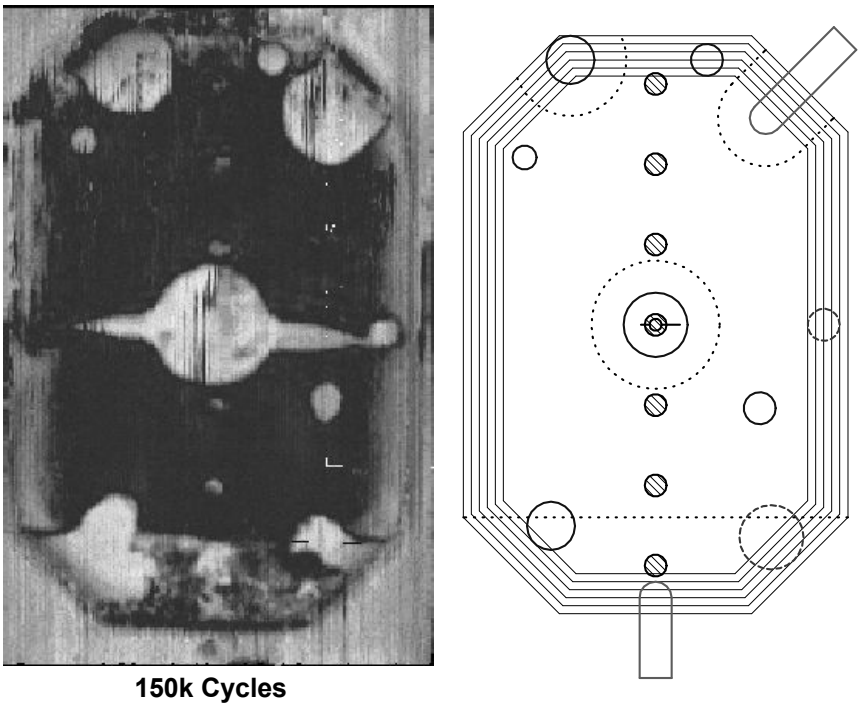

Figure 70: MAUS Resonance Scan of Fatigue Test Article Doubler After 150,000 Fatigue Cycles

4.3 Fatigue Test Results

Strain gages were placed on the doubler and on the aluminum immediately adjacent to the doubler at the locations shown in Figure 71. Static load tests were conducted before the fatigue tests began, as well as after select fatigue plateaus had been reached in order to monitor changes in the strain field and the load transfer between the parent structure and the composite doubler. After the fatigue crack was grown to a length approximately equal to the width of the composite doubler (6"), the fatigue testing was halted and a residual strength failure test was performed. In this test the axial loads were increased monotonically until the structure could no longer sustain an increasing load.

Key strain values for the parent skin and composite repair prior to fatigue testing are given in Figure 72. The maximum axial strain in the aluminum plate (away from the doubler) was around 1700 με (for 16 KSI stress load). When both axial and lateral (Poisson) stresses are considered, the maximum localized stress in the skin was around 21 KSI. Strain reduction in the aluminum plate (open geometric shapes in Fig. 72) and strain shedding into the doubler (solid geometric shapes) is evident. Strain gage #8 was installed directly over a large disbond, however, it still picked up significant strain. This is because a sufficient amount of the load transfer region around the perimeter of the doubler was intact and produced good load transfer from the parent skin.

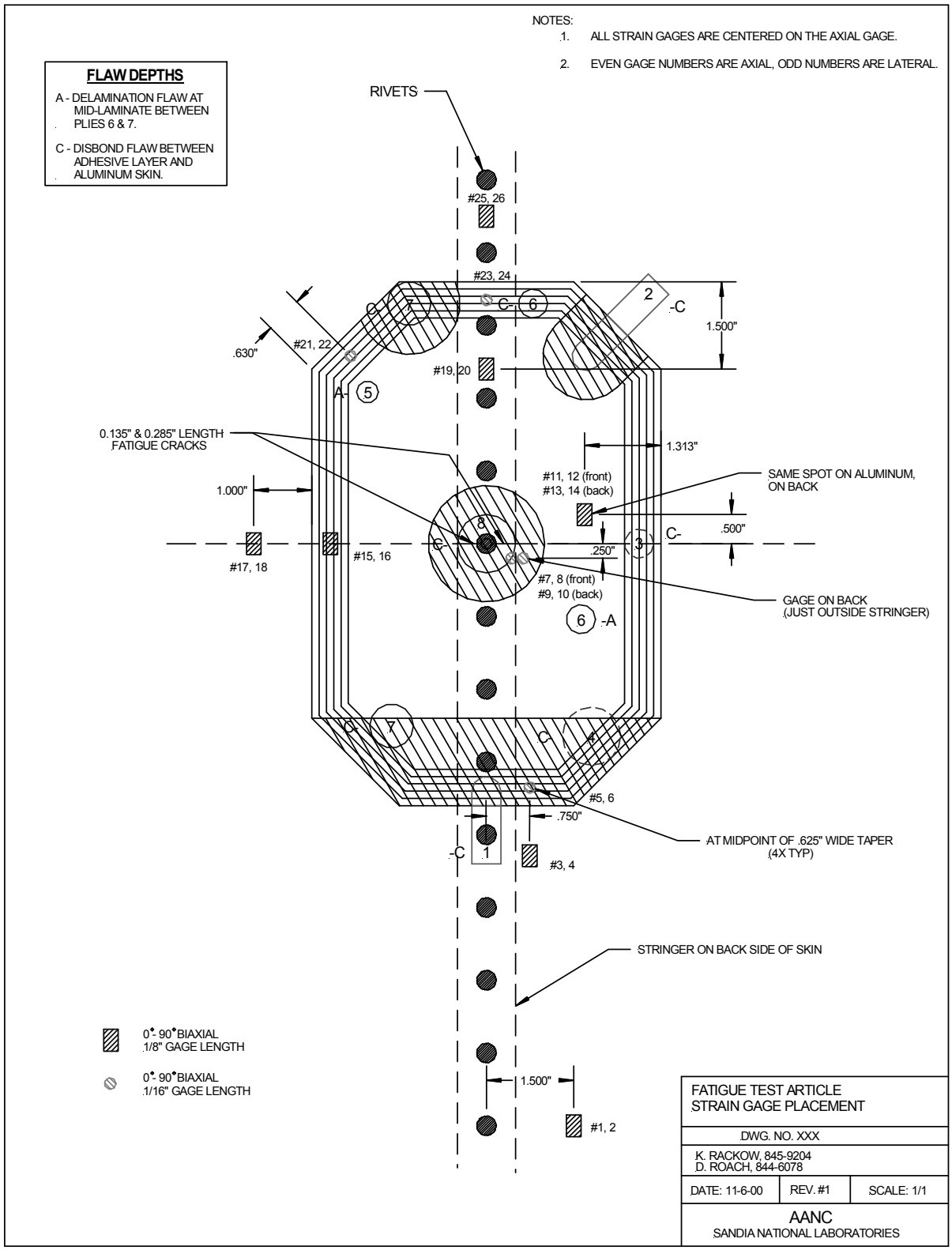

Figure 71: Strain Gage Placement On and Around Composite Doubler

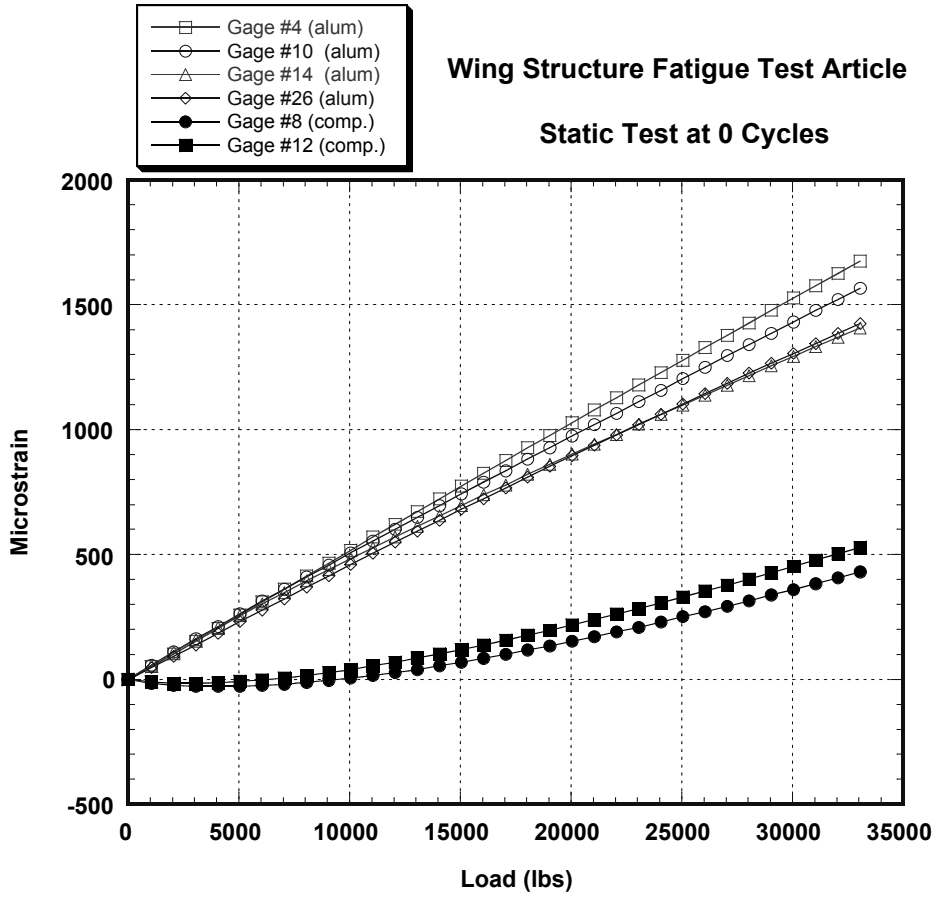

Figure 72: Axial Strain Field in Aluminum and Composite Doubler Prior to Fatigue Testing

The strain data in Figure 72 can be reduced to provide another measure of the doublers performance. Plots of percent load transfer were obtained by calculating the ratio between doubler strains and strains in unrepaired regions of the aluminum skin. Figure 73 shows the resulting load transfer plots for various doubler locations $\{\varepsilon_{doubler} / \varepsilon_{alum(ref)}\}$. In the tapered portion of the doubler, the load transfer was consistently in the 50 - 60 % range. In the center, where the doubler reaches its maximum thickness of 12 plies, the load transfer was in the 30 - 50% range. These results agree with normal aircraft repair approaches that seek to achieve a 30% - 50% stress mitigation in the structure being repaired.

Figure 74 shows that the weak bonds, detected as flaws in the initial MAUS inspections, were brought to complete failure during the course of the fatigue load tests. Prior to fatigue testing, the doubler was weakly bonded to the aluminum skin in the mold release regions shown in Figure 65. After fatigue testing, it was possible to insert a sheet of paper into the lower region of

the doubler indicating a complete disbond over the large region (lower third of doubler) highlighted in the MAUS inspection (Figure 70).

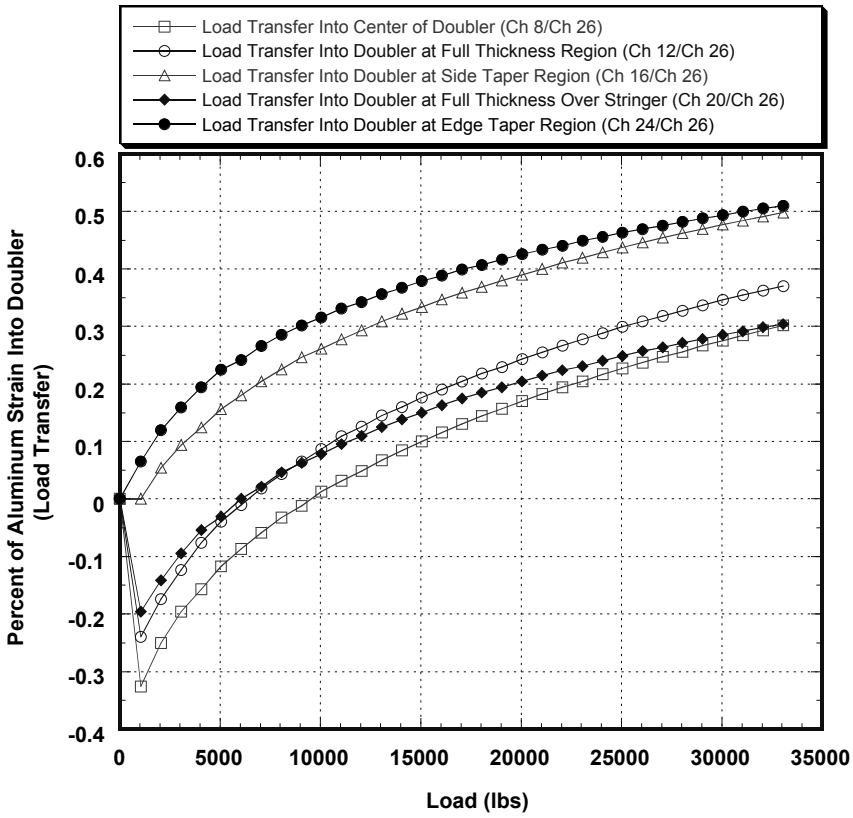

Figure 73: Load Transfer Into Composite Repair Doubler

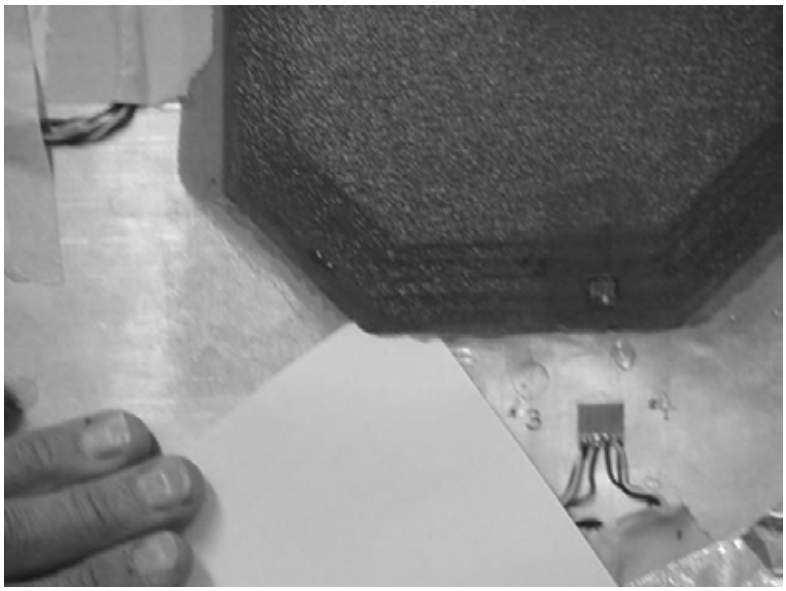

Figure 74: Complete Skin-to-Doubler Disbond After Fatigue Testing

4.4 Residual Strength After Fatigue

After the wing repair test article was subjected to 150,000 cycles, a residual strength tensile test was performed. At this point, the two crack lengths totaled approximately 5.8" in length so the crack under the repair extended essentially across the entire width of the doubler. Thus the doubler and the two small strips of aluminum on each side of the doubler absorbed all of the load. The aluminum skin beneath the doubler and near the crack was almost completely relieved of its stress. As a result, the failure mode during the residual strength test was as follows: 1) as the axial load increased, the composite doubler took an increasingly higher percentage of the load, 2) the test loads produced stresses sufficient to yield the aluminum skin and non-linear strain responses ensued, 3) the crack propagated across the width of the skin and ultimate stress levels were produced in the composite doubler, 4) the composite doubler fractured rapidly at 85 KSI and all loads were transferred to the aluminum material on either side of the doubler, 5) the stress levels in the aluminum immediately exceeded ultimate levels and the aluminum (parent skin and stringer) fractured along the same path as the original fatigue crack. Figure 75 contains front and back view photos of the failed test specimen. The failure occurred rapidly where initial fracture of the doubler and total fracture across the entire width of the panel were within a split second of each other. Next to the photos are two C-scan images produced by TTU inspections on the two halves of the post-failure doubler. It can be seen that the flaw profile did not change even during the failure test when aluminum stress levels increased well into the plastic regime.

This represents especially outstanding doubler performance since the lower third of the doubler was disbonded and extreme shear stresses were produced in the load transfer region (i.e. doubler full thickness region at the edge of the mold release/disbond line). Notice in Figure 75 that this disbond region did not grow any further than the mold release line. Recall that this doubler was severely underdesigned in an attempt to induce flaw growth, however, extreme damage tolerance, crack mitigation, and resistance to flaw growth was still achieved with this composite repair.

Figure 76 shows the strain field in the test article up through failure. Since the crack extended across the entire doubler, the parent skin beneath the doubler was almost completely stress relieved (see Channels 4 and 10). Also, the doubler stresses are now equal to or greater than the stresses in the parent aluminum outside the doubler region. As yield stress levels were reached in the aluminum, the composite doubler mimicked this non-linear response (see Ch. 8 and 12) even though Boron-Epoxy material does not yield or have a plastic deformation regime. This indicates that the adhesive is able to transmit non-linear, yield strains from the aluminum into the doubler and that stresses beyond yield are required to fail a properly installed composite repair.

The fatigue test article results discussed here demonstrate: 1) the ability of the MAUS system to detect flaws that are smaller than the allowable flaw size, 2) the ability of the MAUS to track a changing flaw profile (delineate changes in disbond and delamination boundaries and monitor small crack propagation through doublers), and 3) the robust performance of composite doubler repairs despite a poor, undersized repair design and the presence of large installation flaws covering over 50% of the critical load transfer region, as well as areas around the crack flaw that required reinforcement.

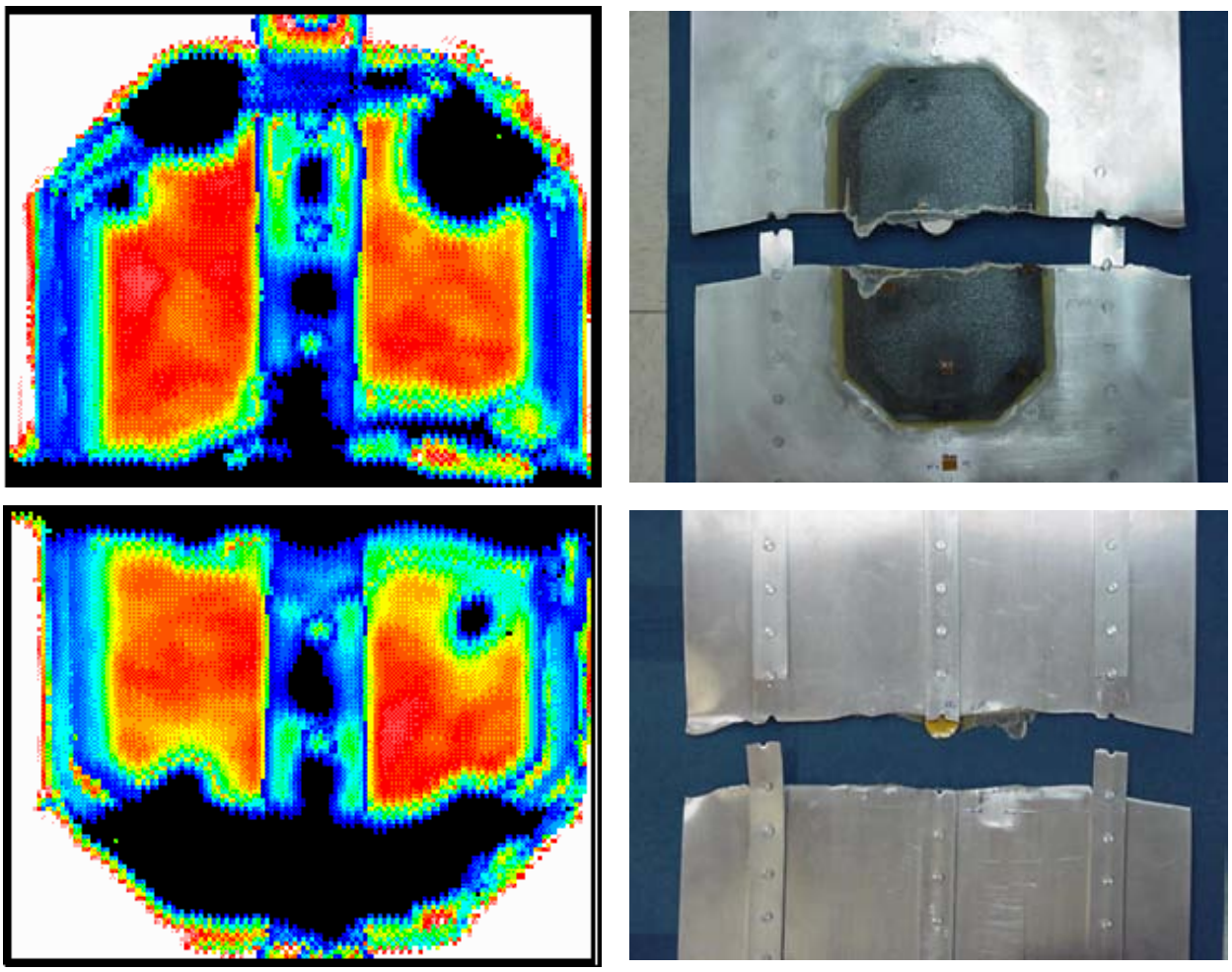

Figure 75: Photos Showing Failure Mode of Fatigue Test Article and TTU Images Showing Zero Flaw Growth After Experiencing Stress Levels Reaching Plastic and Ultimate Levels

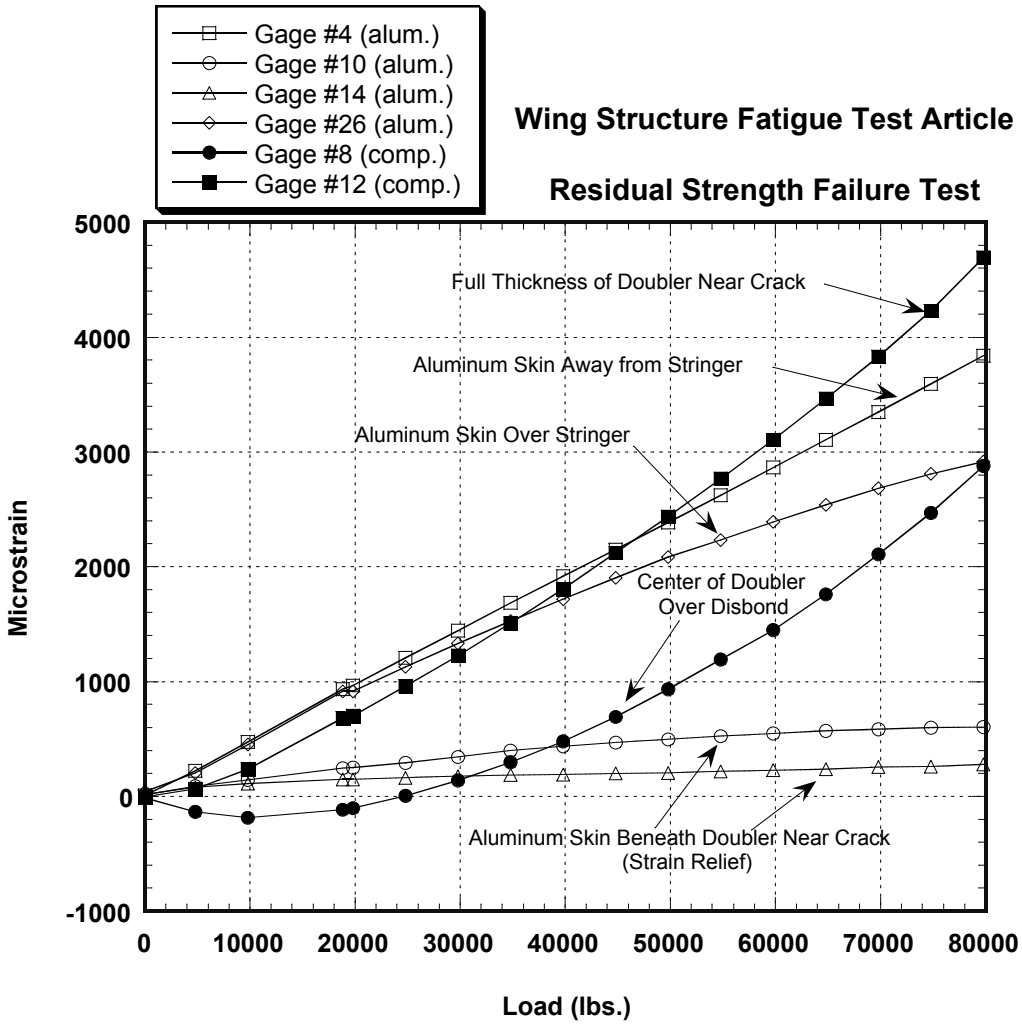

Figure 76: Strain Fields in Composite Doubler and Aluminum Plate During Ultimate Failure Test

5.0 COMPOSITE DOUBLER PERFORMANCE WHEN USING THE SOL-GEL SURFACE PREPARATION METHOD

5.1 Introduction to Sol-Gel Surface Preparation Method

The prebond surface treatment used on metals can significantly influence the resultant initial strengths and long-term durability provided by bonds. The key to structural bonding is that the adherend surfaces must be roughened and free from contamination and weak oxide layers. Proper surface preparation will produce these features on the material and will allow for a reliable joint with sufficient strength and durability [32-33]. In order to optimize surface preparation, the basic mechanisms of adhesion must be considered. The adhesive must be able to wet the entire surface of the adherend so that there is intimate molecular contact at the joint interface. There are two basic mechanisms of adhesion for structural adhesive bonding: 1) mechanical interlocking of the polymer with the adherend surface, and b) chemical enhanced bonding of the polymer molecules with the adherend surface layer.

Thus far, composite doubler evaluations and aircraft repairs for the commercial aviation industry have involved the phosphoric acid anodize (PAA) surface preparation method. While it is recognized that the metal treatment prior to bonding is one of the most important factors in producing a strong and durable adhesive joint, it is also true that the complexity and hazardous chemicals associated with the PAA process has limited the use of bonded composite doublers. Boeing, in conjunction with the Dept. of Defense agencies, has evolved a prebond surface preparation method that utilizes Sol-Gel technology [34]. The Sol-Gel method – sometimes referred to as the Boe-Gel process – is very user friendly in that it is: 1) simple to implement in the field, 2) decreases the repair installation time, 3) eliminates the purchase of expensive in-situ anodize equipment, and 4) avoids the use of hazardous chemicals. All of these advantages are realized without sacrificing the quality and performance of the bonded joint. The purpose of the tests described in this section is to evaluate the fatigue (crack mitigation), strength, and long-term durability of composite doubler repairs that have been installed using the Sol-Gel method.

Roughening surfaces prior to bonding enhances the strength of adhesive joints. The abrasive process removes contaminated layers, including hard-to-remove oxide layers, and the roughened surface provides some degree of mechanical interlocking with the adhesive. The process also forms a larger effective surface area for the bond and can introduce physical/chemical changes which affect surface energy and wettability. All of these issues must be considered in light of the characteristics of the adhesive and its ability to spread on different surface textures. The PAA surface preparation process enhances adhesion by producing a “roughened” high surface area that has both mechanical and chemical interactions with the adhesive primer. Sol-Gel chemistry produces a thin film on metals that promotes adhesion. The bonded joint is optimized through the chemical reaction between the metal and the Sol-Gel and the Sol-Gel and the primer.

Prior to applying the Sol-Gel solution, the surface is roughened by either a grit-blast or sanding process. The introduction and containment of grit in a repair area is often problematic and time-consuming so this study focused on the sanding process as the precursor to the chemical treatment. The Sol-Gel was applied by brushing the mixed solution directly onto the roughened metal surface. The Sol-Gel was cured using heat lamps. After applying the BR-6747 primer, the composite doubler was placed over the area to be repaired. Heat blankets were then used to co-cure the primer, adhesive film, and composite doubler in a single heat cycle. Overall, the Sol-Gel process can reduce the total repair installation time by three to four hours.

5.2 Structural Evaluation of Sol-Gel Surface Preparation

The test results used to quantify the damage tolerance of composite doublers installed using the Sol-Gel process will be presented in three distinct sections: 1) fatigue test results, 2) strain field measurements (evaluation of load transfer), and 3) residual strength tests. Nondestructive inspections, used to relate the above items to flaw initiation and growth, will be discussed in the section on the fatigue test results. The results presented in this section quantify the effectiveness of composite doublers, installed using the Sol-Gel process, in reducing crack growth in aluminum substructure. Fatigue and strength tests were performed on specimens with combinations of crack, disbond, and impact flaws. The flaw sizes, locations, and combinations were engineered to produce extreme worst case conditions. *Disbond, delamination and crack sizes used in these damage tolerance tests were at least twice the size of those which will be detected by the NDI requirements. Thus, there is an inherent safety factor built into this damage tolerance assessment and the doubler performance sited here should be conservative.*

5.2.1 Test Specimen Description

The Sol-Gel specimens consisted of an aluminum plate (2024-T3, 0.071" thick), representing the original aircraft skin, with a bonded composite doubler. The doubler was bonded over a flaw in the aluminum. The specimens had the following basic design configurations: unabated 0.5" fatigue crack at the edge of the aluminum plate with co-located 1.0" dia. disbond between composite doubler and aluminum; 1.0" dia. disbonds along doubler edge as shown in Figure 77. The Boron-Epoxy material was type 5521/4. The adhesive material was FM-73, or accepted substitute AF-163 (0.06 PSF), and the primer was Cytec BR-6747.

The Boron-Epoxy composite doublers were a multi-direction lay-up of 13 plies: $[0, +45, -45, 90]_3$ with a 0^o cover ply on top. The plies were cut to different lengths in both in-plane directions in order to taper the thickness of the resulting doubler edges. This produced a more gradual load transfer between the aluminum and the doubler (i.e. reduces the stress concentration in the bondline around the perimeter). A ply taper ratio of approximately 30:1 was utilized; this results in a reduction in length of 30 times the ply thickness. The number of plies and fiber orientations produced an extensional stiffness ratio of Boron-Epoxy to aluminum of 1.2:1 $\{(Et)_{BE} = 1.2\ (Et)_{Al}\}$.

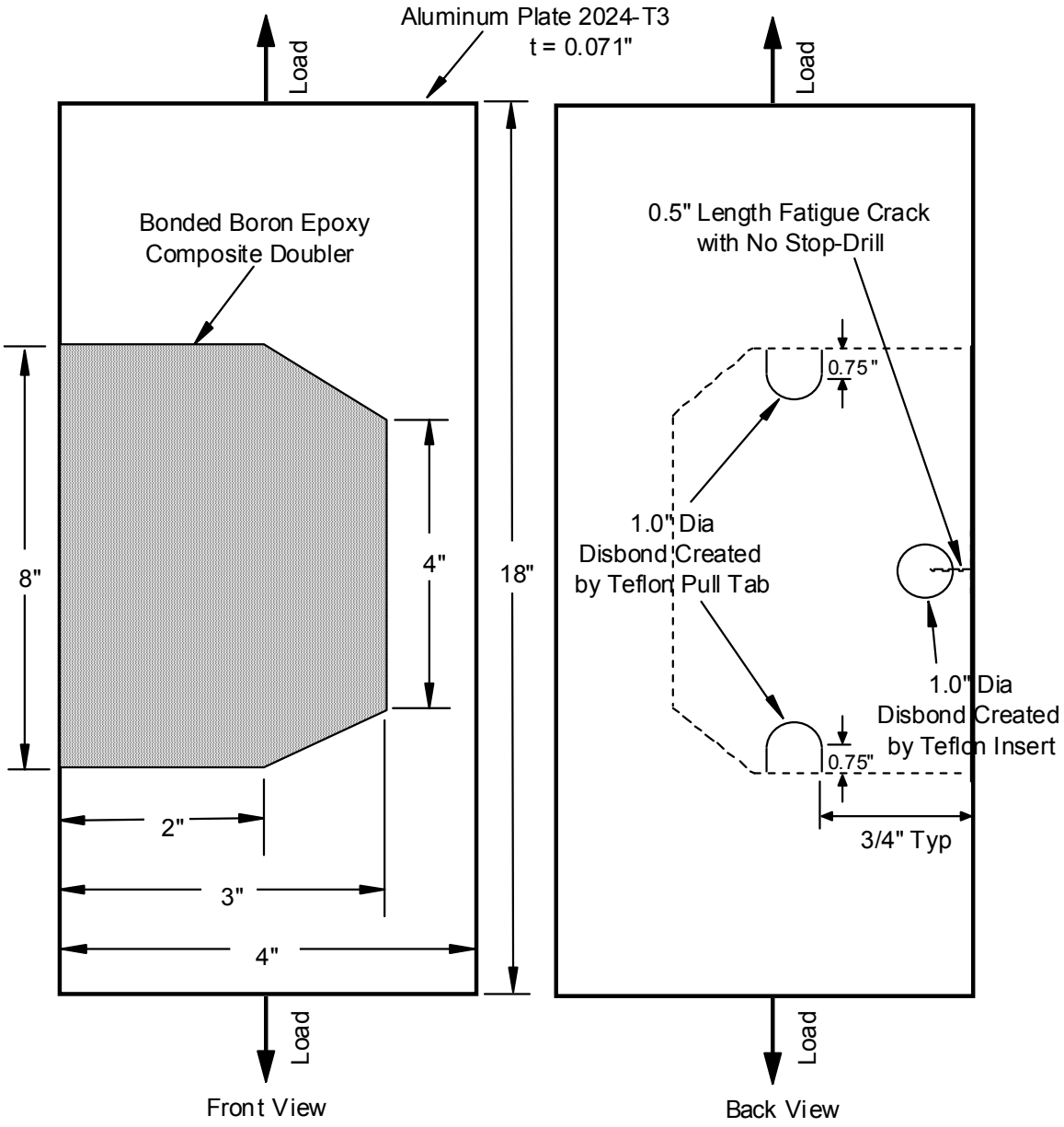

1. **13 Ply Boron/Epoxy doubler**
2. **$[0, +45, -45, 90]_3$ lay-up (fiber orientation to the load) plus a 0° cover ply on top; longest ply on bottom**
3. **30:1 taper ratio drop off**
4. **Stiffness Ratio, $(Et)_{BE} = 1.2\ (Et)_{Al}$**
5. **Fatigue crack (stop-drilled) with 1.0" Dia co-located disbond centered over stop-drill hole**
6. **1.0" Dia disbonds in load transfer region of composite doubler (edges of the bondline)**

Figure 77: Composite Tension Test Coupon for Sol-Gel Evaluation

Generation of Fatigue Cracks in Aluminum Substrate - Cracks were generated in the aluminum substrate plates before the composite doubler repairs were installed. The unabated 0.5" fatigue cracks (i.e. no stop-drill) were then repaired with the composite doubler described above. The applied fatigue loads were 2 ksi to 20 ksi (852 - 5680 lbs. load) to represent the 0 - 18 ksi hoop stress spectrum experienced by fuselage skin during cabin pressurization.

Calculation of Laminate-Aluminum Extensional Stiffness Ratio - This section describes the method that was used to arrive at the stiffness parameter, $E_x t$, for composite doublers. The calculations used classical laminated plate theory, along with Boron-Epoxy lamina properties, to arrive at the average cured laminate modulus E_x (where x is the direction of the fatigue load). The Boron-Epoxy lamina properties at room temperature are:

E_{11}= 28.0 X 106 psi
E_{22} = 2.7 X 106 psi
G_{12} = 0.8 X 106 psi
ν_{12} = 0.21
t_{ply} = 0.0057 in.

The average laminate properties are calculated using the individual lamina properties listed above along with the following specific lay-up configuration: 1) 13 plies $\{[0, +45, -45, 90]_3, 0\}$, and 2) laminate thickness t = 0.0741" (13 plies X 0.0057"/ply). The resulting laminate properties were calculated:

E_x = 11.873 X 10^6 psi
E_y = 10.144 X 10^6 psi
G_{xy} = 3.77 X 10^6 psi
ν_{xy} = 0.32

Compared to a 0.071" thick, 2024-T3 aluminum plate, the stiffness ratio is,

$$R = (E_x t_{laminate})_{BE} / (E_x t)_{Al} \qquad (12)$$

$$= \frac{(11.873 \times 10^6 \text{ psi})(0.0741")}{(10.5 \times 10^6 \text{ psi})(0.071")}$$

$$R = 1.2$$

This method was used to arrive at the 1.2 extensional stiffness ratio

Instrumentation - Load transfer through the composite doubler and stress risers around the defects were monitored using the strain gage layouts shown in Figure 78. Biaxial gages were used to measure both the axial and transverse strains in the anisotropic composite material. Crack growth was monitored using optical measurement devices (resolution 0.003") and eddy current inspections that were applied to the non-composite doubler side of the specimens.

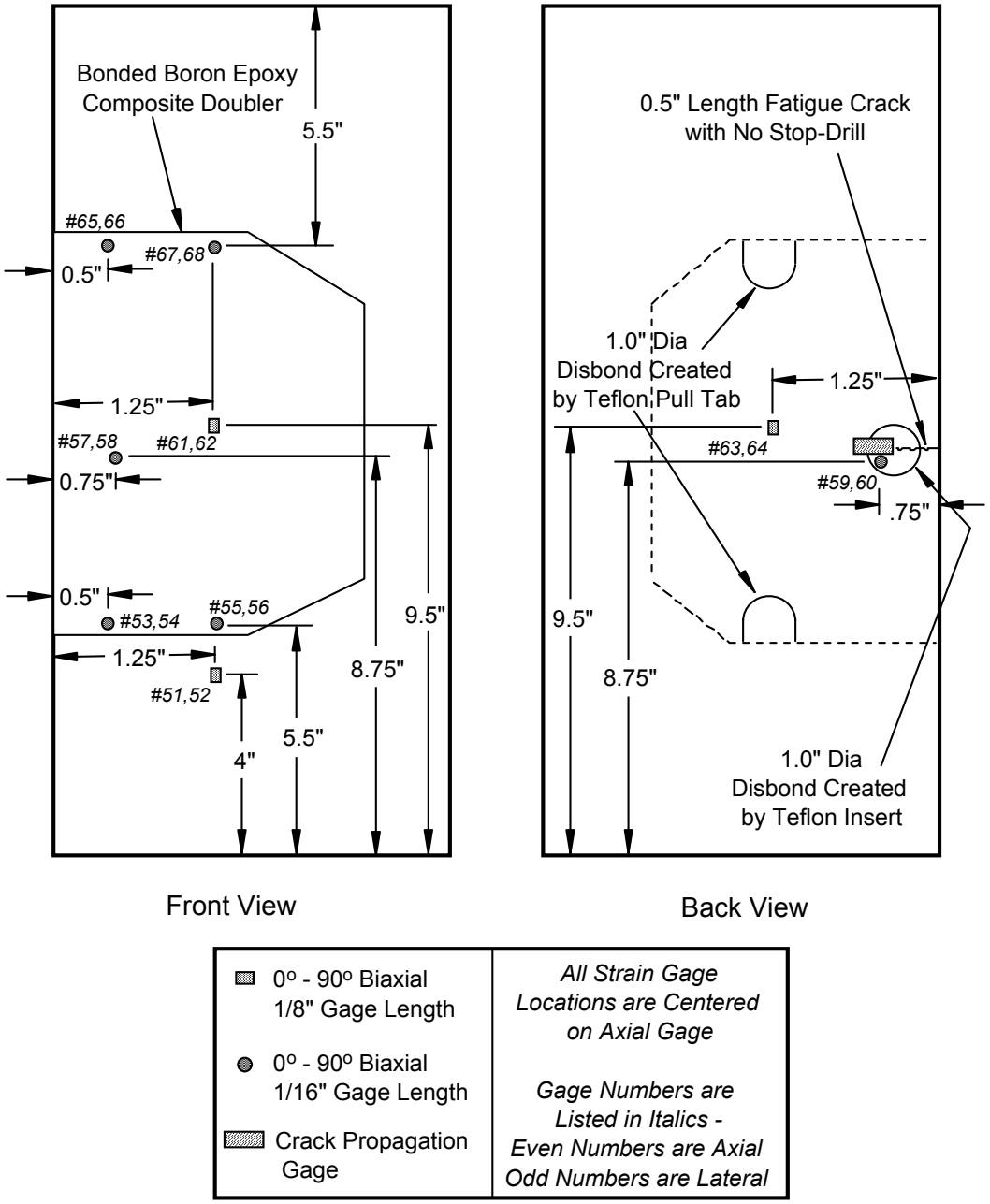

Figure 78: Strain Gage Locations for Sol-Gel Tension Tests

5.2.2 Surface Preparation and Composite Doubler Installation

All test specimens were prepared using the Sol-Gel surface preparation procedure and hot bonding equipment. The complete installation procedure is provided in reference [35] and is Textron Specification No. 200008-001 (may also be referenced as the Boeing Specification D658-10183-1). The key installation steps are described below and summarized in Figures 79-84.

1. Aluminum Surface Preparation - Solvent clean per BAC 5750. Remove the oxide on the aluminum prior to Sol-Gel application using Scotch Brite pads and machine sanding to achieve a 30 second water-break free condition. Apply freshly-mixed Sol-Gel solution to the aluminum surface using brush-on or spray-on application processes.

2. Primer and Adhesive Process - Prime the Sol-Gel surface using Cytec BR-6747 primer. Co-cure the Cytec FM-73 (or equivalent: AF163) structural film adhesive simultaneously with the Boron-Epoxy doubler.

3. Boron-Epoxy Doubler Installation and Cure - Lay up the 5521/4 Boron-Epoxy doubler in accordance with the application design drawing. After sufficient freezer out-time to defrost and remove moisture, apply adhesive film to the doubler base. Cure for 90 minutes at 250^{O}F or 180 minutes at 225^{O}F at 0.54 ATM vacuum bag pressure (equivalent atmospheric pressure is 7.35 psia) using computer-controlled, composite "hot bonder" units. Use heat blankets to provide the proper temperature cure profile in the field. Use a series of thermocouples in an active feedback loop to maintain the proper temperature profile.

The installation process specification [35] requires a wedge test on a composite witness coupon which is installed adjacent to the actual doubler. A plastic wedge is used to pry these witness coupons away from the aluminum skin at the bondline. A successful wedge test result is where adhesive material appears on both the aluminum substrate and the witness coupon. Note the presence of the pink adhesive on both the witness coupon and the parent aluminum skin in Figure 84. This signifies a good installation and assures that the adhesive layer will fracture at high strains rather than disbonding at relatively lower strains. Figure 83 shows the pull tabs placed between the doubler and the aluminum skin. These were used to engineer intentional disbond flaws in the test specimens. An additional interply delamination flaw was produced by leaving the composite ply backing paper (see Fig. 79) in between adjacent plies. This backing paper will prevent adhesion between the plies – in the shape shown in Fig. 79 – and also restrict resin flow during the cure process. The bleeder cloth in the left photo of Figure 84 shows a lack of resin flow in the delamination area caused by backing film. The ability to insert feeler gages between the plies confirms the presence of delamination.

Figure 79: Scotchbrite Abrade to Water Break-Free Surface (left); Laying Up Doubler with Individual Boron-Epoxy Plies (right)

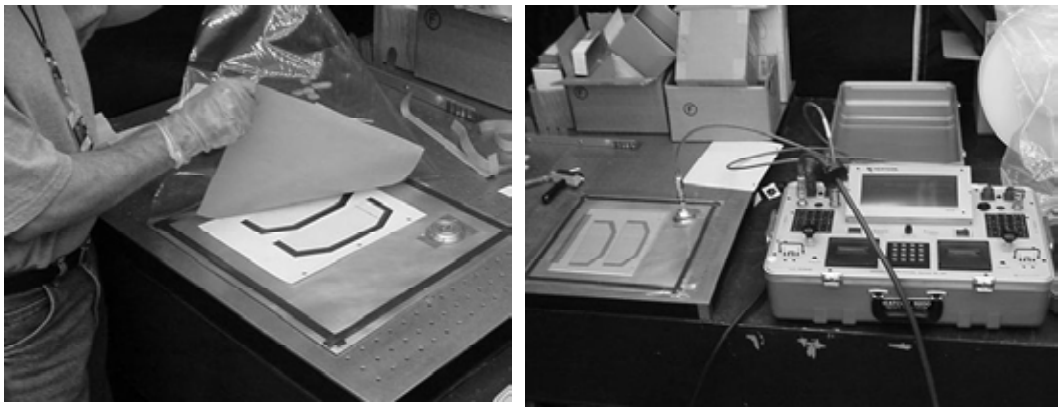

Figure 80: Vacuum Bag Debulk of Doubler Every Four Plies

Figure 81: Sol-Gel Kit and Mixing Sol-Gel Chemicals

Figure 82: Spray-On Application of Sol-Gel Surface Prep Chemicals - 5 applications in 3-4 minutes

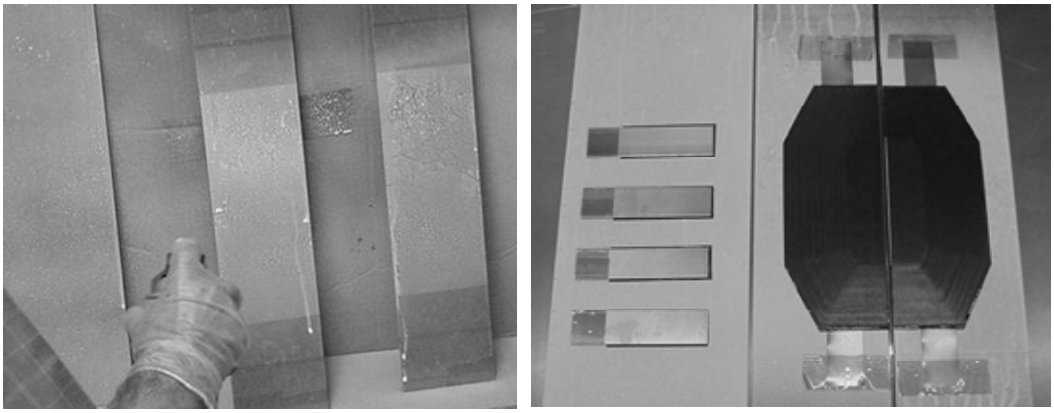

Figure 83: Application of BR-6747-1 primer (left); Witness Coupons and Pull Tab Flaw Inserts Placed Between Doubler and Aluminum Skin

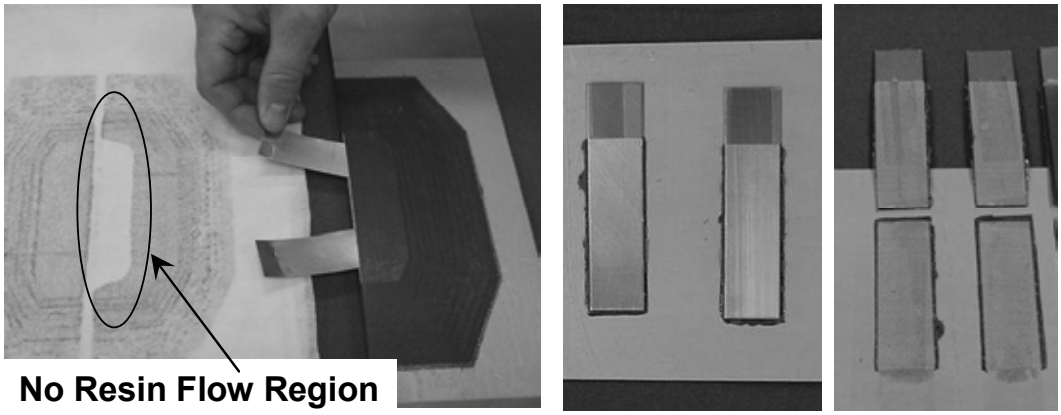

Figure 84: Cured Composite Doubler with Pull Tabs Removed (left); Witness Coupons Before and After Wedge Test Show Successful Surface Preparation (right)

5.2.3 Fatigue Results from Sol-Gel Performance Tests

Figure 85 shows the fatigue test specimen mounted in the mechanical test machine and a close-up view of several strain gages monitoring the strain field along a propagating fatigue crack. The applied fatigue loads were 2 ksi to 20 ksi (852 - 5680 lbs. load) to represent the 0 - 18 ksi hoop stress spectrum experienced by fuselage skin during cabin pressurization. The engineered flaws in the test specimens were as shown in Figure 77. Disbond, delamination and crack sizes used in these damage tolerance tests were at least twice the size of those that can be reliably detected by the NDI methods. Thus, there is an inherent safety factor built into this damage tolerance assessment and the doubler performance sited here should be conservative.

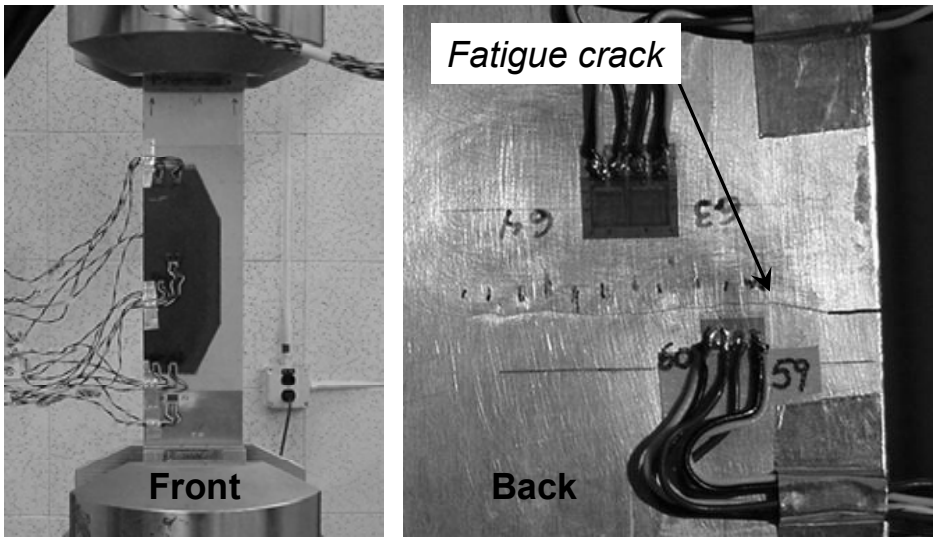

Figure 85: Doubler Fatigue Test - Strain Field Monitoring on Doubler and Adjacent to Crack in Parent Aluminum

Crack Mitigation - Crack growth results from the fatigue tests on specimens Sol-Gel1 and Sol-Gel2 are shown in Figure 86. This plot compares the crack mitigation performance of the previously accepted phosphoric acid anodize (PAA) surface prep method and the Sol-Gel method. The black curves show the crack mitigation performance produced through the PAA process (ref. Fig. 23) while the red curves represent the crack mitigation performance produced by the Sol-Gel installation method.

The plots show that crack growth can be substantially reduced or completely eliminated for a number of fatigue lifetimes using composite doubler repairs. This is true in spite of the disbond and impact impediments - both at the critical load transfer region along the doubler's edge and directly over the crack - which were engineered into the specimens. Note the delay in crack reinitiation until 10,000 and 80,000 cycles in the Sol-Gel specimens. Because of this initial crack growth arrest, these specimens experienced total crack growths of less than 1.5" up through 144,000 fatigue cycles (four design lifetimes of most widebody aircraft). These plots also show

that for similar specimen types, the Sol-Gel method performs as well as the PAA process. The Sol-Gel crack mitigation results also compare favorably with the second set of PAA fatigue performance data shown in Fig. 24.

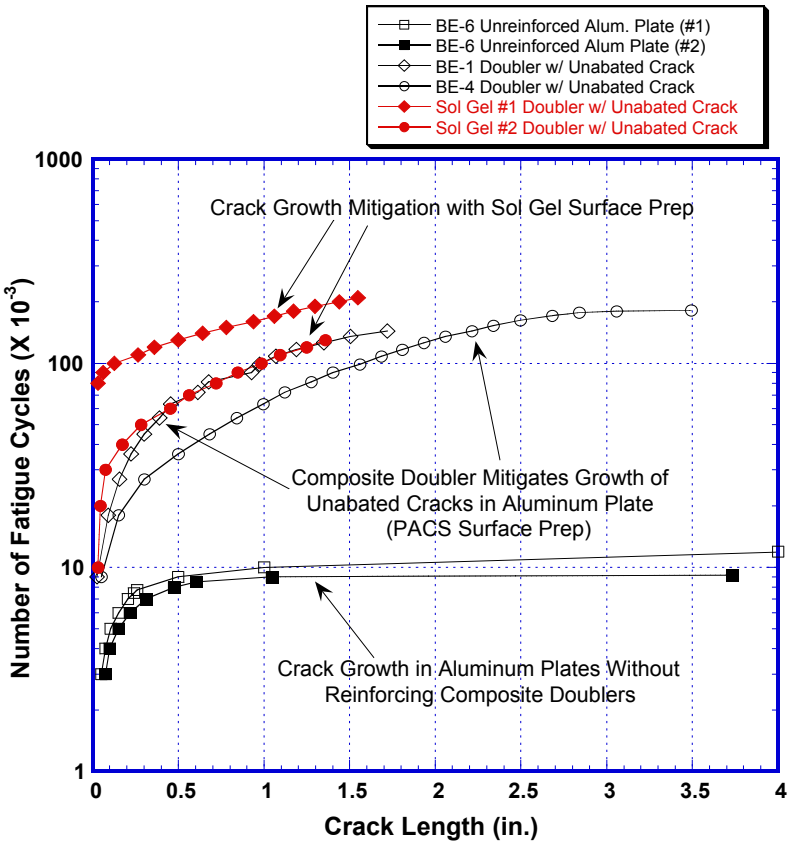

Figure 86: Comparison of Crack Growth Mitigation Produced by Composite Doublers Prepared with Sol-Gel and PAA Surface Preparations

Control Specimens and Comparison of Crack Growth Rates - Two tests were conducted on aluminum "control" specimens that were not reinforced by composite doublers (BE-6 configuration). Unabated fatigue cracks were propagated using the same fatigue spectrum applied to the composite reinforced specimens. Figure 86 shows the crack growth exhibited by the unreinforced plates. In these tests, the fatigue cracks propagated through the width of the specimens after 9,000 and 12,000 cycles. By comparison, configuration BE-4, which had a composite doubler, failed after 182,000 cycles. Thus, the fatigue lifetime as defined in the test coupons, was extended by a factor of approximately 20 through the use of composite doublers. The Sol-Gel specimens were not fatigued to failure. The 150,000 to 200,000 cycles produced crack growth of approximately 1.5" (specimen failure occurred at crack length = 3.5"). Of greater importance, it should be noted that optimum installations without engineered disbond flaws or specimens without fatigue cracks were able to sustain much higher fatigue cycles (see also Section 2.0). Therefore, the life extension factor of 20, calculated using flawed doubler installations, is considered conservative.

In Figure 86, the number of fatigue cycles are plotted using a log scale because it clearly shows the crack arresting affect of the composite doublers. The unreinforced panels asymptotically approach 10,000 cycles-to-failure while the plates reinforced by composite doublers asymptotically approach 100,000 to 200,000 fatigue cycles. Figure 86 also shows that the crack growth rates for all of the specimens can be approximated by a bilinear fit to the data plotted on a semi-log scale. This simply demonstrates the well-known power law relationship between fatigue cycles (N) and crack length (a). The first linear portion extends to (a) = 0.25″ in length. The slopes, or crack growth rates, vary depending on the localized configuration of the flaw (e.g. stop-drilled, collocated disbond, presence of doubler). The second linear portion extends to the point of specimen failure. A comparison of these linear approximations shows that the crack growth rate is reduced 20 to 40 times through the addition of a composite doubler.

Nondestructive Inspection and Propagation of Adhesive Flaws - These damage tolerance tests assessed the potential for loss-of-adhesion flaws (disbonds and delaminations) to initiate and grow in the composite doubler installation. Disbonds can occur between the composite doubler and the aluminum skin while delaminations can develop between adjacent plies of Boron-Epoxy material. It has been shown in related studies that the primary load transfer region, which is critical to the doubler's performance, is around its perimeter [1, 13, 20-24]. The purpose of the engineered disbonds in many of the test configurations (see Fig. 77) were to demonstrate the capabilities of composite doublers when large disbonds exist in the critical load transfer region, as well as around the cracks which the doublers are intended to arrest. In this manner, severe worst case scenarios could be assessed and quantitative performance numbers could be established. In Figures 23, 24, and 86, the specimens with the disbond scenarios were: Sol-Gel-1, Sol-Gel-2, BE-4, BE-8, and BE-9. The 1" wide disbonds in the upper and lower tapered regions amounted to 33% of the load transfer region.

The Sol-Gel fatigue and ultimate strength test coupons were inspected using through-transmission ultrasonics. Figure 87 shows C-scan images generated by the through-transmission ultrasonic inspection of specimen Sol-Gel-1. Signal variations corresponding to disbonds and delaminations are represented by dark black areas on the images [Note the correspondence between the doubler shape and flaw locations shown in Figure 87 and the C-scan image]. The C-scan image on the left in Fig. 87 shows the specimen flaw profile prior to fatigue or ultimate strength testing. It shows the three engineered disbonds and reveals that there were no other flaws in the installation.

Subsequent inspections performed at 1, 2, 3, and 4 fatigue lifetime intervals revealed that there was *no growth in any of the disbonds*. Crack propagation in the specimens, and the accompanying displacements as the crack opened each cycle, produced cohesive failure (cracking) in the adhesive. However, this failure was localized about the length of the crack and did not result in any disbonds (adhesive failure). Figure 87 shows C-scan images produced before and after fatigue testing (210,000 cycles). Side-by-side comparisons of the various flawed specimens show that the original engineered flaws, which were detected prior to testing, remained unchanged even after multiple fatigue lifetimes. The only discernible change in the flaw profile during fatigue occurred around the propagating crack. As the crack opened during

fatigue loading it produced a fracture of the adhesive. This demonstrates the proper failure mode for a doubler installation. That is, the adhesive should fracture instead of disbonding. This assures that the full strength of the adhesive can be realized in the joint.

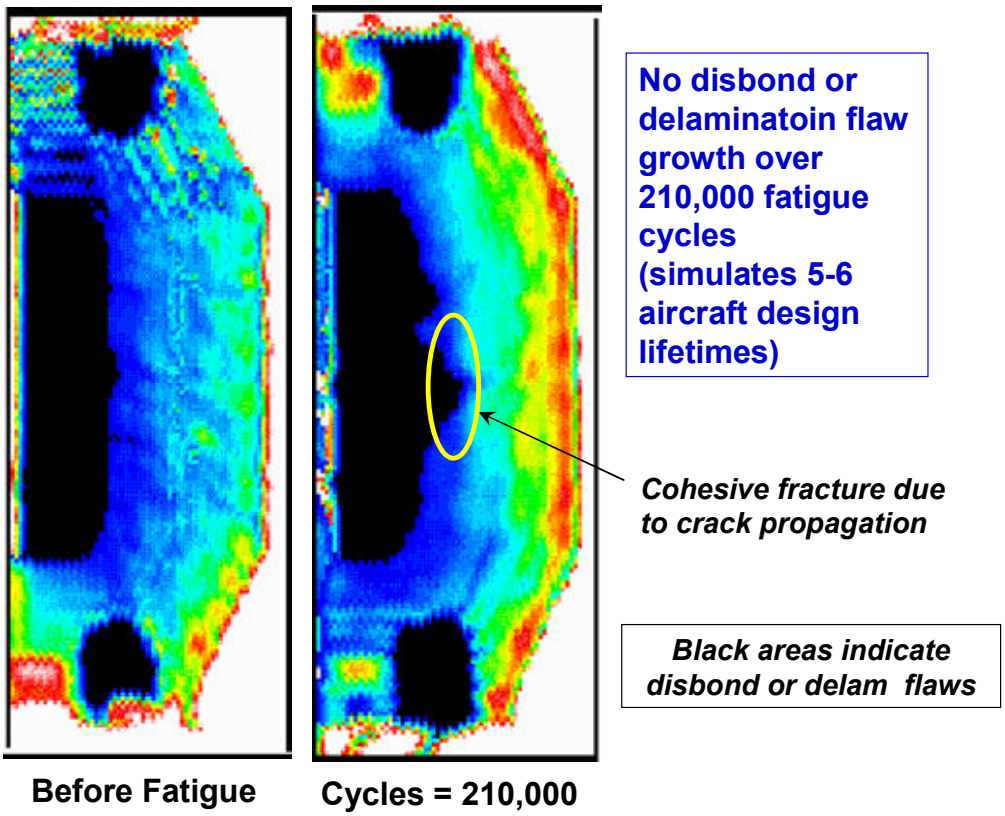

Figure 87: Through-Transmission Ultrasonic Images Show No Flaw Growth Over Multiple Lifetimes of Fatigue Loading (Specimen SolGel-1)

5.2.4 Strain Field Measurements in Sol-Gel Panels

The fatigue tests were conducted using a sinusoidal load spectrum that produced maximum stress value of 20 KSI (5,680 lbs.) and a stress ratio R = 0.1. Load levels were increased beyond the fatigue load levels during the static tests, however, the stress levels were well below yield levels. Figure 78 shows the strain gage layouts that were used to monitor: 1) the load transfer into the composite doublers and, 2) the strain field throughout the composite laminate and aluminum plate. The stress, strain, and load transfer values presented in this section quantify the doubler performance characteristics discussed above. They provide additional insights into the doubler's ability to: 1) resist crack initiation or mitigate crack growth, and 2) perform acceptably in spite of worst-case installations.

A summary of the strain fields in the fatigue test coupons can be seen in the curves shown in Figures 88-89. Sol-Gel-1 and Sol-Gel-2 specimens produced similar strain fields. In general, it

was observed that all strain responses from the simulated fuselage pressurization loads were linear. No residual strains were noted when the specimens were unloaded. The maximum doubler strains were found in the load transfer region around the perimeter (taper region) of the doubler. In all fatigue specimens, the strains monitored in this area were approximately 50% of the total strain in the aluminum plate. This value remained constant over four fatigue lifetimes indicating that there was no deterioration in the bond strength. The strain in the aluminum plate beneath the doubler is reduced in accordance with the strain picked up by the composite doubler. The set of engineered disbonds affected approximately 1/3 of the critical load transfer region. The doublers were able to pick up the strains necessary to accomplishing their intended purpose of strain reduction and crack mitigation in the parent structure. This performance was achieved in spite of collocated flaw scenarios such as impact and disbond flaws. Note also that these flaws were directly over the cracks which the doublers were intended to arrest.

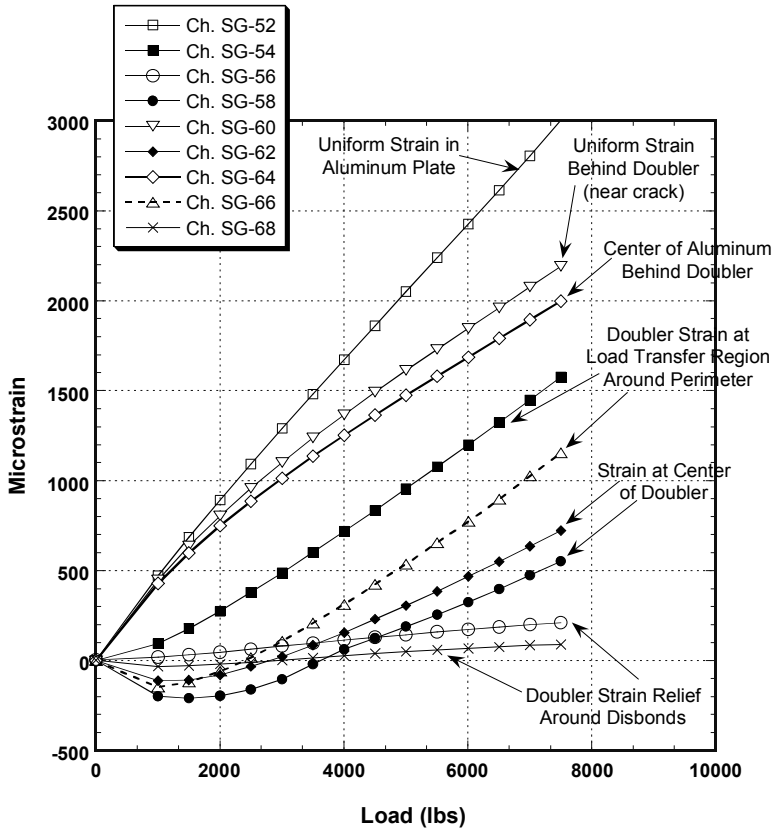

Figure 88: Axial Strain Field in Aluminum and Composite for Sol-Gel-1 Specimen Prior to Fatigue Testing (ref. strain gage locations shown in Figure 78)

The maximum total axial strain in the aluminum plate (away from the doubler) was around 3000 με (for test load P=7,300 lbs.). Axial strains in the aluminum plate beneath the doubler were approximately 50% to 70% of this maximum value while axial strains in the composite doubler ranged from 30% to 50% of the total strain in the specimen. Recall that the axial strains

represent the hoop strains in an actual aircraft. The lateral strains in each of the specimens were produced by the Poisson effect and agreed well with the theoretical relation:

$$\varepsilon_a = - (\nu \text{ X } \varepsilon_l) \qquad (13)$$

where ν is Poisson's ratio, ε_a represents axial strain and ε_l represents lateral strain.

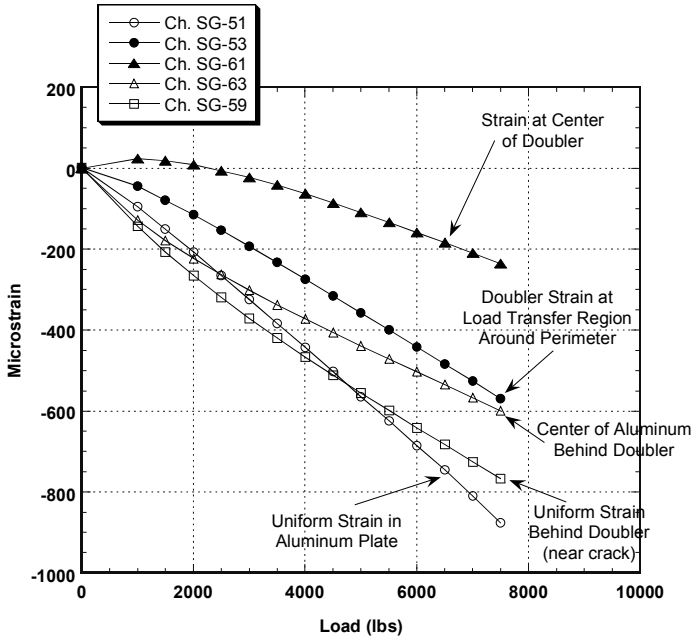

Figure 89: Lateral Strain Field in Aluminum and Composite for Sol-Gel-1 Specimen (ref. strain gage locations shown in Figure 78)

The load transfer is similar at the upper and lower taper regions (compare Ch. 54 and Ch. 66). The strain relief created by disbonds is evidenced by the low strains in Ch. 56 and 68. The large strains in gages immediately adjacent to the disbond (Ch. 54 and Ch. 66) demonstrate that the disbond effects are very localized. The doubler does not create excessive strain risers in the unreinforced aluminum immediately adjacent to the doubler (Ch. 52). Large strains immediately adjacent to the lower disbond (Ch. 54) reiterate the fact that relatively large disbond or delamination flaws (up to 1" diameter) in the composite doubler have only localized effects on strain. Overall, the three disbonds in the Sol-Gel specimens appear to have minimal effect on the doubler's ability to transfer load and relieve the parent aluminum plate.

5.2.5 Aluminum Plate and Composite Doubler Stresses in Sol-Gel Panels

To provide a point of reference for any Boron-Epoxy doubler installation, various stresses sustained by the fatigue test specimens are listed in Table 8. Strain data collected from the

biaxial (axial and lateral) gages were used to calculate the membrane stresses in the composite doubler and parent aluminum skin using the following equations:

$$\sigma_a = \frac{E}{1-\nu^2}(\varepsilon_a + \nu\varepsilon_l) \tag{14}$$

$$\sigma_l = \frac{E}{1-\nu^2}(\varepsilon_l + \nu\varepsilon_a) \tag{15}$$

where E is the modulus of elasticity, ν is Poisson's ratio, σ_a is the axial stress in the skin, σ_l is the longitudinal stress in the skin, ε_a is the hoop strain, and ε_l is the longitudinal strain. From Mil-Handbook 5, the modulus of elasticity and Poisson's ratio for 2024-T3 aluminum are: E =10.5 X 10^6 psi and ν =0.33, respectively. As stated in the Boron-epoxy laminate calculations above, the properties of the Boron-Epoxy laminate are E_x = 11.87 X 10^6 psi and ν = 0.32.

Table 8 shows that the uniform stresses, in excess of those experienced during flight, were produced in the parent skin for each specimen configuration. Away from the fatigue crack, the maximum stresses in the aluminum beneath the doubler (Ch. 63, 64) were roughly 50% of the yield stress for 2024-T3. The maximum stresses in the composite doublers occurred at the edge of the doubler in load transfer region (Ch. 53, 54). Stress risers near fatigue cracks, which normally amount to two or three times the uniform strain field away from the flaw, were essentially eliminated by the composite doubler (Ch. 59, 60). The maximum aluminum stresses immediately adjacent to the fatigue cracks were less than the uniform stress field outside the doubler. A comparison of the stresses at zero and after 144,000 fatigue cycles shows that the doublers picked up additional stresses when the fatigue crack growth reduced the load carrying capacity of the parent aluminum (i.e. stress relief occurred in aluminum).

Biaxial Channels	Peak Load **(lbs) ***	**Stress at Zero Cycles (psi)**	**Stress After Fatigue (psi)**	**No. of Cycles**	**Location on Test Specimen**
51, 52	5,000	22,048	21,490	144,000	Aluminum Away from Doubler
53, 54	5,000	11,850	11,380	144,000	Doubler Edge (lower taper region)
59, 60	5,000	20,670	260	144,000	Aluminum Near Flaw
61, 62	5,000	3,470	8,450	144,000	Doubler Center (full thickness)
63, 64	5,000	16,200	700	144,000	Aluminum Center Beneath Doubler

Table 8: Stresses in Aluminum and Composite Doubler at Maximum Fuselage Pressure Loads

5.2.6 Load Transfer into Composite Doubler

Plots of percent load transfer were obtained by calculating the ratio between doubler strains and strains in corresponding portions of the aluminum parent skin. Figure 90 shows the resulting load transfer plots for various doubler and aluminum reference channels $\{\varepsilon_{doubler} / \varepsilon_{alum(ref)}\}$. The curves indicate that the load transfer into the doubler - and away from the aluminum - was similar in all fatigue specimens regardless of the type and degree of damage in the specimen. In the tapered portion of the doubler, the load transfer was consistently in the 40 - 60 % range. In the center, where the doubler reaches its maximum thickness of 13 plies, the load transfer was in the 30 - 50% range. These load transfer values remained constant over four fatigue lifetimes. This indicates that there was no deterioration in the bond strength.

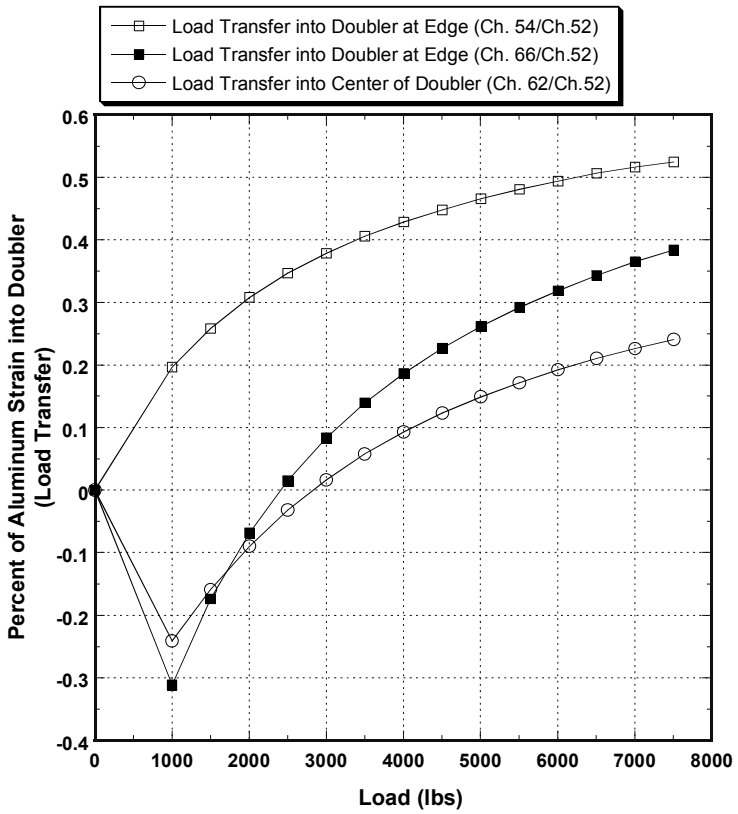

Figure 90: Load Transfer into Doubler for Sol-Gel Surface Prep Specimens

5.2.7 Comparison of Strain Response Between Sol-Gel and Phosphoric Acid Anodize Specimens

Reference [1] describes a set of similarly designed specimens that contained composite doublers installed using the PAA surface prep process. One final assessment of the Sol-Gel method can be performed by comparing the strain levels produced in the two specimen sets. Figure 91

contains plots of strains measured at identical locations on PAA and Sol-Gel test specimens. It can be seen that the strains are the same indicating that the bond strength, and resulting load transfer into the reinforcing composite patch, are the same for both installation methods. This supports the argument that the Sol-Gel process can generate the same repair performance as the PAA process.

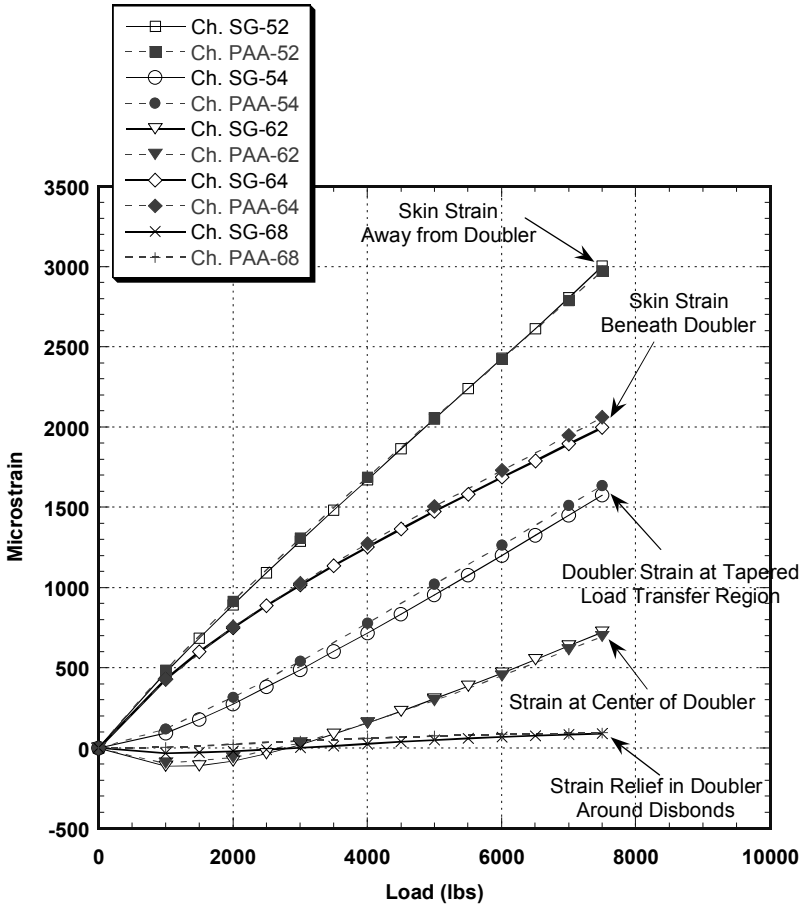

Figure 91: Comparison of Strain Fields in Sol-Gel and Phosphoric Acid Anodize Fatigue Specimens

5.2.8 Residual Strength Failure Tests

After the test specimens were fatigued, they were subjected to static tension tests in order to determine their residual strength and failure modes. These were not ultimate strength tests since the specimens were tested after flaws were engineered into the specimens and the implanted cracks were subsequently grown. By using the maximum load at failure and the original cross section area at the start of the static residual strength test, the resulting "residual tensile strength" numbers were calculated.

Figure 92 shows the extensive crack growth and crack opening that occurred during the failure tests. Both Sol-Gel specimens had plate crack reinitiation during the course of their fatigue tests. Their failure modes were identical: crack propagation and associated cohesive bond failure through the aluminum plate. The doubler separated from the aluminum plate through a cohesive fracture of the adhesive. Thus, there was no disbond growth and adhesive was found on both the aluminum and composite laminate.

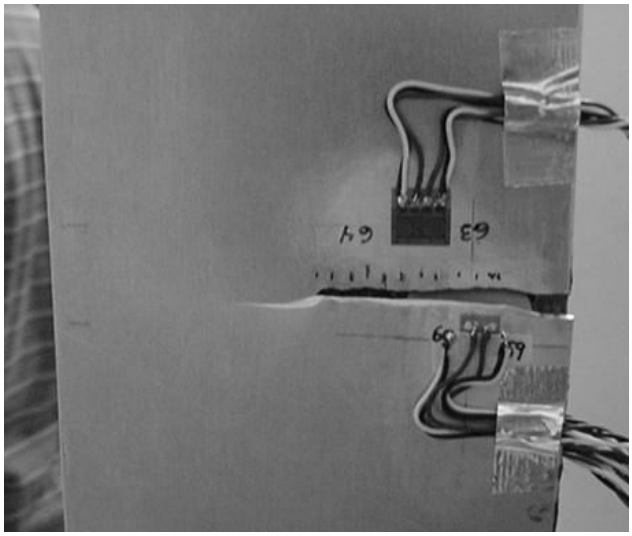

Figure 92: Crack Growth in Failure Tests – Composite Doubler Sustaining Stresses in Aluminum Plastic Regime and Crack Length in Excess of 50% Plate Width

As the crack growth continued beyond the perimeters of the implanted disbond flaw, significant strain changes were observed in the immediate area of the propagating crack. The results, however, highlight the ability of the composite doubler to pick up additional load in response to a loss of strength in the parent structure. Figure 93 shows the strain field in the Sol-Gel-2 specimen up through failure. The aluminum plate away from the doubler (channel 52) began to yield at approximately 10,200 lbs. (36 ksi yield) while the doubler continued to increase its load in a linear fashion. This load/response process continued until failure occurred when the specimen could no longer sustain an increasing load. *Figure 93 illustrates that the composite doubler was able to transmit stresses in the plastic regime and that extensive yielding/loading beyond the initial yield level was required to fail the installation.*

In calculating the ultimate tensile stress, the cross-sectional dimensions of the aluminum and the bonded doubler were used.

1. Specimen Sol-Gel-1: fatigue testing propagated the unabated crack to 2.08” in length; failure load = 17,580 lbs.; measured residual strength = 82.8 ksi.
2. Specimen Sol-Gel-2: fatigue testing propagated the unabated crack to 1.92” in length; failure load = 17,580 lbs.; measured residual strength = 78.3 ksi.

Even in the presence of severe worst case installations (disbonds) and extensive damage growth (fatigue cracks extending through 50% of the specimen width), it was seen that the doubler-reinforced-plates were able to achieve residual tensile strengths (i.e. post-damage tensile strength) which exceeded the 70 ksi Mil handbook listing for the ultimate tensile strength of 2024-T3 material. Thus, the Boron-Epoxy doubler was able to return the parent structure to its original strength and load carrying capability.

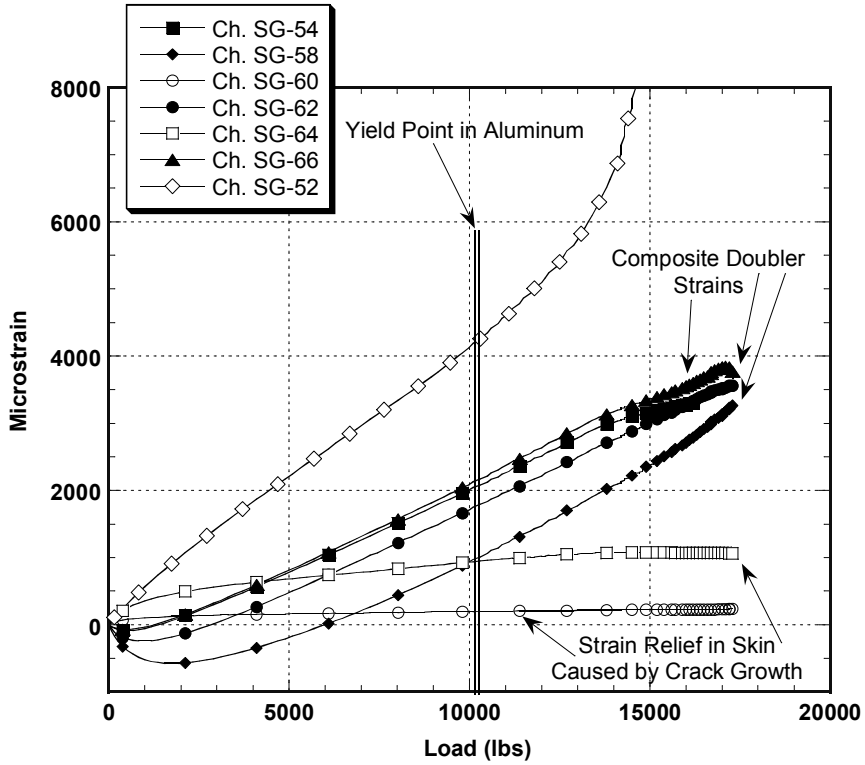

Figure 93: Strain Levels Produced in the Composite Doubler and Aluminum Plate During Failure Test of Sol-Gel-2 Specimen

Ultimate Failure Mode - Figure 94 shows a front and back view of the two failed specimens. The implanted, 1" diameter disbond is clearly visible as is the propagation of the fatigue crack prior to failure. Each of the ultimate tensile strength tests produced the same failure mode which can be described as follows. Upon reaching the yield stress, the aluminum parent skin began to yield (ref. the nonlinear strain region in Fig. 93). Initially, the yielding was primarily in the exposed, unreinforced area of the coupon. As the load was increased further, the aluminum beneath the doubler also began to yield and elongate. The yield zone traveled from the tapered edge of the doubler toward the center of the specimen. This caused the aluminum to sequentially pull away from the doubler which was not yielding or stretching at the same rate as the parent aluminum.

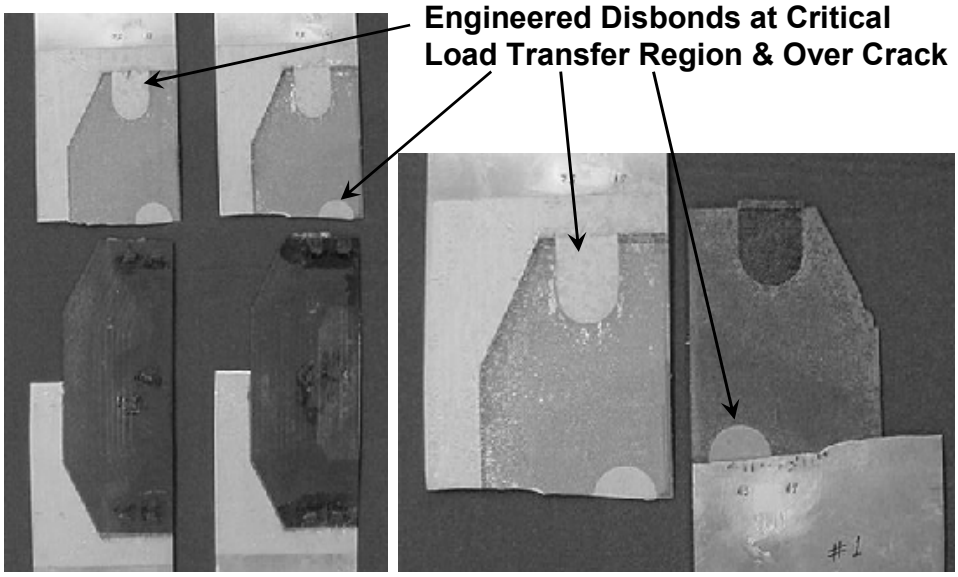

Figure 94: Post Failure View of Sol-Gel Specimens Shows a Cohesive Fracture Failure Mode of the Bond Line

The result was a rolling wave of cohesive failure in the adhesive layer. *There was no disbond growth in the specimen as evidenced by the presence of adhesive on both the aluminum and mating composite doubler in Fig. 94 (i.e. adhesive fractured at high strains but it did not disbond). This indicates that the installation was successful and the full strength of the adhesive was achieved.* During the course of the test it was possible to hear popping sounds corresponding to the fracture of the adhesive. When this cohesive failure (as opposed to adhesive, or disbond, failure) in the adhesive reached the center crack of the coupon, half of the aluminum plate was left without doubler reinforcement. At that point, the crack in the aluminum propagated rapidly across the entire width of the test specimen. Thus, the aluminum was severed in half, as shown in Fig. 94, but the doubler remained in one piece. The contrast between the 1" diameter disbonded area, which has no adhesive, and the adjacent adhesive fracture area, which contains a layer of the adhesive material, is also evident on the aluminum skin in Fig. 94. The damage tolerance tests demonstrated that the loss of doubler integrity at the critical load transfer region produced only localized effects and did not significantly reduce the overall performance of the doubler.

Overall Results

- Strain increases in doubler as alum. sheds load (crack grows)
- Doubler strains are well above alum. yield point ($\sigma \approx 40$ KSI, $\varepsilon \approx 4\mu\varepsilon$)
- Cohesive fracture of adhesive occurs well beyond alum. yield ($\varepsilon \approx 16{,}000\ \mu\varepsilon$)
- Consistency: All Sol-Gel specimens failed above $\sigma u = 70$ KSI (doubler returned damaged structure to original ultimate strength)

6.0 NONDESTRUCTIVE INSPECTION OF BONDED COMPOSITE DOUBLERS AND METALLIC SUBSTRUCTURE

6.1 Inspection Requirements and Intervals for Continued Surveillance

An overall approach to managing the implementation of composite doubler technology is proposed in reference [5]. Reference [5] suggests the use of an Engineering Standard to guide all design, analysis, and QA issues. A series of quality assurance (QA) measures were included in this project's composite doubler installation process to assure: 1) sufficient strength in the adhesive layer, 2) sufficient strength in the Boron-Epoxy laminate, 3) proper surface preparation to allow the best opportunity for complete adherence of the doubler, and 4) the detection of any flaws in the composite doubler. The final QA mechanism is nondestructive inspection which is used for the initial acceptance of a composite doubler installation and for continued surveillance over the life of the doubler.

The three main potential causes of structural failure in composite doubler installations are cracks in the metal, disbonds at the adhesive layer, and delaminations between adjacent plies in the doubler. When disbonds or delaminations occur, they may lead to joint failures. By their nature, they occur at an interface and are, therefore, always hidden. A combination of fatigue loads and other environmental weathering effects can combine to initiate these types of flaws. Periodic inspections of the composite doubler for disbonds and delaminations (from fabrication, installation, fatigue, or impact damage) is essential to assuring the successful operation of the doubler over time. The interactions at the bond interface are extremely complex, with the result that the strength of the bond is difficult to predict or measure. Although extensive testing has shown this repair method to be extremely damage tolerant, disbonds in critical regions may compromise the integrity of the structural assembly. Therefore, it is necessary to detect all areas of disbonding or delamination, as directed by DTA, before joint failures can occur. The overall goals of the NDI effort was to: 1) utilize suitable NDI techniques to detect cracks in the parent structure, interply delaminations in the doubler, and metal interface disbonds, and 2) generate an inspection method (equipment and procedures) that can be easily deployed by personnel in the field.

In any surveillance of aircraft structure there are three main aspects to the inspection requirements: 1) the damage tolerance analysis (DTA) which determines the flaw onset and growth data (especially critical flaw size information), 2) the sensitivity, accuracy, and repeatability of NDI techniques which, in concert with the DTA, establishes the minimum inspection intervals, and 3) the impediments which the NDI techniques must contend with while achieving the required level of sensitivity. Section 1.4.3 presented how a damage tolerance analysis is used to establish the inspection intervals and allowable damage (flaw size to be detected).

6.2 Quality Assurance Coupons to Ensure Proper Surface Preparation

Before moving into routine in-service inspections, it is first necessary to ensure that the initial installation was completed properly. Towards that end, quality assurance testing has been developed for certifying the initial installation. The primary QA test utilizes a witness coupon. The witness coupon is a metal strip that is bonded to the prepared surface alongside the composite doubler. After curing, the witness strip is pried off with a wedge. If the adhesive is found on both the coupon and the steel structure, then the surface preparation is good. The full strength of the adhesive is assured since the failure mode was cohesive failure (fracture) rather than adhesive failure (disbond). Figure 95 depicts this surface preparation QA test and the two potential failure modes.

6.3 Inspections for Cracks in Parent Material Beneath Composite Doubler

In addition to the normal difficulties associated with crack detection in steel structures, the added complexity of inspecting through a composite doubler to assess the structure beneath introduces new impediments. The two NDT inspection techniques commonly used for crack detection were assessed in this study: eddy current and X-ray.

6.3.1 Eddy Current Inspection

Eddy Current (EC) inspection uses the principles of electromagnetic induction to identify or differentiate structural conditions in conductive metals [16, 36]. In this study, it was applied to numerous bonded composite doubler installations in order to assess the ability of EC to detect cracks in steel plates beneath a composite laminate. The presence of a crack is indicated by changes in the flow of eddy currents in the structure. EC signals are physically monitored using impedance-plane plots which show the reactive and resistive components of a coil as functions of frequency, conductivity, or permeability.

When EC inspections are performed, an electrically conductive material is exposed to an alternating magnetic field that is generated by a coil of wire carrying an alternating current. As a result, eddy currents are induced on and below the surface of the material (see Figure 95). These eddy currents, in turn, generate their own magnetic field which opposes the magnetic field of the test coil. Cracks or thickness changes in the structure being inspected influence the flow of eddy currents and change the impedance of the test coil accordingly. EC instruments record these impedance changes and display them in impedance plane plots to aid the flaw detection process.

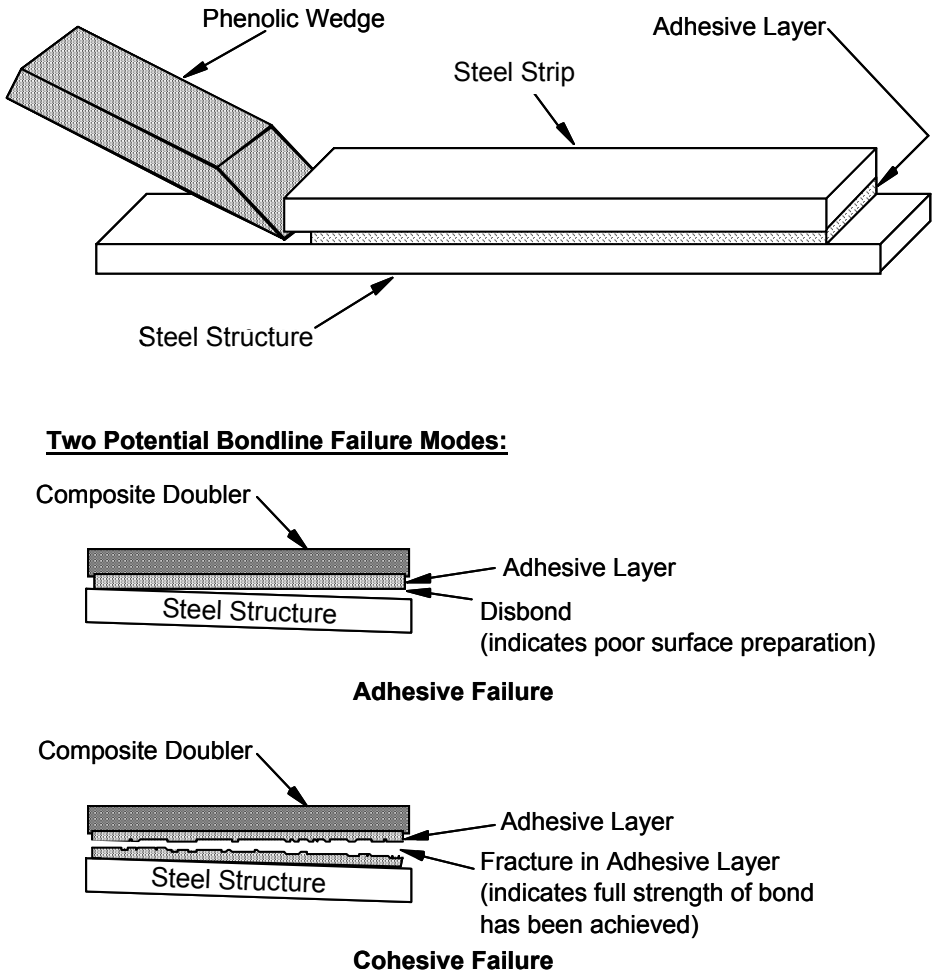

Figure 94: Quality Assurance Wedge Test for Bond Surface Preparation

The depth of penetration of eddy currents is inversely proportional to the product of magnetic permeability, electrical conductivity, and frequency of the inducing currents. Therefore, eddy current tests are most sensitive to discontinuities on the surface next to the coil, which makes them very effective for detecting fatigue cracks in the near surface. High frequency eddy current (HFEC) is generally considered 100 kHz and above and is used to detect near-surface flaws. Low frequency eddy current (LFEC) is in the 100 Hz to 10 kHz range and is used to penetrate deeper to detect flaws in underlying structure. As the structure to be penetrated gets thicker, a lower EC operating frequency is required to reach the desired depth. However, the detectable flaw size usually becomes larger as the frequency is lowered. Eddy currents deeper in the material are weaker and lag in phase compared to the currents near the surface. By measuring the phase, it is possible to determine whether the defect is near the surface or at the inner wall. Figure 96 shows an example of an impedance plane display showing phase and amplitudes of EC signals generated by cracks of varying depths.

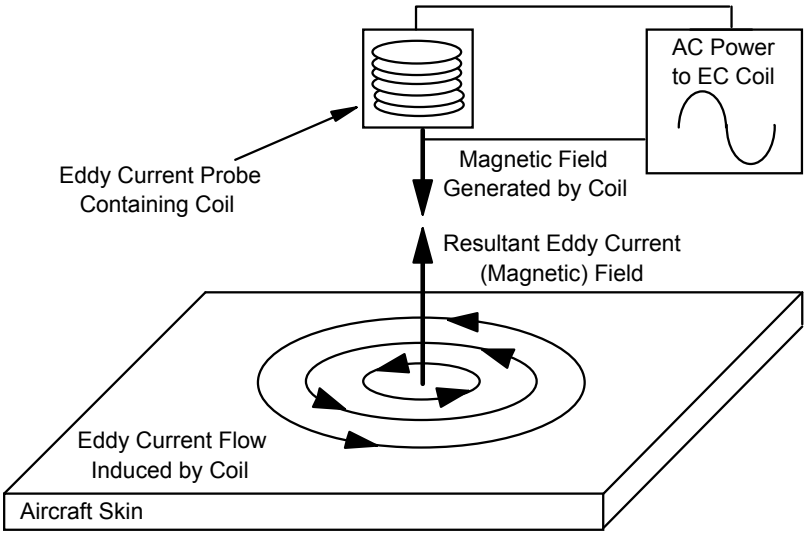

Figure 95: Induction of Eddy Currents in Conductive Materials

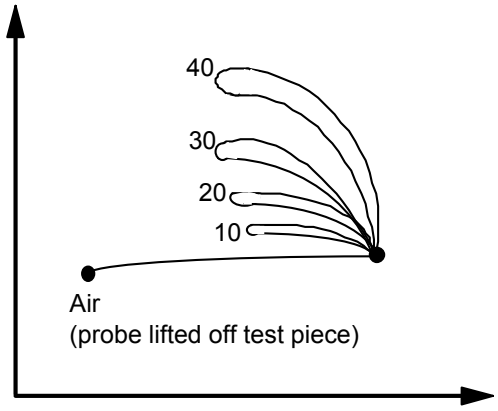

Figure 96: Impedance Plane Display Showing Signal Traces for Surface Cracks of Different Depths (shown in mils)

External surface inspections which may key off visible attributes such as fastener locations (normal origin of fatigue cracks) must now be performed blind since the doubler covers the metal surface. Because eddy currents are created using an electromagnetic induction technique, the inspection method does not require direct electrical contact with the part being inspected. The composite doubler, between the EC transducer and the metal being inspected, does, however, create a lift-off effect which changes the EC signal. This lift-off effect can mask important aspects of flaw detection and must be counteracted by careful equipment set-up, use of suitable calibration standards, and experience in EC signal interpretation. Eddy currents are not uniformly distributed throughout the plate; rather, they are densest at the surface immediately beneath the coil (transducer) and become progressively less dense with increasing distance below

the surface. Thus, the inspection sensitivity through composite doublers is decreased by the lift-off effects (equal to thickness of doubler) and associated need to inspect below the surface of the EC transducer. Lower frequency probes can be used to produce a greater depth of EC penetration, however, this is accompanied by a loss in sensitivity versus higher frequency probes. Thus, the thicker the doubler, the greater reduction in crack detection sensitivity. Therefore, EC inspection through composite doublers becomes a balance between signal resolution and the frequency required to inspect beneath a particular laminate.

Structured EC testing was performed in this study in an attempt to quantify EC performance through composite doublers. Both sliding and spot probes were used in this inspection series. Both probes are suited for this type of inspection and have the low frequencies needed to penetrate the doubler layer. Figure 97 shows several of the cracked specimens, with and without composite doublers, which were used in this study (also see Fig. 85 for view of fatigue crack propagating in aluminum skin behind the doubler. Figure 97 also shows the Nortec 1000 eddy current device being applied to one of the composite doubler fatigue coupon specimens along with photos of the two EC probes tested.

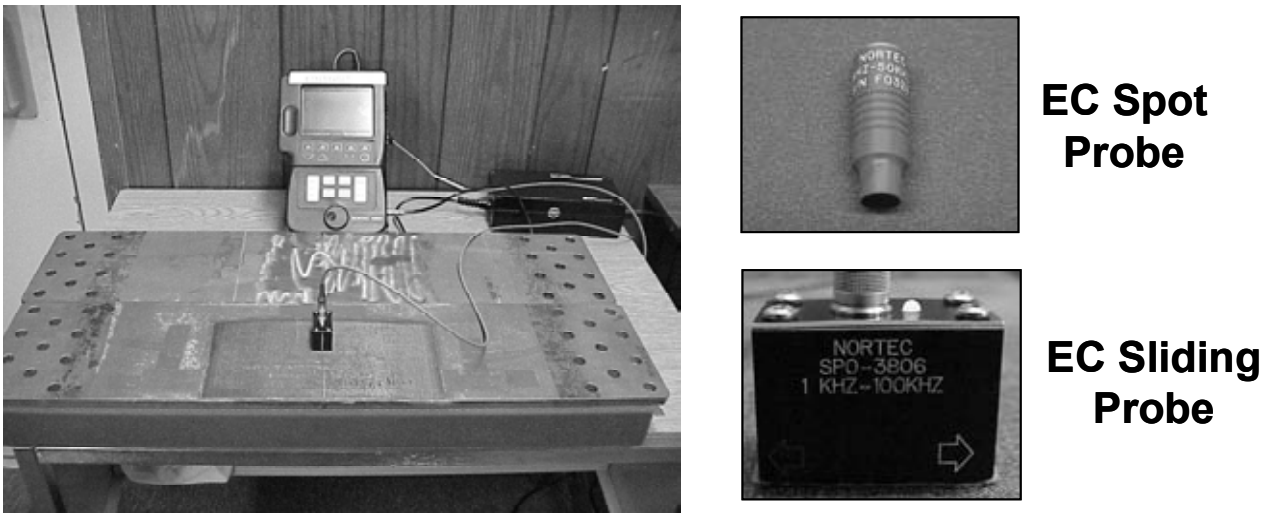

Figure 97: Eddy Current Inspection Set-Up with Nortec 1000 Readout Device Connected to EC Spot probe or EC Sliding Probe

The test series to assess crack detection in metal substructure beneath composite doublers was performed by placing the EC probes on an array of test specimens containing fatigue cracks. Structural configurations included lap splices, butt splices, and finger doubler joints. A step wedge composite doubler was placed over each test specimen and EC inspections were performed through various thicknesses of the Boron-Epoxy laminate (step thicknesses = 0.016", 0.031", 0.093", 0.143", 0.205", 0.251", 0.307", 0.361", and 0.470"). The laminate thickness was sequentially increased until the crack fell below the level of EC detectability.

Figure 98 shows how the composite laminate step wedge was used to evaluate the effects of various lift-offs (patch thickness) on crack detection. Figure 99 shows representative EC signals

from cracked structure located beneath Boron-Epoxy doublers. Two variations are shown to demonstrate the ability of EC to detect both first (surface) and second (substructure) layer cracks in aircraft structure. Initial testing conducted by the AANC on composite doubler specimens with cracks in the parent aluminum skin established the following general limits of crack detectability through composite doublers:

1. a 0.060" long first layer (surface) crack can be detected in the aluminum through a 0.310" thick doubler,
2. a 0.15" length surface crack can be detected through a 0.5" thick laminate, and
3. a 0.15" long subsurface (2nd layer) crack can be detected through a 0.310" thick doubler and a 0.040" thick surface plate.

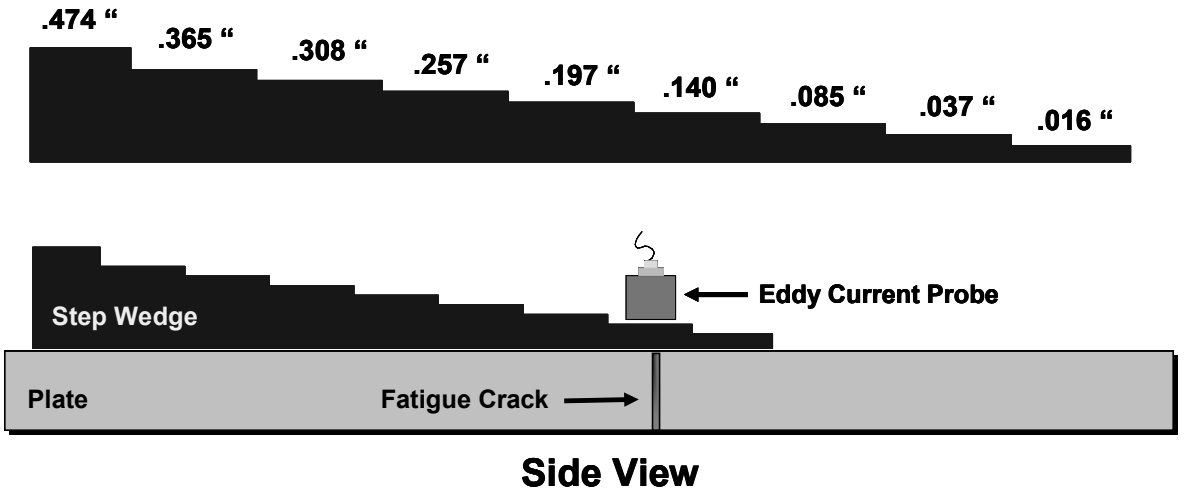

Figure 98: Application of EC Probe Over a Boron-Epoxy Laminate Step Wedge - Used to Assess Crack Detection Beneath Composite Doublers of Different Thicknesses

Figure 100 shows a series of EC signals corresponding to crack detection through increasingly thicker composite doublers. The non-conductive composite laminate serves as a lift-off in the eddy current field and produces a reduction in the signal strength. The results shown in Fig. 100 correspond to spot probe inspections through composite laminates ranging from 3 plies (0.016” th.) to 79 plies (0.474” th.). All of the signal plots indicate that crack detection can be reliably achieved through composite doublers. Furthermore, crack detection signals can be obtained through composite doublers in excess of 100 plies and greater than 0.6” thick. Comparisons were made with the baseline EC signals associated with no crack in the structure. This is essentially the noise associated with the EC probe, the signal acquisition equipment, and the method used to deploy the transducer. Any deviation from this signal can provide a crack indication. From a reliability standpoint, the desired signal-to-noise ratio should be at least 2:1. The signal-to-noise ratios for the EC spot probe ranged from a low of 3:1 to a high of 22:1.

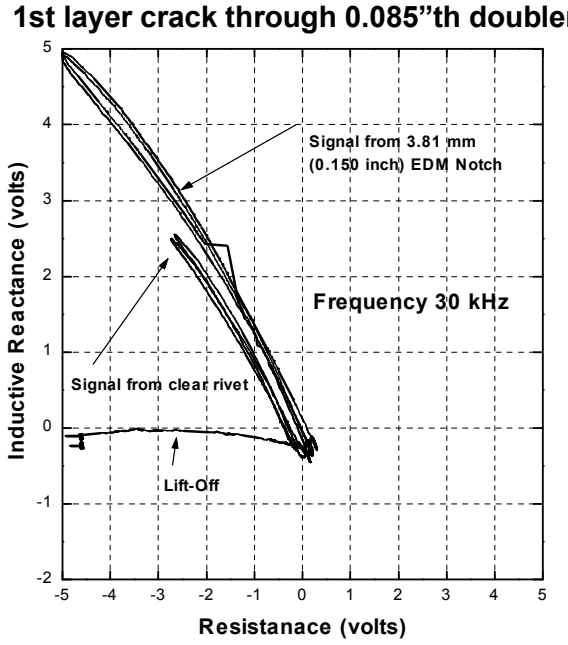

(a)

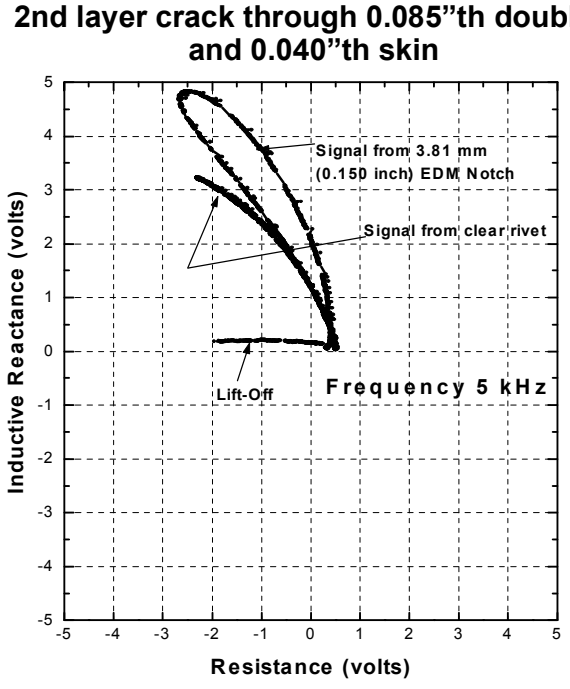

(b)

Figure 99: EC signal for a) 1st layer crack through 0.085" thick doubler (15 plies) and b) 2nd layer crack through 0.085" thick doubler and 0.040" thick skin

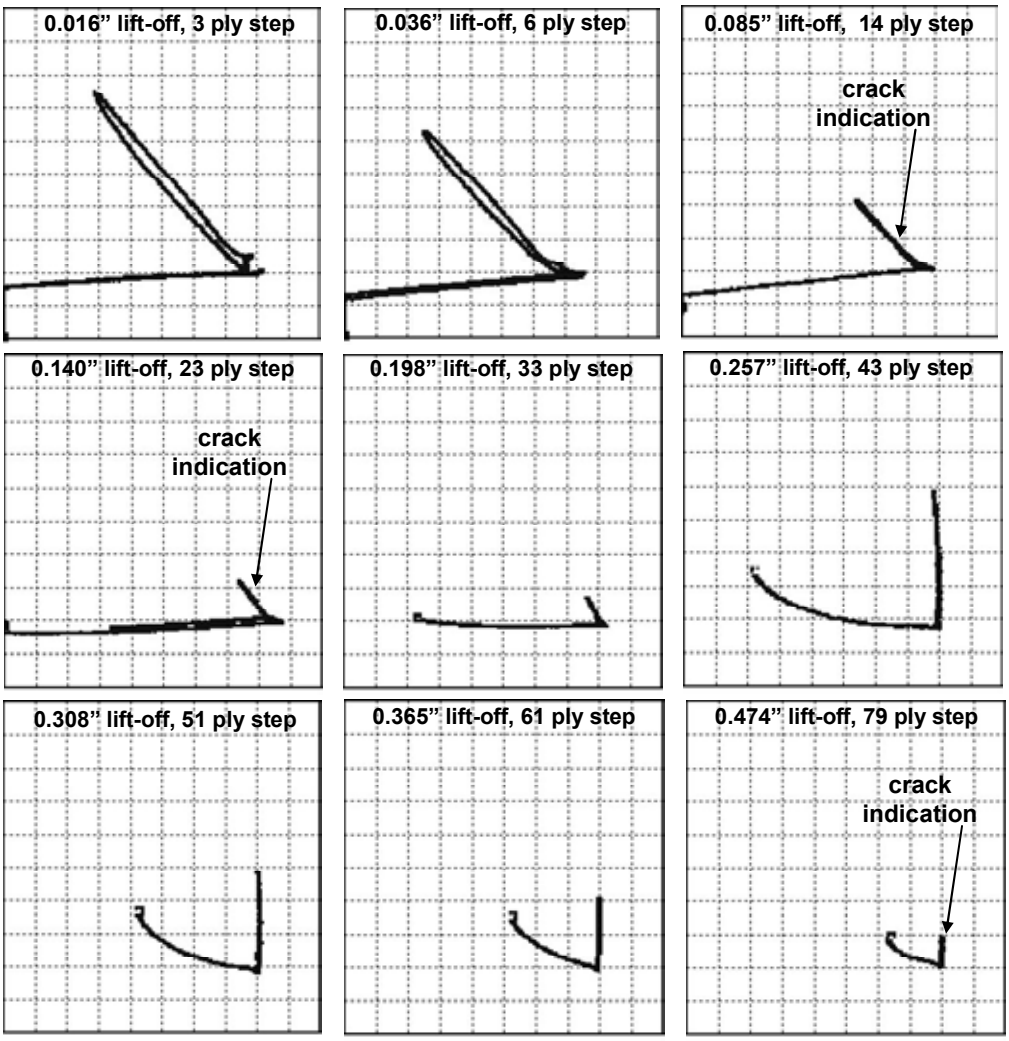

Figure 100: EC Signals from Spot Probe Inspection of a Fatigue Crack Beneath the Composite Laminate Step Wedge

6.3.2 Probability of Crack Detection Using Eddy Current Inspections

True flaw detection performance should be measured through blind experiments where the inspector must make flaw calls from an assortment of cracked and uncracked rivet sites. The specimen set must be statistically relevant and provide: 1) opportunities for flaw calls over the full range of applicable crack lengths, and 2) sufficient unflawed sites to assess the Probability of False Alarm (PoFA). In order to make a valid measurement of the flaw detection capabilities of EC inspections through composite doublers a structured Probability of Detection (PoD) study was performed.

The PoD study utilized a series of surface crack and subsurface crack aircraft panels. These panels, which mimic a Boeing lap splice joint, contain an assortment of fatigue cracks with specific lengths which were carefully engineered in the upper or lower skins [37]. The primary

use of these panels is in the quantitative evaluation of conventional and advanced NDI techniques (Probability of Detection studies). To determine the limits of crack detectability through composite doublers of various thicknesses, the composite laminate step wedge described above was superimposed over the lap splice crack panels as shown in Figure 101. In these specimens, the cracks were located in the upper rivet row of the outer skin (i.e. surface cracks).

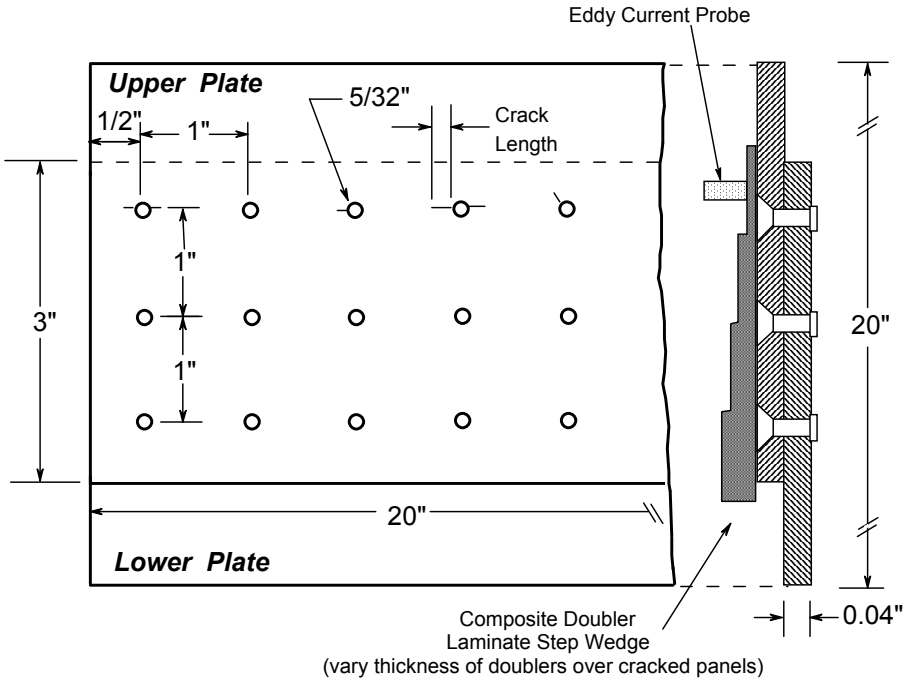

Figure 101: Test Set-Up for Detection of Surface Cracks Through Composite Doublers

Surface Crack PoD - The suite of 18 lap splice panels were inspected through the following four laminate thicknesses: 1) 0.031" th. (5 plies), 2) 0.085" th. (15 plies), 3) 0.143" th. (25 plies), and 4) 0.199" th. (35 plies). Figure 102 shows the resulting PoD curves which were generated from the inspections on surface crack panels. It can be seen that all cracks of 0.17" length and greater were found regardless of the thickness of the composite doubler. Also, the family of curves follow the typical PoD trend where the performance diminishes with increasingly difficult circumstances. In this case, as the doubler becomes thicker, the PoD drops off slightly. These results are quite good in light of the damage tolerance requirement to find fatigue cracks beneath doublers before they reach 1" in length. The EC detection capabilities corresponding to the standard 95% PoD goal are summarized in Table 9.

The surface crack probability of detection experiment used eighteen aircraft panels with a total of 360 rivet inspection sites (upper row of lap splice outer skin only). Since 81 of these inspection sites were cracked, there were 279 opportunities for false calls. Two false calls were made on the panels which were inspected without a composite doubler (0.7%) while no false calls were recorded during any of the inspections through the various composite doublers. Overall, it can be

said that the false call rate for inspections through composite doublers in the 5 to 35 ply regime is less than 1%.

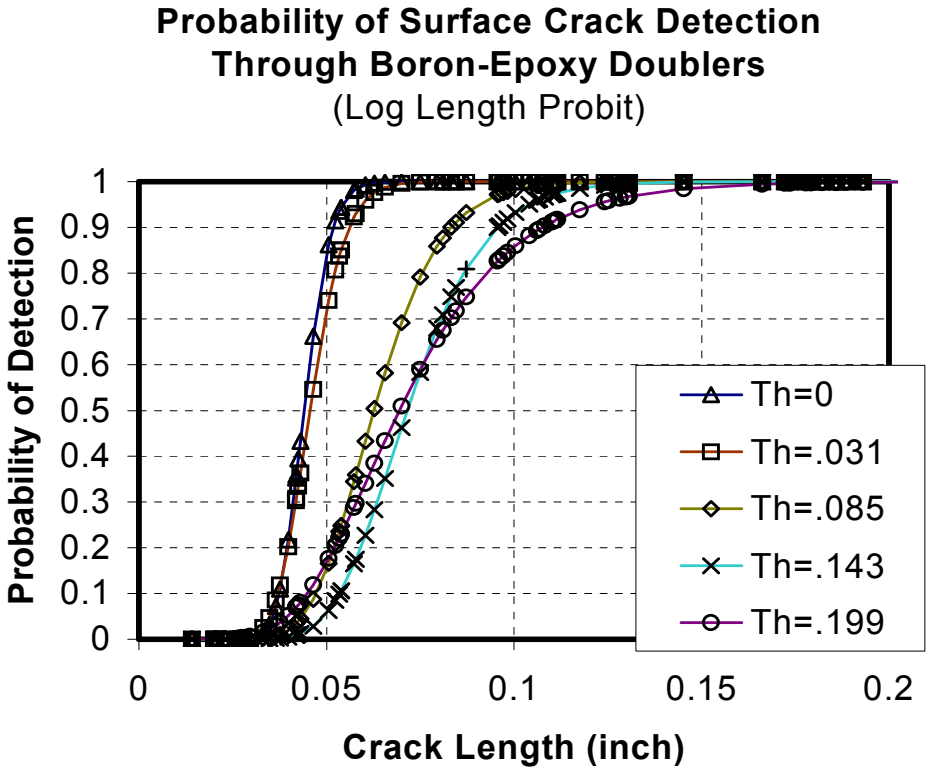

Figure 102: Probability of Detection Curves for Eddy Current Surface Crack Inspections Through Different Thicknesses of Composite Doublers

Composite Doubler Thickness (Number of Plies)	Surface Crack Length at 90% Probability of Detection Threshold
No Doubler (0 plies)	0.053”
0.031" (5)	0.059”
0.085" (15)	0.091”
0.143" (25)	0.103”
0.199" (35)	0.121”

Table 9: Eddy Current Surface Crack Detection Performance Through Bonded Composite Doublers

Interlayer (Third Layer) Crack PoD - A second PoD study was performed to assess eddy current crack detection of subsurface cracks through composite doublers. The subsurface crack test panels were also lap splice joints with two different skin thickness sets: 1) top plate, bonded doubler, and bottom plate were all 0.40" thick, and 2) top plate, bonded doubler, and bottom plate were all 0.36" thick. Figure 103 shows the lap spice configuration where the cracks are in the lower row of the inner skin (third layer). The major difference between these specimens and the surface crack panels shown in figure 101 is the presence of the bonded aluminum doubler between the upper and lower skins. Thus, this experiment challenged eddy current inspections to detect third layer cracks through either 0.80" thick material (2 layers of 0.40" thick each) or 0.72" thick material (2 layers of 0.36" thick each).

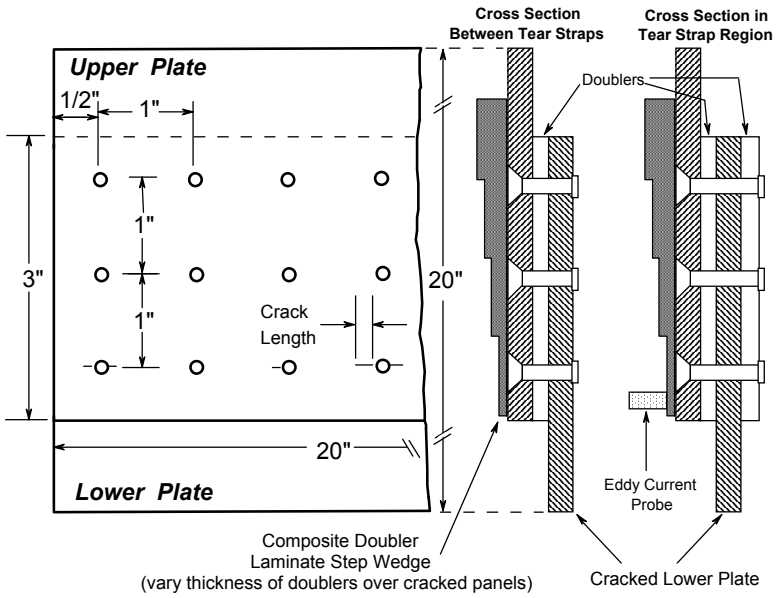

Figure 103: Test Set-Up for Detection of Subsurface Cracks Through Composite Doublers

The suite of 17 lap splice panels were inspected without a doubler in place and then again after placing the 0.031" th. (5 plies) doubler over the cracked panels. Figure 104 shows the resulting PoD curves which were generated from the inspections on the interlayer crack panels. The interlayer crack detection is shifted to the right relative to the surface crack PoD curves because of the added depth of penetration required for the eddy current (and the associated loss in resolution). However, the curves do infer that cracks of 1" and greater can be detected in subsurface structures beneath composite doublers. It should be noted that the curves were generated by producing a fit through the data. There were insufficient crack detections to fully populate the curve and thus, portions of the curves are extrapolations using accepted PoD curve fitting algorithms.

The interlayer crack probability of detection experiment used seventeen aircraft panels with a total of 340 rivet inspection sites (lower row of lap splice inner skin only). Since 98 of these inspection sites were cracked, there were 242 opportunities for false calls. One false call was

made on the panels which were inspected without a composite doubler (0.4%) and one false call was recorded during the inspections through the 0.031" th. composite doubler. The number of cracks detected in this experiment could be higher but the penalty may be a higher number of false calls.

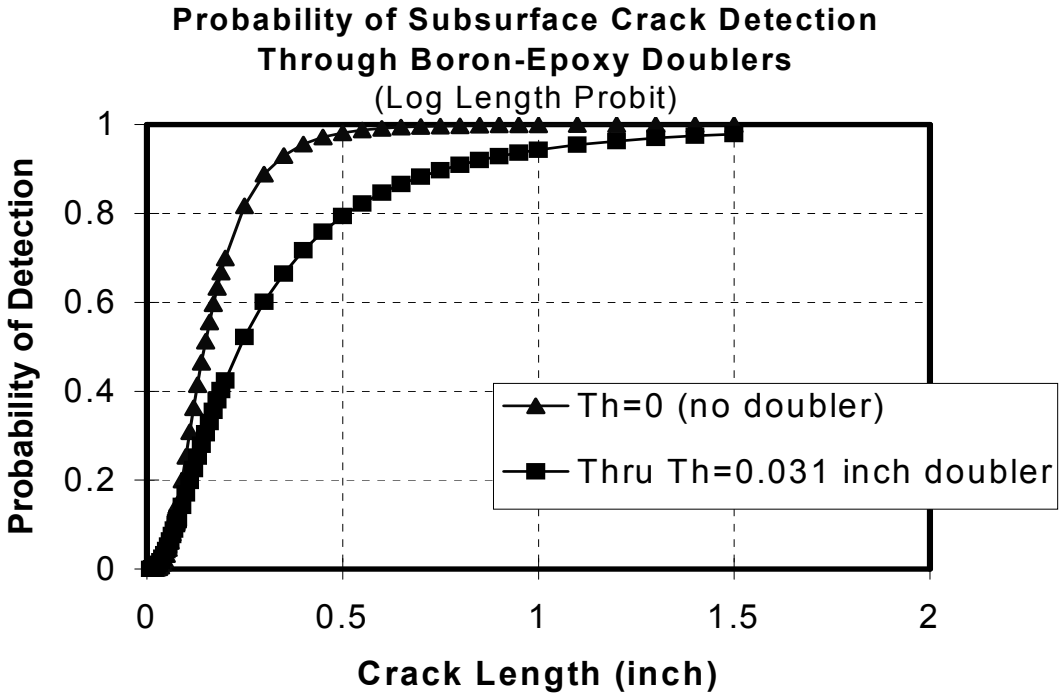

Figure 104: Probability of Detection Curves for Eddy Current Subsurface Crack Inspections Through Different Thicknesses of Composite Doublers

6.3.3 X-Ray Inspection

Radiographic inspection is a nondestructive method of inspecting materials for surface and subsurface discontinuities [38]. The method utilizes radiation in the form of either x-rays or gamma rays, which are electromagnetic waves of very short wavelength. The waves penetrate the material and are absorbed depending on the thickness or density of the material being examined. By recording the differences in absorption of the transmitted waves, variations in the material can be detected. Figure 105 shows an application of X-radiography in a hangar environment. The most common way of measuring X-ray transmission is with film. After exposure and development, the film will become proportionally darker depending on the amount of radiation which reached the film. Areas that are thinner or lower density will allow more radiation to pass through the part. The greater the radiation transmitted through the part, the darker the film will be.

Positioning Film for Cockpit Window Post Inspection

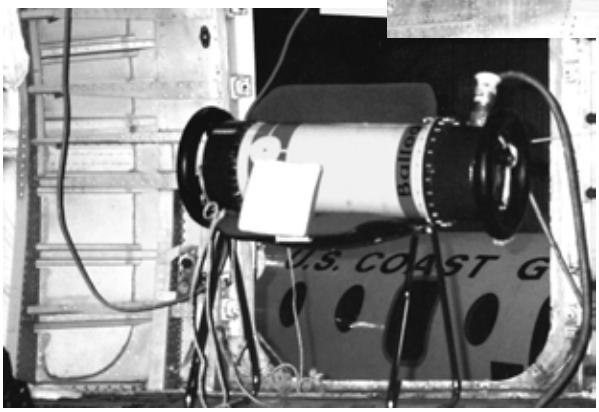

Locating X-Ray Source for Door Frame Crack Inspection

Figure 105: Aircraft Fuselage Inspection for Cracks Using X-Ray

Radiographic Sensitivity (Image Quality) - Radiographic sensitivity is a function of two factors. The ability to see a density variation in the film, which is "radiographic contrast" and the ability to detect the image outline which is "radiographic definition." Radiographic contrast is the difference in darkness of two areas of a radiograph. If contrast is high, small defects or density changes will be noticeable. Using lower power will result in higher subject contrast. However, lower power requires longer exposure times to obtain the adequate film density. If the energy level is too low, it will not penetrate the part at all.

Radiographic Definition - This term is defined as the ability to resolve the defect image on the radiograph. It is affected by the geometric factors of the exposure: size of the radiation source (focal spot size), distance from the target/source to the film, and distance from the part to the film. All of these factors contribute to a loss of geometric sharpness and as geometric sharpness decreases, the ability to see small defects decreases.

Image Quality Indicators - Image Quality Indicators (IQI) are used to measure the quality of the exposure and assure that proper sensitivity has been achieved. They measure the definition of the radiograph. By imaging IQI wires of various thicknesses and lengths it is possible to verify the resolution and sensitivity of a radiographic technique/set-up.

Resolution and Sensitivity - Image Production Through Composite Doublers - The discussion above provides some background on X-ray inspections and difficulties associated with its use. All of the issues described above exist regardless of whether or not the X-ray exposure takes

place through a composite doubler. The primary question to be addressed in this study was: What is the overall effect of a composite doubler on X-ray inspections of structure beneath the doubler? To answer this question, a study was conducted to: 1) demonstrate that composite doublers do not interfere with the ability to perform X-ray inspections for cracks in steel, and 2) identify proper exposure time and power settings to optimize the sensitivity of the X-ray technique when inspecting through thick doublers.

Several fatigue crack specimens were inspected through a 72 ply composite doubler. To form a basis of comparison, X-rays were also taken without the doubler placed over the cracked specimens. The specimens placed beneath the doubler included 1st layer and 2nd layer fatigue crack panels with crack lengths ranging from 0.05" to 1.0". Radiography was found to be a very effective inspection method to interrogate the interior of the parent material covered by a composite doubler. This technique provides the advantage of a permanent film record. To increase the contrast on the film, the X-ray inspection was performed at low kilovoltage (80 kV). Test results showed the ability to detect cracks less than 1" in length. Fatigue cracks on the order of 0.38" in length were found under 0.41" thick (72 ply) Boron-Epoxy doublers. A sample X-ray result of a crack imaged through a 72 ply composite doubler is shown in Figure 106. [Note that significant resolution is lost in translating the X-ray film to a black and white graphic.]

Comparisons with X-rays taken without composite doublers revealed that while the doubler may darken the X-ray image slightly it does not impede the X-ray inspection. Power and exposure times were adjusted in order to restore the desired contrast and maintain the specified film density of between 2 and 3. The initial set-up (80 kV, 12 mA, 6 inch source-to-film-distance and 30 second exposure time) on medium speed film produced a film density of 0.98. Increasing the exposure time to 90 seconds produced a film density of 2.64. Image Quality Indicators (IQI), inserted into the field of view, verified the resolution and sensitivity of the radiographic technique. IQI lines with widths of 0.010" and dots with diameters of 0.10" were clearly imaged on the X-ray film. These results showed that X-ray inspections are as effective as before a doubler is installed.

X-ray Results Summary - The X-ray tests performed in this study determined that there are no additional impediments brought on by the presence of composite doublers. X-ray inspections were able to achieve high levels of resolution when inspecting through thick composite doublers and the films were very comparable with films acquired on similar structures without doublers. All difficulties associated with X-ray inspections - shadowing from substructure elements, accessibility, and safety issues - are the same as in structures without composite doublers.

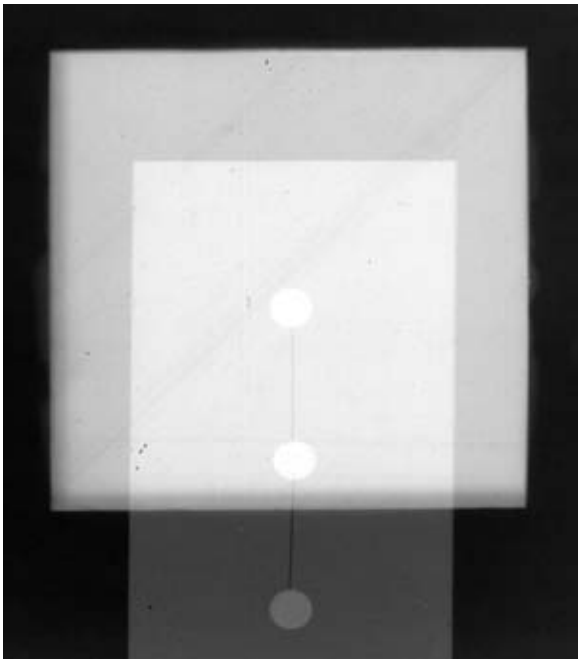

Figure 106: Sample X-Ray Image of a Cracked Structure Beneath a 72 Ply Composite Doubler

6.4 Nondestructive Inspection Methods for Composite Doubler and Bond Integrity

6.4.1 Pulse-Echo Ultrasonic Inspection

Ultrasonic (UT) inspection is a nondestructive method in which beams of high frequency sound waves are introduced into materials for the detection of surface and subsurface flaws in the material. The sound waves, normally at frequencies between 0.1 and 25 MHz, travel through the material with some attendant loss of energy (attenuation) and are reflected at interfaces. The reflected beam is displayed and then analyzed to define the presence and location of flaws. The degree of reflection depends largely on the physical state of the materials forming the interface. Cracks, delaminations, shrinkage cavities, pores, disbonds, and other discontinuities that produce reflective interfaces can be detected. Complete reflection, partial reflection, scattering, or other detectable effect on the ultrasonic waves can be used as the basis of flaw detection. In addition to wave reflection, other variations in the wave which can be monitored include: time of transit through the test piece, attenuation, and features of the spectral response [16, 39].

The principal advantages of UT inspection as compared to other NDI techniques are: 1) superior penetrating power for detection of deep flaws, 2) high sensitivity permitting the detection of extremely small flaws, 3) accuracy in determining size and position of flaws, 4) only one surface needs to be accessible, and 5) portability.

UT Pitch-Catch Pulse-Echo Inspections - In UT pitch-catch pulse-echo inspections, short bursts of ultrasonic energy are interjected into a test piece at regular intervals of time. In most pulse-echo systems, a single transducer acts alternately as the sending and receiving transducer. The mechanical vibration (ultrasound) is introduced into a test piece through a couplant and travels by wave motion through the test piece at the velocity of sound, which depends on the material. If the pulses encounter a reflecting surface, some or all of the energy is reflected and monitored by the transducer. The reflected beam, or echo, can be created by any normal (e.g. in multi-layered structures) or abnormal (flaw) interface. Figure 107 is a schematic of the pulse-echo technique and the interaction of UT waves with various interfaces within a structure. Sometimes it is advantageous to use separate sending and receiving transducers for pulse-echo inspection. The term pitch-catch is often used in connection with separate sending and receiving transducers.

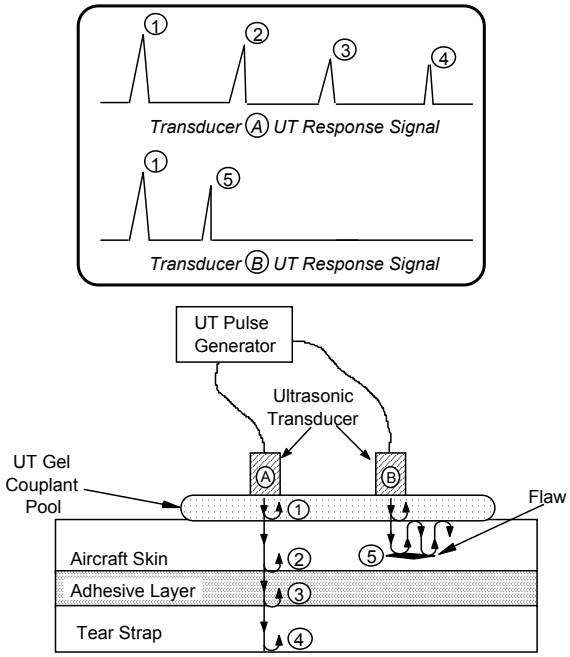

Figure 107: Schematic of Pulse-Echo Ultrasonic Inspection and Reflection of UT Waves at Assorted Interfaces

A-Scan Mode - In conventional Pulse-Echo Ultrasonics (PE UT), pulses of high frequency sound waves are introduced into a structure being inspected. A-Scan signals represent the response of the stress waves, in amplitude and time, as they travel through the material. As the waves interact with defects or flaw interfaces within the solid and portions of the pulse's energy are reflected back to the transducer, the flaws are detected, amplified and displayed on a CRT screen. The interaction of the ultrasonic waves with defects and the resulting time vs. amplitude signal produced on the CRT depends on the wave mode, its frequency and the material properties of the structure. Flaw size can be estimated by comparing the amplitude of a discontinuity signal with that of a signal from a discontinuity of known size and shape. Flaw location (depth) is determined from the position of the flaw echo along a calibrated time base. In the pitch-catch UT

method, one transducer introduces a pressure wave into the specimen and a second transducer detects the transmitted wave. A complex wave front is generated internally in the material as a result of velocity characteristics, acoustical impedance, and thickness. The time and amount of energy is affected by the changes in material properties, such as thickness, disbonds, and discontinuities. The mechanical vibration (ultrasound) is introduced into the specimen through a couplant and travels by wave motion through the specimen at the velocity of sound. If the pulses encounter a reflecting surface, some or all of the energy is reflected and monitored by the transducer. The reflected beam, or echo, can be created by any normal or abnormal (flaw) interface. Complete reflection, partial reflection, scattering, or other detectable effects on the ultrasonic waves can be used as the basis of flaw detection.

Figure 108 shows a pitch-catch UT inspection (pulse-echo mode) of a composite doubler bonded to an aluminum skin. Figure 109 contains a schematic showing the pitch-catch inspection method and the UT wave travel within the structure during this inspection. During testing, the transmitting transducer is placed on top of the composite doubler and the receiving transducer is placed on top of the parent steel material. If the adhesive bond between the two articles is intact, the ultrasonic signal will pass unobstructed to the receiving transducer.

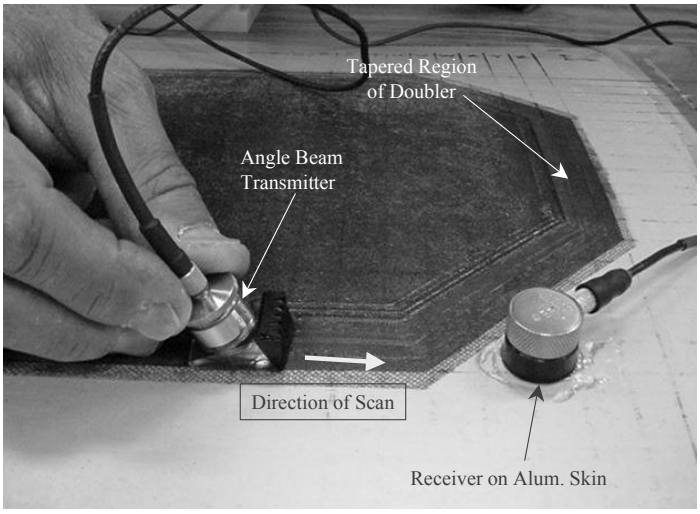

Figure 108: Ultrasonic Pitch-Catch Sensor Set-Up for Inspection of Composite Doubler Laminate and Bond Line

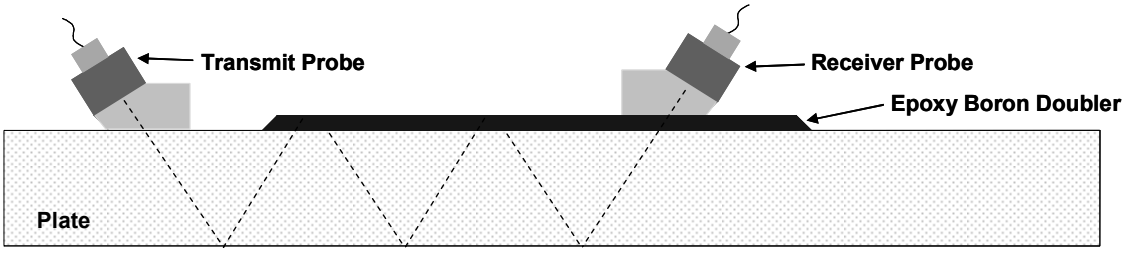

Figure 109: Schematic of Ultrasonic Wave Travel in a Pulse Echo, Pitch-Catch Inspection of a Composite Repair Installation

Figure 110 contains a series of A-scan signals produced by the pulse-echo inspection of a doubler specimen that contained intentional, engineered flaws at discrete locations. Changes in the A-Scan signal (i.e. lack of reflected signal from steel back wall), caused by the presence of the disbond or interply delamination, are clearly visible. Key portions of the signal in Figure 110 are identified to highlight how the A-Scan can be used to detect disbonds and delaminations. The primary items of note are: 1) the unique signature of the amplitude vs. time waveform which allows the user to ascertain the transmission of the ultrasonic pulse through various layers of the test article and which indicate a good bond, and 2) the absence of signature waveforms indicating a disbond. The thickness of the composite doubler does not significantly affect the transmission of the ultrasonic signal so similar flaw detection signals can be produced regardless of the doubler thickness. Another important consideration is that this technique can be deployed quickly. A one square foot region can be inspected in approximately 15 minutes.

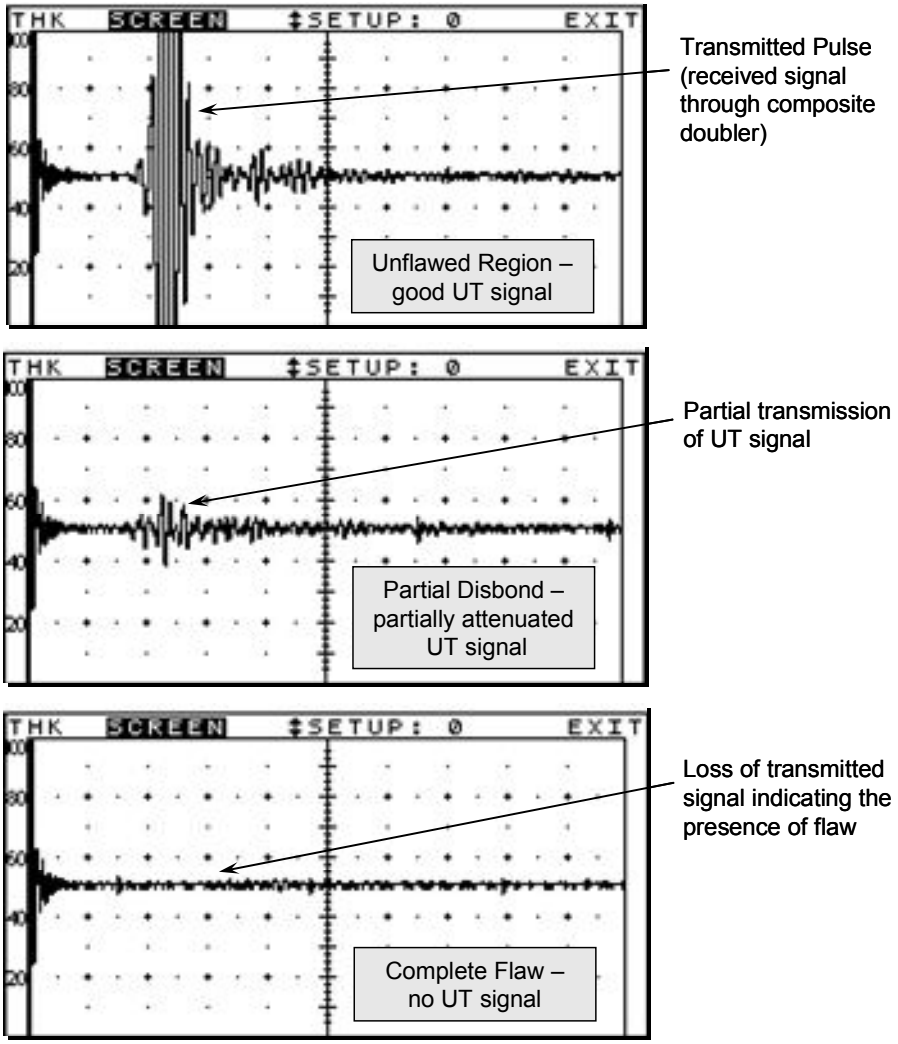

Figure 110: A-Scan Waveforms from Bonded and Disbonded Portions of a Composite Doubler Repair

C-Scan Mode: Use of Scanning Technology - Disbond and delamination detection can be also be achieved by taking the A-Scan signals and transforming them into a single C-Scan image of the part being inspected. C-Scan technology uses information from single point A-Scan waveforms to produce an area mapping of the inspection surface. These 2-D images are produced by digitizing point-by-point signal variations of an interrogating sensor while it is scanned over a surface. C-Scan area views provide the inspector with easier-to-use and more reliable data with which to recognize flaw patterns. This format provides a quantitative display of signal amplitudes or time-of-flight data obtained over an area. The X-Y position of flaws can be mapped and time-of-flight data can be converted and displayed by image processing-equipment to provide an indication of flaw depth. A variety of PC-based manual and automated scanning devices can provide position information with digitized ultrasonic signals. Specific emphasis can be placed on portions of the UT signal - and highlighted in the color-mapped C-Scan - based on user specified amplitude gates, time-of-flight values and signal waveforms.

Figure 111 shows a C-scan image (based on amplitude) from a pulse-echo UT inspection of a thick composite doubler with engineered flaws. The test specimen schematic is also shown to provide doubler lay-up information and the embedded flaws profile. A three-dimensional contour plot is also shown to demonstrate another means of displaying the data and interpreting the results. Disbond and delamination flaws are revealed by continuous and distinct signal loss areas which, depending on the color palette chosen, are either relatively bright or dark compared to the surrounding colors.

Figure 112 is a schematic of the 6 ply composite doubler revealing the size and location of the implanted flaws while Figure 113 shows the C-scan image produced by an X-Y scanner system deployed on pulse-echo UT mode. In the gray-scale image, the flaws are shown as the brighter colored areas within the dark baseline. It can be seen that this inspection was able to detect flaws at a wide range of depths in a single image (see also Figs. 60, 61, 69, 70, and 75).

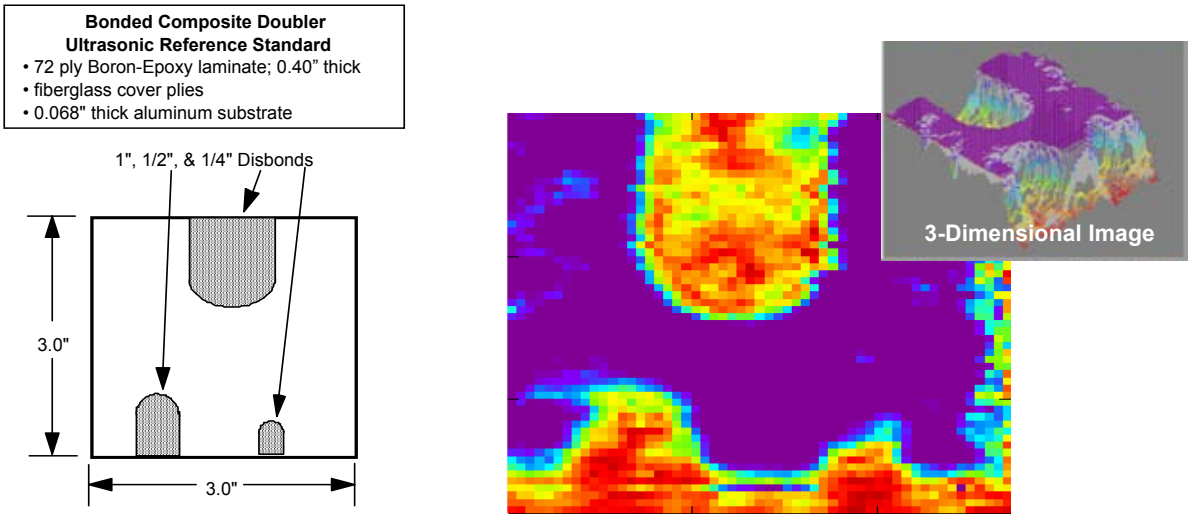

Figure 111: C-Scan Image Produced by Selective Gating on the Amplitude of All Signals Received by the Transducer

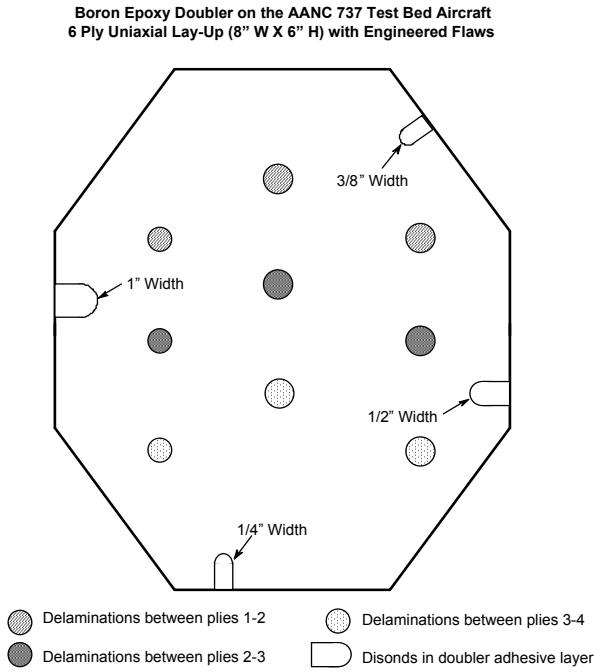

Figure 112: Schematic of Composite Doubler Showing Engineered Flaws

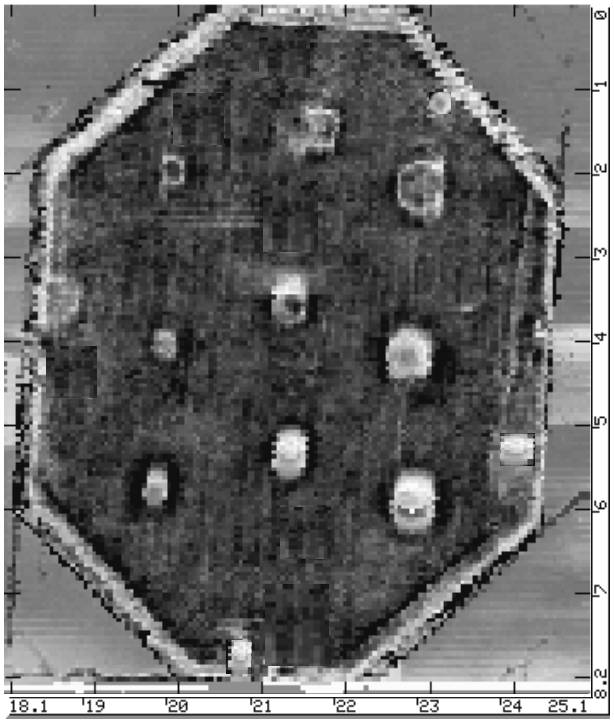

Figure 113: Gray-Scale C-Scan Image of 737 Doubler Produced by Ultra Image Scanning Device

6.4.2 Probability of Disbond and Delamination Detection Using Pulse-Echo UT Inspections

Initial qualification of a repair prior to releasing an aircraft for service is an important consideration as is in-service inspections of repaired flaws. Validation efforts for the DC-10 inspections revealed that the ultrasonic pulse-echo (dual-element pitch/catch mode) inspection method works well in detecting flaws and mapping out flaw shapes in composite doublers. Inspection procedures were written, validated, reviewed by Boeing, and incorporated into the Boeing NDI Standard Practices Manuals.

In order to make a valid measurement of the flaw detection capabilities of the pulse-echo ultrasonic inspection method, a Probability of Detection (PoD) study was performed. Flaw detection performance was measured through blind experiments where inspectors had no knowledge of the specimen flaw profiles. A statistically relevant specimen set was used to provide: 1) opportunities for flaw calls over the full range of applicable flaw sizes and locations, and 2) sufficient unflawed sites to assess the Probability of False Alarm (PoFA).

The AANC designed and fabricated a series of composite doubler specimens with the 13 ply lay-up called out in the DC-10/MD-80 designs. The specimens contain a statistical array of engineered flaws and were inspected by eight different airline inspectors using the pulse-echo UT method. Flaw sizes in the test specimens ranged from 0.375” diameter to 0.75” diameter. The results are as follows: 98% of the flaws at or above 0.5” diameter were found. Seventy percent of the flaws less than 0.5” diameter were also found. The NDI techniques worked well with flaw detection including disbond and delamination flaws as small as 1/8" diameter. Damage tolerance thresholds conservatively require the detection 1” diameter disbond and delamination flaws around the perimeter of the doublers. Inspection intervals can be set up to allow for at least two inspections and two opportunities to find a flaw before it reaches the maximum allowable size. The outcome of this scenario can be simulated by combining the results from two different inspectors. Such a combination produced the following results: 100% detection of all flaws, even those smaller than 0.25” in diameter, and zero false calls. Overall, the test series described above clearly demonstrated that disbond and delamination flaws on the order of 0.5” to 1.0” in diameter can be reliably detected through thick composite doublers.

Inspection Procedures and Reference Standards - In addition to evaluating the performance of the pulse-echo UT inspection method, the PoD exercise allowed for an assessment of the inspection procedures and the NDI reference standard. The necessary reference standard, shown in Figure 114, was deemed suitable by Boeing. It provides all of the appropriate flaw scenarios and transducer null points in a doubler lay-up that mimics the DC-10/MD11 repair family. Appendix A lists the inspection procedure for the pulse-echo UT inspection techniques.

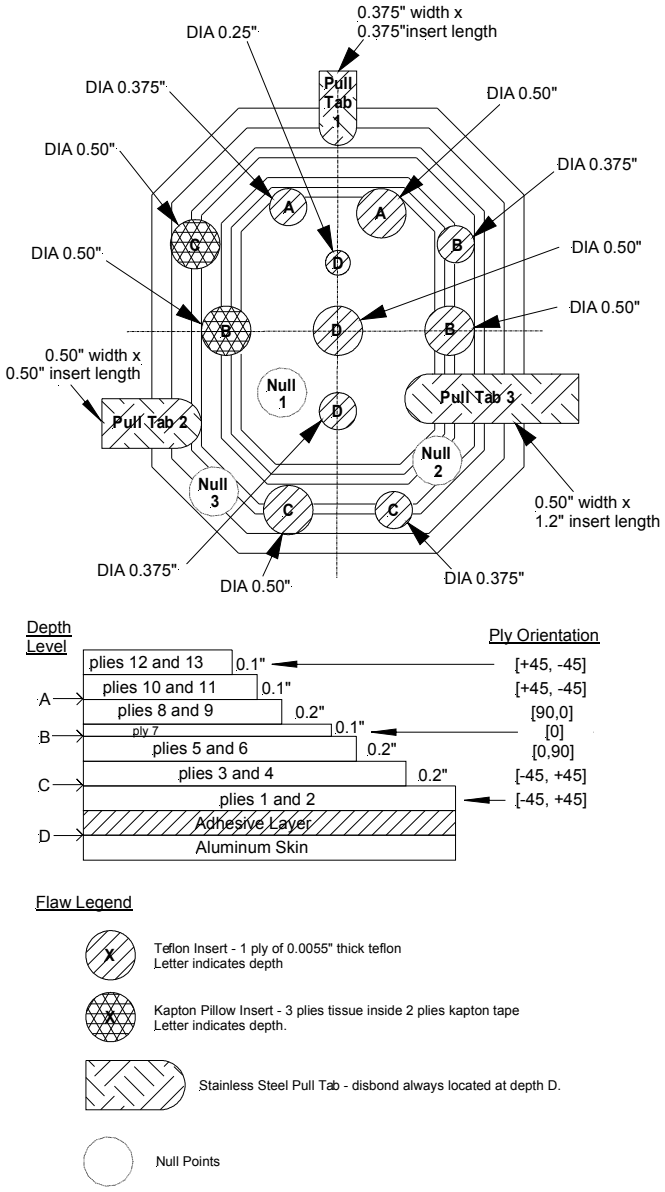

Figure 114: Configuration of Boron-Epoxy Composite Doubler NDI Reference Standard to Support Ultrasonic Inspections

6.4.3 Thermographic Inspection

Thermography is a nondestructive inspection method that uses thermal gradients to analyze physical characteristics of a structure, such as internal defects. This is done by converting a thermal gradient into a visible image using a thermally sensitive detector such as an infrared camera. The temperature distribution on a structure can be measured optically by the radiation that it produces at infrared wavelengths. Many defects affect the thermal properties of materials. Examples are corrosion, disbonds, cracks, impact damage, panel thinning, and fluid ingress into

composite or honeycomb materials. By the judicious application of external heat sources, these defects can be detected by an appropriate infrared survey. In this composite doubler study, a turn-key thermography inspection system, the Thermal Wave Imager (TWI), was used to assess the merits of thermography to detect disbonds and delaminations in composite doublers.

Thermal wave imaging is accomplished using high-power flash lamps, an infrared (IR) video camera, and image processing hardware and software, all of which are controlled by a personal computer. The flashlamps put out a short, high-power pulse of light, which raises the surface temperature of the structure approximately ten degrees when it is absorbed by the surface. This temperature pulse propagates into the material as a thermal wave and gets reflected by any defects which may be present in the material. The resulting temperature distribution is then recorded by the IR camera and displayed on the computer monitor. In practice, the computer actually obtains several images at progressively later times after each flash. This method is particularly useful for imaging and determining the depths of disbonds and delaminations in Boron-Epoxy repair doublers. A photograph of the Thermal Wave Imaging System being applied to an aircraft inspection is shown in Figure 115.

Results from Composite Doubler Inspections - Following are results obtained from Thermal Wave Imaging inspections on composite doubler installations which contain engineered flaws. Figure 116 shows a schematic of a 13 ply composite doubler installed on a metal fatigue coupon. The schematic shows the disbond and crack flaws that were placed in the parent plate and composite doubler installation. The series of images produced at different times during the TWI inspection of this test specimen are shown in Figure 117.

The early time images following the flash clearly resolve the ply drop-off at the edges of composite patch. Beginning at around 0.68 sec, intentionally placed disbonds between the patch and the metal at the left and right edges (where the patch is thinnest) begin to appear. As time progresses, these disbonds begin to show in thicker and thicker layers of the patch. Between 4 and 8 seconds it is possible to see the circular disbond which was implanted over the crack tip and a "tail" extending downward along the induced fatigue crack. The circular disbond is located 13 plies deep in the doubler installation. The disbond tail is also located between the 13 ply doubler and the skin and is associated with a cohesive fracture of the adhesive layer immediately adjacent to the crack growth.

TWI was applied to another Boron-Epoxy doubler which was installed on a DC-9 fuselage section in the Sandia Labs' FAA Airworthiness Assurance hangar. Figure 118 shows a schematic of the 10 ply doubler highlighting the size, shape, and location of the embedded flaws. The resultant sequence of images produced by a TWI inspection is shown in Figure 119. The features seen at early times are defects closest to the outside surface of the patch (note appearance of flaws #1 and #2 in the first few frames). The disbonds, located at the base of the doubler, and the deeper delaminations appear in the later frames corresponding to their delayed effect on the thermal field. All six embedded flaws were identified in the TWI images and flaws smaller than 0.5" in diameter could be detected.

(a) Close-Up View of TWI Equipment

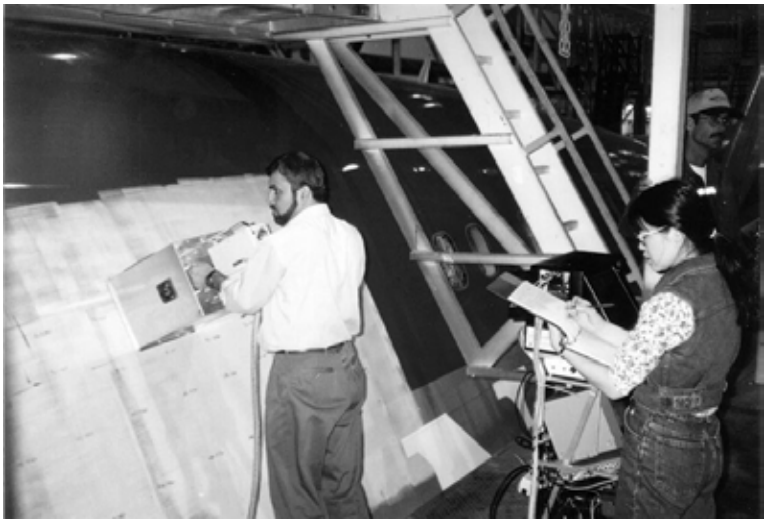

(b) Application of Thermography on 747 Aircraft

Figure 115: Thermal Wave Imaging System Inspecting an Aircraft

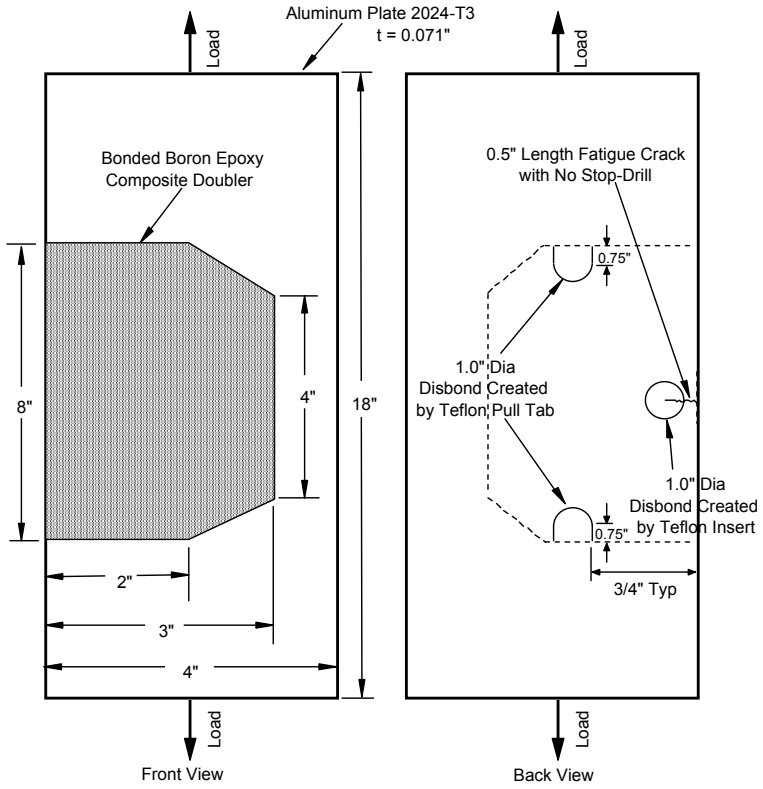

Figure 116: Composite Doubler Damage Tolerance Test Coupon with Engineered Flaws

The advantages of the thermography inspection method include: 1) thermography can be performed without physical contact with the surface, 2) single images can include relatively large areas (1-2 ft^2) allowing for rapid inspections of large surface areas, and 3) two-dimensional image of the inspected surface helps the operator visualize the location and extent of any defect. The primary disadvantages of thermography are: 1) it is often necessary to apply a high-emissivity coating during inspections to obtain an acceptable image; steps have been taken to minimize the labor time associated with this task, 2) damage to layers deep within a structure is more difficult to detect than damage in surface layers because the larger mass of material tends to dissipate the applied heat energy; preliminary experiments have shown that TWI can inspect doublers up to 40 or 50 plies (0.25" to 0.30") thick.

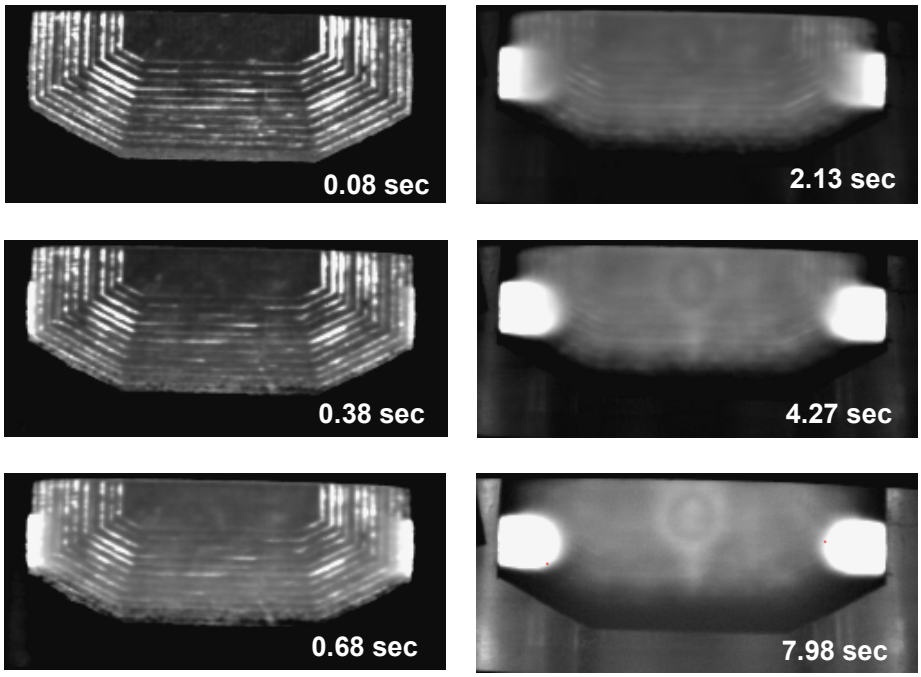

Figure 117: Sequence of Thermal Wave Images of Composite Doubler Specimen

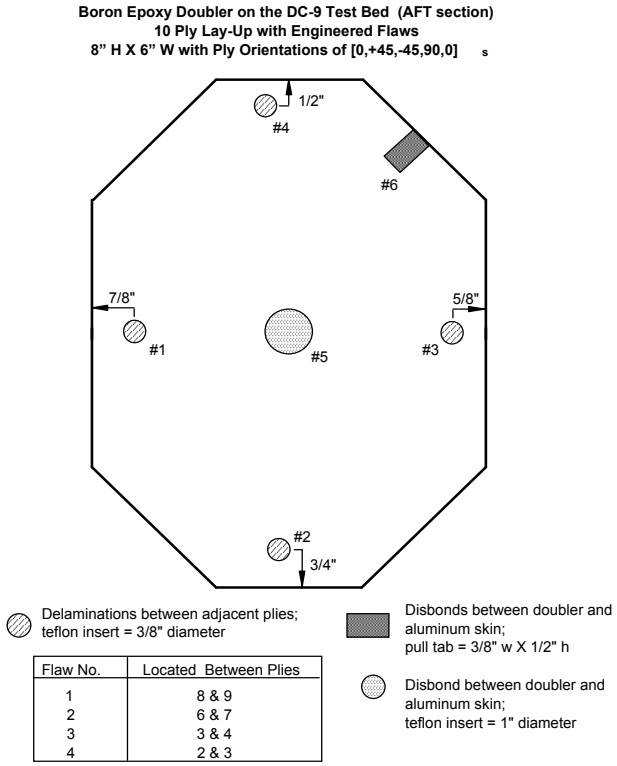

Flaw No.	Located Between Plies
1	8 & 9
2	6 & 7
3	3 & 4
4	2 & 3

Figure 118: Composite Doubler Installation on DC-9 Testbed

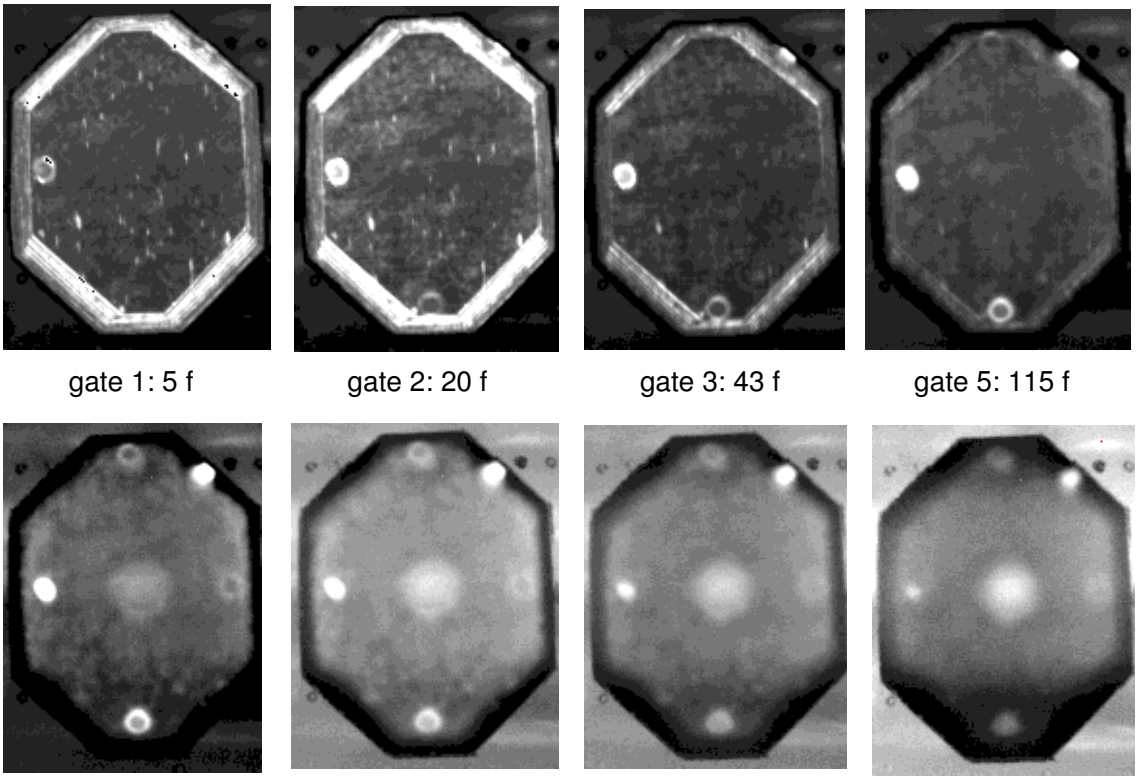

Figure 119: Sequence of Thermal Wave Images from DC-9 Composite Doubler Inspection

7.0 Structural Health Monitoring Using In-Situ Sensors

7.1 Introduction

Nondestructive Inspection (NDI) – examination of a material to determine geometry, damage, or composition by using technology that does not affect its future usefulness.

- Involves a high degree of human interaction
- Local, focused inspections
- Requires access to area of interest
- Time-based monitoring - applied at predetermined intervals
- Portable and applied to numerous areas.

Structural Health Monitoring (SHM) – "Smart Structures;" use of NDI principles coupled with in-situ sensing to allow for rapid, remote, and even real-time condition assessments; goal is to reduce operational costs and increase life of structures.

- Allows for greater vigilance in key areas – address damage tolerance needs
- Overcomes accessibility limitations, complex geometries, depth of hidden damage
- Eliminates costly and potentially damaging disassembly
- Minimizes human factors with automated sensor deployment and data analysis
- Supports adoption of condition-based maintenance.

Reliable, structural health monitoring systems can automatically process real-time data, assess structural condition, and signal the need for human intervention. Prevention of unexpected flaw growth and structural failure could be improved if on-board health monitoring systems exist that could continuously assess structural integrity. Reliable, structural health monitoring systems can automatically process real-time data, assess structural condition, and signal the need for human intervention. Such systems would be able to detect incipient damage before catastrophic failures occur. The replacement of our present-day manual inspections with automatic health monitoring would substantially reduce the associated life-cycle costs. Structural Health Monitoring (SHM) systems using distributed sensor networks will allow for condition-based maintenance practices to be substituted for the current time-based maintenance approach. Other advantages of on-board distributed sensor systems are that they can eliminate costly, and potentially damaging, disassembly, improve sensitivity by producing optimum placement of sensors with minimized human factors concerns in deployment, and decrease maintenance costs by eliminating more time-consuming manual inspections. This chapter focuses on developments in mountable and embedded sensors for monitoring composite structures (composite doublers) and how they can be integrated into such a Structural Health Monitoring (SHM) system to guide condition-based maintenance activities.

Whether the sensor network is hardwired to an accessible location within the aircraft or monitored in a remote, wireless fashion, the sensors can be interrogated easily and often, even in a real-time mode. It is anticipated that the sensors will most likely be examined at discrete intervals; probably at normal maintenance checks. The important item to note is that the ease of monitoring an entire network of distributed sensors means that structural health assessments can occur more often, allowing operators to be even more vigilant with respect to flaw onset. Figure

120 depicts a sensor network deployed on an aircraft to monitor critical sites over the entire structure. Specific SHM methods and sensors, that can address the inspections needs of composite doubler repairs, were investigated in this study. Following is a description of the SHM approaches and their ability to monitor composite repairs in the field.

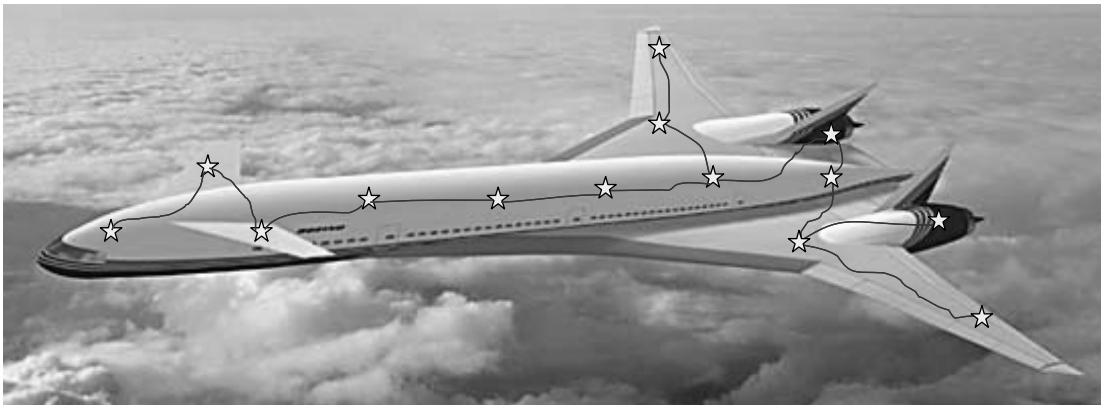

Figure 120: Depiction of Distributed Network of Sensors to Monitor Structural Health

7.2 Piezoelectric Transducers (PZT)

Prime candidates for sensors based on active-material principles utilize thin piezoelectric wafers of 0.125”-0.25” diameter with thicknesses of 0.010” - 0.030”. They can be easily attached to existing aging structures without changing the local and global structural dynamics [40-42]. PZT sensors can also be embedded inside composite structures to closely monitor for internal flaws. These sensors can act as both transmitters and receptors. As transmitters, piezoelectric sensors generate elastic waves in the surrounding material. As receptors, they receive elastic waves and transform them into electric signals. It is conceivable to imagine arrays of active-sensors, in which each element would take, in turn, the role of transmitter and receptor, and thus scan large structural areas using ultrasonic waves. The structural interrogation strategies using active piezoelectric sensors are two fold:

(a) For local area detection, the electro-mechanical (E/M) impedance method is applied to detect changes in the point wise structural impedance resulting from the presence and propagation of structural damage.
(b) For large area detection, wave propagation techniques using Lamb and Love waves methods are used to identify zones in the monitored area that have undergone changes in their structural integrity.

In the high-frequency E/M impedance approach, pattern recognition methods are used to compare impedance signatures taken at various time intervals and to identify damage presence and progression from the change in these signatures. In the Lamb/Love waves approach, the acousto-ultrasonic methods identifying changes in transmission velocity, phase, and additional reflections generated from the damage site are used. Both approaches can benefit from the addition of artificial intelligence neural network algorithms that can extract damage features based on a learning process.

Mountable PZT Networks and Lamb Wave Interrogation Methods - This structural health monitoring approach uses a built-in network of piezoelectric transducers embedded in a think dielectric carrier film. The SHM system included the PZT network connected to portable, diagnostic hardware and software developed by Acellent Technologies, Inc. The system performs in-situ monitoring, data collection, signal processing, and real-time data interpretation to produce a two-dimensional image of the structure being interrogated. The Acellent software instructs the actuators to generate pre-selected diagnostic signals and transmit them to neighboring sensors. Multiple diagnostic wave types can be generated including 3-peak, 5-peak, and 10-peak narrow band frequency waveforms, chirp, random, and user defined excitations. The software links each sensor with its neighbors to form a web, or network, covering the structure. The system then collects the total set of responses from each of the sensor sets as each PZT takes its turn as the actuator. Changes in the Lamb waves generated within the structure are used in concert with triangulation methods to detect the presence of structural anomalies and to determine the size and location of the flaws.

Damage Identification through Elastic Wave Propagation - The wave propagation approach uses the pitch-catch method for detecting damage in a structure. Acousto-ultrasonic methods are used to identify changes in wave transmission. Figure 121 shows some of the wave motion from sensors (1) and (9) when they are used as the source of excitation for the structure. The mechanical vibration is introduced into the structure by the PZT element and travels by wave motion through the test piece at the velocity of sound, which depends on the material. If the pulses encounter a reflecting surface, some or all of the energy is reflected and monitored by adjacent PZT sensors in the network. The reflected beam, or echo, can be created by any normal (e.g. in multi-layered structures) or abnormal (flaw) interface. Figure 121 highlights the interaction of the UT waves with a flaw within the structure. The degree of reflection depends largely on the physical state of the materials forming the interface. Cracks, delaminations, shrinkage cavities, pores, disbonds, and other discontinuities that produce reflective interfaces can be detected. Complete reflection, partial reflection, scattering, or other detectable effects on the ultrasonic waves can be used as the basis for flaw detection.

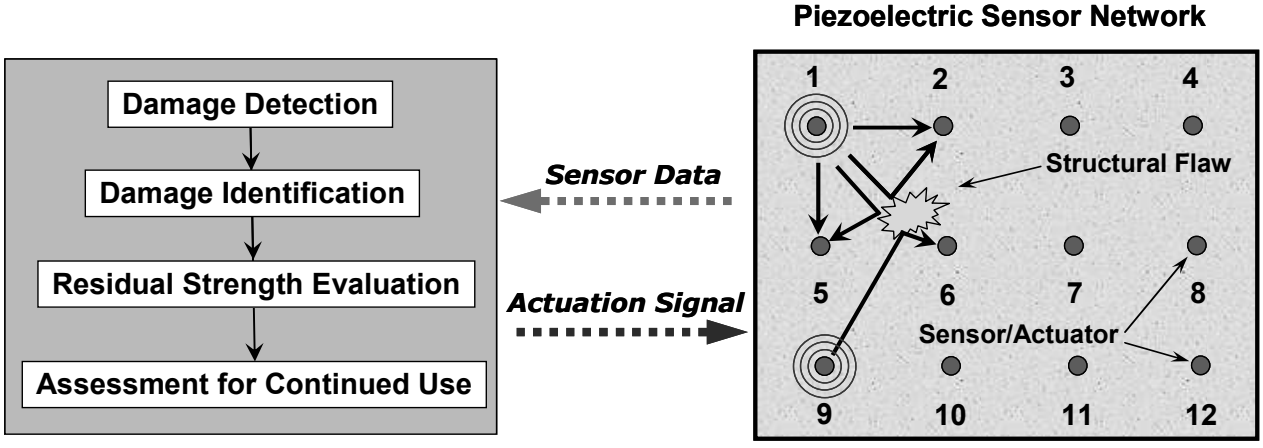

Figure 121: Flaw Detection Using the Wave Propagation Method

Validation Testing of PZT Sensor Network - In this test series, the network of PZT sensors was deployed to assess bonded joints and crack growth in a composite doubler repair installation. Figure 122 shows a schematic and photos of the Boron-Epoxy laminate repair on a metal parent structure along with the set of PZTs distributed over the structure to be monitored. Note that the network of sensors/actuators is embedded in a custom polyamide film to allow for accurate placement of the network and eliminating the need for each sensor to be installed individually. The test specimen, containing engineered disbonds and a central crack, was subjected to constant-amplitude fatigue loads with maximum stresses in excess of 80% of yield levels.

Similar to conventional ultrasonic testing, the PZT data analysis can include one or more of the following measurements: time of wave transit (or delay), path length, frequency, phase angle, amplitude, and angle of wave deflection (reflection and refraction). In this test series, the pitch-catch method studied the transmission of sound waves as they traveled from each actuator to all other receiving sensors. The sum total of received beams were then analyzed to define the presence and location of flaws. In order to optimize flaw detection, a series of excitation frequencies were used: 50 KHz, 200 KHz, 350 KHz, and 500 KHz. Overall test results revealed that disbond flaws were most strongly detected with the lower, 50 KHz excitation while the crack growth was monitored best with the highest, 500 KHz excitation. Figure 123 shows raw PZT response data produced during the Lamb wave interrogation method. Signal attenuations, corresponding to disbonds between the laminate and parent skin, are apparent. When all of the signals are analyzed with the Acellent imaging software and flaw locations are determined by using the time base and triangulation methods, a two dimensional image of the disbond flaws was produced. Figure 124 shows the engineered disbonds in the test specimen along with the image produced by the PZT sensor network. Note that both disbond flaws were clearly imaged even though one is a weak bond produced by a mold release agent and one is a complete disbond produced by a Teflon insert.

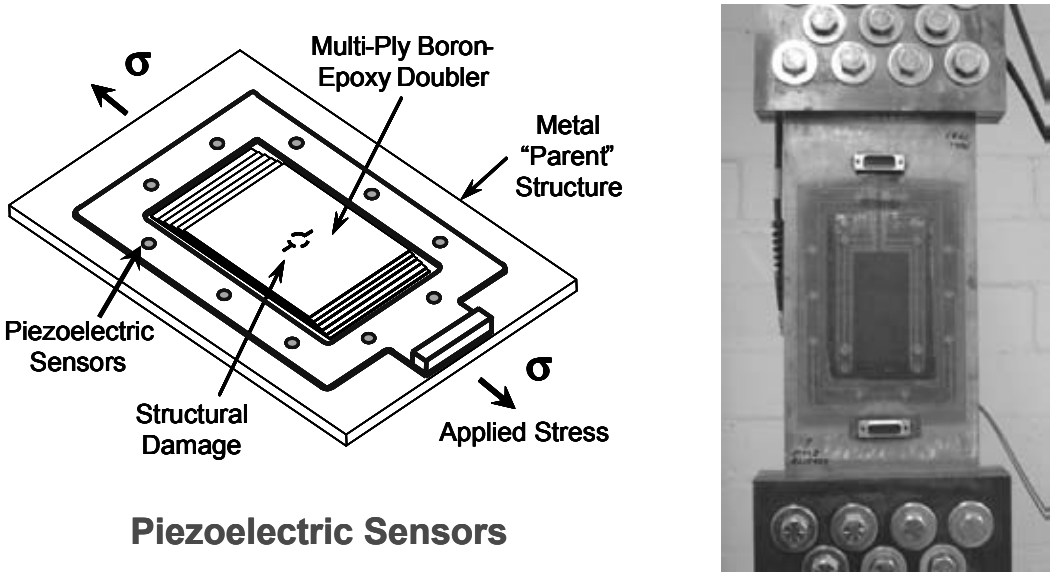

Figure 122: Set of Piezoelectric Sensors Used to Monitor Crack Growth and Disbonds in a Composite Doubler Bonded to a Metal Plate

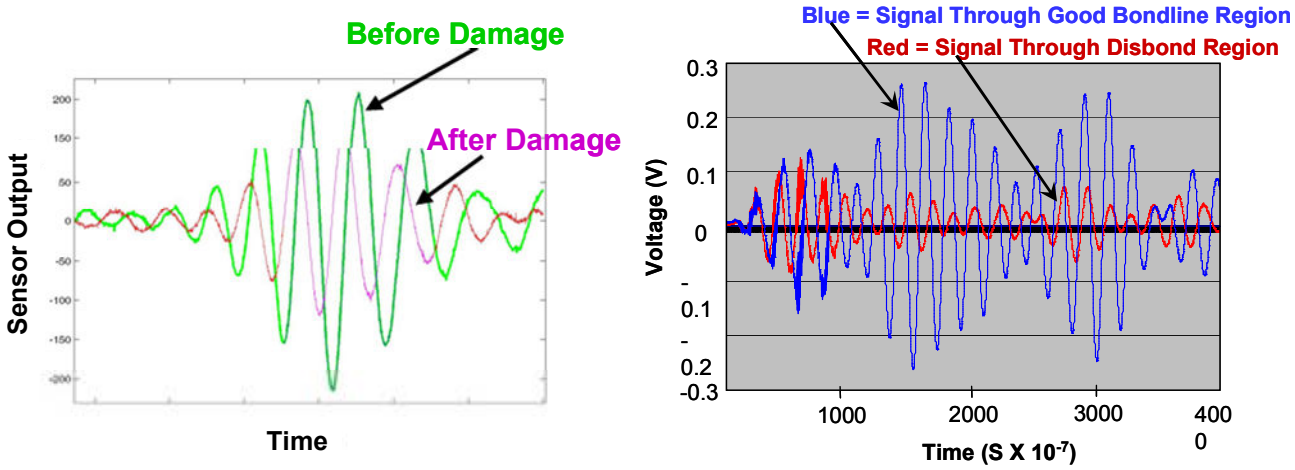

Figure 123: Sample Signals Observed by PZTs During 50 KHz Lamb Wave Interrogation Showing the Attenuation Corresponding to Disbonds in the Structure

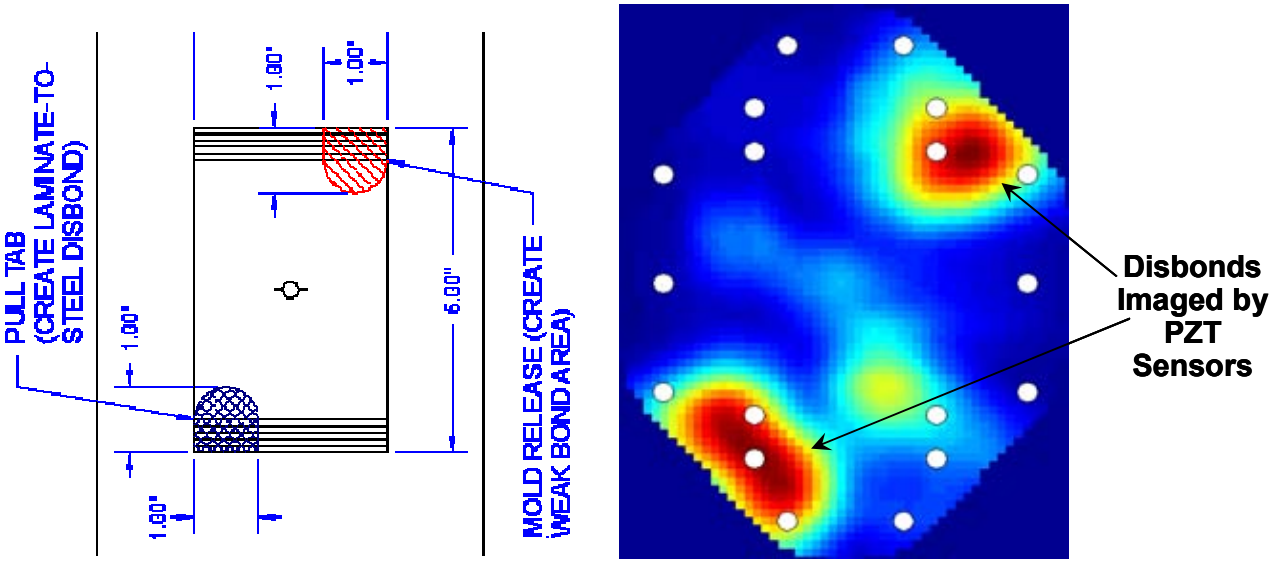

Figure 124: Color-Coded Image of Disbond Flaws Produced by the PZT Sensor Network

Crack detection and growth was monitored using the same approach. PZT data was acquired at discrete intervals during the crack growth process. In addition, eddy current and microscopic inspections were conducted to measure the crack lengths at each cycle count. Figure 125 shows PZT response signals before and after crack growth occurred into the sensor path. A set of images produced by the PZT network are shown in Figure 126. The crack growth (two fatigue cracks emanating from a central hole) can be clearly seen. The PZT crack growth data was analyzed further to produce crack length predictions. The Acellent software contains an algorithm that allows for system learning. After inputting several crack lengths to match with the PZT data at discrete fatigue intervals, it was possible for the system to predict all subsequent crack lengths using the PZT data alone. Table 10 compares the crack lengths predicted by the PZT sensor network with the crack lengths determined from eddy current and microscopic measurements. The PZT predictions were all within 5% of the actual crack lengths for data taken at max load (34 kips) and, for the most part, within 10% of actual values for PZT data taken in the unloaded condition.

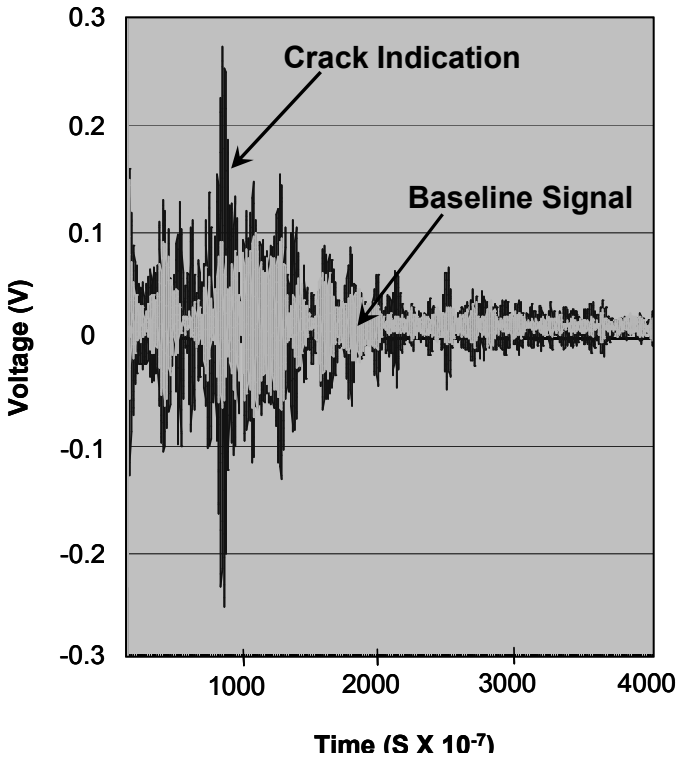

Figure 125: Sample PZT Signals Showing the Indication of a Fatigue Crack with a 500KHz Excitation

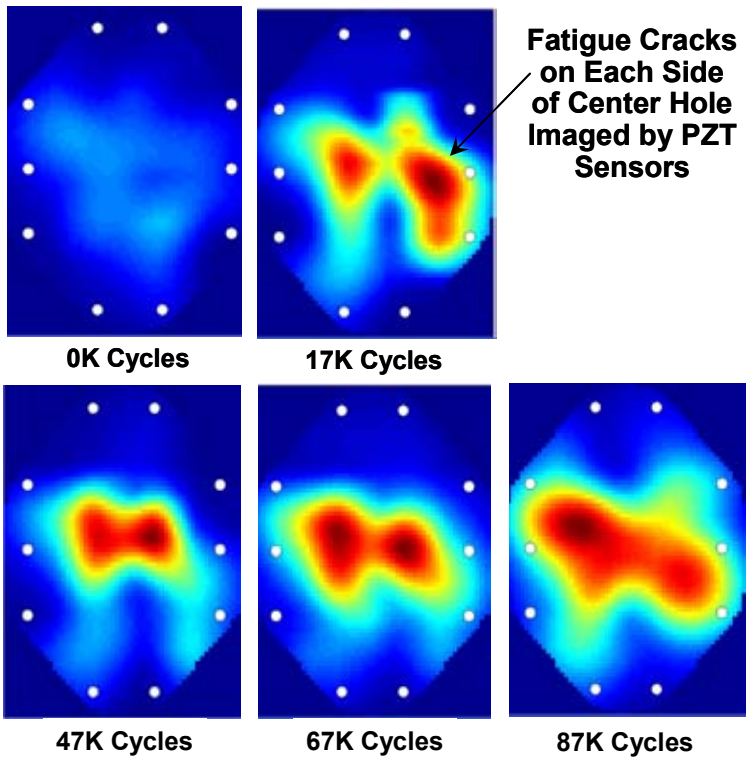

Figure 126: Color-Coded PZT Images Showing Crack Growth

Composite Doubler with PZT Health Monitoring			
Fatigue Cycles	**Measured Total Crack Length**	**Estimated Crack Length from PZT Sensor Data (0 lbs. load)**	**Estimated Crack Length from PZT Sensor Data (34 kips load)**
Specimen 1 - Unflawed Composite Doubler			
0	0.00		
26,218	0.32	PZT Learning Data	PZT Learning Data
47,000	0.70	PZT Learning Data	PZT Learning Data
67,000	1.50	1.274	1.385
87,000	2.44	1.956	2.367
Specimen 2 - Composite Doubler with Disbond Flaws			
0	0.00		
19252	0.16	PZT Learning Data	PZT Learning Data
29274	0.32	PZT Learning Data	PZT Learning Data
38064	0.48	PZT Learning Data	PZT Learning Data
51576	0.80	PZT Learning Data	PZT Learning Data
60438	1.08	0.981	1.099
66439	1.34	1.35	1.349
76444	1.76	1.567	1.762
82446	2.02	1.909	2.08

Table 10: Comparison of Crack Lengths Predicted by PZT Sensors with Actual Crack Lengths Measured Using Eddy Current and Microscopic Methods

7.3 Fiber Optic Sensors

Rapid growth in the optoelectronics and telecommunications industries has resulted in the evolution of highly-sensitive fiber optic sensors. Fiber optic (FO) sensors have been developed for a wide variety of applications including the measurement of rotation, acceleration, vibration, strain, temperature, pressure, electric and magnetic fields, moisture, and humidity. Fiber optic sensors are light weight, low profile (typically 145 microns in diameter with a polyimide coating), are corrosion resistant, and multiple sensors are easily multiplexed into a single fiber. These factors make them ideal for embedding in or surface mounting on composite and metallic structures without affecting structural performance. Other advantages of fiber optic sensors include their high sensitivity, wide bandwidth, EMI resistance, low power requirements, and environmental ruggedness. Fiber optic sensors can also be configured to monitor crack growth and corrosion in civil and aerospace structures [43-45]. Omni-directional fiber optic sensors can be used to measure large strains (up to 150% strain), small displacements (10 μm range), and crack growth in any material. The major disadvantages include their high cost, mechanical frailty (during handling stage) and unfamiliarity to the end user. The introduction of low-cost laser diodes, the alternative use of LEDs as light sources, and the development of inexpensive, single mode optical fibers have greatly reduced the costs associated with deploying FO sensors.

Information about the environment to which a fiber optic is exposed can be inferred by analyzing the guided light transmitted through the optical filaments. In this approach the entire length of the fiber acts as a continuous sensor. The fiber can be mounted in a serpentine path or fiber optic tentacles can be created to provide full coverage over a large area of concern. The presence of a crack can be determined by monitoring changes in the magnitude and phase of the returned light in the fiber. Optical time domain reflectometry can then be applied to determine the exact location of the crack. Fiber optic sensors can also aid in the detection of structural corrosion. Sacrificial corrosion sensors can be mounted on the end face of the fiber optic. These sensors are designed to corrode at the same rate as the parent material to which they are mounted. Degradation in these sensors, and thus the parent structure, can be calibrated to changes in the intensity of the reflected light within the fiber optics. Further refinements in the packaging, attachment and monitoring hardware are needed to allow fiber optic crack and corrosion sensors to be rapidly deployed in structural health monitoring applications.

Optical Fibers as Uniaxial Sensors - Fiber optics work on the principle that light can be guided by an interface between materials of different indices of refraction. The components of a fiber optic line consist of a core with a higher index of refraction surrounded by a cladding with a lower index of refraction. The fiber is made mostly of silicone dioxide (SiO_2), with the core containing germanium dopants. The dopants in the core create a differential in the index of refraction between the core and the cladding. These differences in the index of refraction in the core and the cladding cause light to be guided through the core. To better protect the fiber, a Polyimide coating around the cladding is used. Fiber optic sensors (core and cladding) are 80 μm - 120μm in diameter which is about the size of a human hair. With the protective coating added, the fiber is approximately 125 - 150 μm in diameter.

If a short wavelength light is used to illuminate the core region of the fiber, the core material is rearranged to produce an increase in the index of refraction in that region. A quartz phase mask can be used, as in Figure 127, to image an interference pattern through the side of the optical fiber. This results in a localized periodic index of refraction modulation along the length of the optical fiber (sensor grating). A typical sensor grating consists of thousands of grating lines with approximately 0.5 micron spacing. The mask shown in Figure 127 controls the laser exposure to induce a customized interference pattern on the optical core. This fiber grating can then be used to measure strain since axial stretching or compression of the fiber will change the grating period and, thus, the peak wavelength reflected back from the sensor. When the fiber grating is illuminated by a broadband light source or a tunable laser source the fiber grating will reflect a narrow band of light corresponding to its period. The reflected light will be centered in a narrow band at the Bragg wavelength according to the relationship:

$$\lambda_B = 2n_e\Lambda \qquad (16)$$

where n_e is the effective index of refraction at the core of the fiber and Λ is the grating line spacing. Measuring the shift in wavelength of light reflected back from the grating can thus be used to determine strain or temperature changes. If strain is applied to the Fiber Bragg Grating, the resonant reflected wavelength λ_B will shift by an amount $\Delta\lambda_B$ given by:

$$\Delta\lambda_B / \lambda_B = (1-P_\varepsilon)\varepsilon \qquad (17)$$

where P_ε is the photoelestic constant for the fiber core. By tracking $\Delta\lambda_B$ it is possible to accurately measure strain levels in the structure.

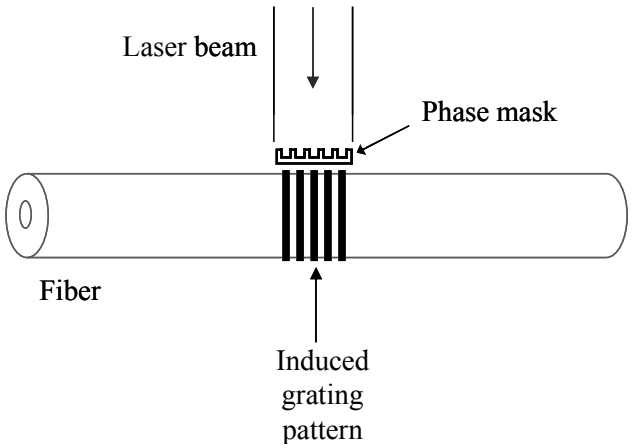

Figure 127: Process to Install a Fiber Grating onto an Optical Fiber Using a Short Wavelength Laser in Combination with a Phase Mask

Multi-Parameter Fiber Grating Strain Sensors – A method of generating multiple fiber gratings capable of measuring multi-directional strain is to write a fiber grating into a special type of fiber called polarization maintaining or birefringent fiber [45-46]. The birefringence (difference in index in refraction depending on the polarization state of light) in the fiber is created with a built

in residual stress introduced during the fiber draw (manufacture). This stress results in a slight change in the index of refraction along two mutually orthogonal directions (termed the polarization axes). This creates two spectral peaks for each optical grating written into the optical fiber, one associated with each polarization axis. By measuring the wavelength of these peaks it is possible to generate two equations in two unknowns effectively allowing two environmental parameters (in this case, two strain tensors) to be monitored.

For this type of fiber grating strain sensor, a single fiber grating results in two distinct spectral peaks. These peaks correspond to each of the polarization axes of the polarization preserving fiber, which differ slightly in index of refraction. Two spectral reflection peaks, corresponding to the effective fiber gratings along each birefringent (polarization) axis, will move apart or together uniformly providing a means to measure transverse strain. This results in the two major spectral peaks moving apart or together. Each of the two spectral peaks maintains its original unloaded profile. Figure 128 shows how changes in the spectral output from birefringent fiber gratings can be used to measure both axial and transverse strain. When the fiber is loaded transversely, the relative index of refraction of the polarization axes of the fiber changes and the net result is that the difference in wavelength between the spectral peaks changes as well (peak-to-peak separation changes). When the fiber is strained axially, the fiber elongates or compresses, changing the fiber grating spectral period. As a result the output spectrum shifts to longer or shorter wavelengths, respectively.

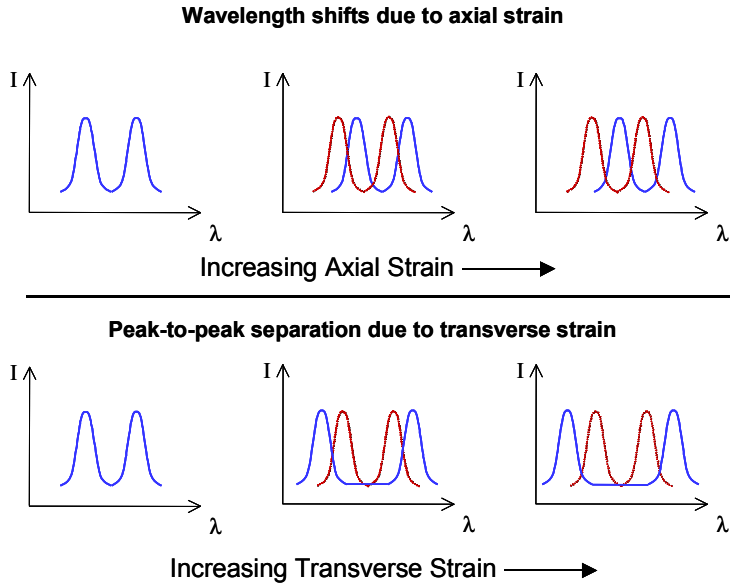

Figure 128: Change in Spectral Reflection of a Multi-Axis Fiber Grating Strain Sensor When Subjected to Axial and Transverse Loads

Measuring the Complex Grating Reflection Profile with a Scanning Laser Interferometer – Traditionally, fiber grating strain measurements are made with high reflectivity fiber gratings, which allow detailed information about the spectral peaks to be accessed directly via illuminating the fiber gratings with broadband light sources and then recording the reflected grating spectrum

with an optical spectrum analyzer. By peak-fitting the spectrum and applying wavelength-to-strain conversion coefficients it is possible to obtain strain values. Multiplexing large numbers of high reflectivity fiber gratings can be limited by shading effects wherein gratings with nearby wavelengths are permitted to operate in the same wavelength space such that their spectra may become confused.

An approach to conducting high density multiplexing while avoiding shading effects is to use Optical Frequency Domain Reflectometry (OFDR) to characterize low reflectivity fiber grating strain sensors [43, 46]. This method employs a tunable light that is used to scan a low-reflectivity fiber grating. A Fourier transform of the detector signals will give the locations of each fiber-grating sensor. With the knowledge of the sensor locations, the detector signal can be passed through narrow band frequency filters in order to separate out spectral information from individual grating sensors, even if the sensors occupy the same wavelength space. The OFDR approach was used in the tests described below to interrogate the FBG sensors and calculate the axial and transverse strains as a function of grating position along the fiber.

Use of Fiber Optic Strain Measurements to Monitor Cracks and Disbonds - The sensors consisted of long chirped Fiber Bragg gratings (FBG) in polarization maintaining fiber. For chirped gratings, the line width function varies linearly with grating length. Thus, for a chirped grating, the wavelength of light which is reflected from the grating is a function of grating position. This allows the FBG to have an extremely long gage length such that strain gradients over long distances of the fiber can be measured. A scanning laser interferometer was used to readout the grating period as a function of grating position. Both strain along the fiber axis and the differential transverse strain could be deduced from the grating period.

The test specimens, similar to the ones shown in Figure 122 and 124, were cycled in tension to grow cracks and disbonds while the sensors were monitored. To implant disbonds, a Teflon insert was placed in the bond line at one location and a mold release agent was applied in a controlled region to produce a weak bond in another location. Figure 129 shows the overall design of the instrumented test specimen and placement of the FBG sensors within the bondline between the composite laminate repair and the parent metal structure. The objectives of the tests were to: 1) show that these sensors could be successfully installed into the specimen bond line and survive the cure process, 2) demonstrate that the distributed strain profile along the gratings could be measured, and 3) prove that the distributed axial and transverse differential strain profiles could be used to track the presence and location of flaws. The test article was subjected to extreme fatigue loads (peak loads = 80% of yield) to rapidly grow fatigue cracks from notches placed in each side of a center hole in the metal.

A series of 110 mm long FBG were embedded into the bond lines between the metal panel and the boron fiber composite doublers. Gratings A and C were routed between the plate and adhesive across the doubler end (and across the Teflon insert), while gratings B and D were routed in a parabolic path roughly parallel to the long axis of the doubler. The optical fiber was taped down to the steel surface prior to the application of the adhesive and the doubler and survived the high temperature (225^{o}F) and vacuum bag process used to bond the composite doubler to the metal plate. The gratings were purposely oriented so that the polarization axes of

the fiber were oriented at 45 degrees to the plane of the metal panel as shown in Figure 130. This orientation gave the sensor sensitivity to changes in shear in the bond line between the doubler and the panel.

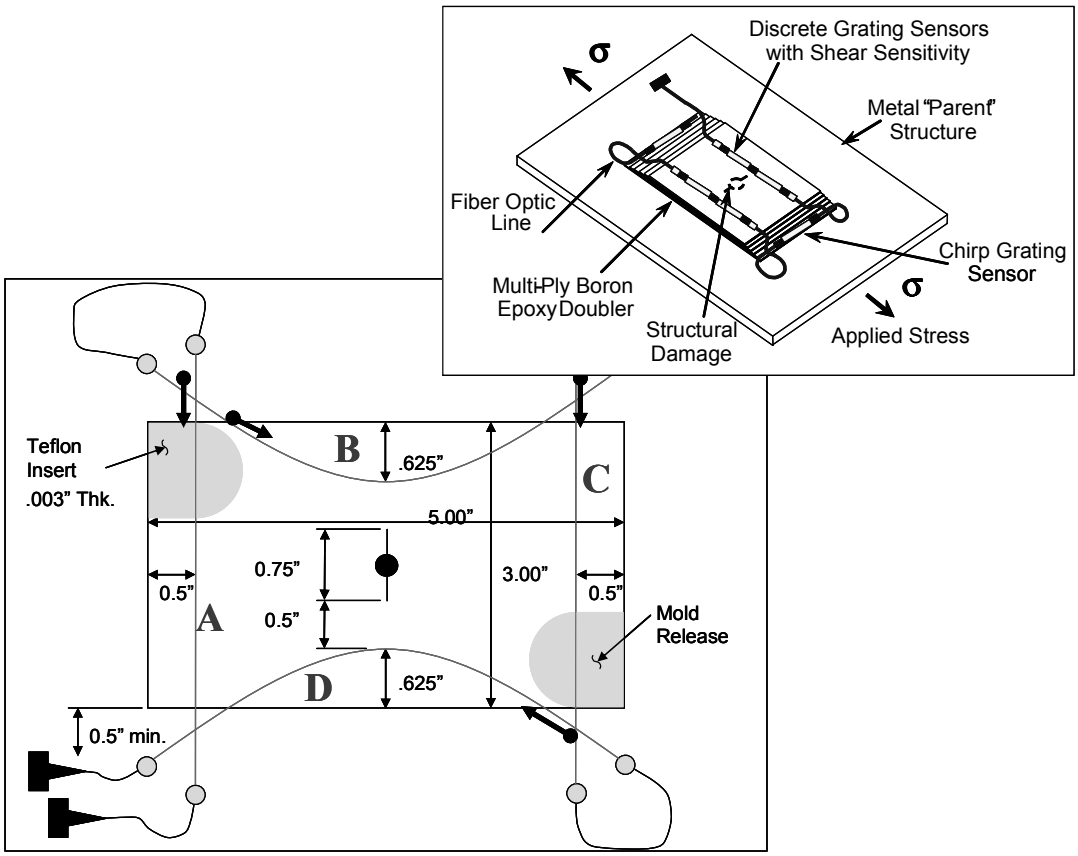

Figure 129: Fiber Bragg Grating Sensor Layout and Engineered Flaws in Bonded Composite Repair Test Specimens

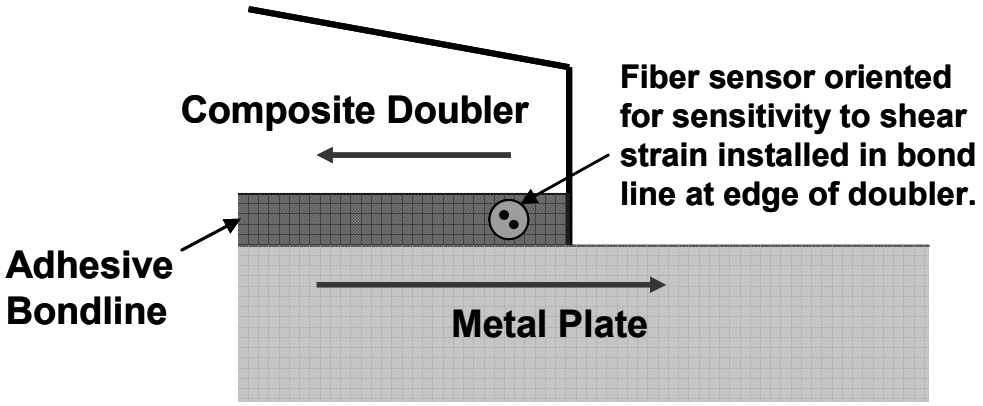

Figure 130: FBG Sensor Embedded in Adhesive Layer with Polarization Axis of Grating A Oriented for Maximum Sensitivity to Bondline Shear Strain

Figure 131 shows a close-up of the FBG sensors, and associated end connectors, as they enter and exit the bondline of the test specimen. Typical data acquisition equipment used to monitor the FBG sensors is also pictured. During the course of the structural tests, the cyclic loading was periodically paused to allow the grating sensors to be interrogated. At these intervals, crack lengths were measured using eddy current and optical magnification methods. The presence of disbonds was monitored using hand-held ultrasonic pulse-echo inspections. Strain gage readings were acquired for comparison to FO strain measurements and to monitor the overall performance of the composite doubler repair.

Figure 131: Fiber Optic Sensors in Adhesive Bondline and FO Monitoring Equipment

Figure 132 contains sample results from the FBG sensors (sensors B & D) as they monitored fatigue crack growth. Both plots show the strain distribution along the sensors as a crack tip approaches. The plot on the left shows the strain levels produced by the crack when there was no load on test specimen 1. Specimen 1 contained a central crack but no disbond flaws. Note that the strain levels are close to 0 με in regions away from the cracks in the center of the plate. The plot on the right shows the strain levels along the axis of sensor B when specimen 2 was loaded to its maximum tension load of 34,000 lbs. A similar strain profile is observed, however, the strain levels produced away from the center cracks is now 1000 με. Normal stress-strain calculations determined that the maximum strain in the plate at 34,000 lbs. load was 1000 με. In addition, strain gage readings in the uniform strain region away from the cracks were between 950 με and 1020 με. Data such as this demonstrated the accuracy of the strain levels obtained from the FBG sensors.

As the cycle number increased and the crack propagated further out from the center of the panel, the strain near the center position of the grating started to rise dramatically. At 63,000 and 67,000 cycles the strain at the 45 mm point in Sensor B (right side plot) finally falls to 0 as the crack passes through the fiber and relieves the strain in that portion of the sensor. Although the FBG sensors were 0.5” or further away from the crack tip, significant and localized strain changes were observed near the center of the sensors with less than 0.100” crack growth.

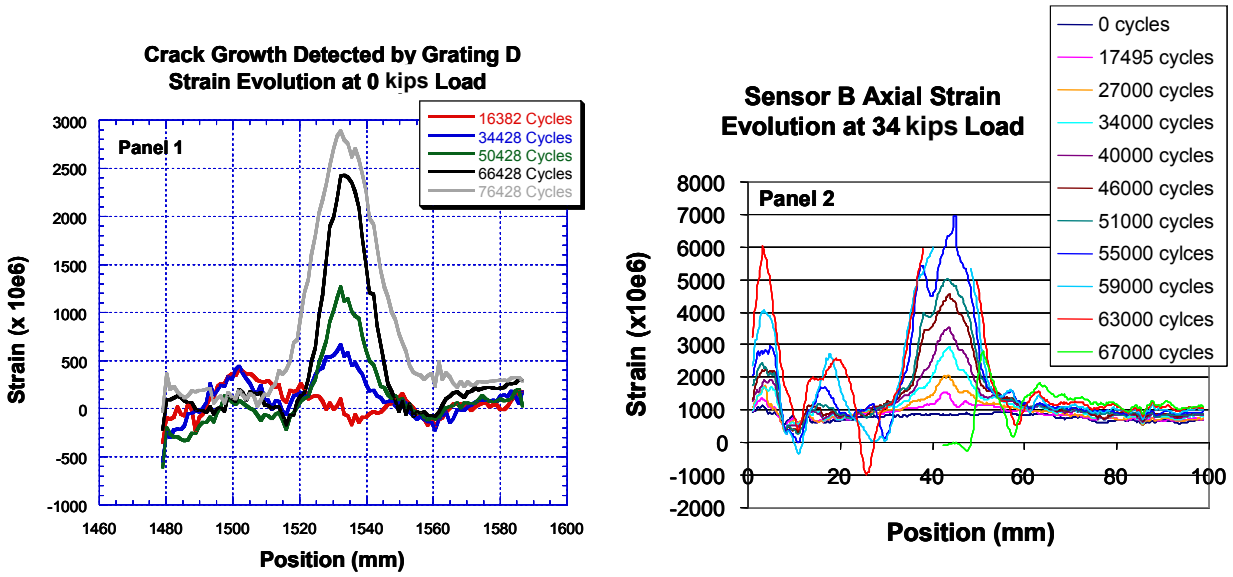

Figure 132: Strain Distribution Along Sensors *B* and *D* Determine Strain Levels in the Specimen and Indicate Crack Growth During Fatigue Testing

Sensors A and C were used to interrogate the bondline along the edge of the test specimens. As shown in Figure 129, these edges contain the tapered portion of the doubler and are critical, high shear strain areas because the majority of the load transfer into the composite repair occurs here. As a result, it is important to monitor the taper region for disbonds. Since the fibers containing sensors A and C run across the width of the bondline (perpendicular to the direction of load), the shear strain component provided the best measure for identifying disbonds. Figure 133 shows the shear strain distribution along sensor A while the specimen was under load.

Note the 1000 με level across most of the taper region (from 1185 mm to 1235 mm where the bond line is intact). As observed in the sensor B data above, the maximum strain of 1000 με in the direction of the load is confirmed by sensor A. However, in the region of the disbond produced by the Teflon insert, the shear strains are almost 0 indicating the presence of an extreme strain relief (i.e. disbond eliminates load transfer into doubler in this region). This plot indicates that the disbond extends from the 1160 mm position to the 1185 mm position correctly predicting the size of the one inch (25 mm) Teflon insert.

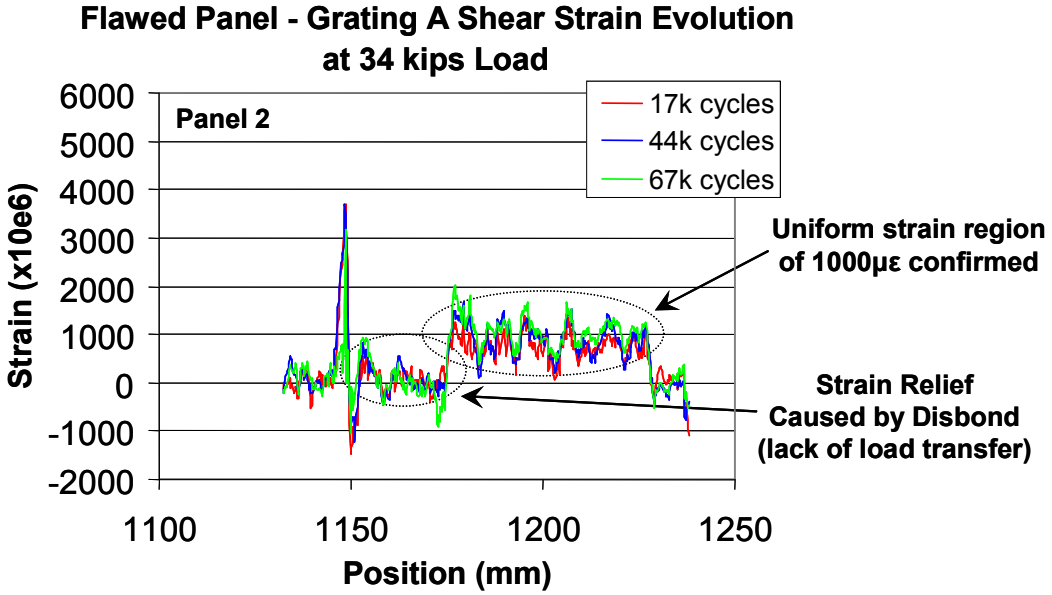

Figure 133: Shear Strain Levels Monitored by Sensor *A* Indicating the Presence of a Disbond

7.4 Deployment of Health Monitoring Sensor Networks

Distributed sensor networks can be deployed in any of the three approaches listed below. These options are listed in the order of increasing complexity, however, less labor is required to monitor the systems as they become more complex.

1. *In-Situ Sensors Only* – The sensors are the only items permanently installed on the structure. At the desired inspection intervals, power, signal conditioning, and data acquisition electronics are manually transported to the structure to be monitored. The sensors are linked to the monitoring electronics via an electrical connector and flaw detection is completed by an inspector at the site.
2. *Sensor Network with In-Situ Data Acquisition* – In this system, miniature, packaged electronics is also placed in-situ with the sensor network. The electronics contains the necessary power, memory and programmable circuitry for automated data logging. The data is periodically downloaded to a laptop through manual hook-ups at the site.
3. *Sensor Network with Real-Time Data Transmission to a Remote Site* – This approach is similar to item #2 with the addition of a telemetry system that allows for continuous, wireless transmission of data to a remote site. A web site can be programmed to interrogate critical aspects of the data and use pre-set thresholds to provide continuous green light/red light information regarding the health of the structure. The web site can even be programmed to automatically send an e-mail to maintenance personnel if the condition monitoring process indicates the need for repairs or other maintenance. In this

mode of operation it may be desirable to incorporate interface electronics to condition the signals and analyze data in-situ. This eliminates the need to transmit larger raw data files.

The latter approach allows for true condition-based maintenance in lieu of maintenance checks based on time of operation. A series of expected maintenance functions will already be defined, however, they will only be carried out as their need is established by the health monitoring system. The use of condition-based maintenance coupled with continuous on-line structural integrity monitoring could significantly reduce the cost of inspection, maintenance, and repair.

7.5 Overall Assessment of SHM for Aircraft and Composite Doubler Health Monitoring

Detection of unexpected flaw growth and structural failure could be improved through the use of on-board health monitoring systems that could continuously assess structural integrity. Such systems would be able to detect incipient damage before catastrophic failures occur. Local sensors, such as the ones described in this paper, can be used to directly detect the onset of crack, corrosion, or disbond flaws. Whether the health monitoring approach is local or global, the key element in a SHM system is a calibration of sensor responses so that damage signatures can be clearly delineated from sensor data produced by unflawed structures.

This section focused on local flaw detection using embedded sensors. While some of these leave-in-place sensors are able to produce wide area inspections, their use is predicated on the identification of primary flaw regions to be monitored. The ease of monitoring an entire network of distributed sensors means that structural health assessments can occur more often, allowing operators to be even more vigilant with respect to flaw onset. When accessibility issues are considered, distributed sensors systems may also represent significant time savings by eliminating the need for component tear-down. In addition, corrective repairs initiated by early detection of structural damage are more cost effective since they reduce the need for subsequent major repairs. Aerospace structures have one of the highest payoffs for SHM applications since damage can quickly lead to expensive repairs and aircraft routinely undergo regular, costly inspections.

In general, SHM sensors should be low profile, lightweight, easily mountable, durable, and reliable. To reduce human factors concerns with respect to flaw identification, the sensors should be easy to monitor with minimal need for users to step through additional data analysis. For optimum performance of the in-situ sensor based approaches, the signal processing and damage interpretation algorithms must be tuned to the specific structural interrogation method.

This section has highlighted the ability of various sensors to detect common flaws found in composite and metal structures with sensitivities that often exceed current flaw detection requirements. These sensor systems range in maturity from laboratory-based prototypes to turnkey systems that appear ready for aircraft use. Ongoing, focused validation programs at the AANC – conducted jointly with aircraft manufacturers and airlines - seek to integrate SHM sensors into aircraft maintenance programs. These evaluations are incorporating both cost-benefit analyses, as well as statistically-derived performance reliability numbers.

8.0 PILOT PROGRAM WITH FEDERAL EXPRESS – REPAIR OF DC-10 AND MD-11 WIDEBODYAIRCRAFT

8.1 Background on Pilot Program at Federal Express Aircraft Maintenance Depot

The Pilot Program for the DC-10 fuselage repairs consisted of a series of on-aircraft, composite doubler installations. The repairs were closely monitored for one year and inspections are continuing every D-check thereafter. During the first year of operation, the doublers were inspected at 60 day, 6 month, and one year intervals. A quality assurance inspection was also conducted immediately after each repair was installed. Extensive testing, along with flight history data on flying composite doublers, has shown that if a composite doubler installation survives its first 6 months to 1 year of operation without any flaw growth, then a good installation has been achieved and little or no flaw growth is expected over the doubler's lifetime. All aspects of the DC-10/MD-11 composite doubler repair program were approved via an 8110-3 form with appropriate sign-off from a Boeing Designated Engineering Representative. This pilot program placed a series of composite doublers on FedEx aircraft to repair fuselage skin damage in accordance with the Boeing ROD drawing 11-98-11-09-007 [47]. The accompanying set of drawing notes used to guide the installation process is contained in Appendix B.

An infrastructure for supporting routine use of composite doublers was demonstrated at the Federal Express LAX maintenance facility. The family of composite doubler repairs were laid up in advance in order to be quickly available for repairs. Composite doubler installation job cards were prepared from Engineering Authorization (EA) documents produced by FedEx engineers. Specialized training for composite shop and NDI shop personnel was completed to allow workers to properly carry out each job card. All composite doublers installed during the Pilot Program were closely monitored by frequent inspections to accumulate flight performance history and to validate the entire repair process as implemented by a commercial carrier. This approach demonstrated to the FAA that composite doubler repair technology can be safely transferred to industry.

8.2 Summary of FedEx Aircraft Repairs

In total, eight composite doubler repairs were installed on seven aircraft in the FedEx fleet. No access to the inside structure was required for any of the repairs. After over seven years of operation, and multiple in-service inspections, none of the repairs have experienced any problems and all are acquiring successful flight history to increase confidence in this advanced repair technology. Table 11 summarizes the aircraft that were included in this Pilot Program, the fuselage repair locations and the installation process (PANTA or Sol-Gel) used to install the composite doubler.

Aircraft 056 and 058 - The Pilot Program was launched in 2000 when two repairs were installed on DC-10 skin damage. Fuselage damage was repaired on aircraft 056 and 058 in the areas shown in Figures 134 and 135. The figures show approximate locations for the doublers which

actually crossed a number of substructure elements such as stringers and frames. Figures 136-141 show the damage locations, several of the installation steps and a completed fuselage repair. At the top of the photo in Fig. 141 is a witness coupon that is part of the quality assurance check for every doubler installation. The witness coupon is an aluminum strip that is bonded to the prepared surface alongside the composite doubler. After curing, the witness strip is pried off with a wedge. If the adhesive is found on both the coupon and the fuselage skin, then the surface preparation is good. The full strength of the adhesive is assured since the failure mode was cohesive failure (fracture) rather than adhesive failure (disbond). The pitch-catch ultrasonic inspection of the composite doubler on the aircraft is shown in Figure 142.

Aircraft Registry Number	Aircraft Hours/Cycles	Repair Location	Date of Repair	Installation Process	Figures
N68056	54,984/25,075	FS 495-515 @ Long. 39-40; Fuselage R/H Side	July 2000	PANTA	134-142
N68058	41,888/20,420	FS 1059 – 1079 @ Long. 25-26; Fuselage R/H Side	July 2000	PANTA	134-142
N384FE	61,561/23,874	FS 2234 -2239 @ Z = 39; Tailcone R/H Side	Mar. 2001	PANTA	143-146
N375FE	72,763/28,681	FS 1902 - 1921 @ Long 30-32; Fuselage R/H Side	Oct. 2001	PANTA	147-151
N10060	43,327/15,560	FS 1000 @ Long 35-36; Fuselage L/H Side	Jan. 2002	PANTA	152-153
N10060	43,327/15,560	FS 2234 -2239 @ Z = 39; Tailcone R/H Side	Jan. 2002	PANTA	152-153
N395FE	70,085/28,393	FS 1019 – 1039 @ Long. 36-37; Fuselage R/H Side	May 2003	Sol-Gel	154
N566FE	65,685/22,044	FS 735 – 755 @ Long. 41-42; Fuselage L/H Side	March 2004	Sol-Gel	155

Table 11: Summary of the Aircraft Included in the Composite Doubler Pilot Program with Federal Express

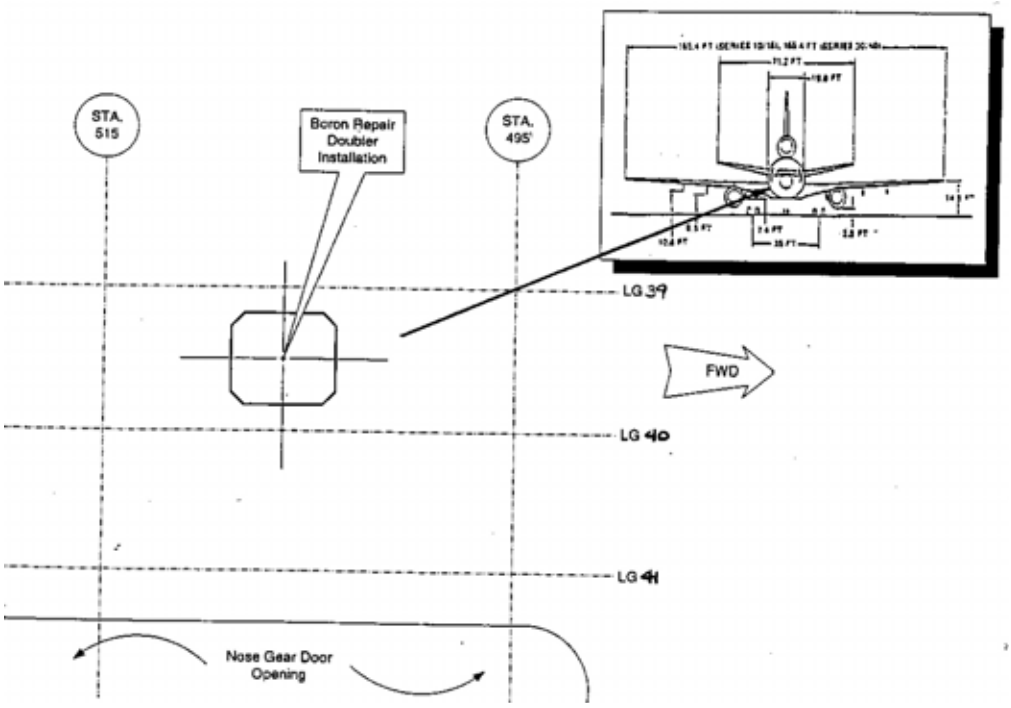

Figure 134: Composite Doubler Repair Location on Aircraft 056

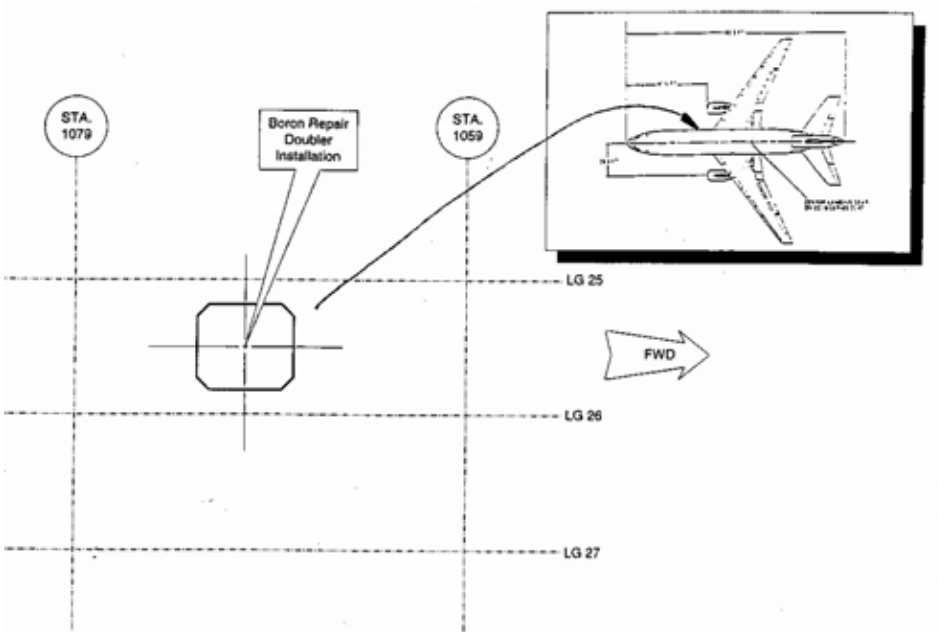

Figure 135: Composite Doubler Repair Location on Aircraft 058

Figure 136: Repair Location on Aircraft 056 Adjacent to Nose Gear

Figure 137: Repair Location on Aircraft 058 Right Side Forward of Wing

Figure 138: Scotch Brite Abrasion for Water - Break Free Surface

Figure 139: Application of Epoxy Adhesive Filler to Impact Damage

Figure 140: Monitoring Temperature and Vacuum During Cure Cycle

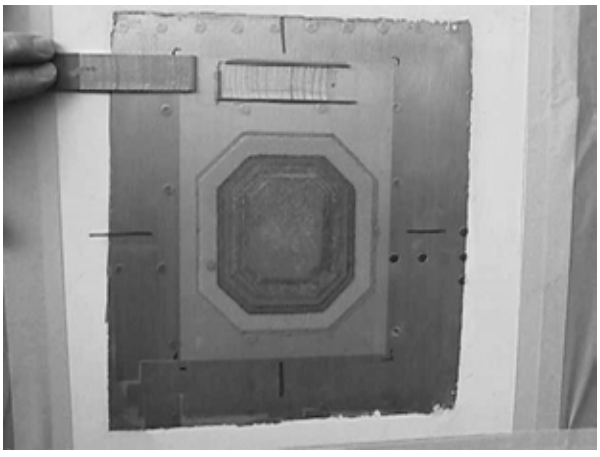

Figure 141: Completed Composite Doubler Repair; QA Witness Coupon at Top

Figure 142: Pitch-Catch Ultrasonic Inspection of Aircraft 058 Composite Doubler

Aircraft 384 - Figure 143 shows the repair region on the right hand side of the tailcone between station 2234 and 2239 at Z=39. The tailcone repair is of particular interest because it produced performance history for a composite doubler located in a sonic fatigue area near the aft engine. Figures 144-146 show the installation process, the completed fuselage repair, and the inspection process, respectively.

Figure 143: Composite Doubler Repair Location on Aircraft 384 Tailcone

Figure 144: Doubler Cure Cycle on Tailcone

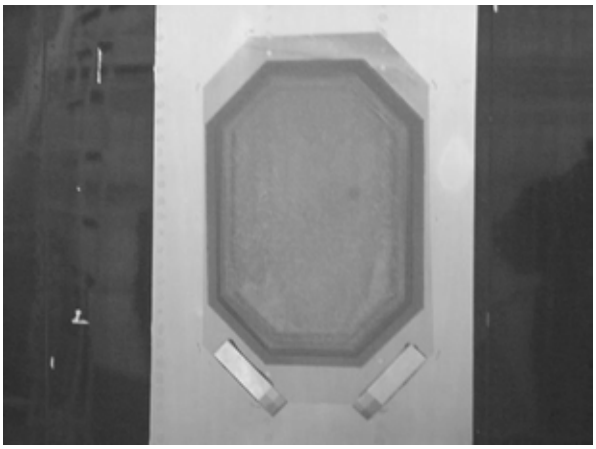

Figure 145: Completed Tailcone Composite Doubler Repair

Figure 146: Pitch-Catch Ultrasonic Inspection of Aircraft 384 Composite Doubler

Aircraft 375 - Fuselage damage was repaired on aircraft 375 in the area shown in Figure 147. The doubler crossed two stringers and the first frame aft of the cargo door. A description of the damaged area location is as follows: R/H side of fuselage between station 1902 and 1921; between LG 17R and 18R; approximately 26" aft of center cargo door.

Several of the installation steps are shown in Figures 148 and 149. No access to the inside structure was required for this repair. Figures 150 and 151 show the completed fuselage repair and a close-up of the pitch-catch ultrasonic inspection, respectively.

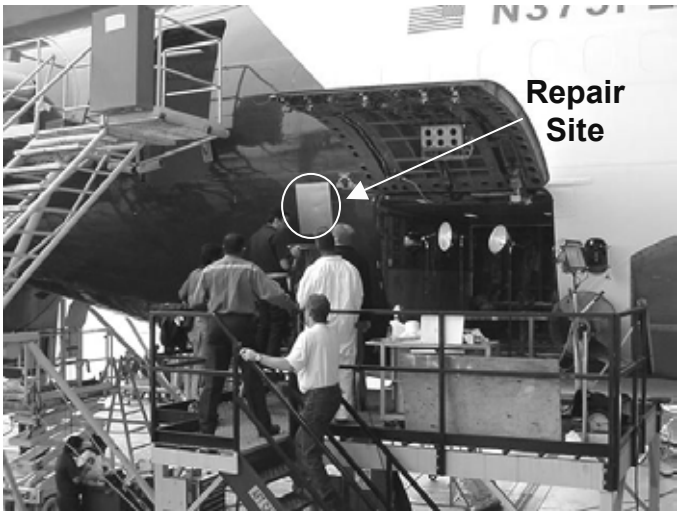

Figure 147: Composite Doubler Fuselage Repair Location on Aircraft 375

Figure 148: Surface Prep - Phosphoric Acid Anodize on Aircraft 375 Adjacent to Cargo Door

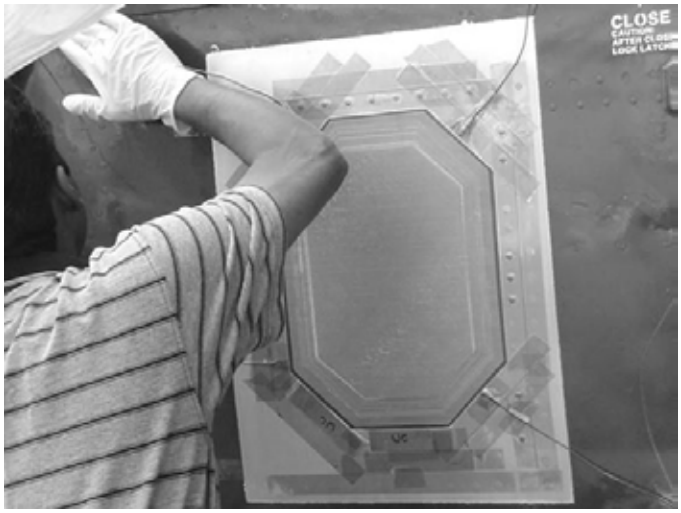

Figure 149: Positioning Composite Doubler for Vacuum Bag Assembly and Heat Cure

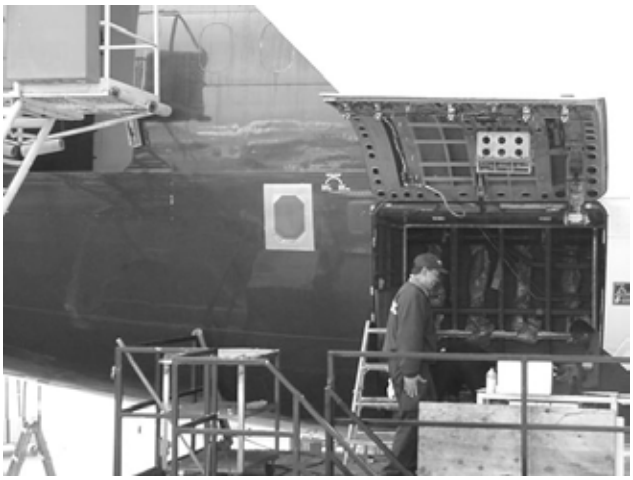

Figure 150: Completed Fuselage Composite Doubler Repair

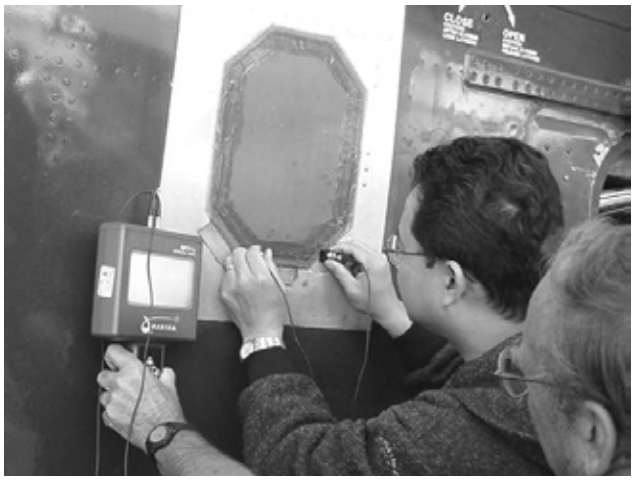

Figure 151: Pitch-Catch Ultrasonic Inspection of Aircraft 375 Repair

Aircraft 060 - Fuselage impact damage was repaired on aircraft 060 in the two areas shown in Figure 152. Descriptions of the two damaged area locations are as follows:

1. L/H side of fuselage between station 1000 and 1020; between LG 35 and 36; aft of primary static ports.
2. R/H side of tailcone between station 2186 and 2191 at Z=39.

Figure 153 shows the completed fuselage repair. Beside the doubler in Fig. 153 is the remaining adhesive from the witness coupon. After curing in the same environment as the composite doubler repair, the witness strips are pried off with a wedge as shown in Fig. 153 (right).

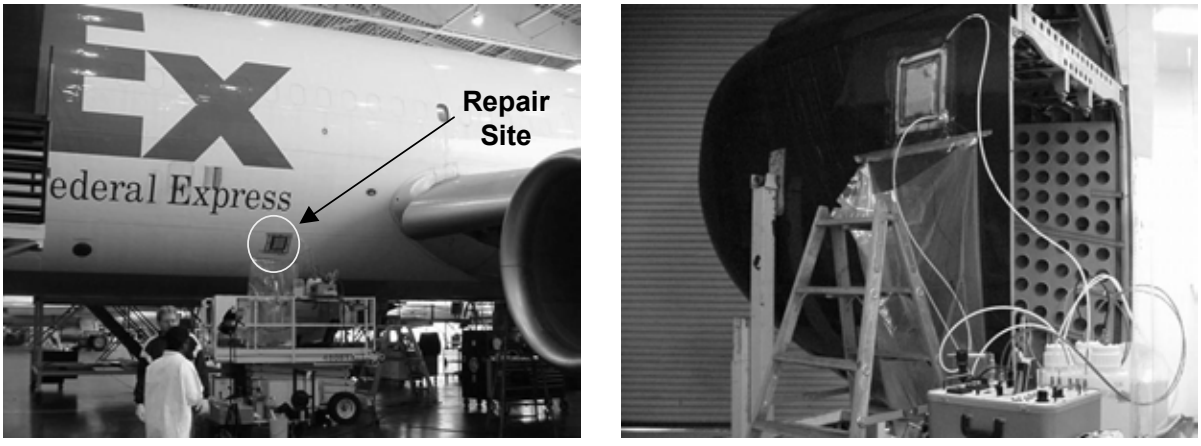

Figure 152: Composite Doubler Fuselage Repair Locations on Aircraft 060 – Fuselage R/H Side and Tailcone

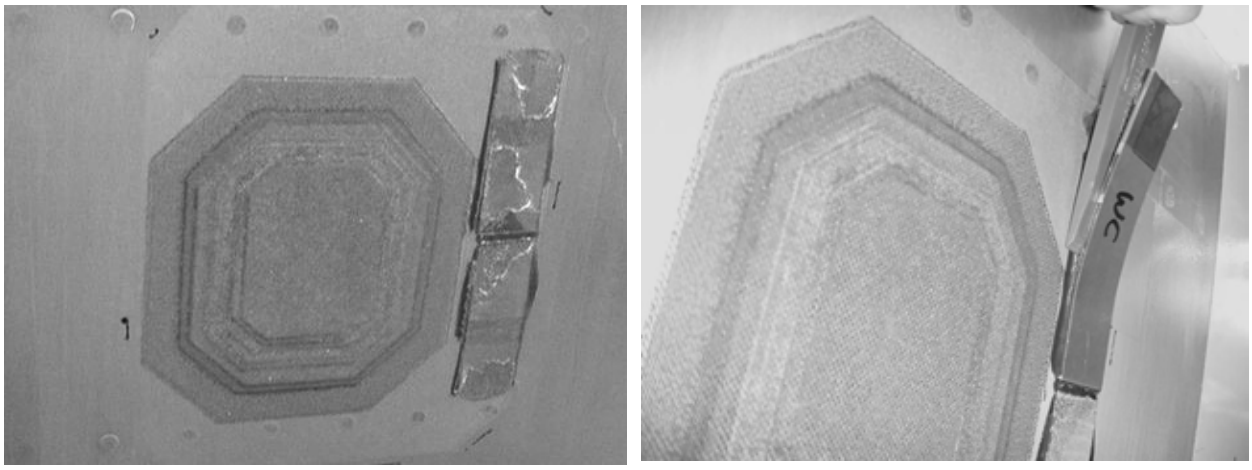

Figure 153: Completed Fuselage Composite Doubler and Removal of QA Witness Coupons in Surface Prep Assessment Region Beside Doubler

Aircraft 395 - A composite doubler was used to repair fuselage skin damage on the R/H side of aircraft 395 between stations 1019 and 1039 and between stringers 36 and 37. This was the first composite repair on a commercial aircraft to use the new Sol-Gel surface preparation process. Through our Pilot Program partner Federal Express, a Telex was submitted to Boeing and the FAA ACO requesting the substitution of the Sol-Gel aluminum surface preparation process for the currently-used Phosphoric Acid Anodize (PANTA) process. The Sol-Gel process has less room for human error, is more environmentally friendly, and results in a significant time savings during installation. This repair was completed in one day versus the two day approach that had been used on all of the previous PANTA-based repairs. Figure 154 shows the repair location on aircraft 395 along with the finished composite doubler repair. Use of the Sol-Gel process allowed the repair installation to be completed in a single shift. This process will permit overnight repairs such that aircraft can be available for their first flight the next day.

Figure 154: Composite Doubler Fuselage Repair Location on Aircraft 395 and Completed Fuselage Skin Repair

Aircraft 566 - A composite doubler was used to repair skin impact damage on the R/H side of aircraft 566 at fuselage station 540 between stringers 41 and 42. This was the second composite repair on a commercial aircraft to use the new Sol-Gel surface preparation process. Figure 155 shows the repair location on aircraft 566 along with the finished composite doubler repair. No access to the inside structure was required for this repair. The witness coupons, showing a successful QA check on the surface preparation process, are also shown in Fig. 155.

Figure 155: Composite Doubler Fuselage Repair Location on Aircraft 566 and Completed Fuselage Skin Repair

One goal of the Pilot Program was to demonstrate that aircraft maintenance personnel can be trained to install and inspect composite doublers. As a result, workers from FedEx's composite and NDI shops were key participants in the repairs. During the course of this project, the AANC gradually reduced its role in the composite doubler installations until FedEx personnel were able to safely install and inspect them without supervision. In-service inspections were performed on all composite doublers using the pitch-catch ultrasonic method. Subsequent 30 day, 6 month, and 1 year inspections were completed in accordance with via the Engineering Authorization that FedEx maintenance planners generated for each repair. All aircraft returned to service and subsequent inspections have not detected any flaws.

8.3 Revision of Structural Repair Manual

After successful completion of the Pilot Program, the Structural Repair Manuals were modified to include this set of three composite doubler designs. This allows for more routine use of composite doubler repairs within the allowable application regime specified in the manuals. The SRM revisions – incorporating DC-10, MD-11, MD-80, MD-90, and 717 aircraft - takes the form of a look-up table that allows users to match flaw type/size with either a metallic repair or the equivalent composite doubler repair. Using these look-up tables, maintenance facilities can have the option of choosing the traditional metallic repair or the "equivalent" composite doubler repair. The engineering drawing for the composite repairs was integrated into the SRM. The NDT procedure for bonded composite doublers (ultrasonic resonance technique) was also included in the Boeing NDT Standard Practices Manual. Finally, a set of training classes are being developed to safely integrate composite doubler technology into the commercial maintenance depots. The classes will cover all aspects of design, analysis, installation, quality control, and in-service inspection. They will describe the infrastructure and personnel capabilities/training that must be present at an aircraft maintenance depot in order to safely utilize the technology.

CONCLUSIONS

Economic barriers to the purchase of new aircraft have created an aging aircraft fleet and placed even greater demands on efficient and safe repair methods. The use of composite doublers offers the airframe manufacturers and aircraft operators a cost-effective method to safely extend the lives of their aircraft. Instead of riveting multiple metal plates to facilitate an aircraft repair, it is possible to bond a single Boron-Epoxy composite doubler to the damaged structure. The FAA's Airworthiness Assurance Center (AANC) at Sandia National Labs, Boeing, and Federal Express completed a Pilot Program to validate and introduce composite doubler repair technology to routine commercial aircraft use. As composite doubler repairs gradually appear in the commercial aircraft arena, flight operation data is being accumulated to demonstrate the successful application of this repair technique. The engineering activities in this program investigated design, analysis, fatigue performance, installation, and nondestructive inspection issues. The key results are:

1. Composite doubler repair technology is viable for the commercial aircraft industry.
2. While recognizing the value of composite doublers, there is also a need emphasize the safe integration their use into aircraft maintenance facilities.
3. Doublers are able to withstand extensive damage and non-optimum installations while improving fatigue life and ultimate strength.
4. Nondestructive inspection methods are available to safely monitor the integrity of the composite repair and the parent metal structure.
5. Project activities have addressed many obstacles to the use of composite doublers and allow airlines to take advantage of potential time and cost savings.
6. This effort has further demonstrated the performance of composite doublers in commercial aircraft repairs by accumulating flight history.
7. The composite doubler repair process, including inspection methods, can aid aircraft Service Life Extension Programs.
8. A formal documentation package has been placed in the public domain via the FAA in order to safely integrate this technology into the U.S. commercial fleet. In addition, OEM Nondestructive Testing Structural Repair Manuals have been revised to include composite doubler repairs as a viable alternative to riveted metallic repairs.

One of the concerns surrounding composite doubler technology pertains to long-term survivability, especially in the presence of non-optimum installations. This test program demonstrated the damage tolerance capabilities of bonded composite doublers. The fatigue and strength tests quantified the structural response and crack abatement capabilities of Boron-Epoxy doublers in the presence of worst case flaw scenarios. The engineered flaws included cracks in the parent material, disbonds in the adhesive layer, and impact damage to the composite laminate.

Damage Tolerance and Crack Mitigation - Large strains immediately adjacent to the doubler flaws emphasize the fact that relatively large disbond or delamination flaws (up to 1" diameter)

in the composite doubler have only localized effects on strain and minimal effect on the overall doubler performance (i.e. undesirable strain relief over disbond but favorable load transfer immediately next to disbond). Obviously, disbonds will affect the capabilities of composite doublers once they exceed some percentage of the doubler's total footprint area. The point at which disbonds become detrimental depends upon the size and location of the disbond and the strain field around the doubler. This study did not attempt to determine a "flaw size vs. effect" relation. Rather, it used flaws which were twice as large as the detectable limit to demonstrate the ability of composite doublers to tolerate potential damage. Similarly, the crack mitigation capabilities of Boron-Epoxy doublers were evaluated using crack sizes which exceeded the inspection threshold. The damage tolerance tests presented in this document looked at crack growth beneath doublers of up to 3". Comparisons with control specimens that did not have composite doubler reinforcement showed that the fatigue lifetime was extended by a factor of 20.

Adhesive Layer Performance Indicates Critical Need for Proper Surface Preparation - Previous analyses of bonded doublers have demonstrated that the most critical part of the repair installation is the adhesive. It must transfer the load to the composite doubler and hold up under many load cycles. The adhesive must also resist moisture and other environmental effects. In order to obtain the optimal adhesive strength and assure a satisfactory performance over time, it is essential to strictly comply with the installation process. Surface preparation is one of the key steps in the installation process. This study demonstrated the ability of the accepted adhesives to transfer loads over multiple fatigue lifetimes of a commercial aircraft. Strain field analyses and fatigue tests showed that large disbonds - in excess of those which will be detected by NDI - and Boron-Epoxy water absorption did not affect the performance of the adhesive layer.

Residual Strength - Post-fatigue load-to-failure tests produced residual strength values for the composite-aluminum specimens. Even the existence of disbonds and fatigue cracks did not prevent the doubler-reinforced-plates from achieving static ultimate tensile strengths in excess of the 70 ksi Mil-Hndb-5 listing for 2024-T3 material. Thus, a properly designed and installed composite doubler is able to restore the structure to its original load carrying capability.

Nondestructive Inspection - Before the use of composite doublers can be accepted by the civil aviation industry, it is imperative that methods be developed which can quickly and reliably assess the integrity of the doubler and the parent, metal structure beneath the doubler. Sensitivity studies showed that a team of NDI techniques can identify flaws well before they reach critical size. An ultrasonic method was successfully applied to the problem of disbond and delamination detection. Pulse-Echo ultrasonics can be implemented on an aircraft using hand held inspection devices. Anomalies in A-Scan signals can be used to reliably detect flaws in the laminate and bondline. Successful results also demonstrated the viability of thermography for inspecting bonded composite doublers. Thermography can detect flaws smaller than 0.5" in diameter and can accurately determine their depth. Crack detection in the parent aluminum material can be accomplished using conventional eddy current and X-ray techniques.

Overall Evaluation of Bonded Boron-Epoxy Composite Doublers - By combining the residual strength results with the crack mitigation results, it is possible to truly assess the capabilities and damage tolerance of bonded Boron-Epoxy composite doublers. In this test series, relatively

severe installation flaws were engineered into the test specimens in order to evaluate Boron-Epoxy doubler performance under worst case, off-design conditions. The engineered flaws were at least two times larger than those which can be detected by NDI. It was demonstrated that even in the presence of extensive damage in the original structure (cracks, material loss) and in spite of non-optimum installations (adhesive disbonds), the composite doubler allowed the structure to survive more than four design lifetimes of fatigue loading. Since the tests were conducting using extreme combinations of flaw scenarios (sizes and collocation) and excessive fatigue load spectrums, the performance parameters were arrived at in a conservative manner.

Final Cautions Regarding the Use of Bonded Composite Doubler Repairs - Although the composite doubler repair method can be used in a wide array of aircraft repair applications, it must be recognized that it cannot be directly substituted for all traditional aircraft repairs. Certain limitations, such as poor performance in compression load environments, require that an in-depth analysis be performed before undertaking any composite doubler repair. In addition, it is essential that all composite doubler repair efforts be carried out by properly trained personnel. Design/analysis (engineering), installation (composite shop), and inspection (NDT shop) personnel must have appropriate knowledge of composite materials and hot bonding processes.

Finally, it should be noted that despite the successful results achieved in this effort, the use of composite doubler repairs includes a number of potential pitfalls and engineering challenges. In addition to assuring a quality installation, design and analysis efforts must address difficult issues such as thermally induced residual stresses and stress risers around the doubler's outer perimeter. This report adds to the growing database of composite doubler performance characteristics, however, a comprehensive engineering approach is always necessary to ensure the safe application of these aircraft repairs.

The entire aviation industry can receive the engineering and economic benefits provided by this composite doubler repair technology. Technical advantages include: 1) improved fatigue life, 2) increased strength, 3) decreased weight, 4) eliminates introduction of crack initiation sites (i.e. fastener holes), 5) does not corrode, and 6) improves aerodynamics. Economic benefits include: 1) cost savings through reduction in man-hours required to install a repair, and 2) reduced aircraft downtime. The aviation industry and the FAA are continuously searching for ways to improve aircraft maintenance practices. Enhanced safety is the primary goal while cost reduction is necessary to the airline's competitiveness in the global air transportation market. In the proper applications, composite doubler repairs can successfully address both of these issues.

REFERENCES

1. Roach, D.P, “Damage Tolerance Assessment of Bonded Composite Doublers for Commercial Aircraft Applications", Sandia National Laboratories/ Dept. of Energy Report No. SAND98-1016, August 1998; also FAA Report SNL96ER0189 under Atlanta Aircraft Certification Office Project SP1798AT-Q, November 1997.
2. Elvidge, R., “Structures in Service – An Airline Point of View,” Canadian Aeronautics and Space Journal, Vol. 30, December 1984.
3. Jones, R. and Callinan, R., “A Design Study in Crack Patching,” Fibre Science and Technology, Vol. 14, 1981.
4. Bakuckas, Jr, J.G., Chen, C.C., Yu, J., Tan, P.W., and Bigelow, C.A., “Engineering Approach to Damage Tolerance Analysis of Fuselage Skin Repairs,” Dept. of Transportation Report No. DOT/FAA/AR-95/75, November 1996.
5. Davis, M., “The Development of an Engineering Standard for Composite Repairs,” AGARD-CP-550, Proceedings of AGARD Meeting, Seville, October 1994.
6. Christian Jr., T., Hammond, D., and Cochran, J., “Composite Material Repairs to Metallic Airframe Components,” Journal of Aircraft, Vol. 29, 1992.
7. Roach, D., "Commercial Application of Composite Doublers for DC-10 Fuselage Repairs," Int'l SAMPE Symposium on Composites in Engineering, May 2005.
8. Baker, A.A., "Fatigue Studies Related to Certification of Composite Crack Patching for Primary Metallic Aircraft Structure," FAA-NASA Symposium on Continued Airworthiness of Aircraft Structures, Dept. of Transportation Report No. DOT/FAA/AR-97-2,I, July 1997.
9. Fredell, R.S., "Damage Tolerant Repair Techniques for Pressurized Aircraft Fuselages", PhD Dissertation, Delft University, 1994.
10. Rice, R., Francini, R., Rahman, S., Rosenfeld, S., Rust, S., Smith, S., and Broek, D., "Effects of Repair on Structural Integrity", Dept. of Transportation Report No. DOT/FAA/CT-93/79, December 1993.
11. Jones, R., Chiu, C., Paul, J., “Designing for Damage Tolerant Bonded Joints,” *Composite Structures*, Vol. 25, 1993.
12. Chiu, W.K., Rees, D., Chalkley, P., and Jones, R., “Designing for Damage Tolerant Repairs,” ARL Aircraft Structures Report 450, August 1992.
13. Roach, D.P., and Walkington, P., “Full Scale Structural and NDI Validation Tests on Bonded Composite Doublers for Commercial Aircraft Applications", Sandia National Laboratories/ Dept. of Energy Report No. SAND98-1015 , November 1998.
14. Roach, D.P., and Walkington, P., “Development and Validation of Nondestructive Inspection Techniques for Composite Doubler Repairs on Commercial Aircraft Applications", Sandia National Laboratories/ Dept. of Energy Report No. SAND98-1014 , May 1998.
15. Grills, R.H., and Mullis, T., “C-141 Weep Hole External Inspection of Bonded Boron Patches”, Air Force 3rd Aging Aircraft Conference, Sept. 1995.
16. Roach, D.P., Moore, D., and Walkington, P., "Nondestructive Inspection of Bonded Composite Doublers for Aircraft", Proceedings of SPIE Conference on Nondestructive Evaluation of Aging Aircraft, December 1996.

17. Gieske, J.H., Roach, D.P., Walkington, P.D., "Ultrasonic Inspection Technique for Composite Doubler/Aluminum Skin Bond Integrity for Aircraft," SPIE Nondestructive Evaluation Techniques for Aging Infrastructure & Manufacturing Conf., vol. 3258, April 1998.
18. Fredell, R.S., van Barnveld, W., and Vlot, A., "Analysis of Composite Crack Patching of Fuselage Structures: High Patch Modulus Isn't the Whole Story", SAMPE Int'l Symposium 39, April 1994.
19. Rose, L.R., "Influence of Disbonding on the Efficiency of Crack Patching", *Theoretical Applied Fracture Mechanics*, vol. 7 , 1987.
20. Baker, A.A., "Growth Characterization of Fatigue Cracks Repaired with Adhesively Bonded Boron/Epoxy Patches," Proc. Of Int'l Conf. Fracture, ICF-9, April 1997.
21. Rose, L.R., "A Cracked Plate Repaired by Bonded Reinforcements," Int'l Journal of Fracture, Vol. 18, 1982.
22. Hart-Smith, L.J., "Extension of the Rose Bonded Crack-Patching Analysis to Orthotropic Composite Patches Also Accounting for Residual Thermal Stresses," FAA/NASA/DoD Aging Aircraft Conference, Sept. 2001
23. Callinan, R.J., Rose, L.R., and Wang, C.H., "Three Dimensional Stress Analysis of Crack Patching," Proc. Of Int'l Conf. Fracture, ICF-9, April 1997.
24. Rose, L.R., "Design Analysis and Validation for a Bonded Composite Repair to Primary Aircraft Structure," Proc. Of Int'l Conf. Fracture, ICF-9, April 1997.
25. Davis, M.J., "A Call for Minimum Standards in Design and Application Technology for Bonded Structural Repairs", Int'l Symposium on Composite Repair of Aircraft Structures in concert with ICCM-10, August 1995.
26. Fredell, R.S., and Marr, J., "An Engineering Approach to the Design and Analysis of Fuselage Crack Patching with the Computer Program CalcuRep for Windows", Int'l Symposium on Composite Repair of Aircraft Structures in concert with ICCM-10, August 1995.
27. Xiong, X., Raizenne, D., "A Design Methodology and PC-Based Software for Bonded Composite Repair in Aircraft Structure", Int'l Symposium on Composite Repair of Aircraft Structures in concert with ICCM-10, August 1995.
28. Jones, K.M., Roach, D.P., and Shah, S., "Composite Repair - Upper Forward Corner of P-3 Door - Model L-1011 Aircraft, Strength and Damage Tolerance Analysis", Report No. LG95ER0157, Part of Documentation Package for FAA Atlanta Aircraft Certification Office Project No. SP1798AT-Q, analysis plan December 1995, final report October 1996.
29. Duong, C., and Yu, J., "The Stress Intensity Factor for a Cracked Stiffened Sheet Repaired with an Adhesively Bonded Composite Patch, Int. Journal of Facture, Vol. 4 No.1, Oct. 2004.
30. Jappe, W., Wood, N., Johnson, M., "The Transition Process from Emerging NDT Technology to Production Inspection Application," SPIE, Vol. 2455, March 1995.
31. Palmer, D.D., Wood, N.O., "Development of MAUS Enhancements for Large Area Wing Inspections," Air Force Structural Integrity Conf., Dec. 1999.
32. Brewis, D., "Factors Affecting Bonding of Metals," *Materials and Technology*, Vol. 2, August 1986.
33. Roach, D., Rackow, K., Dunn, D., "Installation of Adhesively Bonded Composites to Repair Carbon Steel Structure," *Joining and Repair of Composite Structures, ASTM STP 1455*, K. T. Kedward and H. Kim, Eds., ASTM International, West Conshohocken, PA, 2004.

34. Blohowiak, K., et al., “Bonded Repair Techniques Using Sol-Gel Surface Preparations,” DOD/FAA/NASA Conf. on Aging Aircraft, September 1998.
35. Berg, S.D., “Process Specification for the Fabrication and Application of Boron-Epoxy Doublers onto Aluminum Structures”, Textron Specialty Materials Specification No. 200008-001 (may also be referenced as the Boeing Specification D658-10183-1 which was written for Textron), dated November 30, 1995, Textron Specialty Materials, Lowell, MA, 01851.
36. Cox, J., “*Nondestructive Testing: Eddy Current*,” PH Diversified Pub., 1997.
37. Spencer, F., Borgonovi, G. , Roach, D., Schurman, D. , Smith, R.; "Reliability Assessment at Airline Inspection Facilities, Volume II: Protocol for an Eddy Current Inspection Reliability Experiment"; Dept. of Transportation Report, DOT/FAA/CT-92/12-II, May 1993.
38. Metals Handbook Ninth Edition “Volume 17 Nondestructive Evaluation and Quality Control”, ASM International, 1989, pp 241 - 246.
39. Roach, D., Beattie, A., Dahlke, L., Gieske, J., Hansche, B., Phipps, G., Shagam, R., and Thompson, K., "Emerging Nondestructive Inspection Methods for Aging Aircraft"; Dept. of Energy SAND Report 92-2732, March 1994; Dept. of Transportation Report No. DOT/FAA/CT-94/11, October 1994.
40. Giurgiutiu, V., Redmond, J., Roach, D., and Rackow, K, "Active Sensors for Health Monitoring of Aging Aerospace Structures," *International Journal of Condition Monitoring and Diagnostics Engineering*, February 2001.
41. Lin, M., Beard, S., Kumar, A., Qing, X., Development of Structural Health Monitoring Systems Using SMART Layer Technology,“ American Society for Composites 17th Technical Conference, October 2002.
42. Kumar, A., Beard, S., Hannum, R. (Acellent Technology), and Roach, D. (Sandia Labs), **“**In-Situ Monitoring of the Integrity of Bonded Repair Patches on Civil Infrastructures,” SPIE Conference on NDE for Health Monitoring and Diagnostics, February 2006.
43. Roach, D., Wanser, K., and Griffiths, R., "Application of Fiber Optics to Health Monitoring of Aircraft,” Advanced Aerospace Materials and Processes Conference, June 1994.
44. E. Udd, W.L. Schulz, J.M. Seim, E. Haugse, A. Trego, P.E. Johnson, T.E. Bennett, D.V. Nelson, A. Makino, “Multidimensional Strain Field Measurements using Fiber Optic Grating Sensors”, SPIE Proceedings, Vol. 3986, p. 254, 2000
45. M. Froggatt and J. Moore, "Distributed Measurement of Static Strain in an Optical Fiber with Multiple Bragg gratings at Nominally Equal Wavelengths", Applied Optics, Vol. 37, p. 1741, 1998.
46. Udd, E., Kreger, S., Calvert, S., Kunzler, M., and Davol, K., “Usage of Multi-Axis Fiber Grating Strain Sensors to Support Nondestructive Evaluation of Composite Parts and Adhesive Bond Lines,” 4th International Workshop on Structural Health Monitoring, September 2003.
47. Delgado, M, Hu, J., Composite Doubler Repairs for DC-10/MD-11 Fuselage, Boeing ROD SKETCH 11-98-11-09-007, March 11, 1999.

Appendix A

Inspection Procedure for Ultrasonic Pitch-Catch Technique

Nondestructive Inspection Procedure for Bonded Boron–Epoxy Composite Doublers Using an Ultrasonic Pitch-Catch Technique

FAA Airworthiness Assurance NDI Validation Center
Sandia National Laboratories - Albuquerque, NM

Specification No. AANC-UT-PC-Comp-5521/4-001

Purpose

The purpose of this inspection is to detect delaminations between the boron epoxy plies and disbonds between the boron epoxy doubler and the aluminum substrate. This procedure uses an ultrasonic test instrument and several contact transducers.

1) References

Operation Manual: Quantum + Plus Series

2) Equipment

A. The equipment used to develop this procedure was an NDT Systems, Inc. QUANTUM Model QFT-1+ portable ultrasonic flaw detector with an A-trace display.
B. Use ultrasonic transducers: Krautkramer Branson Composite MSW-QC contact transducers, frequency 1 MHZ, alpha or gamma series, 0.5 inch diameter. The transmitter transducer product code number is 113-141-591. Any of the following transducers can be used as a receiver: 113-141-591, 113-241-591, and 389-036-490.
C. Mount the transmitting transducers in a 30 degree Lucite wedge (angle beam transducer) which is designed to produce a shear wave of a particular angle in a specified material with minimal wedge noise. The produce code for the 30^{o} Lucite wedge is W-210 30^{o}. It will fit product code numbers 113-141-591 and 113-241-591. When installing the transducer in the wedge, apply an ultrasonic couplant between the transducer and the wedge. The receiving transducer can mount directly on the aluminum skin (90^{o}) or be mounted in a 30 degree Lucite wedge to create an angle beam receiver.
D. Set up the ultrasonic flaw detector equipment using a boron epoxy doubler NDI calibration standard, with known disbonds and delaminations, as shown in Figure A-1.
E. Use an ultrasonic couplant to couple the high frequency signal in and out of the calibration standard.

3) Personnel

The inspector using this procedure should be experienced and knowledgeable in the fundamentals of ultrasonic testing. Inspectors should fully possess the qualification of ultrasonic testing personnel as defined in Recommended Practice No. ASNT-TC-1A, Personnel Qualification and Certification in Nondestructive Testing, available from ASNT (American Society for Nondestructive Testing), ATA 105 or other approved certification standard.

4) Material Preparation

If the boron epoxy surface has irregularities, lightly sand the surface to obtain a smooth working surface. Removal of surface irregularities will enhance the ultrasonic signals for this inspection technique. Note: If the surface has been painted, paint removal may not be required as long as the inspection surface is smooth and not scaling.

5) Instrument Calibration for Inspection of the Tapered Area on the Boron Epoxy Doubler

A. Connect a microdot / LEMO-00 cable between the transmitting transducer and the Quantum red dot input connector. Apply couplant between the transducer and the 30 degree lucite wedge. This combination will be referred to as the angle beam transducer (T).

B. Connect a microdot / LEMO-00 cable between the receiver transducer (R) and the Quantum right side input connector. The receiver can be a contact transducer or an angle beam transducer with the 30 degree lucite wedge attached.

C. Turn the instrument power on and check the battery status. The instrument should have at least 40% of available battery life. The screen brightness and contrast should be adjusted to match the environmental conditions (i.e., outside sunlight or inside a hangar).

D. Select or verify the dual probe setting on the probe selection menu. In the display menu, select inches as the units of measure and select RF wave type for the A-scan display. In the cal menu, set the material velocity to 0.250 inches per microsecond and set the instrument range to 8.00 inches.

E. Position the angle beam transducer on the calibration standard at position (PT1) and the receiving transducer to the perimeter of the doubler at position (PR1) on the aluminum as shown in Figure A-2. A sample set-up showing the transmitter and receiver transducers and the scanning motion are shown in Figure A-3.

Always use adequate ultrasonic couplant between the transducers, doubler and the aluminum. The signal on the display screen, as shown in Figure A-4, from left to right represents the initial pulse and the received signal through the doubler and the aluminum. The received signal will vary in amplitude and delay time depending on the spacing between the angle beam transducer (T), receiving transducer (R) and the material thickness of the doubler. Change the gain (dB) in order to adjust the amplitude of the signal through the doubler and the aluminum until it reads 80% Full Screen Height (FSH) as shown in Figure A-4. The 80% FSH cannot be maintained as the transmitting transducer is moved further away from the receiving transducer. The amplitude should be adjusted as necessary, via the gain setting, to maintain sensitivity. To eliminate the large amplitude variations in the received signal, the inspector can use an ultrasonic flaw detector that has a Distance Amplitude Correction (DAC) mode.

F. Move the angle beam transducer to position (PT2) (see Figure A-2) which represents a delamination between the plies in the boron epoxy composite. Note the signal on the display screen (Figure A-5) which shows the absence of a received signal through the doubler into the aluminum. The received signal completely disappears when the size of the delamination is larger than the diameter of the angle beam transducer (T).

G. Move the angle beam transducer to position (PT3) (see Figure A-2) which represents a disbond area between the doubler and the aluminum. Move the receiving transducer to the perimeter of the doubler at position (PR2) on the aluminum as shown in Figure A-2. Note the signal on the display screen (Figure A-5) which shows the absence of a received signal through the doubler into the aluminum. The received signal completely disappears when the size of the disbond is larger than the diameter of the angle beam transducer (T).

6) Inspection Procedure for Tapered Region of Doubler

On the aircraft, position the receiving transducer (R) on the aluminum along the edge of the taper region with ultrasonic couplant. Add couplant to the taper region to be inspected. Monitor the received signal on the display screen and adjust the signal amplitude if necessary. To assure proper coupling to the doubler, slowly move the angle beam transducer (T) along the taper region while monitoring the received signal on the display screen (see Fig. A-3 for sample inspection set-up). Position the transmitter and receiver transducers as matched pairs and scan the doubler in accordance with the schematic shown in Figure A-6. For example, transmitter location (TA) is matched with receiver location (RA) and the transmitter is moved along the taper toward the receiver. Continue in this fashion until the (TJ) to (RJ) strip has been inspected. This will complete the inspection of one perimeter strip of the tapered region.

By observing the A-trace on the screen, the inspector should always see a signal present. If the signal disappears, check for adequate coupling. Next, move the transmitting transducer to all of the areas immediately adjacent to the signal drop-out area while simultaneously looking for any disappearance and reappearance of the received signal. If the coupling is adequate and there is a signal present all around this signal drop-out area then a disbond or delamination lies below the angle beam transducer (T). Use a grease pencil to mark this flawed area.

Once the inspector has completely inspected one edge perimeter of the tapered region, the transmitting and receiving transducer locations shown in Figure A-6 can be shifted slightly to inspect a thicker portion of the taper. Repeat the inspection process for each new perimeter strip that is inspected as the taper increases in thickness. The transducer pairs listed in this procedure can cover perimeter strips of 0.5" in width. A straight edge can be used to guide the transmitting transducer along the taper.

7) Instrument Calibration for Inspection of the Full Thickness Area and Tapered Region on the Boron Epoxy Doubler

Repeat steps 5A,B,C and D if necessary.

A. Position the angle beam transducer on the calibration standard at position (PT4) and the receiving transducer around the perimeter of the doubler at position (PR4) on the aluminum as shown in Figure A-7. Always use adequate ultrasonic couplant between the transducers, doubler and the aluminum. The signal on the display screen, as shown in Figure A-4, from left to right represents the initial pulse and the received signal through the doubler and the aluminum. The received signal will vary in amplitude and delay time depending on the spacing between the angle beam transducer (T), receiving transducer (R) and the material thickness of the doubler. Adjust the amplitude of the signal through the doubler and the aluminum until it reads 80% Full Screen Height (FSH) as shown in Figure A-4. The 80% FSH can not be maintained as the

transmitting transducer is moved further away from the receiving transducer. The amplitude should be adjusted as necessary, via the gain setting, to maintain sensitivity. To eliminate the large amplitude variations in the received signal, the inspector can use an ultrasonic flaw detector that has a Distance Amplitude Correction (DAC) mode.

B. Move the angle beam transducer to position (PT5) (see Figure A-7) which represents a delamination between the plies in the boron epoxy composite. Note the signal on the display screen (Figure A-5) which shows the absence of a received signal through the doubler into the aluminum. The received signal completely disappears when the size of the disbond is larger than the diameter of the angle beam transducer (T).

8) Inspection Procedure for Full Thickness Area and Tapered Region of Doubler

On the aircraft, position the receiving transducers (R) on the aluminum along the edge of the doubler with some ultrasonic couplant. Add couplant to the full thickness area to be inspected. Monitor the received signal on the display screen and adjust the signal amplitude if necessary. To assure proper coupling to the doubler, slowly move the angle beam transducer along the surface of the doubler while monitoring the received signal on the display screen (see Fig. A-9 for sample inspection set-up). Position the transmitter and receiver transducers as matched pairs and scan the doubler in accordance with the schematic shown in Figure A-8. For example, transmitter location (TA) is matched with receiver location (RA) and the transmitter is moved toward the receiver as shown. To assure sufficient coverage of the doubler, mark a 0.5" grid alongside the doubler using a grease pencil. This will produce a series of inspection strips each having its own transmitter-receiver transducer pair. Use a straight edge to ensure proper transducer motion along the inspection strips. Follow this process until the full area of the doubler has been completely inspected.

Note that this inspection procedure includes the tapered region of the doubler. The tapered region was inspected in a previous part of this procedure, however, the dual coverage will provide additional flaw detection opportunities in the critical tapered region. Note also that the doubler is divided into two halves for inspection purposes and the transmitter is moved from the center of the doubler out towards the receiver (see Figure A-8). The entire width of the doubler is not inspected with a single scan in order to maintain the signal strength and optimize the sensitivity of the inspection. If the DAC option is used, it may be possible to inspect the entire width of the doubler in a single scan. The inspector must ensure that sufficient signal strength is being maintained throughout the inspections.

By observing the A-trace on the screen, the inspector should always see a signal present. If the signal disappears, check for adequate coupling. Next, move the transmitting transducer to all of the areas immediately adjacent to the signal drop-out area while simultaneously looking for any disappearance and reappearance of the received signal. If the coupling is adequate and there is a signal present all around this signal drop out area then a disbond or delamination lies below the angle beam transducer (T). Use a grease pencil to mark this flawed area. Repeat this process for each new strip that is to be inspected.

9) Evaluation

Any areas where the signal dropped out and was marked with the grease pencil, should be identified on a map according to flaw size.

10) Inspection Results

Report all flaw indications greater than 0.50 inches in diameter to the appropriate engineering personnel for further evaluation/action.

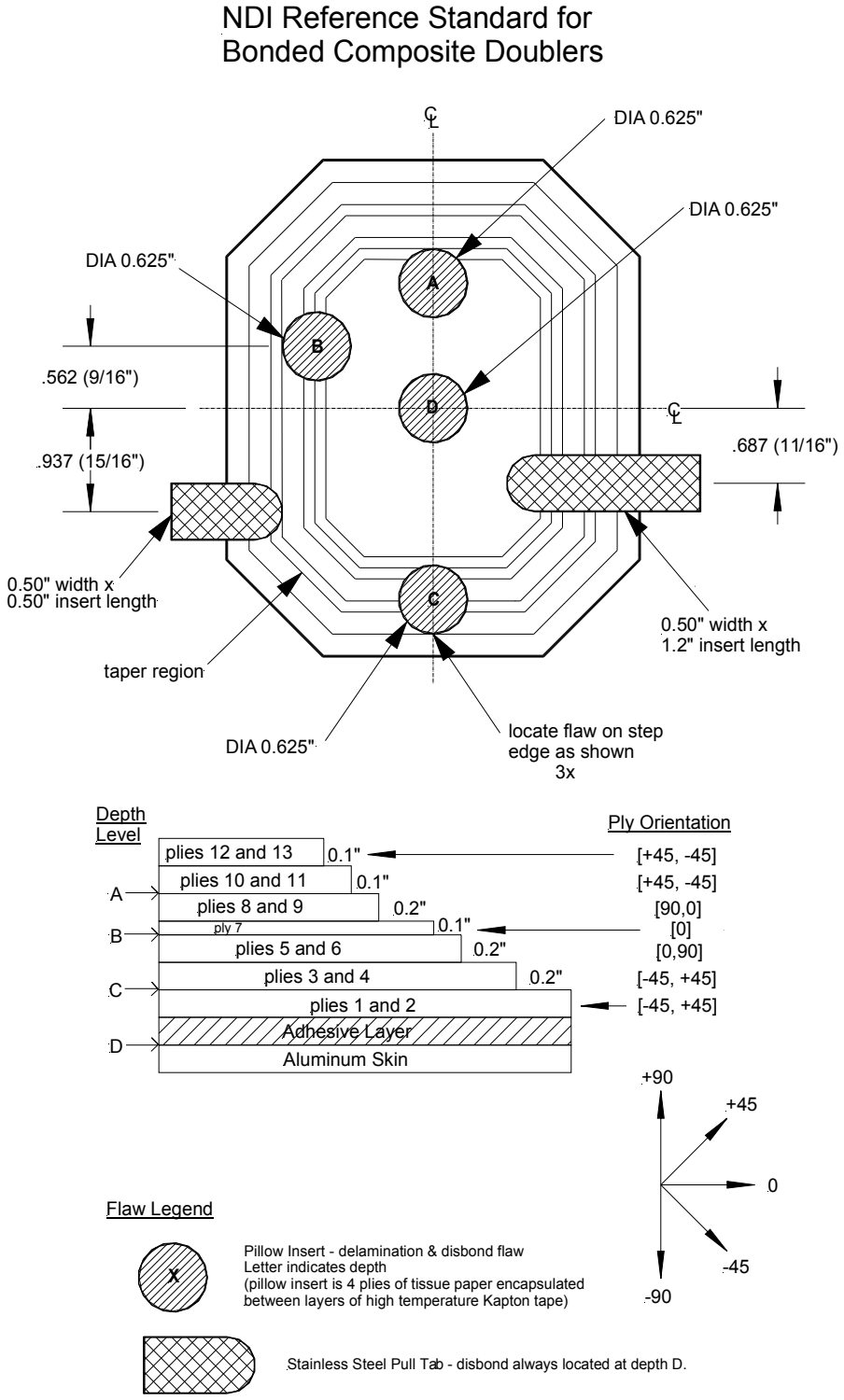

Figure A-1: Composite Doubler NDI Reference Standard - 13 Ply Doubler Mounted to 0.071" Thick Aluminum Skin

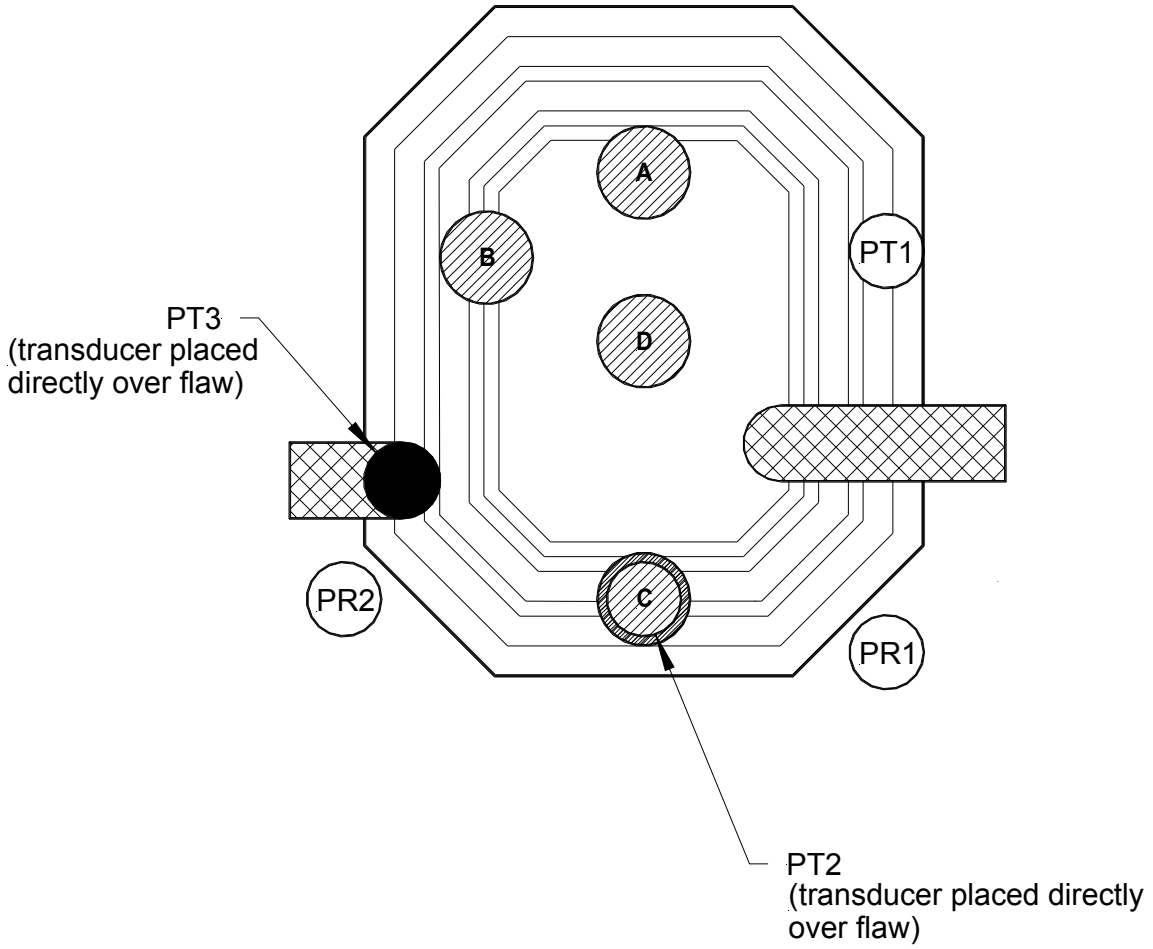

Figure A-2: Transducer Set-Up for Calibration on Tapered Region of Doubler

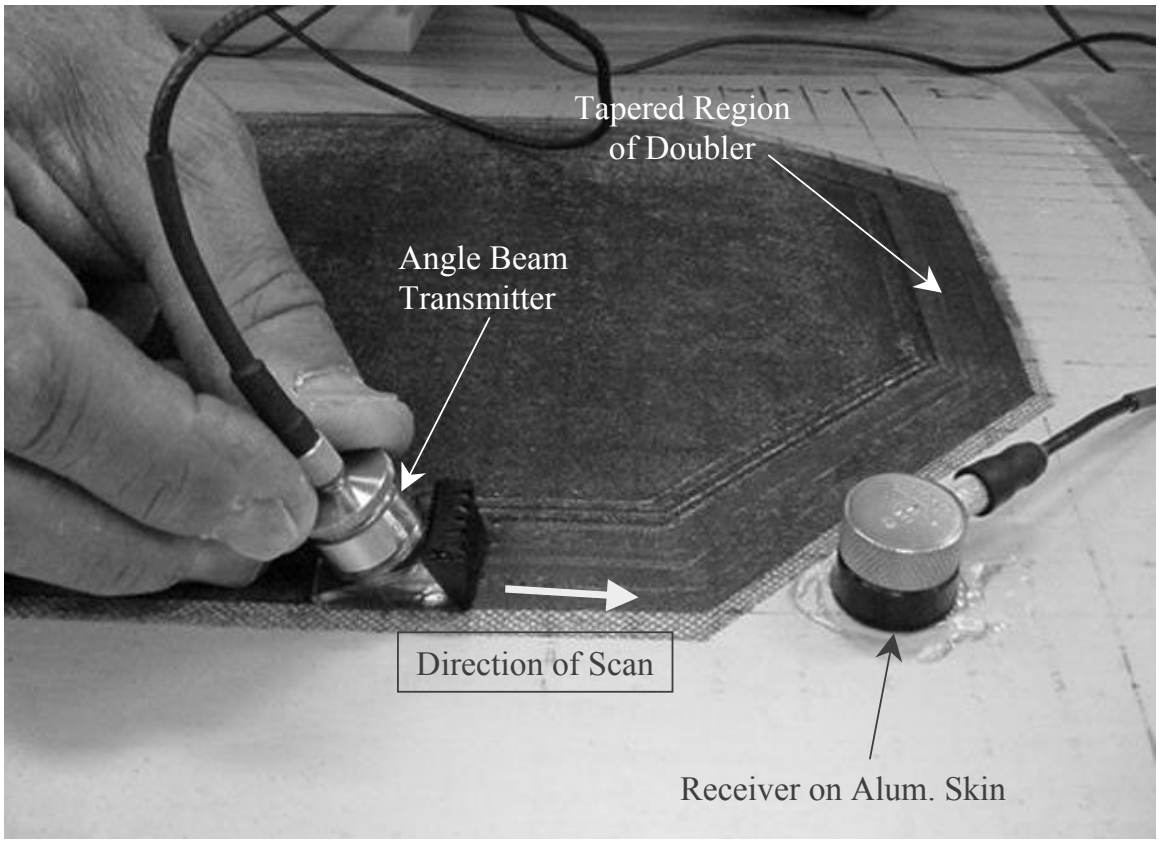

Figure A-3: Ultrasonic Pitch-Catch Sensor Set-Up on Composite Doubler for Inspections Around Tapered Perimeter of Doubler

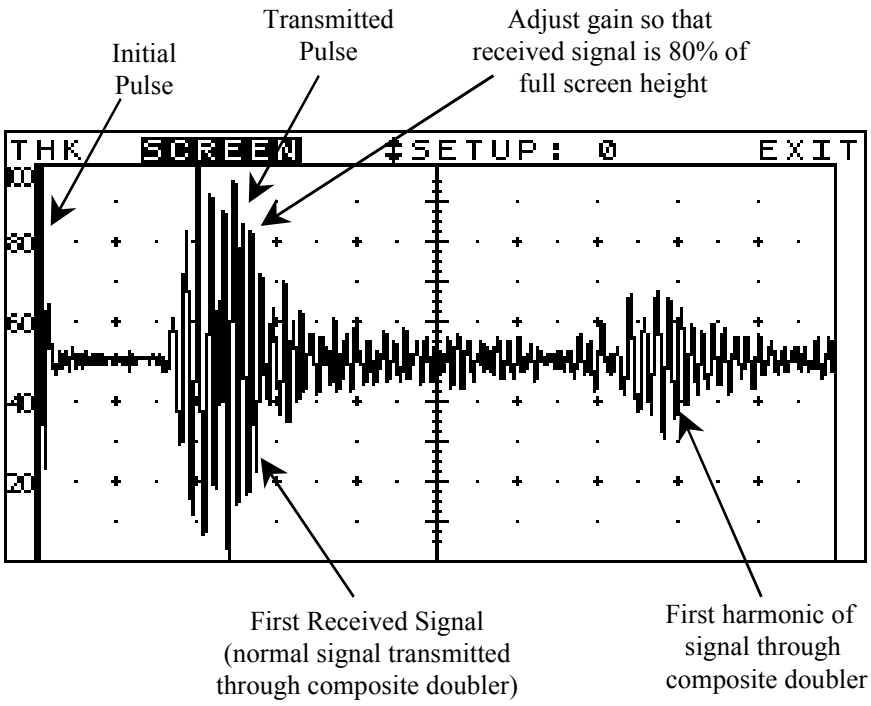

Figure A-4: Sample Ultrasonic Pitch-Catch Signal from an Unflawed Area of a Composite Doubler

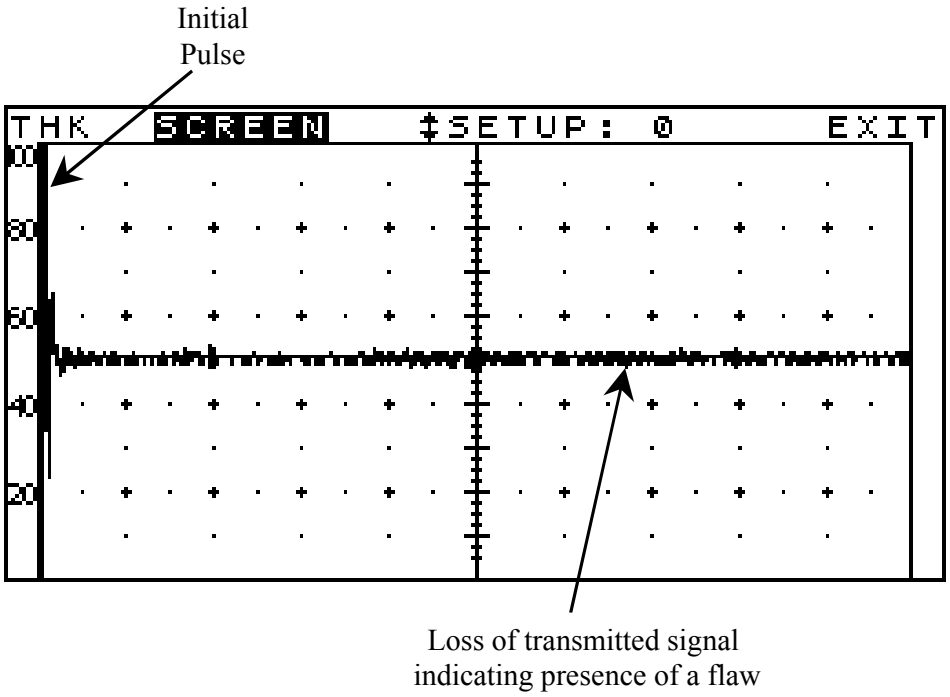

Figure A-5: Sample Ultrasonic Pitch-Catch Signal Corresponding to a Flaw Between Transmitter and Receiver Transducers

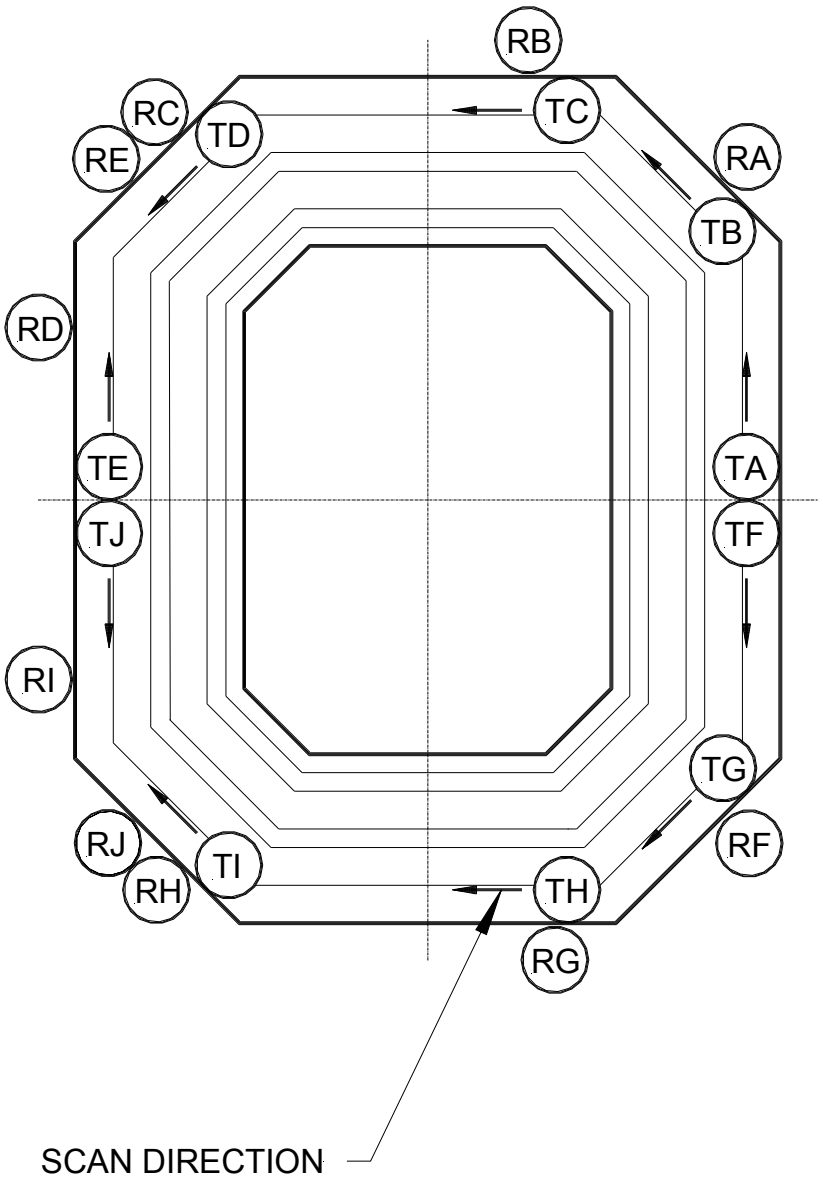

Figure A-6: Transmitter and Receiver Transducer Set-Up (Matched Pair Sets) to Inspect the Tapered Region of the Doubler

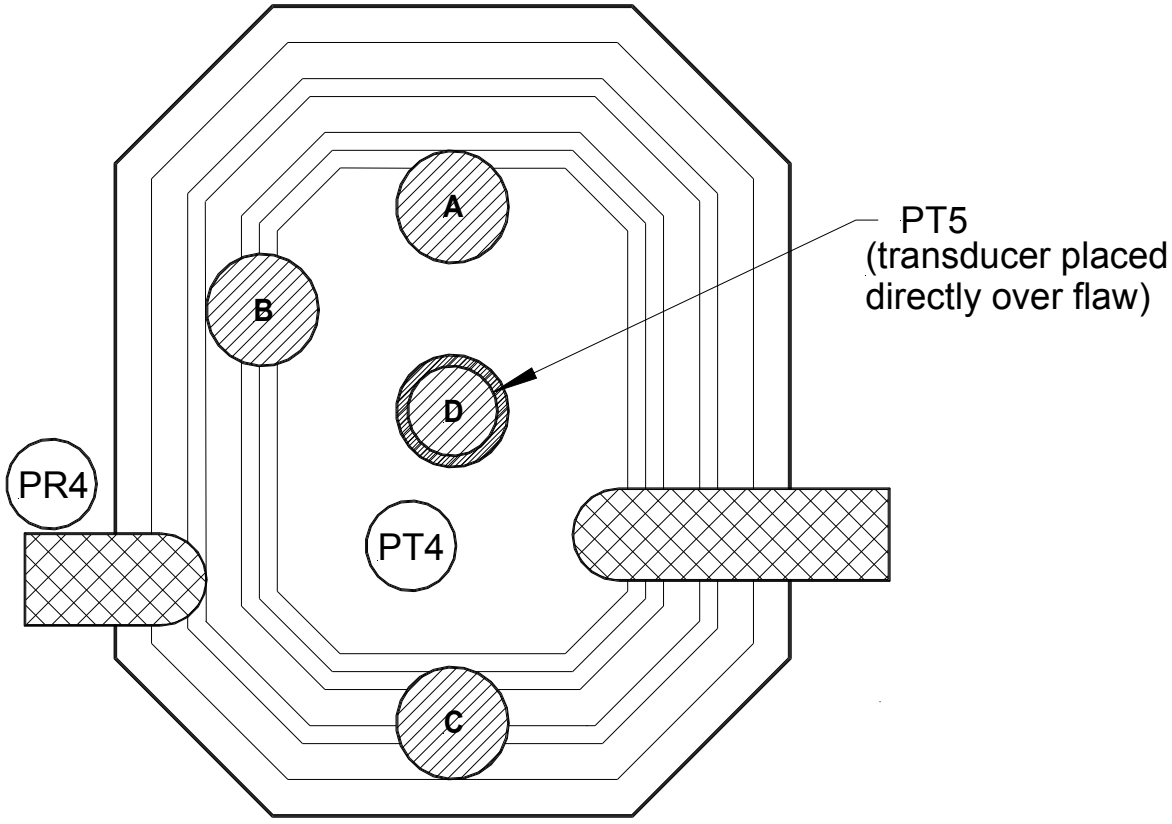

Figure A-7: Transducer Set-Up for Calibration on Full Thickness of Doubler

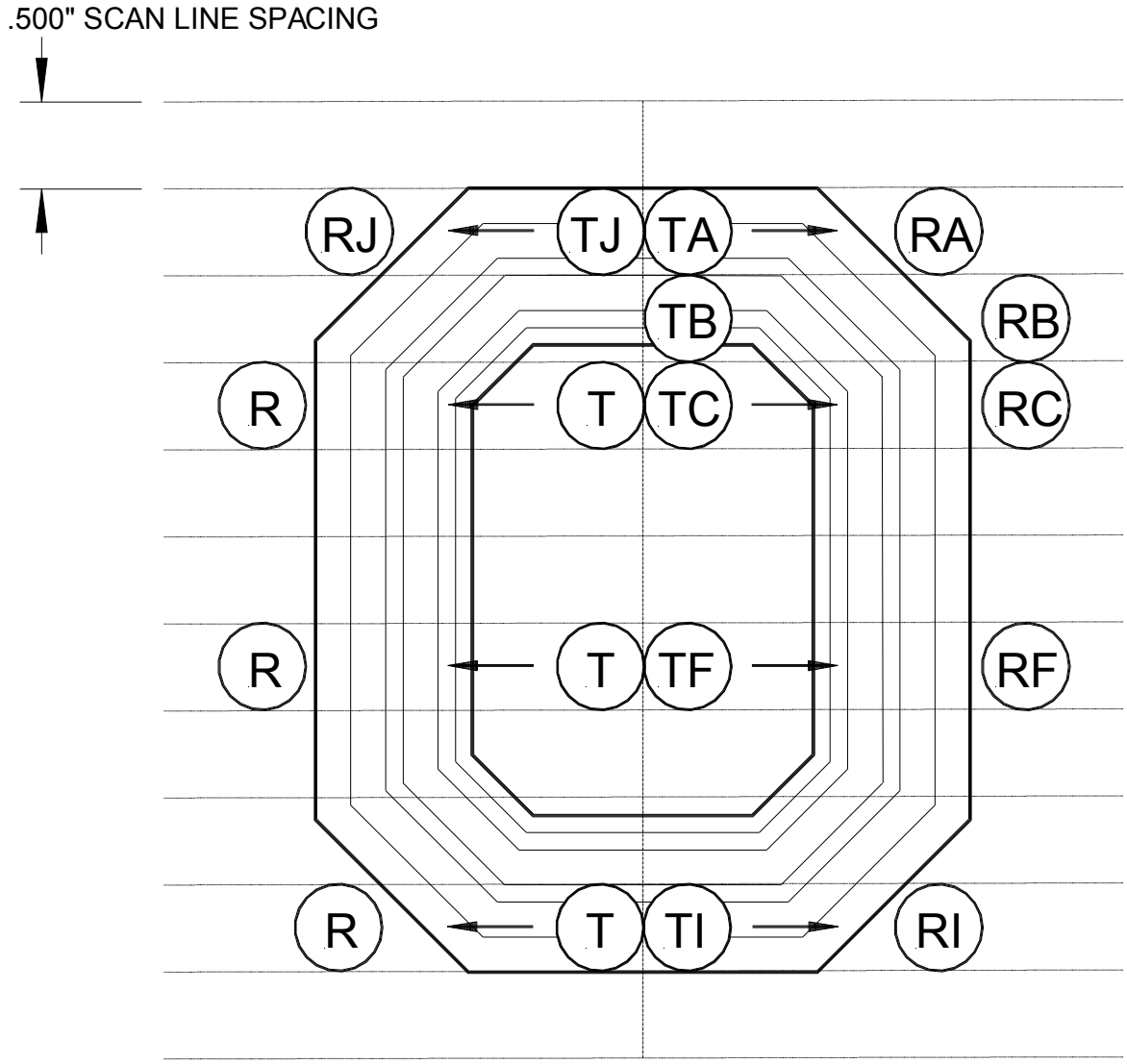

Figure A-8: Transmitter and Receiver Transducer Set-Up (Matched Pair Sets) to Inspect the Full Thickness Area and Tapered Region of the Doubler; Arrows Indicate Scan Direction for Transmitter

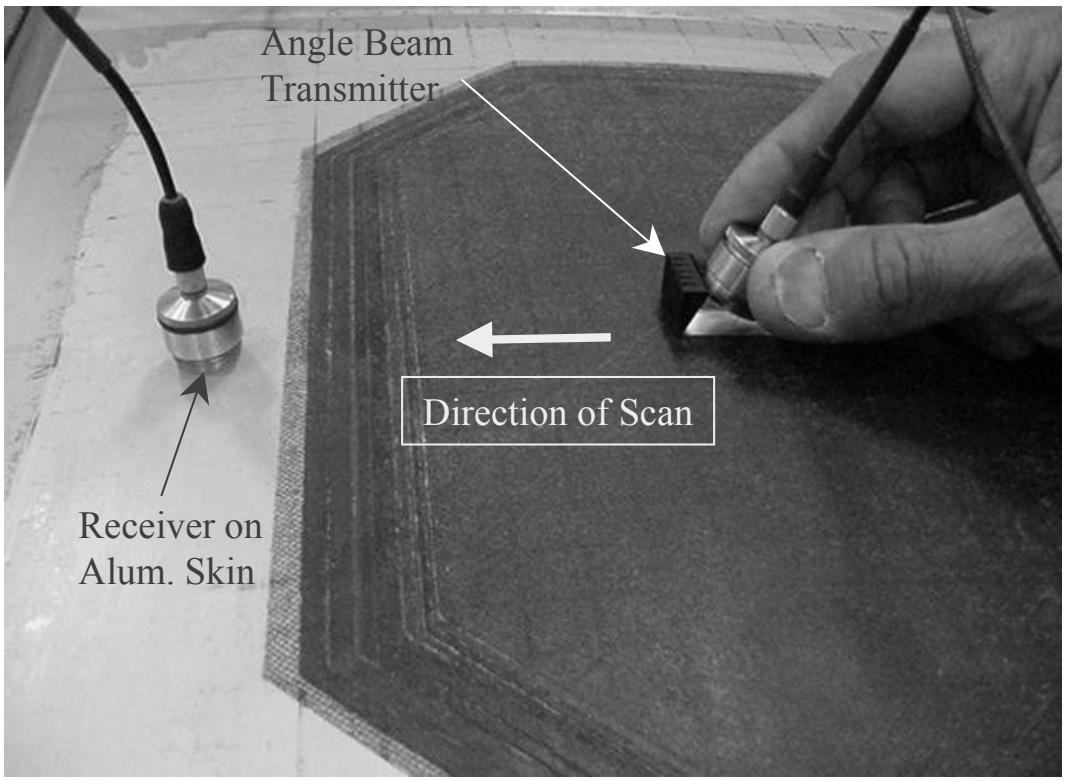

Figure A-9: Ultrasonic Pitch-Catch Sensor Set-Up on Composite Doubler for Inspections of Full Thickness Region and Tapered Area of Doubler

Appendix B

Design Drawing Notes to Guide the Composite Doubler Repair Process

General Notes for DC-10 Composite Doubler Skin Repair Drawing:

1. The purpose of this ROD drawing is to repair damage in DC-10 and MD-11 fuselage skins stemming from impact damage (dent, gouges), lightning strike, and corrosion removal (thinning). The repairs use bonded Boron-Epoxy doublers in lieu of conventional aluminum doubler repairs. No hole cutouts allowed. Skin damage may be grind outs up to 50% of skin thickness.

2. Doubler Material: Boron-Epoxy pre-preg unidirectional tape; Textron Specialty Materials 5521/4. Install and cure per the installation specification Boeing Specification D658-10183-1 (also listed as Specification Number TSM 200008-001.

3. Cover Ply Material: Style 120 glass fabric; pre-preg material, one half inch larger footprint than the patch.

4. Clean up scratches and gouges and blend out corrosion as per DC-10 SRM vol. I, ch.53

5. Inspect all holes that have fasteners removed for cracks using bolt hole eddy current technique. Re-install same strength hi-tigue fasteners where fasteners are removed. Use over sized fasteners as required to meet hi-tigue installation requirements. Wet install fasteners using MIL-S-81733.

6. Particular attention should be given to flushness of fasteners on fuselage contour to facilitate installation of the Boron-Epoxy doubler. Any fastener that protrudes 0.005" or greater shall be removed and same type reinstalled so that it is within +0.000"/-0.005" of flush with outside contour of fuselage skin.

7. For any external butt gap that is 0.040" or larger, the following should be done prior to installation of the Boron doubler.
   A. Remove all sealant in gap so that no sealant is under the footprint of the doubler.
   B. Fill butt gap where sealant was removed with MMM-A-132, Type I, Class 3 adhesive (EA 934NA or equivalent).

8. Cover fasteners and fill cracks, holes, and voids as pre procedures in Boeing Spec. D658-10183-1.

TITLE: BORON EPOXY FUS. SKIN REPAIR				
STRESS APPR		DATE:	SCALE:NONE	MODEL:DC-10
DESIGN APPR		DATE:	**ROD SKETCH**	
PREP BY	M. DELGADO	DATE:	**11-98-11-09-007**	

9. Prepare filler in step no. 8 and prepare the boron patch to minimize the exposure time of repair surface after surface preparation.
10. Prepare the repair area for bonding using non-tank phosphoric acid anodize method and prime as per Boeing Spec. D658-10183-1.

11. Fill dents and corrosion grind-out voids with an epoxy fill after the surface preparation. Use the following procedure:
    A. Cut woven fiberglass cloth into pieces ¼" or smaller.

    B. If additional viscosity is needed, mix fibers thoroughly with epoxy EA9396 A/B or EA 9394 in equal volumes. If additional viscosity is not needed, use the two part epoxy without any fiberglass fibers.
    C. Use trowel or similar tool to fill the void area taking precautions to avoid air entrapment.
    D. Co-cure the fiberglass/epoxy fill simultaneously with the boron doubler following step 12 to 15.

12. Before bonding doubler perform water break test as per Boeing Spec. D658-10183-1 (see also DC-10 SRM chapter 51-71-00) and optical primer inspection as per Boeing Spec. D658-10183-1.

13. Lay up Boron doubler as per design drawing.

14. Apply layer of film adhesive FM-73 (or equivalent AF-163) over aircraft repair area and then apply Boron repair doubler to the surface.

15. Install vacuum bag over repair and cure Boron repair doubler as per Boeing Spec. D658-10183-1. Choose appropriate temperature vs. time curing cycle to match ability of heat blankets to maintain the cure temperatures within allowable limits as per Boeing Spec. D658-10183-1.

TITLE: BORON EPOXY FUS. SKIN REPAIR				
STRESS APPR		DATE:	SCALE:NONE	MODEL:DC-10
DESIGN APPR		DATE:	**ROD SKETCH**	
PREP BY	M. DELGADO	DATE:	**11-98-11-09-007**	

16. Inspections shall be made with an instrument that can detect a 0.5” diameter disbond or delamination flaw. A maximum of 5% of the central area of the doubler may have voids or contain porosity. The central area is defined as the region of the Boron doubler that is full thickness. Voids must be separated by 3 inches minimum. Flaws found will be reported to engineering for disposition. The following periodic inspections of the Boron doubler and bondline shall be performed:
    A. After 30-45 days – inspect doubler and bondline per Boeing NDT Standard Practices Manual
    B. After one year– inspect doubler and bondline per Boeing NDT Standard Practices Manual, intervals not to exceed 4500 flight hours.

17. Fillet seal periphery of doubler using MIL-S-81733 or equivalent in accordance with Boeing Spec. D658-10183-1.

18. Prime the aluminum surface and paint the aluminum and Boron doubler using approved paint material.

19. Stencil the following note, using 3/8” high letters and in a contrasting color, and locate the note on the Boron doubler: “Bonded Repair, Do Not Apply Paint Strippers in This Area”

20. The quality of the surface preparation and the resulting bond between the doubler and the structure, will be determined as per Boeing Spec. D658-10183-1.
    A. Fabricate two 0.063” th. X 1” W X 4" L test strips from 7075-T6 or 2024-T3 aluminum bare plate.
    B. Prepare one surface of each strip for bonding using the same process used for the surface preparation of the aircraft structure (Boeing Spec. D658-10183-1).
    C. Place the two test strips adjacent to the Boron doubler but still on a portion of the aircraft skin that has been prepared for bonding.
    D. Bond and cure the test strips concurrently with the Boron doubler.
    E. Following cure, use a Phenolic wedge to remove the test strip.
    F. Note any adhesive bond failure and report to engineering for disposition.

21. Ref. Boeing Contract # 96D-084

TITLE: BORON EPOXY FUS. SKIN REPAIR				
STRESS APPR		DATE:	SCALE:NONE	MODEL:DC-10
DESIGN APPR		DATE:	**ROD SKETCH**	
PREP BY	M. DELGADO	DATE:	**11-98-11-09-007**	

DISTRIBUTION:

Frances Abrams
AFRL/MLMP
2977 Hobson Way
Bldg 653, Rm 215
Wright-Patterson AFB OH 45433-7739

Paul Acres
Lockheed-Martin Aero
Lockheed Blvd.
Bldg. 4, 1st Floor, Column 22C
Ft Worth, TX 76108

Cyro Areco
Embraer
Av. Brigadeiro Faria Lima, 2.170
12227-901 Sao Jose Dos Campos - SP
BRAZIL

Aydin Akdeniz
Boeing
PO Box 3707 MC 03-XP
Seattle, WA 98124-2207

Jay Amos
Cessna Aircraft
Dept. 352, M/S 1
P.O. Box 7704
Wichita, KS 67277-7704

Paulo Anchieta da Silva
Embraer
Av. Brigadeiro Faria Lima 2.170
12227-901 São José dos Campos, São Paulo
BRAZIL

James Arnold
NDT Manager
Continental Airlines
4849 Wright Road
Houston. TX 77032

Mike Augustin
Bell Helicopter Textron
P.O. Box 482
Ft. Worth, TX 76101

Brian Baggot
Laser Technology Inc.
1055 West Germantown Pk
Norristown, PA 19403

Eric Bartoletti
American Airlines
1725 W 20th Street
MD1200-DFW
DFW Airport, TX 75261

John Bakuckas
FAA William J. Hughes Technical Center
AAR-480
Atlantic City Int'l Airport, NJ 08405

Andrew Bayliss
British Airways
Aircraft Structures & Qual Standards
P.O. Box 10 B4 TBA S343
Hounslow, Middlesex
UNITED KINGDOM, TW6 2JA

Marc Berger
Lufthansa Technik
Weg beim Jaeger 193
22335 Hamburg
GERMANY

Phil Berkley
GKN Westland Aerospace
Materials Laboritory
Box 103 Yeovil
BA20 2YB UNITED KINGDOM

Subra Bettadapur
NAVAIR 4.3.4.2
Bldg. 2188 MS-5
48066 Shaw Rd.
Patuxent River, MD 20670-1908

Wolfgang Bisle
AIRBUS Deutschland GmbH
Dept.: ESWNG / Testing Tech. Germany
Huenefeldstr. 1-5
28199 Bremen, GERMANY

Bryce Boe
Raytheon Aircraft Co.
P.O. Box 85
Wichita, KS 67201-0085

Pete Boudreau
Delta Air Lines
Technical Operations Center - Dept. 554
1775 Aviation Blvd.
Atlanta, GA 30354

Rudy Braun
Boeing Canada Technology Ltd.
Winnipeg Division
99 Murray Park Road
Winnipeg, Manitoba R3J 3M6
CANADA

John Brausch
AFRL/MLSA
2179 12th Street, Bldg 652, Rm 122
Wright-Patterson AFB, Ohio 45433-7718

Nick Brinkhoff
Cessna Aircraft Co.
Box 7704
Wichita, KS 67277-7704

Al Broz
Chief Scientist and Technical Advisor
FAA NRS NDI
FAA New England, ANE 105N
12 New England Exec. Dev. Park
Burlington, MA 01803

Alistair Burns
Air New Zealand
Eng. Base, Geoffrey Roberts Road
Auckland International Airport
P.O. Box 53098
Auckland NEW ZEALAND

Michael Canipe
Lockheed Martin Aeronautics Company
Dept 6E5M, Zone 0199
86 South Cobb Drive
Marietta, GA 30063-0199

Michael Canning
GKN Westland Aerospace
Avonmouth Rd.
Avonmouth, Bristol BS11 9DU
UNITED KINGDOM

Steve Cargill
Aerospace Structural Integrity
8637 SE Sharon Street
Hobe Sound, FL 33455

LCDR Mark Carmel
Chief, HH-60J Engineering Branch
USCG Aircraft Repair and Supply Center
Elizabeth City, NC 27909

Jerry Carr
Corpus Christi Army Depot
P.O. Box 81325
Corpus Christi, TX 78468-1325

Fu-Kuo Chang
Dept. of Aeronautics and Astronautics
Durand Buiilding Room 250
Stanford University
Stanford, CA 94305

Randy Chappelear
Northwest Airlines Inc.
Department C8520
7500 Airline Drive
Minneapolis, Minnesota 55450-1101

Eric Chesmar
United Airlines
Maintenance Operations - SFOEG
San Francisco Int'l Airport
San Francisco, CA 94128-3800

Stef Chiovelli
Syncrude Canada Ltd.
9421 17 Avenue NW
Edmonton, Alberta T6N 1H4
CANADA

Bill Claus
Lockheed Martin - Palmdale
MZ 1115 / Bldg 611
1011 Lockheed Way
Palmdale CA 93599-1115

Francisco Coelho
TAP Air Portugal
P.O. Box 50194
Lisbon,1704 Lisbon Codex
PORTUGAL

Mark Collins
FedEx
7401 World Way West
Los Angeles, CA 90045

Matt Conaway
Cessna Aircraft Company
Dept 352, M/S 1
2617 S. Hoover Rd
Wichita, KS 67215

Jack Conrad
American Airlines
Mail Drop 8948 Hangar
2000 Eagle Parkway
FT. Worth, TX 76161

Vicente Cortes
Airbus España
Materials & Processes
John Lennon S/N
28906 Getafe, Madrid
SPAIN

Ed Cosgro
Petroleum Helicopters, Inc.
P.O. Box 90808
Lafayette, LA 70509-0808

Vance Cribb
Bell Helicopter Textron
P.O. Box 482
Ft. Worth, TX 76101

Ed Cuevas
FAA Rotorcraft Directorate
2601 Meacham Blvd
Ft Worth, TX 76137

Dave Cummins
GKN Westland Helicopters
Box 103 Yeovil BA20 2YB
UNITED KINGDOM

James Dalton II
Lockheed Martin Aeronautics
Dept. 6E5, Mail Zone 8662
P. O. Box 748
Fort Worth, TX 76101

Wayne Davis
Manager, Aircraft Inspection
United Airlines - INDIQ
2825 W. Perimeter Rd.
Indianapolis, IN 46241

Victor del Valle
Syncrude Canada Ltd.
9421 17 Avenue NW
Edmonton, Alberta T6N 1H4
CANADA

Ken Horne
Delta Air Lines
Dept. 382
P.O. Box 20706
Atlanta, GA 30320

Jacques Desjardins
Bombardier Transportation North America
Structure and Truck Engineering
1101 Parent St.
St-Bruno, Quebec J3V 6E6
CANADA

Juan Garcia Diaz
IBERIA Airlines
IBERIA Dirección de Material
Zona Industrial # 2
Madrid 28042
SPAIN

Christopher Dragan
Air Force Insitute of Technology
Ks. Boleslawa 6
P.O. Box 96
01-494 Warsaw
POLAND

Tommy Drake
Lockheed Martin Aeronautics - Fort Worth
One Lockheed Blvd. MZ 6852 Bldg.4/1/23C
Fort Worth, TX 76108

Marco Dube
Lufthansa Technik AG
Airframe Related Components WD51
Weg Beim Jager 193
22335 Hamburg
GERMANY

Philippe Dupont
Air France
Hangar H2
Le Bourget Overhaul Center
F93352 Le Bourget
FRANCE

Edmond Dusablon
Lockheed Martin - Palmdale
MZ 1105 / Bldg 611
1011 Lockheed Way
Palmdale CA 93599-1105

Phil Edwards
Flight Sergeant Customer Focus- NDET
Royal Air Force St Athan BARRY
Vale of Glamorgan CF62 4WA
UNITED KINGDOM

Ewald Ekart
Lufthansa Technik
Dept. WF21
60546 Frankfurt
GERMANY

David Elazar
Israel Aircraft Industries
Dept 4416
70100 BG Int'l Airport
ISRAEL

Matt Exner
American Airlines
2000 Eagle Parkway
Ft. Worth, TX 76177-2300

Allen Fawcett
Boeing
PO Box 3707 MC OY-EL
Seattle, WA 98124-2207

Peter Feddern
Lufthansa Technik
Department: HAM WO 484
Weg beim Jaeger 193
D-22335 Hamburg
GERMANY

Ernie Fidgeon
Air Canada
Base 891 - 2450 Saskatchewan Ave
Winnipeg, MB R3C2N2
CANADA

Tom Flournoy
FAA WJ Hughes Technical Center
AJP-6360
Atlantic City Int'l Airport, NJ 08405

Joe Floyd
Boeing
Box 3707 MC 2M-13
Seattle, WA 98124-2207

Laurent Fontaine
Airbus Industries
1 Rond Point Maurice Bellonte
31707 Blagnac Cedex
FRANCE

Joe Gabris
Boeing
PO Box 516 MS S270-4360
St Louis, MO 63166-0516

Lori Flansburg
Lockheed Martin Aeronautics
Mail Zone 0567/ B95
86 S. Cobb Dr.
Marietta GA 30063-0567

Andrew Freese
Air New Zealand
Engineering Base, Geofffrey Roberts Rd.
Aukland Int'l Airport
Po Box 53098
Aukland, NEW ZEALAND

Yolanda de Frutos Galindo
Airbus España
Materials & Processes
John Lennon S/N
28906 Getafe (Madrid) SPAIN

Jean-Baptiste Gambini
Airbus Industrie
1 Rond Point Maurice Bellonte
31707 Blagnac Cedex, FRANCE

Michel Gadbin
Airbus
Nantes - Rue de l'Aviation
44340 Bouguenais
FRANCE

Steve Galea
Aeronautical and Maritime Res. Lab
Defense Science Technology Org.
P.O. Box 4331
Melbourne, Victoria 3001
AUSTRALIA

Dave Galella
FAA WJ Hughes Technical Center
AJP-6360
Atlantic City Int'l Airport, NJ 08405

Donald Gauronski
United Parcel Service
A/C Maintenance - Quality Control
3121 East Jurupa Street
Ontario,CA 91761

Bill Gerrish
Aerostructures Customer Support
BF Goodrich
850 Lagoon Dr
Chula Vista, CA 91910-2001

Jon Goo
Aloha Airlines
P.O. Box 30028
Honolulu, Hawaii 96820

Bert Groenewoud
Eng. & Maintenance (SPL/CF)
KLM Royal Dutch Airlines
P.O. Box 7700
1117 ZL Schiphol Airport
NETHERLANDS

Mike Gutierrez
Federal Express
7401 World Way West
Los Angeles, CA 90045

Colin Hanna
Bombardier Aerospace
Materials and Processes Eng. Dept.
Airport Road, Belfast BT3 9DZ
UNITED KINGDOM

Robert Hawley
BP Exploration Alaska
Alaska Gas Team
900 E. Benson Blvd
Anchorage, AK 99508

Pekka Hayrinen
Finnair
Helsinki-Vantaa -Airport
XU-28
Helsinki, 01053
FINLAND

Todd Herrington
Delta Air Lines
Dept. 554
P.O. Box 20706
Atlanta, GA 30320

Pam Herzog
Air Force NDI Office
AFRL/MLS-OL
4750 Staff Drive
Bldg. 3230 Rm. 111
Tinker Air Force Base, OK 73145

John Hewitt
Airbus
Materials Laboratory
No. 1 Flight Shed
Filton, Bristol BS99 7AR
UNITED KINGDOM

Keith L. Hickman
Lockheed Martin
P.O. Box 650003 M/S SK-04
Dallas, TX. 75265-0003

Colin Hockings
Qantas Airlines
NDT Section, C/- Central Stores M189
Mascot, 2020
AUSTRALIA

Jim Hofer
Boeing
2401 E. Wardlow Rd.
MC C098-0100
Long Beach, CA 90807-4418

Ed Hohman
Bell Helicopter
PO Box 482
Fort Worth, TX 76101

Mike Hoke
ABARIS Training
5401 Longley Lane, Suite 49
Reno, NV 89511

Quincy Howard
The Boeing Company
P.O. Box 3707 M/S 04-EH
Seattle, WA 98124

David Hsu
Center for Nondestructive Evaluation
1917 Scholl Road
Iowa State University
Ames, IA 50011

David Huddleston
United Space Alliance
8550 Astronaut Blvd.
Cape Canaveral, FL 32920-4304

Larry Ilcewicz
Chief Scientist and Advisor
FAA NRS Composites
1601 Lund Ave. SW
ANM-115N
Renton, WA 98055

Ed Ingram
Lockheed-Martin
Zone 0441, D/6E5M
86 South Cobb Drive
Marietta, GA 30063-0441

Darrel Jone
The Boeing Company
PO Box 3707
MS 2L-24
Seattle, Washington 98124-2207

Russell Jones
National Resource Specialist NDI
FAA National Headquarters
800 Independance Ave S.W.
Washington DC, 20591

Birgit Junker
Vestas Wind Systems A/S
Quality and Enviromental Dept.
6940 Lem St.
Smed Hansens Vej 27 DENMARK

Barbara Kanki
NASA Ames Research Center
MS 262-4
Moffett Field, CA 94035-1000

Tap Kartiala
Lockheed Martin - Palmdale
MZ 1133 / Bldg 611
1011 Lockheed Way
Palmdale CA 93599-1133

Tony Kepczyk, SQNLDR
Royal Australian Air Force
DGTA - DAIRMAINT
RAAF Base Hangar 410
Amberley, Queensland 4306
AUSTRALIA

Slawomir Klimaszewski
Air Force Institute of Technology;
ul. Ks. Boleslawa 6
P.O. Box 96
01 - 494 Warsaw
POLAND

Bryan Knowles
Southwest Airlines
2832 Shorecrest Dr
DAL-2MX
Dallas, TX 75235-1611

Jeff Kollgaard
Boeing
P.O. Box 3707, MS 2T-42
Seattle, WA 98124-2207

Hans Kramer
Eng. & Maintenance (SPL/CF)
KLM Royal Dutch Airlines
P.O. Box 7700
1117 ZL Schiphol Airport NETHERLANDS

Jim Krone
Cessna Aircraft Company
P.O. Box 7704
Wichita, KS 67277-7704

Paul Kulowitch
Navy
Naval Air Warfare Center Aircraft Division
48066 Shaw Rd.
Building 2188, Unit 5
Patuxent River, MD 20670

Chakib Lahlou
Alaska Airlines-SEAME
PO BOX 68900
Seattle, WA 98168

Al Kumnick
Specialty Materials Inc.
1449 Middlesex St.
Lowell, MA 01851

James Lance
Lockheed-Martin Aero
D/6E5M B-95 Zone 0595
86 S Cobb Dr
Marietta, GA 30063-0441

Lloyd Landburg
Quality Control NDT Analyst
Southwest Airlines
2832 Shorecrest Dr DAL/2MX
Dallas, TX 75235

Silvia Lazcano-Urena
Airbus Espana
Pso. John Lennon s/n
28906 Getafe, Madrid
SPAIN

Eric Le Nir
Air France
Hangar H2
Le Bourget Overhaul Center
F93352 Le Bourget
FRANCE

Dec Lee
Northwest Airlines Inc.
Department C8020
7500 Airline Drive
Minneapolis, Minnesota 55450-1101

Arne Lewis
Boeing
P.O. Box 3707 M.C. 2L-24
Seattle, WA 98124

John Linn
Boeing Commercial Airplanes
P.O.Box 3707 M/S 2M-12
Seattle, WA 98124-2207

Fabiano Garcia Lobato
Embraer
Av. Brigadeiro Faria Lima, 2170
12227-901 Sao Jose Dos Campos - SP
BRAZIL

Maria Lodeiro
Centre for Materials Measurement
National Physical Laboratory
Queens Rd.
Teddington, Middlesex TW11 0LW
UNITED KINGDOM

John Lundeen
NDI Engineer
Naval Air Warfare Center, Aircraft Div
Bldg. 2188, MS-5
Patuxent River, MD 20670

Matt Malkin
Boeing/Phantom Works
Mail Stop 42-25
9725 East Marginal Way S.
Seattle, WA 98108

Pekka Manninen
Finnair
PL 15, EN / 28
Helsinki-Vantaa Airp, FIN - 01053
FINLAND

Rod Martin
Chief Executive Officer
Materials Engineering Research Lab
Wilbury Way
Hitchin, SG4 0TW
UNITED KINGDOM

Mike Matthews
Delta Air Lines
Technical Operations Center - Dept. 578
1775 Aviation Blvd.
Atlanta, GA 30354

Maria-Angeles Marti Martinez
Airbus
Ctra. Nac. Madrid-Toledo km32
Señorio de Illescas
Area Terciaria
45200 Illescas - Toledo
SPAIN

Greg Marshall
Bell Helicopter
PO Box 482
Fort Worth, TX 76101

Sergio Mayer
Embraer
Av. Brigadeiro Faria Lima, 2170
1227-90 San Jose dos Campos – SP
BRAZIL

Glae McDonald
US Airways
5020 Hangar Rd.
Charlotte, NC 28219

Alexander Melton
Northwest Airlines
NDT Dept. C8843
1914 Benjamin Street NE
Minneapolis, Minnesota, 55418-4810

Bill Miller
Transport Canada
330 Sparks Street Tower C
Ottawa, Ontario K1A ON5
CANADA

Scott Miller
Alaska Airlines-SEAMQ
P.O. Box 68900
Seattle, WA 98168

Calvin Moore
Air Force NDI Office
AFRL/MLS-OL
4750 Staff Drive
Bldg. 3230 Rm. 111
Tinker Air Force Base, OK 73145

Matt Moye
Air Force NDI Office
AFRL/MLS-OL
4750 Staff Drive
Bldg. 3230 Rm. 111
Tinker Air Force Base, OK 73145

Tamotsu Nagasaka
All Nipon Airways
3-5-4, Haneda Airport
Ota-ku, Tokyo 144-0041
JAPAN

Sergio Nascimento
TAP Air Portugal
Maintenance & Engineering
P.O. Box 50194
Lisbon, 1704-801
PORTUGAL

Cu Nguyen
FAA WJ Hughes Technical Center
AAR-480
Atlantic City Int'l Airport, NJ 08405

Khaled Obaia
Syncrude Canada Ltd.
9421 17 Avenue NW
Edmonton, Alberta T6N 1H4
CANADA

John O'Connell
Cargolux Airlines Int'l S.A.
Luxembourg Airport,
Findel, Luxembourg L-2990
LUXEMBOURG

Paul Oulton
United Airlines SFOIQ
San Franciso Intl Airport
San Francisco, CA 94128

Georgios Papageorgiou
Olympic Airways
Athens International Airport, Tech. Base
OA.TD/IC
Spata-Athens, 19019
GREECE

Rob Pappas
FAA WJ Hughes Technical Center
AJP-6360
Atlantic City Int'l Airport, NJ 08405

Marvin Paschal
American Airlines
Mail Drop 8948 Hangar
2000 Eagle Parkway
Ft. Worth, TX 76161

Nilesh Patel
Goodrich Corp
111 Airport Dr
Foley, ALABAMA 36535

John Petrakis
FAA
800 Independence Av, SW
Washington, DC 20591

Wilfried Pieles
AIRBUS Deutschland GmbH
Dept.: ESWNG / Testing Tech. Germany
Huenefeldstr. 1-5
28199 Bremen GERMANY

David Piotrowski
Delta Air Lines
Department 572
PO Box 20706
Atlanta, GA 30320-6001

Rob Pitts
Naval Aircraft Materials Lab
Fleetlands Gosport
Hampshire PO130FL
UNITED KINGDOM

Richard Rachowiecki
British Airways
North Block Annex TBD E148
PO Box 10
Heathrow Airport
Hounslow, Middlesex TW 6 2JA
UNITED KINGDOM

Bernd Rackers
Airbus Deutschland GMBH
Hunefeldstrasse 1-5
21899 Bremen
GERMANY

Doug Ragsdale
Soutwest Airlines
Maintenance Control X-5929
2832 Shorecrest Dr
DAL-2MX
Dallas,TX 75235-1611

Kevin Rees
U.S. Army Aviation & Missiles Command
ATTN: AMSAM-MMC-VS-EC
Corpus Christi, TX 78419

Wayne Richmond
Federal Express
Mail Code 5413
3131 Democrat Road
Memphis, TN 38118

Michael Roach
Amtech Aeronautical Ltd.
765 McTavish Road NE
Calgary, Alberta T2E 7G8
CANADA

Jim Roberts
Delta Air Lines
Technical Operations Center - Dept. 496
1775 Aviation Blvd.
Atlanta, GA 30354

Mark Rodekuhr
BF Goodrich Aerospace
8200 Arlington Ave.
Riverside, CA 92503-0428

Ana Rodriguez
Airbus Espana
Pso. John Lennon s/n
28906 Getafe, Madrid
SPAIN

Olaf Ronsdorf
Lufthansa Technik AG
Customer Engrg FRA WI 21
Phein Main Airport
60546 Frankfurt
GERMANY

Thomas Rood
US Airways
8704 Totteridge Dr
Charlotte, NC 28277

Chris Root
NAVAIR Support Center North Island
Code 433, Bldg 378-2
PO BOX 357058
San Diego, CA 92135-7058

Jean Rouchon
Ministry of Defence
CEAT – 23 Avenue Henri Guillaumet
31056 Toulouse Cedex
FRANCE

Carl Rousseau
Lockheed Martin
PO Box 748, MZ 6527
Ft. Worth, TX 76101

Bob Saathoff
Cessna Aircraft Company
P. O. Box 7704
Dept. 352, M/S 1 - W1
Wichita, KS 67277-7704

Engin Sabuncu
Cessna Aircraft Company
Pawnee Engineering
5800 E. Pawnee
Wichita, KS 67218

Radovan Sarunac
Booz Allen Hamilton
Columbia Square, Suite 480 East
555 Thirteenth Street, N.W.
Washington, DC 20004

Adam Sawicki
Boeing Company
P.O. Box 16858 Mail Code P38-13
Philadelphia, PA 19142

Christine Scala
Aeronautical and Maritime Res. Lab
Defense Science Technology Org.
P.O. Box 4331
Melbourne, Victoria 3001
AUSTRALIA

Jeffery Schaff
Sikorsky Aircraft
6900 Main Street
Mail Stop: S352A
Stratford CT 06601-1381

Bob Scoble
United Airlines
Maintenance Operations - SFOIQ
San Francisco Int'l Airport
San Francisco, CA 94128-3800

Nikhilesh Sheth
Boeing
3855 N. Lakewood BLVD
Long Beach, CA 90846

Luiz Siegmann
VARIG Airlines
Engineering and Maintenance
Augusto Severo, 851 – POABS
Porto Alegre RS, 90240-480
BRAZIL

Vilmar da Silva do Valle
Embraer
Av. Brigadeiro Faria Lima, 2170
1227-90 San Jose dos Campos – SP
BRAZIL

Reinhardt Spiegel
Airbus
Ottenbecker Damm
21684 Stade
GERMANY

Holger Speckmann
AIRBUS Deutschland GmbH
Dept.: ESWNG / Testing Technology
Huenefeldstr. 1-5
28199 Bremen
GERMANY

Giancarlo Spera
Alitalia
Areoporto Leonardo da Vinci
Piazza Almerico da Schio
Fiumicino, Rome, 50
ITALY

Jack Springer
Federal Express
3131 Democrat Road
Memphis, TN 38118

Tim Stapleton
Boeing Canada Technology
Winnipeg Division
99 Murray Park Rd
Winnipeg, Manitoba R3J 3M6
CANADA

Robert Stevens
United Airlines
San Francisco Int'l Airport - SFOEP
NDT Process Engineering
San Francisco, CA 94128-3800

Timo Stöven
Airbus Deutschland GmbH
Hünefeldstrasse 1-5
28199 Bremen
GERMANY

Barry Sturgis, AIR-4.3.3
NAVY
Attn Bldg. 2187 Suite 2340A
NAVAIRSYSCOMHQ
48110 Shaw Rd Unit 5
Patuxent River, MD 20670-1906

Larry Sullivan
Goodrich Aerostructures
850 Lagoon Dr. mz 107P
Chula Vista, CA 91910-2098

Paul Swindell
FAA WJ Hughes Technical Center
AJP-6360
Atlantic City Int'l Airport, NJ 08405

Vagnaldo Teles de Carvalho
Embraer
Av. Brigadeiro Faria Lima, 2170
12227-901 - S.J. dos Campos - SP
BRAZIL

Roland Thevenin
Airbus
1 rond point Maurice Bellonte
31707 BLAGNAC
FRANCE

Vasu Thirumalai
Applied Aerospace Structures Corp.
3437 South Airport Way
P.O. Box 6189
Stockton, CA 95206

Darrell Thornton
UPS
750 Grade Lane
Louisville, KY 40213

Patrick Timmers
Northwest Airlines Inc.
Department C8020
7500 Airline Drive
Minneapolis, Minnesota 55450-1101

Alain Tissenier
Airbus Industries
1 Rond Point Maurice Bellonte
31700 Blagnac FRANCE

Gustav Tober
AIRBUS Deutschland GmbH
Dept.: ESWNG / Testing Tech. Germany
Huenefeldstr. 1-5
28199 Bremen
GERMANY

Ana Beatriz Tocalino
Embraer
Av. Brigadeiro Faria Lima, 2.170
(PC: 144/2)
12227-901 Sao Jose Dos Campos - SP
BRAZIL

Jeff Tom
Boeing
Phantomworks
5301 Bolsa Ave
Huntington Beach, CA 92647-2099

Albert Urdiroz
Airbus
1 Rond-Point Maurice Bellonte
31707 Blagnac Cedex
FRANCE

K. Dick Vaughn
Rocky Mountain Composites
301 W. 3000 N.
Spanish Fork, UT 84660

Victor Vilents
PK Design
Sevanskaya st. 3 app 170
Moscow 115516
RUSSIA

John Vogt
The Nordham Group
11200 E. Pine St.
Tulsa, OK 74116

Simon Waite
European Aviation Safety Agency
Postfach 10 12 53
D-50452 Köln
GERMANY

William Wall
FAA William J Hughes Technical Center
AJP-6360
Atlantic City Int'l Airport, NJ 08405

Patrick Walter
Texas Christian University
Engineering Dept., Box 298640
Ft. Worth, TX 76129

Richard Watkins
Delta Air Lines
Dept. 530
P.O. Box 20706
Atlanta, GA 30320-6001

Guenter Wehmann
AIRBUS Deutschland GmbH
Dept.: ESWNG / Testing Tech. Germany
Huenefeldstr. 1-5
28199 Bremen
GERMANY

Bud Westerman
Boeing
Box 3707 MC 42-23
Seattle, WA 98124-2207

Brian Williams
British Airways
North Block Annex TBD E148
PO Box 10
Hounslow, Middlesex, TW6 2JA
UNITED KINGDOM

Scott Williams
Southwest Airlines
2620 George Street
Pearland, TX 77581

Roy Wong
Bombardier Aerospace
P.O. Box 6087, Succursale, Centre-ville
Montreal, Quebec H3C 3G9
CANADA

Roman Wottle
Austrian Airlines
Austrian Base / TDWM
Vienna Airport, A-1300
AUSTRIA

John Yadon
Navy
NAVAIR Depot Jacksonville, Code 49730
NAS Jacksonville, FL 32212-0016

Jun Yamanaka
Japan Airlines International
M1 Bldg. 3-5-1, Haneda Airport
Ota-ku, Tokyo 144-0041
JAPAN

Sandia National Labs:
MS-0116 Alton Romig, 0004
MS-0724 Les Shephard, 6000
MS-1104 Margie Tatro, 6200
MS-1104 Rush Robinett, 6330
MS-1124 Jose Zayas, 6333
MS-0734 Bernard Zak, 6338
MS-0769 Dennis Miyoshi, 6400
MS-0762 Brad Parks, 6410
MS-0615 Roger Hartman, 6416
MS-0615 Mike Bode, 6416
MS-0615 Waylon Delong, 6416
MS-0615 Tonimarie Dudley, 6038
MS-0615 Joe Dimambro, 6416
MS-0615 Gerry Langwell, 6416
MS-0615 Ciji Nelson, 6416
MS-0615 Kirk Rackow, 6416
MS-0615 Dennis Roach, 6416 (30)
MS-0791 Art Shanks, 6417
MS-0782 William Rhodes, 6418
MS-0762 Rebecca Horton, 6420
MS-0757 John Russell, 6423
MS-0768 Basil Steele, 6430
MS-0762 Joe Roesch, 6450
MS-0768 Tommy Woodall, 6460
MS-1003 Phil Heermann, 6470
MS-0768 Billy Marshall, 6480
MS-0557 Tom Carne, 1525
MS-0888 Dave Reedy, 1526
MS-1073 Steve Yepez, 1712
MS-0887 Duane Dimos, 1800
MS-0889 Mike Hosking, 1813
MS-0885 Jeff Braithwaite, 1826
MS-0885 Justine Johanes, 1810
MS-1245 John Emerson, 2453
MS-1245 David Zamora, 2453
MS-0507 Jim Woodard, 2600
MS-0968 Dan Schmitt, 2611
MS-1064 Stephen Lott, 2614
MS-1219 Walt Caldwell, 5923
MS-1218 Joe Sanders, 5924
MS-0131 Dick Perry, 12130
MS-0899 Technical Library, 4536 (2)
MS-9018 Central Technical Files, 8944